



**HAL**  
open science

# Study of granular platforms behaviour over soft subgrade reinforced by geosynthetics : Experimental and numerical approaches

Nicole Khoueiry

► **To cite this version:**

Nicole Khoueiry. Study of granular platforms behaviour over soft subgrade reinforced by geosynthetics : Experimental and numerical approaches. Civil Engineering. Université de Lyon, 2020. English. NNT : 2020LYSEI027 . tel-03098453

**HAL Id: tel-03098453**

**<https://theses.hal.science/tel-03098453v1>**

Submitted on 5 Jan 2021

**HAL** is a multi-disciplinary open access archive for the deposit and dissemination of scientific research documents, whether they are published or not. The documents may come from teaching and research institutions in France or abroad, or from public or private research centers.

L'archive ouverte pluridisciplinaire **HAL**, est destinée au dépôt et à la diffusion de documents scientifiques de niveau recherche, publiés ou non, émanant des établissements d'enseignement et de recherche français ou étrangers, des laboratoires publics ou privés.



N°D'ORDRE NNT: 2020LYSEI027  
ANNÉE 2020

THÈSE de DOCTORAT DE L'UNIVERSITÉ DE LYON  
*OPÉRÉE AU SEIN DE  
INSA-Lyon*

ECOLE DOCTORALE MÉCANIQUE, ENERGÉTIQUE, GÉNIE CIVIL, ACOUSTIQUE  
(MEGA)

SPÉCIALITÉ/ DISCIPLINE DE DOCTORAT  
GÉNIE CIVIL

SOUTENUE PUBLIQUEMENT LE 16/04/2020, PAR  
**KHOUEIRY Nicole**

---

**Study of granular platforms behaviour over soft  
subgrade reinforced by geosynthetics:  
experimental and numerical approaches**

---

Devant le jury composé de:

VILLARD Pascal	Professeur des Universités	UGA	Rapporteur
REIFFSTECK Philippe	Directeur de recherche	Université G. EIFFEL	Rapporteur
TOUZE Nathalie	Ingénieure des ponts, des eaux et des forêts, HDR	INRAE	Examinatrice
DELMAS Philippe	Professeur des Universités	Cnam	Examineur
DAOUADJI Ali	Professeur des Universités	INSA Lyon	Directeur de thèse
BRIANÇON Laurent	Maitre de Conférences	INSA Lyon	Co-Directeur de thèse
RIOT Mathilde	Ingénieure	AFITEXINOV	Invitée

GEOMAS, INSA-Lyon 17 rue des Arts, F-69621, Villeurbanne CEDEX-France



## Département FEDORA – INSA Lyon - Ecoles Doctorales – Quinquennal 2016-2020

SIGLE	ECOLE DOCTORALE	NOM ET COORDONNEES DU RESPONSABLE
<b>CHIMIE</b>	<b><u>CHIMIE DE LYON</u></b> <a href="http://www.edchimie-lyon.fr">http://www.edchimie-lyon.fr</a> Sec. : Renée EL MELHEM Bât. Blaise PASCAL, 3e étage <a href="mailto:secretariat@edchimie-lyon.fr">secretariat@edchimie-lyon.fr</a> INSA : R. GOURDON	<b>M. Stéphane DANIELE</b> Institut de recherches sur la catalyse et l'environnement de Lyon IRCELYON-UMR 5256 Équipe CDFA 2 Avenue Albert EINSTEIN 69 626 Villeurbanne CEDEX <a href="mailto:directeur@edchimie-lyon.fr">directeur@edchimie-lyon.fr</a>
<b>E.E.A.</b>	<b><u>ÉLECTRONIQUE,</u></b> <b><u>ÉLECTROTECHNIQUE,</u></b> <b><u>AUTOMATIQUE</u></b> <a href="http://edeea.ec-lyon.fr">http://edeea.ec-lyon.fr</a> Sec. : M.C. HAVGOUDOUKIAN <a href="mailto:ecole-doctorale.eea@ec-lyon.fr">ecole-doctorale.eea@ec-lyon.fr</a>	<b>M. Gérard SCORLETTI</b> École Centrale de Lyon 36 Avenue Guy DE COLLONGUE 69 134 Écully Tél : 04.72.18.60.97 Fax 04.78.43.37.17 <a href="mailto:gerard.scorletti@ec-lyon.fr">gerard.scorletti@ec-lyon.fr</a>
<b>E2M2</b>	<b><u>ÉVOLUTION, ÉCOSYSTÈME,</u></b> <b><u>MICROBIOLOGIE, MODÉLISATION</u></b> <a href="http://e2m2.universite-lyon.fr">http://e2m2.universite-lyon.fr</a> Sec. : Sylvie ROBERJOT Bât. Atrium, UCB Lyon 1 Tél : 04.72.44.83.62 INSA : H. CHARLES <a href="mailto:secretariat.e2m2@univ-lyon1.fr">secretariat.e2m2@univ-lyon1.fr</a>	<b>M. Philippe NORMAND</b> UMR 5557 Lab. d'Ecologie Microbienne Université Claude Bernard Lyon 1 Bâtiment Mendel 43, boulevard du 11 Novembre 1918 69 622 Villeurbanne CEDEX <a href="mailto:philippe.normand@univ-lyon1.fr">philippe.normand@univ-lyon1.fr</a>
<b>EDISS</b>	<b><u>INTERDISCIPLINAIRE</u></b> <b><u>SCIENCES-SANTÉ</u></b> <a href="http://www.ediss-lyon.fr">http://www.ediss-lyon.fr</a> Sec. : Sylvie ROBERJOT Bât. Atrium, UCB Lyon 1 Tél : 04.72.44.83.62 INSA : M. LAGARDE <a href="mailto:secretariat.ediss@univ-lyon1.fr">secretariat.ediss@univ-lyon1.fr</a>	<b>Mme Emmanuelle CANET-SOULAS</b> INSERM U1060, CarMeN lab, Univ. Lyon 1 Bâtiment IMBL 11 Avenue Jean CAPELLE INSA de Lyon 69 621 Villeurbanne Tél : 04.72.68.49.09 Fax : 04.72.68.49.16 <a href="mailto:emmanuelle.canet@univ-lyon1.fr">emmanuelle.canet@univ-lyon1.fr</a>
<b>INFOMATHS</b>	<b><u>INFORMATIQUE ET</u></b> <b><u>MATHÉMATIQUES</u></b> <a href="http://edinfomaths.universite-lyon.fr">http://edinfomaths.universite-lyon.fr</a> Sec. : Renée EL MELHEM Bât. Blaise PASCAL, 3e étage Tél : 04.72.43.80.46 <a href="mailto:infomaths@univ-lyon1.fr">infomaths@univ-lyon1.fr</a>	<b>M. Luca ZAMBONI</b> Bât. Braconnier 43 Boulevard du 11 novembre 1918 69 622 Villeurbanne CEDEX Tél : 04.26.23.45.52 <a href="mailto:zamboni@maths.univ-lyon1.fr">zamboni@maths.univ-lyon1.fr</a>
<b>Matériaux</b>	<b><u>MATÉRIAUX DE LYON</u></b> <a href="http://ed34.universite-lyon.fr">http://ed34.universite-lyon.fr</a> Sec. : Stéphanie CAUVIN Tél : 04.72.43.71.70 Bât. Direction <a href="mailto:ed.materiaux@insa-lyon.fr">ed.materiaux@insa-lyon.fr</a>	<b>M. Jean-Yves BUFFIÈRE</b> INSA de Lyon MATEIS - Bât. Saint-Exupéry 7 Avenue Jean CAPELLE 69 621 Villeurbanne CEDEX Tél : 04.72.43.71.70 Fax : 04.72.43.85.28 <a href="mailto:jean-yves.buffiere@insa-lyon.fr">jean-yves.buffiere@insa-lyon.fr</a>
<b>MEGA</b>	<b><u>MÉCANIQUE, ÉNERGÉTIQUE,</u></b> <b><u>GÉNIE CIVIL, ACOUSTIQUE</u></b> <a href="http://edmega.universite-lyon.fr">http://edmega.universite-lyon.fr</a> Sec. : Stéphanie CAUVIN Tél : 04.72.43.71.70 Bât. Direction <a href="mailto:mega@insa-lyon.fr">mega@insa-lyon.fr</a>	<b>M. Jocelyn BONJOUR</b> INSA de Lyon Laboratoire CETHIL Bâtiment Sadi-Carnot 9, rue de la Physique 69 621 Villeurbanne CEDEX <a href="mailto:jocelyn.bonjour@insa-lyon.fr">jocelyn.bonjour@insa-lyon.fr</a>
<b>ScSo</b>	<b><u>ScSo*</u></b> <a href="http://ed483.univ-lyon2.fr">http://ed483.univ-lyon2.fr</a> Sec. : Véronique GUICHARD INSA : J.Y. TOUSSAINT Tél : 04.78.69.72.76 <a href="mailto:veronique.cervantes@univ-lyon2.fr">veronique.cervantes@univ-lyon2.fr</a>	<b>M. Christian MONTES</b> Université Lyon 2 86 Rue Pasteur 69 365 Lyon CEDEX 07 <a href="mailto:christian.montes@univ-lyon2.fr">christian.montes@univ-lyon2.fr</a>



*To my Beloved parents, Hanna and Aida.*

*“Say not, ‘I have found the truth,’ but  
rather, ‘I have found a truth.’”*

*Khalil Gibran*



# Acknowledgments

---

*First, I would like to thank my supervisors, Dr. Laurent Briançon, Prof. Ali Daouadji and Eng. Mathilde Riot for their support and their insight. In particular, Laurent for his inspiration, support, motivation, positive vibes and more importantly his human kindness. No progress of this work would have been possible without his guidance and support. Moreover, I would like to thank Dr. Abdelkader Abdelouhab for his support and advice especially in the professional environment during the time spent in AFITEXINOV the first two years of my PHD.*

*This study was performed in the framework of the new French Laboratory of Technical Innovations applied to Reinforcement GSYs (PITAGOR) funded in December 2015 by the French National Research Agency. I would like to thank the French National Research Agency that made this experimental study possible.*

*Furthermore, I wish to thank the two reviewers of this manuscript, Prof. Pascal Villard and Prof. Philippe Reiffsteck, who kindly and graciously accepted to review this thesis, as well as Prof. Philippe Delmas and Prof. Nathalie Touze for being part of the jury of my public defense.*

*This thesis work could not be accomplished without the assistance of the technicians and engineers of GEOMAS and AFITEXINOV. In no particular order, Emric Bruyer, Stéphane Vacherie, Jostar Laforet, Mario Masapollo, Romain Trunfio, Jean Gioratto.*

*These three years were easier, and more pleasant in the friendly environment we had between colleagues, they are not only colleagues but friends. Alexis, Adnan, Atefe, Danai, Gianluca, José, Nour, Rosy and Thomas, thank you guys and girls for all the funny and joyful times we spent together.*

*Living abroad away from your family and beloved ones is not easy. Maria, Nathalia, Layal, Khalil and David my friends in France who turned into my family. I am grateful for having you by my side during this journey, and hope we will always be there for each other.*

*Finally and most importantly, I wish to thank my parents Hanna and Aida, my brother Antoun, my sister Désirée, my brother in law Yves and my fiancé Samer for believing in me. You were always my motivation source and my support. Your love was and will always be my strength.*





# Abstract

---

Since the 1970s, Geosynthetics have been used in base course reinforcements supported by soft subgrade in unpaved road application. The experiences gained over the years have shown the benefits of reinforcement in improving the fill material compaction, the bearing capacity of the platform, the reduction of base course thickness and the increase of the structure service life.

The underlying mechanisms observed in this reinforced structure are complex and are classified as follow: the lateral restraint mechanism and reinforcement of base course aggregates, tension membrane effect in rutted areas, and reduction of mixing between the subgrade and base course soils. In fact, the road structure becomes more heterogeneous and the mechanisms more complex with the reinforcement addition. In literature, and based on a supposed dominant mechanism different theories are suggested, and different analytical methods are proposed to design the base course thickness needed. The more recent proposed analytical method gives the privilege to the lateral restrain mechanism, contrary to the first studies in this field that were based on the tension membrane effect. The various factors and parameters influencing the dominant mechanism and its relative contribution on the platform improvement explain the need for more investigations in this topic.

In this research work, large-scale laboratory tests were developed to study the reinforcement contribution in the unpaved road improvement. Therefore, an unpaved platform was built of 600 mm of artificial subgrade with a  $CBR < 2\%$  supporting a base course layer either of 350 or 220 mm with a  $CBR > 12\%$ . A detailed experimental Protocol was established regarding the soil preparation, the installation and the soils compaction procedure to reproduce the site conditions and insure the platform repeatability for each test.

Ten tests were performed under a circular plate load test, in a box of 1.8 m in large, 1.9 m in length and 1.1 m in height. Cyclic load was performed on the prepared platform, with a maximum load of 40 kN resulting in a maximum applied pressure of 560 kPa. The platform was subjected to 10,000 cycles with a frequency of 0.77 Hz. An advanced and complete soil instrumentation was provided in order to collect the maximum data needed for thorough analysis.

Under this test configuration, three repeatability tests were performed to verify the developed protocol. Quality control tests were performed before each test to verify the soil layers homogeneity and properties. Two base course thicknesses were tested under this test condition, 350 and 220 mm. Moreover, three geogrids were tested, an extruded geogrid with triangular aperture, a knitted geogrid with 1,000 kN/m of stiffness at 2% strain and another knitted geogrid with 2,500 kN/m at 2% strain. An additional performed test consisted of placing the geogrid at the base course half depth.

Once the developed protocol was confirmed under the circular plate load tests, further tests using the Simulator Accelerator of Traffic (SAT) were performed. Actually, the laboratory prepared platform was placed in a larger box of 1.8 m in large, 5 m in length and 1.1 m in height. The prepared platform was subjected to two solicitations: a particular plate and a traffic load. The particular plate had the

shape and dimensions of the wheel contact area, and the same load of 28 kN was applied under the plate and the wheel in order to compare the experimental results. The Simulator Accelerator of Traffic was especially developed for this application. A machine that simulates the traffic load under an effective length of 2 m and a velocity of 4 km/h. The two areas were instrumented as follow: an area under the circulation load, and an area under the plat load, they are located aside.

The 350 mm of base course of reinforced and unreinforced platforms showed no reinforcement effect on the platform behaviour. For all that, the circular plate load results highlighted the reinforcement effect in reducing the developed settlement with a base course platform of 220 mm. The most important platform improvement was shown for the knitted geogrid with the highest stiffness. Nevertheless, the extruded geogrid has provided a more significant platform improvement during the first cycles due to its special geometry, and it is designed mainly to provide lateral restrain mechanism.

Under the traffic and particular plate load, the stiffer knitted geogrid and extruded geogrid provided the same improvement to the platform. This can be due to the fact, that the extruded geogrid is more mobilized under a localized load. Although, the results showed that the traffic load is more damaging to either the base course layer or the subgrade layer.

In addition, a numerical model based on the differential element method using FLAC 3D was developed. The model simulated the circular plate load test with the same platform configuration under monotonic load. The results were compared to the first monotonic load applied on the rigid plate experimentally. The material parameters have been calibrated based on the laboratory characterization tests. The results showed that the model illustrates perfectly the platforms behaviour under the first loading. However, a parametric study shows that the interface reduction to an elastic perfectly plastic model in a continuous model does not simulate properly the geogrids apertures, aggregates interlocking mechanism and the geogrid lateral restrain behaviour.

**Keywords:** unpaved roads, large-scale test, geosynthetic, geogrid, reinforcement, soft soil, subgrade, base course, cyclic plate load, traffic load, numerical model, differential element method.

# Résumé

---

Les géosynthétiques sont utilisés depuis les années 70 dans le renforcement des plateformes granulaires reposant sur des sols de faible portance ayant pour applications de routes non revêtues. Le retour d'expérience a validé l'efficacité de ces produits dans l'amélioration du compactage de la couche de forme, la capacité portante de la plateforme, la réduction de l'épaisseur de la couche de forme et l'augmentation de la durée de service de la plateforme.

Les mécanismes développés dans ce renforcement de sol sont complexes. Dans la littérature, différents mécanismes ont été identifiés pour expliquer le transfert de charge : le confinement des agrégats par enchevêtrement des particules de sol dans la géogridde et par frottement entre le sol et le géosynthétique, par effet membrane du géosynthétique. Selon le type de géosynthétique, la fonction de séparation peut aussi être assurée entre la couche de forme et le sol de support. Ces différents mécanismes ont été mis en équations dans des méthodes analytiques de dimensionnement des géosynthétiques. La méthode la plus récente suppose que le mécanisme prépondérant du transfert de charge est dû au blocage du mouvement latéral des agrégats par enchevêtrement dans la géogridde. Cette méthode a été spécifiquement développée pour le dimensionnement de nouvelles géogriddes assurant ce rôle de confinement. La complexité des mécanismes développés et la diversité des produits de renforcement nécessitent encore d'étudier ces plateformes renforcées pour mieux appréhender leur comportement, développer des géosynthétiques adaptés et proposer des méthodes de dimensionnement.

C'est avec ces objectifs qu'un essai de laboratoire permettant de tester des plateformes à échelle réelle a été développé. Une plateforme granulaire non revêtue reposant sur un sol de faible portance a été reproduite au laboratoire. Les deux épaisseurs de plateformes ont été testées (220 mm et 350 mm) en respectant les règles de portance imposées dans les normes ( $CBR > 12\%$ ). La plateforme repose sur une couche de 600 mm de sol peu porteur ( $CBR < 3\%$ ). De nombreux mélanges de sable et d'argile ont été testés pour trouver la bonne composition du sol peu porteur. Un protocole de mise en place de ce sol a été élaboré pour assurer son homogénéité et la répétabilité des essais. Le géosynthétique et le matériau granulaire ont aussi fait l'objet d'un protocole de mise en œuvre adapté pour se rapprocher des conditions réelles de chantier. Des essais de contrôle de qualité ont été opérés avant chaque essai sur le sol peu porteur et la plateforme préparée pour vérifier leurs propriétés et s'assurer que le sol est homogène et toujours sous les mêmes conditions avant chaque essai.

Après de nombreux essais de faisabilité, dix essais ont été effectués sous un chargement cyclique sur plaque circulaire, la plateforme testée a été placée dans un banc d'essai de 1,8 m de large, 1,9 m de long et 1,1 m de haut. La charge maximum appliquée sur la plaque était de 40 kN donnant une contrainte à la surface de 560 kPa. La plateforme testée a été soumise à 10,000 cycles avec une fréquence de 0.77 Hz pour respecter les recommandations des normes du domaine. Une instrumentation spécifique a été développée pour ces essais pour collecter le maximum de mesures

utiles pour l'interprétation de transfert de charge et du comportement des géogrilles. Cette instrumentation a aussi permis de vérifier que les dimensions du banc d'essai étaient suffisantes pour éviter les effets de bords.

Trois essais de répétabilité ont été effectués dans le but de vérifier le protocole de mise en place et la possibilité de reproduire le même sol avec les mêmes propriétés à chaque essai. Trois types de géogrille ont été testés : une géogrille extrudée avec des ouvertures triangulaires, deux géogrilles tricotées d'une rigidité de 1,000 kN/m et 2,500 kN/m à 2% de déformation. En complément, un essai avec la géogrille tricotée d'une rigidité de 1,000 kN/m à 2% de déformation placée à mi-hauteur de la couche de forme a été effectué pour tester l'effet de la position du renforcement.

Sur la base du même protocole de mise en œuvre, des essais de circulation avec un Simulateur Accélérateur de Traffic (SAT) ont été effectués. Pour ces essais la plateforme testée a été placée dans le banc d'essai allongé à 5 m. La plateforme de 220 mm d'épaisseur sur sol peu porteur a été soumise à deux types de sollicitations : un chargement cyclique sur plaque et un chargement de circulation. La plaque utilisée a été découpée pour avoir la forme de l'empreinte de la roue sur le sol. Dans les deux cas, la charge maximum appliquée par cycle est de 28 kN donnant une contrainte en surface de 680 kN. Le simulateur de circulation a été conçu et développé spécifiquement pour cette application avec notamment la possibilité d'un enfoncement important dans le sol sans perte de contact. Cette machine applique une contrainte de circulation sur une longueur effective de chargement de 2 m avec une vitesse de 4 km/h. Deux sections ont été instrumentées : la section sous la charge cyclique sur plaque et la section au milieu de la longueur circulée par le simulateur de circulation.

A partir de ces quelques essais, plusieurs observations ont pu être faites sur le comportement des plateformes granulaires sur sol peu porteur. La présence d'un géosynthétique n'a pas permis d'améliorer la portance et de réduire le tassement des plateformes de 350 mm d'épaisseur soumises à des essais de chargement cyclique à la plaque de 300 mm de diamètre. Par contre, ils se sont avérés efficaces pour les plateformes de 220 mm d'épaisseur de couche de forme. En particulier, le renforcement par la plus rigide des géogrilles tricotées a permis d'obtenir la meilleure réduction du tassement en surface. Il ressort des essais que la géogrille extrudée améliore le plus le comportement de la plateforme sous faible déplacement au niveau des premiers cycles ; ceci peut être due à la forme géométrique et à la configuration de ce produit limitant le plus le déplacement horizontal des agrégats.

Sous le chargement de Traffic et la charge cyclique avec la petite plaque, les deux produits testés (la géogrille extrudée et la géogrille tricotée la plus rigide) ont présenté le même facteur d'amélioration. Sous ce type de chargement plus concentré, la géogrille extrudée a été plus sollicitée, et ceci peut être due au mouvement latéral des agrégats important sous une charge plus localisée. Toutes les plateformes testées ont beaucoup plus tassé sous les sollicitations de circulations avec un orniérage différent de celui observé sous chargement sous plaque. Enfin l'utilisation de fibres optiques insérées dans les nappes géosynthétique a permis d'étudier les mécanismes de mise en tension différents selon le type de géosynthétique.

D'autre part, un modèle numérique a été développé en se basant sur la méthode des éléments différentielles en utilisant le logiciel FLAC 3D®. La modélisation de l'essai de chargement par l'intermédiaire d'une plaque circulaire ayant la même configuration a été faite, mais sous uniquement

un chargement monotone croissant que représente le premier chargement appliqué expérimentalement sur la plateforme. La calibration des modèles de comportement des matériaux a été faite en se basant sur des essais de caractérisation expérimentale au laboratoire. Les résultats ont montré que le modèle illustre bien le comportement des plateformes renforcées et non renforcées lors de la première charge appliquée. D'autre part, une étude paramétrique a montré que la réduction du comportement de l'interface de la couche de forme et de la géogridde a une loi de comportement élastique parfaitement plastique n'illustre pas correctement l'interaction de ces deux matériaux. En effet, un modèle plus élaboré qui peut modéliser l'enchevêtrement des agrégats dans les ouvertures de la géogridde peut présenter une réponse plus proche de la réalité expérimentale.

**Mots clés** : routes non revêtue, essai à grand échelle, géosynthétique, géogridde, sol de faible portance, sol support, couche de forme, charge cyclique sur plaque, charge de circulation, modèle numérique, méthode des différences finies.



# Contents

---

<b>General introduction .....</b>	<b>1</b>
<b><u>Chapter 1: State Of The Art</u></b>	
<b>1.1. Introduction.....</b>	<b>5</b>
<b>1.2. GSYs types and functions.....</b>	<b>6</b>
1.2.1. Geotextiles .....	6
1.2.2. Watertightness GSYs .....	6
1.2.3. The apparent products .....	6
<b>1.3. Unpaved roads .....</b>	<b>7</b>
1.3.1. Lateral restraint of base course material.....	7
1.3.2. Tension membrane effect.....	8
1.3.3. Separation.....	9
<b>1.4. Reinforcement influencing parameters .....</b>	<b>9</b>
1.4.1. The base course thickness.....	10
1.4.2. The reinforcement position .....	10
1.4.3. The GSY type and stiffness.....	10
1.4.4. The geogrid aperture shape and dimension .....	11
1.4.5. The geogrid aperture stability modulus.....	11
<b>1.5. Experimental testing on unpaved roads .....</b>	<b>12</b>
1.5.1. Large-scale laboratory plate load tests .....	12
1.5.2. Large-scale in situ tests.....	20
1.5.3. Reduced-scale laboratory cyclic Traffic load tests .....	22
1.5.4. Large-scale laboratory cyclic Traffic load tests .....	24
<b>1.6. Unpaved roads tests synthesis: .....</b>	<b>31</b>
<b>1.7. Analytical and Empirical design methods.....</b>	<b>40</b>
<b>1.8. Numerical Approaches .....</b>	<b>46</b>
<b>1.9. GSY installation damage .....</b>	<b>51</b>
<b>1.10. Conclusion .....</b>	<b>55</b>
<b><u>Chapter 2: Experimentation</u></b>	
<b>2.1. Introduction.....</b>	<b>57</b>
<b>2.2. Experimental configurations and devices.....</b>	<b>57</b>
2.2.1. Tests benches.....	57
2.2.2. Cyclic plate load test .....	58
2.2.3. Traffic load test.....	59
<b>2.3. Materials .....</b>	<b>62</b>
2.3.1. Soft subgrade.....	63
2.3.1.a. Subgrade constitution .....	63



2.3.1.b. Subgrade characterization .....	67
2.3.2. Base course .....	69
2.3.2.a. Base course identification.....	69
2.3.2.b. Base course characterization .....	70
2.3.3. GSYs.....	72
2.3.4. Geosynthetic / Base course interface characterization .....	74
<b>2.4. Installation procedure.....</b>	<b>77</b>
<b>2.5. Quality control tests .....</b>	<b>81</b>
2.5.1. The water content profile .....	81
2.5.2. Shear vane test .....	81
2.5.3. Static penetrometer test .....	82
2.5.4. Dynamic penetrometer test .....	82
<b>2.6. Instrumentation .....</b>	<b>83</b>
2.6.1. Earth pressure cell .....	85
2.6.2. Hydraulic settlement sensor .....	85
2.6.3. Inclination sensor .....	86
2.6.4. Displacement laser sensor .....	86
2.6.5. Data recording equipment .....	87
2.6.5.a. Data-Taker logger .....	88
2.6.5.b. Scaimex measurements acquisition instrument.....	88
2.6.6. Optical fibre.....	89
<b>2.7. Conclusion .....</b>	<b>89</b>
<b><u>Chapter 3: Plate Load Test</u></b>	
<b>3.1. Introduction.....</b>	<b>91</b>
<b>3.2. Performed tests.....</b>	<b>91</b>
<b>3.3. Quality control tests results .....</b>	<b>92</b>
3.3.1.a. Water content .....	92
3.3.1.b. Shear vane test .....	93
3.3.1.c. Static penetrometer test .....	94
3.3.1.d. Dynamic penetrometer test.....	95
<b>3.4. Results and analysis.....</b>	<b>97</b>
3.4.1. Measurements verifications.....	98
3.4.2. Repeatability tests.....	99
3.4.1. Base course thickness influence .....	102
3.4.1. GSY benefit.....	102
3.4.1.a. Settlement .....	103
3.4.1.b. Vertical stress.....	108
3.4.1.c. TBR comparison.....	112
3.4.2. GSY strain.....	113
3.4.2.a. After the base course installation.....	113
3.4.2.b. During the loading .....	114
<b>3.5. Aggregates damage.....</b>	<b>116</b>

<b>3.6. GSY damages</b> .....	<b>118</b>
<b>3.7. Empirical and analytical design methods</b> .....	<b>119</b>
<b>3.8. Conclusions</b> .....	<b>122</b>
<b><u>Chapter 4: Traffic Load Test</u></b>	
<b>4.1. Introduction</b> .....	<b>124</b>
<b>4.2. Performed tests</b> .....	<b>125</b>
<b>4.3. Quality control tests results</b> .....	<b>125</b>
4.3.1. Water content.....	126
4.3.2. Shear vane test.....	126
4.3.3. Static penetrometer test .....	127
4.3.4. Dynamic penetrometer test .....	128
<b>4.4. Results and analysis</b> .....	<b>129</b>
4.4.1. Measurements verifications.....	130
4.4.2. GSY benefit.....	132
4.4.2.a. Settlement .....	132
4.4.2.b. Vertical stress.....	138
4.4.3. GSY strain.....	141
4.4.3.a. After the base course installation.....	141
4.4.3.b. During the loading .....	143
<b>4.5. Circular and particular plate shape tests results comparison</b> .....	<b>146</b>
<b>4.6. Conclusions</b> .....	<b>150</b>
<b><u>Chapter 5: Numerical Modelling</u></b>	
<b>5.1. Introduction</b> .....	<b>153</b>
<b>5.2. Soil constitutive models</b> .....	<b>154</b>
5.2.1. Elasticity.....	154
5.2.2. Elastoplasticity .....	154
5.2.3. Hypoplasticity .....	156
5.2.4. Literature revue .....	156
5.2.4.a. Models used to simulate the aggregates behaviour .....	156
5.2.4.b. Models used to simulates the clay behaviour.....	157
5.2.4.c. Unified models.....	157
<b>5.3. The numerical computation code: FLAC 3D</b> .....	<b>157</b>
5.3.1. The computation code background .....	158
5.3.2. Numerical formulation .....	159
5.3.3. Constitutive model in FLAC .....	160
5.3.4. Interface elements.....	161
5.3.5. Structural elements .....	161
5.3.6. Geogrid structural elements .....	162
5.3.7. Cap-yield model implemented in FLAC .....	162
5.3.7.a. Incremental elastic law .....	163
5.3.7.b. Shear yield and Potential functions.....	163
5.3.7.c. Volumetric Cap Criterion and Flow Rule .....	164

5.3.7.d. Tensile Yield Criterion and Flow Rule .....	164
5.3.7.e. Friction Hardening .....	164
5.3.7.f. Cap Hardening .....	165
5.3.7.g. Dilation Hardening .....	165
5.3.8. Model geometry .....	166
<b>5.4. Parameters calibration.....</b>	<b>167</b>
5.4.1. Base course .....	167
5.4.2. Subgrade .....	168
5.4.2.a. The triaxial test .....	169
5.4.2.b. The plate load test.....	171
5.4.3. Base course/Subgrade interface .....	171
5.4.4. Geosynthetic .....	171
5.4.5. Base course/Geosynthetic interface .....	174
<b>5.5. Monotonic loading simulation.....</b>	<b>175</b>
5.5.1. Base course thickness 220 mm.....	176
5.5.1.a. Settlement .....	176
5.5.1.b. Vertical stress.....	177
5.5.1.c. The Geosynthetic developed efforts .....	180
5.5.2. Base course thickness 350 mm.....	182
<b>5.6. Parametric sensitivity study.....</b>	<b>184</b>
5.6.1. Base course parameters effect.....	184
5.6.2. Base course thickness effect.....	185
5.6.3. Geosynthetic/ base course interface effect.....	186
5.6.4. Subgrade / Base course interface effect.....	186
5.6.5. Geosynthetic stiffness effect.....	187
5.6.6. Geosynthetic position effect .....	188
<b>5.7. Geosynthetic effect regarding the developed settlement .....</b>	<b>189</b>
<b>5.8. Conclusion .....</b>	<b>191</b>
<b>Conclusions .....</b>	<b>193</b>
<b>Further Perspectives .....</b>	<b>199</b>

# List of Figures

---

## **Chapter 1: State Of The Art**

Figure 1.2-1: Some GSY products and applications (AFITEXINOV: <a href="http://www.afitex.com">http://www.afitex.com</a> ) .....	7
Figure 1.1-1: Lateral restraint mechanism- IGS (International GSYs Society).....	8
Figure 1.1-2: Tension membrane mechanism-IGS (International GSYs Society).....	9
Figure 1.1-3: Separation mechanism- IGS (International GSYs Society).....	9
Figure 1.5-1: (a) Earth pressure distribution, (b) Vertical stress distribution on the subgrade layer along the centre line of the plate at 1724 kPa applied plate pressure for a 300 mm of base course thickness. (Akond, 2012) .....	13
Figure 1.5-2: Plate load test setup. (Akond, 2012) .....	13
Figure 1.5-3: (a) Equipment used in the tests, (b) Plate settlement versus number of load repetitions- 1 <sup>st</sup> loading stage. (Palmeira & Antunes, 2010).....	14
Figure 1.5-4: Setup of the cyclic plate load test. (Qian et al., 2011).....	16
Figure 1.5-5: Permanent deformations of loading plate versus the number of cycles. (Qian et al., 2011).....	16
Figure 1.5-6: Schematic of large-scale model experiment (LSME). (Kim et al., 2006). .....	17
Figure 1.5-7: Schematic diagram of the pavement test facility. (Christopher & Perkins, 2008). .....	18
Figure 1.5-8: Schematic sketch and photograph of the large-scale cyclic plate loading test setup. (Sarici et al., 2016). .....	19
Figure 1.5-9: (a) Delivery and distribution of the artificial subgrade in the test pit, (b) Installation of geosynthetics. (Cuelho & Perkins, 2009) .....	21
Figure 1.5-10: (a) Prepared testing sections, (b) 76 mm rut developed with few truck passes. (Mekkawy et al., 2011) .....	22
Figure 1.5-11: Schematic diagram of the test section, (a) plan view, (b) cross section. (Mekkawy et al., 2011) .....	22
Figure 1.5-12: Schematic illustration of the One-third scale MMLS3. (Tang et al., 2008).....	23
Figure 1.5-13: Test setup. (Farhan et al., 2012) .....	24
Figure 1.5-14: View of PTF carriage fitted with dual wheel assembly. (Cook et al., 2016) .....	25
Figure 1.5-15: TRL pavement testing facility. (Watts et al., 2004) .....	26
Figure 1.5-16: Profile of test section. (Jersey et al., 2012),.....	27
Figure 1.5-17: Dual-wheel tandem axle configuration. (Robinson et al., 2017).....	27
Figure 1.5-18: Profile view of instrumentation layout. (Robinson et al., 2017) .....	28
Figure 1.5-19: Tested platform section. (Yang et al., 2012).....	28
Figure 1.5-20: Tested platform top view. (Yang et al., 2012) .....	29
Figure 1.5-21: ALF with insertion of dual-wheel assembly. (Tang et al., 2015).....	30
Figure 1.5-22: Testing platforms cross section. (Tang et al., 2015) .....	30

Figure 1.7-1: Load distribution by base course layer: (a) case without geotextile; and (b) case with geotextile. (Giroud & Noiray, 1981).....	41
Figure 1.7-2: Assumed parabolic shape of deformed geotextile. (Giroud & Noiray, 1981).....	42
Figure 1.7-3: Soil block in equilibrium analysis. (Milligan et al., 1989). ....	43
Figure 1.8-1: Complete and partial 3D mesh geometry of the in-soil FE model. (Hussein et al., 2016) .....	47
Figure 1.8-2: Meshes with beam elements. (a) Geogrid with rectangular apertures. (b) Geogrid with triangular apertures. (Dong et al., 2011) .....	48
Figure 1.8-3: DEM model of Asphalt Pavement Analyser (APA) machine test simulation. (Bhandari & Han, 2010) .....	49
Figure 1.8-4: (a) Axisymmetric FE model deformed mesh of an unpaved road. (b) Model prediction of rutting curves for unreinforced Test Section I Georgia aggregate and subgrade. (Perkins et al., 2012) .....	50
Figure 1.8-5: (a) Geometry of the axisymmetric finite element model for the test section. (b) Measured and modelled subgrade permanent deformation for sections in APT II. (Tang et al., 2016).....	51
Figure 1.9-1: Example of a woven geotextile abrasion surface. (Brady et al., 1994).....	52
Figure 1.9-2: Example of notches on extruded polyethylene grid. (Brady et al. 1994) .....	52
Figure 1.9-3: Example of geotextile punching. (Brady et al. 1994) .....	53
Figure 1.9-4: Deformation failure of geotextile due to traffic load.....	53
Figure 1.9-5: Fibres failure of a non-woven polyester geogrid. (Brady et al. 1994) .....	54
Figure 1.9-6: Geotextile damage by tear failure. ....	54
<b><u>Chapter 2: Experimentation</u></b>	
Figure 2.2-1: (a) Load waves diagram, (b) Hydraulic Jack. ....	58
Figure 2.2-2: Test setup. ....	59
Figure 2.2-3: SAT plan. ....	60
Figure 2.2-4: SAT placed over the tested platform. ....	61
Figure 2.2-5: Tire contact area. ....	61
Figure 2.2-6: Illustration of the circulation and plate load platform test. ....	62
Figure 2.3-1: Platform soil layers constitution.....	62
Figure 2.3-2: (a) Particles size distribution of the used Hostun sand, (b) Particles size distribution of the mixture 20% kaolinite Clay and 80% Hostun sand, (c) Particles size distribution of the mixture 40% kaolinite Clay and 60% Hostun sand.....	64
Figure 2.3-3: Calcium bentonite and Hostun sand mixtures proctor and CBR curves.....	65
Figure 2.3-4: Kaolinite and Hostun sand mixtures proctor and CBR curves. ....	66
Figure 2.3-5: Triaxial prepared specimens. ....	67
Figure 2.3-6: Deviatoric stress versus the axial strain. ....	67
Figure 2.3-7: Volumetric strain versus the axial strain. ....	68
Figure 2.3-8: Deviatoric stress versus the axial strain under cyclic loading. ....	68
Figure 2.3-9: (a) GNT particles size distribution, (b) The GNT Proctor and CBR curves.....	69
Figure 2.3-10: Configuration of the large shear box for soil test. ....	70

Figure 2.3-11: (a) Maximum shear versus the normal stress of the reinforced and unreinforced interface, .....	71
Figure 2.3-12: Shear stress versus horizontal displacement for cyclic solicitation at a normal stress of 200 kPa. ....	71
Figure 2.3-13: Geometry of the Geosynthetic GSY 1. ....	72
Figure 2.3-14: GSY 1 and GSY 2 tensile curves. ....	73
Figure 2.3-15: GSY 1 tensile curve under cyclic load. ....	73
Figure 2.3-16: Installation of the GSY 1 and aggregates. ....	74
Figure 2.3-17: Installation of the GSY 3 and aggregates. ....	74
Figure 2.3-18: Configuration of the large shear box for GSY tests. ....	75
Figure 2.3-19: Shear stress versus horizontal displacement at different normal stresses for the reinforced and unreinforced interface. ....	75
Figure 2.3-20: Maximum shear stress versus the normal stress of the reinforced and unreinforced interface. ....	76
Figure 2.3-21: Shear stress versus horizontal displacement for cyclic solicitation at a normal stress of 200 kPa with reinforcement. ....	76
Figure 2.4-1: The mixer, plate compactor and mini excavator used for the soil installation.....	77
Figure 2.5-1: Instrument used for the quality control tests : (a) Shear vane test instrument, (b) Static penetrometer instrument, (c) Dynamic penetrometer instrument. ....	81
Figure 2.6-1: Platform instrumentation in the plate load test, view from above. ....	83
Figure 2.6-2: Sensors installation plan for the plate load test, a section. ....	83
Figure 2.6-3: Platform instrumentation plan in the traffic load test, view from above. ....	84
Figure 2.6-4: Sensors installation plan in the Traffic load test, a section. ....	85
Figure 2.6-5: Illustration of the sensors installation in the traffic load test. ....	85
Figure 2.6-6: Laser sensor installation and measurements. ....	87
Figure 2.6-7: Scame measurements acquisition setup and interface.....	88

### **Chapter 3: Plate Load Test**

Figure 3.3-1: (a) Water content profile before and after the test for the reinforced test 6, (b) Cloud of water content points of all the performed tests before the test. ....	93
Figure 3.3-2: (a) $S_t$ profile in two different positions for the Test 1 and Test 2, (b) Cloud of $S_t$ points of all the performed tests. ....	94
Figure 3.3-3: (a) The CI/CBR (%) profile in two different positions for the Test 1 and Test 2, (b) Cloud of the CI/CBR (%) points of all the performed tests.....	94
Figure 3.3-4: (a) CBR (%) profile in two different positions for the Test 1 and Test 2 with H = 350 mm, before the base course installation, (b) CBR (%) profile in two different positions for the Test 1 and Test 2 with H = 350 mm, after the base course installation. ....	95
Figure 3.3-5: (a) CBR (%) profile in two different positions for the Test 3 and Test 5 with H = 220 mm, before the base course installation, (b) CBR (%) profile in two different positions for the Test 3 and Test 5 with H = 220 mm, after the base course installation. ....	96
Figure 3.3-6: (a) CBR (%) profile of all the performed tests with 220 mm of base course thickness before the base course installation, (b) CBR (%) profile of all the performed tests with 220 mm of base course thickness after the base course installation.....	97

Figure 3.4-1: Illustration of rut measurement.....	97
Figure 3.4-2: Subgrade settlement profile after 10,000 cycles.....	98
Figure 3.4-3: (a) Centre earth pressure cell inclination over the X direction, (b) Earth pressure cell placed at 200 mm from the load centre inclination over the X direction, (c) Earth pressure cell placed at 400 mm from the load centre inclination over the X direction, (d) Centre earth pressure cell inclination over the Y direction, (e) Earth pressure cell placed at 200 mm from the load centre inclination over the Y direction, (f) Earth pressure cell placed at 400 mm from the load centre inclination over the Y direction.....	99
Figure 3.4-4: Subgrade surface centre settlement evolution with cycles. ....	100
Figure 3.4-5: Subgrade surface centre vertical stress evolution with cycles. ....	101
Figure 3.4-6: Subgrade surface central vertical stress evolution with settlement. ....	101
Figure 3.4-7: Base course surface settlement after 10,000 cycles. ....	103
Figure 3.4-8: Base course surface centre settlement evolution with cycles (for H = 220 mm). ....	104
Figure 3.4-9: Base course surface centre settlement evolution after 200 cycles with cycles, (for H = 220 mm). ....	105
Figure 3.4-10: Subgrade surface centre settlement evolution with cycles(for H=220 mm).....	106
Figure 3.4-11: Subgrade surface centre settlement evolution after 200 cycles with cycles (for H=220 mm). ....	106
Figure 3.4-12: Base course thickness variation evolution with cycles(for H=220 mm).....	107
Figure 3.4-13: Subgrade surface settlement profile from the plate centre to the edge, at the first cycle and after 10,000 cycles. ....	108
Figure 3.4-14: Subgrade surface central vertical stress evolution with cycles. ....	109
Figure 3.4-15: Vertical stress distribution at the subgrade surface after 1 cycle. ....	109
Figure 3.4-16: Vertical stress distribution at the subgrade surface after 10,000 cycles.....	110
Figure 3.4-17: Vertical stress in subgrade depth evolution with cycles at the plate centre, (for H=220 mm). ....	111
Figure 3.4-18: Subgrade surface central vertical stress evolution with settlement. ....	112
Figure 3.4-19: GSY 1 strain and equivalent force developed after the base course gravel installation. ....	114
Figure 3.4-20: GSY 2 strain the equivalent force developed after the base course gravel installation in four different positions.....	114
Figure 3.4-21: GSY 1 unanchored strain and equivalent force developed at the first loading cycle. ....	115
Figure 3.4-22: GSY 2 unanchored strain and equivalent force developed at the first loading cycle. ....	115
Figure 3.4-23: GSY 1 unanchored and unanchored strain and equivalent force developed after 1,000 cycles at the loading and unloading stage. ....	116
Figure 3.5-1: Particles size distribution of the virgin and damaged aggregates. ....	117
Figure 3.5-2: Shear stress versus horizontal displacement at different normal stresses for the virgin and damaged aggregates.....	118
Figure 3.6-1: GSY 1 tensile curves for virgin specimen and damaged specimens under the plate load and at the box edges. ....	119

## **Chapter 4: Traffic Load Test**

Figure 4.3-1: (a) Water content profile under the plate and Traffic load areas for Test 1, (b) Water content profile for Tests 1, 2 & 3. ....	126
Figure 4.3-2: (a) $S_t$ profile under the plate and Traffic load areas for Test 1, (b) $S_t$ profile for Tests 1, 2 & 3. ....	127
Figure 4.3-3: CI/CBR (%) profile under the plate and Traffic load areas for Test 1, (b) CI/CBR (%) profile for Tests 1, 2 & 3. ....	127
Figure 4.3-4: (a) CBR (%) profile under the plate and Traffic load areas for Test 1 before the base course installation, (b) CBR (%) profile under the plate and Traffic load areas for Test 1 after the base course installation. ....	128
Figure 4.3-5: (a) CBR (%) profile under the plate and Traffic load areas for Tests 1, 2 & 3 before the base course installation, (b) CBR (%) profile under the plate and Traffic load areas for Tests 1, 2 & 3 after the base course installation. ....	129
Figure 4.4-1: Rutting plate and Traffic load tests measurements. ....	130
Figure 4.4-2: (a) Central earth pressure cell inclination over the X direction, (b) Earth pressure cell placed at 200 mm from the plate centre inclination over the X direction, (c) Central earth pressure cell inclination over the Y direction, (d) Earth pressure cell placed at 200 mm from the plate centre inclination over the Y direction. ....	131
Figure 4.4-3: (a) Base course surface settlement after 10,000 cycles, under the plate load test, (b) after 1,200 cycles under the Traffic load test for two different positions. ....	133
Figure 4.4-4: (a) Base course surface centre settlement evolution with cycles under the plate load test, (b) under the Traffic load test. ....	134
Figure 4.4-5: (a) Subgrade surface centre settlement evolution with cycles under the plate load test, (b) under the Traffic load test. ....	135
Figure 4.4-6: (a) Base course thickness variation evolution with cycles under the plate load test, (b) under the Traffic load test. ....	136
Figure 4.4-7: (a) Subgrade surface settlement profile from the load centre to the edge, for the plate load and Traffic load after 200 cycles, (b) after 500 cycles. ....	137
Figure 4.4-8: Subgrade surface central vertical stress evolution with cycles, under the plate and Traffic load. ....	139
Figure 4.4-9: Subgrade surface central vertical stress cycles, for the unreinforced platform (Test 1). ....	140
Figure 4.4-10: Vertical stress distribution at the subgrade surface, (a) after 1 cycle, (b) after 100 and 150 cycles. ....	141
Figure 4.4-11: GSY 2 strain and the equivalent force developed after the base course installation in three different positions. ....	142
Figure 4.4-12: GSY 3 strain and the equivalent force developed after the base course installation in four different positions. ....	142
Figure 4.4-13: GSY 2 and GSY 3 strain developed at the first loading and after the unloading, (a) GSY 2 under the plate load, (b) GSY 3 under the plate load, (c) GSY 2 under the Traffic load, (d) GSY 3 under the Traffic load. ....	143



Figure 4.4-14: GSY 2 stain evolution with cycles. (a) Under the pate load, (b) Under the Traffic load. .....	144
Figure 4.4-15: GSY 3 stain evolution under the plate load with cycles. (a) Evolution at the unloading stage, (b) after 10,000 cycles under the loading and unloading. ....	145
Figure 4.4-16: Geogrids Maximum strain evolution with the base course central settlement evolution. .....	146
Figure 4.5-1: Base course surface centre settlement evolution with cycles, for the circular plate load tests (Test 3, 7 & 10); and the particular plate load tests (Test 1, 2 & 3). ....	147
Figure 4.5-2: Base course surface centre settlement evolution with cycles after 200 cycles, for the circular plate load tests (Test 3, 7 & 10), and the particular plate load tests (Test 1, 2 & 3).....	148
Figure 4.5-3: Subgrade surface vertical stress evolution with cycles, for the circular plate load tests (Test 3, 7 & 10), and the particular plate load tests (Test 1, 2 & 3). ....	149
Figure 4.5-4: GSY 2 strain at the first loading cycle, under the circular and the particular plate load test. ....	149

## **Chapter 5: Numerical Modelling**

Figure 5.2-1: Yield function. (a) Loading case, (b) Unloading case. ....	155
Figure 5.2-2: (a) isotropic hardening, (b) cinematic hardening.....	155
Figure 5.3-1: General computation sequence(Billaux & Cundall (1993)) .....	158
Figure 5.3-2: A discretized quadrilateral element used in FLAC.....	159
Figure 5.3-3: (a) Stresses acting on the geogrid elements surrounding a node, (b) Interface behaviour of a geogrid node (FLAC manual report).....	162
Figure 5.3-4: Mohr circles at in-situ stress and at failure. ....	164
Figure 5.3-5: The model geometry. ....	167
Figure 5.4-1: Shear stress versus displacement in the numerical and physical simulations of the shear box test, on the base course material. ....	168
Figure 5.4-2: Deviatoric stress versus the axial strain in the numerical and physical simulations of the triaxial test, on the subgrade material. ....	170
Figure 5.4-3: Volumetric strain versus the axial strain in the numerical and physical simulations of the triaxial test, on the subgrade material. ....	170
Figure 5.4-4: Deviatoric stress versus the axial strain under cyclic load in the numerical and physical simulations of the triaxial test, on the subgrade material.....	171
Figure 5.4-5: Plate load test performed directly on the subgrade soil. ....	172
Figure 5.4-6: Subgrade loading simulation geometry. ....	173
Figure 5.4-7: Surface settlement in the numerical and physical models. ....	173
Figure 5.4-8: Surface stress developed in the numerical and physical models.....	173
Figure 5.4-9: Stress developed at the plate centre in the subgrade depth in the numerical and physical models.....	174
Figure 5.4-10: Shear stress versus displacement in the numerical and physical simulations of the shear box test, on the Geosynthetic and base course interface. ....	175
Figure 5.5-1: Subgrade surface settlement for the reinforced and unreinforced numerical and physical model.....	176

Figure 5.5-2: Settlement (a) reinforced model, (b) unreinforced mode in m.....	177
Figure 5.5-3: Vertical stress distribution (a) reinforced model, (b) unreinforced model in Pa. ....	178
Figure 5.5-4: Subgrade surface vertical stress distribution for the reinforced and unreinforced numerical and physical model. ....	179
Figure 5.5-5: Vertical stress in depth under the plate centre for the reinforced and unreinforced numerical and physical model. ....	179
Figure 5.5-6: Geosynthetic nodes displacement in X-direction in m. ....	180
Figure 5.5-7: Geosynthetic nodes resultant force in X-direction in N/m. ....	181
Figure 5.5-8: Force in kN/m developed in the geosynthetic in the numerical and physical model.	181
Figure 5.5-9: Geosynthetic/Base course interface shear stress in Pa.....	182
Figure 5.5-10: Subgrade surface settlement for the reinforced and unreinforced numerical and physical model.....	183
Figure 5.5-11: Subgrade surface vertical stress distribution for the reinforced and unreinforced numerical and physical model. ....	183
Figure 5.5-12: Force in kN/m developed in the geosynthetic in the numerical model with two base course thicknesses (220 mm and 350 mm). ....	184
Figure 5.6-1: Base course dilatancy, friction angle and elasticity modulus effect on the maximum vertical stress on the subgrade surface. ....	185
Figure 5.6-2: Base course thickness effect on the maximum vertical stress on the subgrade surface. ....	185
Figure 5.6-3: The interface elastic modulus and friction angle effect on the maximum vertical stress on the subgrade surface.....	186
Figure 5.6-4: Interface subgrade/ base course friction angle effect on the maximum vertical stress on the subgrade surface.....	187
Figure 5.6-5: Geosynthetic stiffness effect on the maximum vertical stress on the subgrade surface. ....	187
Figure 5.6-6: Geosynthetic position depth effect on the maximum vertical stress on the subgrade surface. ....	188
Figure 5.6-7: Geosynthetic position depth effect on the maximum vertical stress on the subgrade surface .....	189
Figure 5.7-1: Ratio of maximum vertical stress on the subgrade in the reinforced and unreinforced model versus the ratio of subgrade maximum settlement over the base course thickness. ....	189
Figure 5.7-2: The subgrade surface settlement for the five imposed settlements models with reinforcement (5, 10, 15, 20 and 25 mm), with the radius of curvature at the point P. ....	190
Figure 5.7-3: The subgrade surface vertical stress in the reinforced and unreinforced models for the five imposed settlements (5, 10, 15, 20 and 25 mm) for base course thickness of 220 mm. ....	191

# List of Tables

---

Table 2.2-1: The SAT facility principal characteristics. ....	60
Table 2.3-1 : Mixtures degree of saturation at the water content giving a CBR of 2% under proctor compaction conditions. ....	66
Table 2.3-2 : Geogrid properties. ....	72
Table 2.4-1 : Installation Protocol details.....	78
Table 3.2-1: Performed tests details.....	92
Table 3.4-1: Reinforced and unreinforced cycles number needed to reach the base course settlement of 45 mm, 60 mm, and 75 mm.....	113
Table 3.4-2: Reinforced TBR = $N_{\text{reinforced}}/N_{\text{unreinforced}}$ for 45 mm, 60 mm, and 75 mm of the base course surface settlement. ....	113
Table 3.5-1: The Virgin and damaged aggregates classification. ....	117
Table 3.7-1: Designed base course thicknesses estimation in the unreinforced case .....	122
Table 4.2-1: Performed tests details.....	125
Table 5.4-1: The base course Mohr-Coulomb Model calibrated properties.....	167
Table 5.4-2: Subgrade Cap-Yield Model calibrated properties. ....	169
Table 5.4-3: The Base course/Subgrade interface. ....	171
Table 5.4-4: Geosynthetic properties. ....	174
Table 5.4-5: Interface Base course/Geosynthetics interface properties.....	175

# General introduction

---

Nowadays, a significant part of the economic development is directly related to the transportation and infrastructure network. In the USA trucks carry approximately 60% of total shipments by weight according to FHWA, 2006. In Brazil, roads haul approximately 61% of the freights with almost 90% of the total roads network length consisting of unpaved roads according to GEIPOT, 2008. With the roads network expansion, the unpaved roads construction on soft subgrade becomes often an issue due to excessive ruts development. The traditional soil replacement solution is not economically efficient, although other stabilization solutions were used such as the geosynthetic reinforcement. Mc-Gown in the UK and Leflaive in France firstly used geotextiles in this application thanks to pioneering work in the late 1960s (Giroud, 2009). Geotextile became extensively used during the 1970s, first in Europe and then worldwide. The geogrids developed in the 1970s by Mercer, entered this application in the early 1980s.

The mechanisms that govern the unpaved roads behaviour are complex: First because of the platform heterogeneity, indeed it consists of a cohesive loose subgrade that supports a granular layer, and second because of the road structure properties modification under the traffic cyclic load. The reinforcement addition makes the structure and the underlying mechanisms even more complex. Over the years, the sites experiments proved the geosynthetics efficiency in reducing the unpaved platforms surface rutting and increasing the platform serviceability. Thirty years of research in this field, provided a lot of knowledge and explanations. In literature, the developed mechanisms with reinforcements were well distinguished: the separation between the soft subgrade and the granular material, the base course lateral restraint and the tension membrane mechanism. Regarding the problem complexity and the various parameters that affect the platform behaviour, there are no clear ideas about the dominant mechanism and its relative contribution on the platform behaviour improvement. Moreover, various analytical and empirical design methods were developed based on different mechanisms. However, these methods have some particularities and limitations. Therefore, more investigations and studies are still needed to clarify the developed mechanisms and provide more knowledge in this field.

The present research work was done in the context of the LabCom PITAGOR joining the laboratory GEOMAS of INSA de Lyon and the company AFITEXINOV, the Labcom PITAGOR was funded by the National agency of research in France (ANR Agence National de la recherche) for 3 years. This thesis was proposed with the aim of providing more knowledge and clarities about the developed mechanisms and their relative contribution in improving the platform behaviour. Thus, a large-scale laboratory experimental setup was designed, developed and tested. In fact, a cyclic plate load test was conducted, and a special attention was given to the platform layers preparation and installation protocol. The platform preparation repeatability was checked by comparing experimental results for identical performed tests. Furthermore, this cyclic plate load test was used to compare between the

different geogrids performance and to verify their benefits on the platform behaviour. In addition, this plate load test was a preparation for further performed traffic load tests using the developed apparatus the "Simulator Accelerator of Traffic" (SAT). In this research project, a numerical model was also proposed using the differential element methods under static load, and a comparison between the numerical and experimental results was done. This report is divided into five Chapters, detailed as follow:

Chapter 1 presents a detailed literature review regarding the unpaved road geosynthetic reinforcement. In this Chapter, the performed laboratory small-scale and large-scale tests were presented and detailed, moreover in-situ tests and the tests performed using an Accelerated Pavement Tests Facility were detailed. The developed empirical and analytical methods and their limits were presented. Furthermore, the models developed to simulate this application were shown. A clear explanation of the work in relation to our research was discussed as well in this Chapter.

Chapter 2 presents the developed test protocol, devices, used materials, instrumentations and quality control tests. In fact, a detailed presentation of the plate load and the Traffic load test performed were given. The Simulator Accelerator of Traffic (SAT) developed in this research in order to fit these application requirements was described. The used material for the subgrade soil, the base course layer and the three geogrids used in the tests were also presented. Moreover, the platform layers' installation and compaction developed protocol was detailed. A special attention was given to this protocol in order to insure the platform preparation repeatability. Furthermore, a protocol for the quality control tests was established and detailed in this Chapter in order to control the platform homogeneity and properties before each performed test. Finally, the platform instrumentation under the plate load and traffic load tests was presented.

Chapter 3 presents the plate load tests results performed in a box of 1.8 m in large, 1.9 m in length and 1.1 m in height. A plate with 300 mm of diameter was used to apply a load of 40 kN resulting in applied stress of 560 kPa. The cycles were performed under a frequency of 0.77 Hz. Each tested platform was subjected to 10,000 cycles. The quality control tests performed for each prepared platform results were presented. Different tests were performed under these loading conditions: three different geogrid types placed at the interface between the base course and the subgrade, two base course thicknesses, and one geogrid placed at the base course middle depth. Three repeatability tests were performed. The results were presented in terms of vertical stress distribution at the subgrade, base course settlement, subgrade settlement and the geogrid strain.

Chapter 4 presents the tests performed in a larger box of 1.8 mm in large, 5 m in length and 1.1 m in height. The same prepared platform was subjected on a side to a plate load test under a particular plate shape similar to the wheel contact area, and on the other side to the circulation traffic load performed using the developed SAT machine. The SAT apparatus has a specific mechanical concept that allows the load application even after high rut development. In this test, the load applied on the wheel was equal to 28 kN resulting in a contact stress of 650 kPa. The circulation load was applied with a velocity of 4 km/h under an effective circulation length of 2 m. On the other hand, the particular plate load test was performed under the same load conditions of 28 kN maximum load, resulting in a contact stress of 650 kPa, and a loading frequency of 0.77 Hz. In order to compare the

solicitation effect, the circulation traffic load test results were compared to the particular plate load tests. Three different platforms were tested under these loading conditions.

In Chapter 5, a continuous three-dimensional model based on the finite differential method using FLAC 3D software was developed. This model simulated the plate load test performed experimentally in Chapter 3 with the same configuration. The simulation of the first monotonic load was performed and compared to the monotonic first load applied experimentally. The material parameters have been calibrated based on the laboratory characterization tests. Moreover, a parametric study was performed to identify the influence of the various parameters.

Conclusions and Perspectives are drawing at the end of this report.



# Chapter 1. State Of The Art

---

## 1.1. Introduction

In the last few decades, geosynthetics (GSYs) were widely used in Civil engineering and especially in geotechnical field. In fact, GSYs can provide seven different functions as separation, drainage, filtration, protection, barrier, erosion protection and reinforcement. Due to their high mechanical properties, the GSYs are used for soil reinforcement in geotechnical constructions: retaining walls, pile supported embankments, unpaved roads and soft subgrade, etc... In some cases different GSY types can be assembled to provide several functions and this assembly is referred to geocomposites. The GSYs were used in the unpaved road application since 1970. According to the National Highway Institute (NHI), the application of GSYs for unpaved roads reinforcement is one of the more intensively used GSY field (NHI, 2008). For the first GSY applications, the geotextiles were used in unpaved roads reinforcement. After the development of the geogrids by Mercer in 1970, the geogrids integrated this application in 1980. Nowadays the geocells have been used in a relatively small number of cases in unpaved roads reinforcement.

A statistic done in the beginning of 21<sup>st</sup> century regarding the use of GSYs in unpaved areas was reported by Giroud (2009):

- 25% in real unpaved roads,
- 50% in unpaved roads that will eventually become a paved roads,
- 25% in unpaved areas.

Along these years, the experience proved the efficiency of the reinforcement in increasing the load support capacity and the serviceability of the unpaved roads structures.

Previous studies have highlighted the effect of the GSY-reinforcement. Indeed, Bloise and Ucciardo (2000) noted that the reinforcement presence facilitates the aggregate platform compaction. Floss and Gold (1994), Huntington and Ksaibati (2000) and Meyer and Elias (1999) reported that the GSY improves the platform bearing capacity. Bloise and Ucciardo (2000), Cancelli and Montanelli (1999), Huntington and Ksaibati (2000), Jenner and Paul (2000), Martin (1988) and Miura et al. (1990) concluded that the GSY allows the reduction of the granular platform thickness. Cancelli and Montanelli (1999), Knapton and Austin (1996) and Meyer and Elias (1999) reported the effect of the reinforcement on the rut development delay.

More than 20 years of research in this field provided a lot of knowledge and scientific bases that we will be presented in this chapter. In fact, a general presentation of the application, the developed mechanisms and the influencing parameters are presented below. Moreover, the experimental tests and results, the empirical and analytical design methods and the numerical simulations developed in literature to characterize the GSYs effect on this application are also presented. Supported by this knowledge bases we will try to go further and add clarification to the mechanisms developed in this application.



## 1.2. GSYs types and functions

The GSYs have been widely used in Civil engineering to replace traditional materials, especially in environmental geotechnical field.

The period between 1975 and 1990 was very important in innovation polymer inclusion for soil reinforcement. The advantages in reduction of materials cost and increasing in the service duration are proved either by the researches performed or by the experiences of the projects achieved.

The synthetic polymers for GSYs production usually used in soil reinforcement are mainly: polypropylene (PP), Polyvinyl chloride (PVC), high-density polyethylene (HDPE), polyamide (PA) and polyester (PET). For special application, polyvinyl alcohol (PVA), aramids fibres (Aar) and expanded polystyrene (EPS) foam are also used.

### 1.2.1. Geotextiles

The geotextiles are permeable polymer textile products. There are three types of geotextile, the woven, the non-woven and the knitted geotextiles.

The different polymer types, which are used in geotextile fabrication, are polypropylene (PP), polyamide (PA), polyester (PET), polyethylene (PE).

### 1.2.2. GSY barrier

Low-permeability geosynthetic material, used in geotechnical and civil engineering applications with the purpose of reducing or preventing the flow of fluid through the construction.

- Geomembrane is defined by the French standard NF P84-500 as following: A manufactured product adopted in civil engineering, with a minimum width of 1.5 m, thin, flexible, continuous, fluid-tight at the end of the fabrication line, with an effective minimum thickness of 1 mm. The sealing factor of a membrane must be lower than 0.1 L/day/m<sup>3</sup> on a hydraulic charge equal to 100 kPa (excluding the joints area).
- Bituminous geomembrane: based on oxidized bitumen or modified bitumen by a polymer.
- GSY Clay Liners: it is a geosynthetics and sodium bentonite clay combination, which forms an impermeable barrier.

Every product has specific characteristics and behaviours that have to be taken into consideration when choosing the appropriate GSY.

### 1.2.3. The apparent products

The permeable products other than geotextiles are:

- The geogrids used for soils reinforcement.
- The geomats used as anti-erosion.
- The geospacers used for drainage.
- The geocells used for a thin soil layer confinement.
- The geocontainers used as soil or other materials containers.



Figure 1.2-1: Some GSY products and applications (AFITEXINOV: <http://www.afitex.com>)

### 1.3. Unpaved roads

The considered structure is composed of an unbounded aggregate layer supported by a soft subgrade layer and subjected to a traffic load. The traffic load is a cyclic load characterised by the magnitude of the axle load and the number of the axle passes. The road structure support this load under a certain service life.

In general, the reinforcement by GSY is placed at the interface between the granular platform and the soft subgrade. As mentioned previously, the reinforcement increases the bearing capacity of the structure and increases its service life.

The behaviour of this structure is complex due to the structural heterogeneity and the variation of the materials property under the cyclic traffic load. Moreover, the addition of the reinforcement complicates even more its behaviour. Especially because in this application the load is vertical and the reinforcement is horizontal.

The contribution of the reinforcement in improving the structure behaviour depends on different mechanisms developed in the road structure:

- The base course lateral restraint,
- Tension membrane effect,
- Separation.

#### 1.3.1. Lateral restraint of base course material

By adding a tension stiffness at the bottom of the base course, the lateral movement of the aggregate under the wheels' load is blocked. This mechanism reduces the shear stress on the subgrade top and increases the stiffness of the base course layer. Consequently, the vertical stress on the surface

of the subgrade decreases. In fact, this is a two-layer system, and the stress distribution on the lower layer depends on the relative moduli contrast of the two layers.

It is important to note that, the GSY adds the tension stiffness to the base course by two mechanisms: interface friction between GSY and aggregate when a geotextile is used, interlocking between GSY and aggregate and the friction between the geogrid strips and the aggregate when a geogrid is used (Giroud, 2009). Based on previous studies, the lateral restraint mechanism does not imply high rutting form (Collin et al., 1996; Perkins & Ismeik, 1997).

As mentioned before, the restraint mechanism differs between geotextile-reinforcement and geogrid-reinforcement. Palmeira and Antunes (2010) noted, based on large-scale laboratory tests, that the geogrid is more efficient than the geotextile in restraining the material lateral movement.

In addition, Cuelho and Perkins (2009) proved, based on in-situ tests, that the geogrids provide a better overall performance than geotextiles.

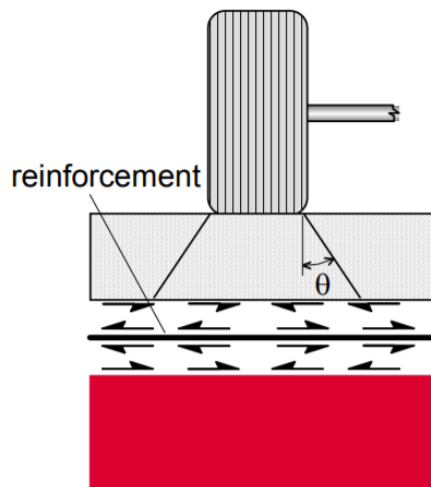


Figure 1.3-1: Lateral restraint mechanism- IGS (International GSYs Society)

### 1.3.2. Tension membrane effect

The tension developed in a curved GSY results in an upward force supporting the wheel load, so the pressure applied at the upper side of the reinforcement will be higher than the pressure applied on the lower side.

In early studies on the GSY reinforcement mechanisms, the membrane effect was considered as the dominant mechanism. It was noted in literature that the tension membrane is predominant for small fill material thickness, low value of base course shear stiffness (Ghosh & Madhav, 1994), significant rut development and high GSY stiffness (Perkins & Ismeik, 1997).

More recently, (Giroud & Han, 2004; Giroud, 2009; Qian et al., 2011 and Cook et al., 2016; Giroud, 2016) stated that the tension membrane mechanism is not the dominant mechanism, and highlighted the important contribution of the lateral restraint mechanism in improving the structure bearing capacity.

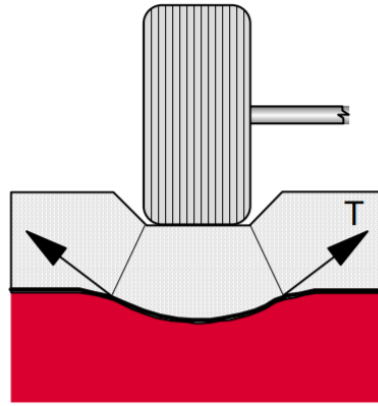


Figure 1.3-2: Tension membrane mechanism-IGS (International GSYs Society)

### 1.3.3. Separation

The separation between the soil layers is important to conserve the well-compacted base course layer properties. In fact, the separation prevents the loss of aggregates particles in the soft soil and the incorporation of the fine materials into the base course layer.

Geotextiles are typically used to provide the separation function. However, Giroud (2009) mentioned that a geogrid with appropriate aperture size can also provide the separation function.

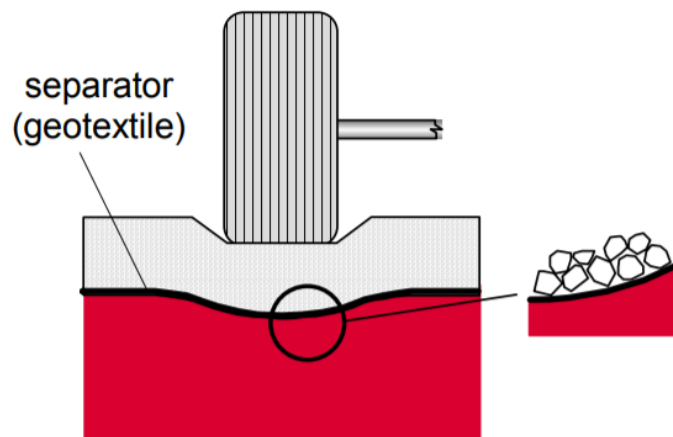


Figure 1.3-3: Separation mechanism- IGS (International GSYs Society)

As shown before, the mechanisms that take place in the reinforced structure are complex. In spite of the important researches in this field, there is still a lack of knowledge. In fact, the mechanisms are not perfectly clear and the dominance of the mechanisms is not well defined. In order to understand better the above-defined mechanisms, the parameters influencing the reinforcement behaviour are presented in section 1.4.

## 1.4. Reinforcement influencing parameters

In order to clarify the mechanisms developed and propose a design method for this structure, the influencing parameters should be defined. Based on experimental, analytical or numerical results, different influencing variables are identified:

- the base course thickness,
- the reinforcement position,
- the GSY type and stiffness,
- the geogrid aperture shape and dimension,
- the geogrid aperture stability modulus.

### 1.4.1. The base course thickness

Many authors noted that the GSY impact is significant in the case of a base course thickness less than 0.4 m (Collin et al., 1996; Meyer and Elias, 1999). In contrast, Hufenus et al. (2006) based on an in situ test, concluded that the reinforcement reduces the rut development even for a base course thickness higher than 0.5 m. However, to prevent the GSY damage under the traffic load the GSY must be covered by a minimum 0.2 m of fill material (Meyer and Elias, 1999).

### 1.4.2. The reinforcement position

The GSYs are placed usually at the subgrade and base course interface. However, other locations of reinforcement can be considered. In literature, the authors stated that the optimum GSY position depends on the subgrade strength and the fill material thickness. With a soft subgrade and a thin base course thickness the optimum position is at the interface (Cancelli and Montanelli, 1999; Walters et al., 1999). However, the optimum position is between 0.25 - 0.35 m under the surface of the base course layer, in the case of a higher bearing capacity subgrade and a higher fill material thickness (Perkins et al., 1999). Akond (2012) noted, based on the results of laboratory cyclic plate load tests, that the optimum location of reinforcement for thick base course layer is at the upper one-third position of the base course thickness. However, the author noted that for a thin base course layer placing the GSY at the interface is very effective.

### 1.4.3. The GSY type and stiffness

The lateral restraint mechanism can be insured by the friction at the interface when a geotextile is used and by the interlocking mechanism in the case of a geogrid. Therefore, the effect of the GSY type is important. Moreover, the GSY manufacturing type (knitted woven geogrid, extruded geogrid...) changes the GSY performance and affects the mechanisms that take place at the interface. In the case of a geotextile, the stiffness of the product affects the performance of the reinforcement. The geogrid ribs stiffness is also an important factor that affects the reinforcement influence in the case of a geogrid. In fact, the effectiveness of reinforcement is increased by the use of a stiffer geogrid (Brown et al., 2007; Hufenus et al., 2006; Sun et al., 2015; Qian et al., 2013). However, Giroud (2009) stated that if the geogrid is too stiff it may disturb the aggregate structure during compaction.

#### 1.4.4. The geogrid aperture shape and dimension

The confinement is one of the mechanisms developed at the interface, and recently various studies have proved the important impact of this mechanism on the structure behaviour. The confinement mechanism, in the case of geogrids, depends on the interlocking between the geogrid apertures and the aggregate arrangements and the friction between the geogrid bands and the aggregate.

Qian et al. (2011, 2013) performed laboratory plate load tests on unpaved roads and compared the effect of geogrid aperture shape. The authors showed that a triangular aperture shape performed better than a rectangular aperture shape. Dong et al. (2011), based on a numerical model, concluded that the triangular aperture geogrid has a better ability to distribute the load through 360 degrees. In contrast to the traditional biaxial geogrid, which has the tensile stiffness predominant in two directions.

In addition to the aperture shape, the aperture size influences the interlocking mechanism. Szatmári (2016) stated, based on the results of a multi-level shear box tests, that the correct aperture size can improve the soil shear strength even 200 mm above the reinforcement level.

McDowell et al. (2006) modelled the grid and the ballast using the Discrete Element Method; based on this theoretical and computational work, the authors stated that the ratio between grid aperture size and nominal size of the aggregate should be 1.4. Consequently, for 50 mm ballast, the best aperture size should be 70 mm. Brown et al. (2007) noted, based on a full-scale railway test facility, that for the 50 mm ballast (the maximum ballast diameter) the optimum aperture size is between 60-80 mm.

#### 1.4.5. The geogrid aperture stability modulus

More recently, an additional influencing parameter was introduced which is the aperture stability modulus. The geogrid torsion stiffness and the junction stiffness are combined in the aperture stability modulus property. Giroud & Han (2004) used this parameter in the developed design method to take into consideration the geogrid impact.

The wide variation of these influencing parameters explains why this topic is still a research topic even after more than 20 years of studies.

In fact, many authors proposed various empirical and analytical design methods to determine the fill material thickness by considering the reinforcement effect. These methods are limited due to their testing on limited range of the influencing parameters. Therefore, there are still an absence of an acceptable design technique that can cover the maximum number of situations.

To overcome this issue and provide more knowledge regarding these impacting parameters, various authors have developed an experimental testing system on unpaved roads, and these tests are presented in the next section.

## 1.5. Experimental testing on unpaved roads

In this application, many parameters affect the role of reinforcement on their behaviour. In literature, numerous experimental studies were performed to characterise the reinforcement influence and the variation impact of each parameter. These testings' can be classified in four different categories:

- large-scale laboratory plate load tests,
- large-scale in situ tests,
- reduced scale laboratory cyclic traffic load tests,
- large-scale laboratory cyclic traffic load tests.

### 1.5.1. Large-scale laboratory plate load tests

Two laboratory test approaches have been used in previous studies for the plate load test: the static loading plate load test and the cyclic loading plate load test.

Dong et al. (2010) performed static laboratory plate load tests, and compared the ratio of bearing capacity of every test in order to study the influence of variable factors: the aperture shape, the geogrid location and the number of geogrid layers. Based on the results of these tests the authors concluded that the geogrid placed at the depth of  $2/3$  of the plate diameter performed better than other positions.

Akond (2012) conducted two series of laboratory tests: a monotonic plate load test and a repeated load triaxial test (RLT) (Figure 1.5-2). A monotonic load plate was applied on the aggregate base course surface placed over the subgrade in a box of 1.5 m in length, 0.91 m in width and 0.91 m in height. ASTM test procedure (ASTM D1196-93) came after in this study. The subgrade soil consists of a silty clay soil. The Kentucky limestone was used for the granular base course layer with variable thickness of 200 mm, 300 mm and 450 mm. The installation and compaction procedures are detailed in the report, and in situ tests were performed in order to control the compaction quality (The nuclear density gauge, the geogauge stiffness device, the dynamic cone penetrometer, and the light falling weight deflectometer). Several types of geosynthetics were used in this research: biaxial geogrids, triaxial geogrids and geotextiles. A total of 47 tests were performed during this thesis, with different geosynthetic types, different geosynthetic locations in base course and different base course and subgrade thicknesses (first case 600 mm of subgrade and 300 mm of aggregate, second case: 457 mm of subgrade and 457 mm of aggregate, third case: 711 mm of subgrade and 203 mm of aggregate). The subgrade was instrumented with earth pressure cells; more over the geosynthetics were instrumented with strain gauges.

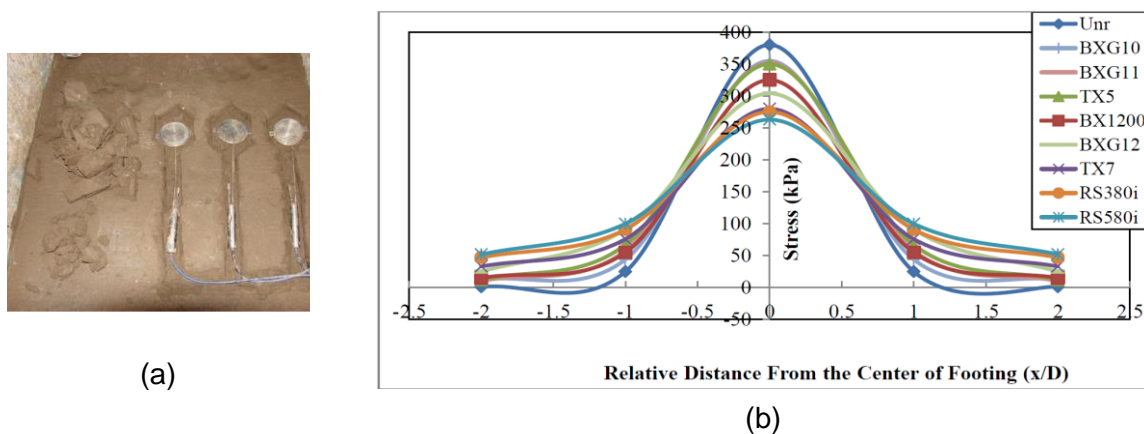


Figure 1.5-1: (a) Earth pressure distribution, (b) Vertical stress distribution on the subgrade layer along the centre line of the plate at 1724 kPa applied plate pressure for a 300 mm of base course thickness. (Akond, 2012)

Based on the results in Figure 1.5-1, the authors mentioned above discussed the effect of the reinforcement on the stress distribution angle. However, it should be pointed out that when an earth pressure cell is used in soft subgrade there is an uncertainty caused by the sensor settlement, its rotation and the possible arching effect around the sensor. Nevertheless, this fact was not taken into account by the authors. Moreover, the earth pressure cell placed at the borders of the box shows a non-negligible vertical pressure that can demonstrate the box's boundary condition effects. The authors noted as well that the optimum location of reinforcement is located at the upper one-third position of thick base course. However, for a thin base course layer such as 20.32 mm of thick crushed limestone base, placing geosynthetic reinforcement at the interface is very effective. It is worth noting that not only the base course thickness was changing but also the thickness of the subgrade layer and this can affect the results.

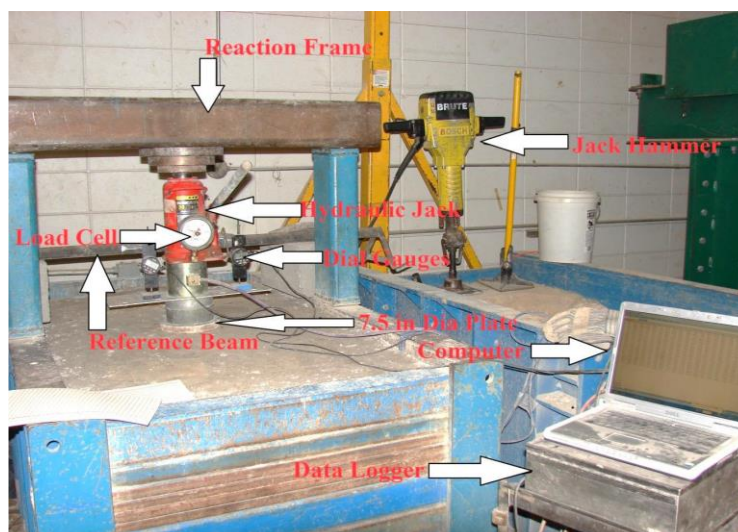


Figure 1.5-2: Plate load test setup. (Akond, 2012)

Demir et al. (2013) performed large-scale field monotonic plate load tests with different plate diameters (0.3, 0.45, 0.6 and 0.9 m). The tests were performed in field test pit with 2.8 m in width, 2.8 m in length and 2 m in depth. Sixteen field tests were respectively performed on unreinforced clay soil, granular fill reinforced clay soil and geogrid reinforced granular fill over clay soil. In-situ static penetrometer and pressuremeter tests were performed to characterise the in-situ clay.



Moreover, in-situ unconfined compression tests were performed to determine the undrained shear strengths CU. A white coloured, secugrid Q type geogrid with maximum tensile strength of 60 kN/m was used. No instrumentation was included in the platforms. The testing procedure was performed according to the ASTM D 1196-93 standard. The authors concluded that when the clay is placed with a compacted layer of fill material the bearing capacity increases by 40%. Furthermore, they observed no effect adding a geogrid at the base course and subgrade interface. However, they observed an additional improvement adding a second geogrid layer with the same type and properties in the base course.

Another static plate load test was performed by Abu-Farsakh et al. (2016) aiming to evaluate the effect of the GSY type, the GSY location, the number of GSY layers, and the tensile modulus. The tests were conducted at the geotechnical engineering research laboratory of Louisiana Transportation Research Centre (LTRC). The model tests were placed inside a steel box with the dimensions of 1.5 m in length, 0.91 m in width and 0.91 m in height. The used subgrade was a silty clay classified as a CL soil according to the USCS with a target CBR of 1%. Crushed limestone was used for the base course layer. Two types of geogrids were tested: the extruded biaxial and triaxial aperture shape geogrids with different stiffness. The tests were performed regarding the ASTM D1196-93 standard using a plate of 190 mm diameter. The platform preparation and preparation protocol were detailed in the journal paper. The soil layers properties were controlled using a nuclear density gauge, a Light Falling Weight Deflectometer (LWD) and a dynamic cone penetrometer (DCP). Earth pressure cells were placed at the surface of the subgrade and strain gauges were fixed on the geosynthetics. Abu-Farsakh et al. (2016) performed 22 different tests. Based on their comparison of the bearing capacity ratio between these tests, they concluded that the double reinforcement location with the same type and same stiffness contributes to a platform improvement and that the upper one-third location of a single layer reinforcement yields the highest improvement under static loading conditions.

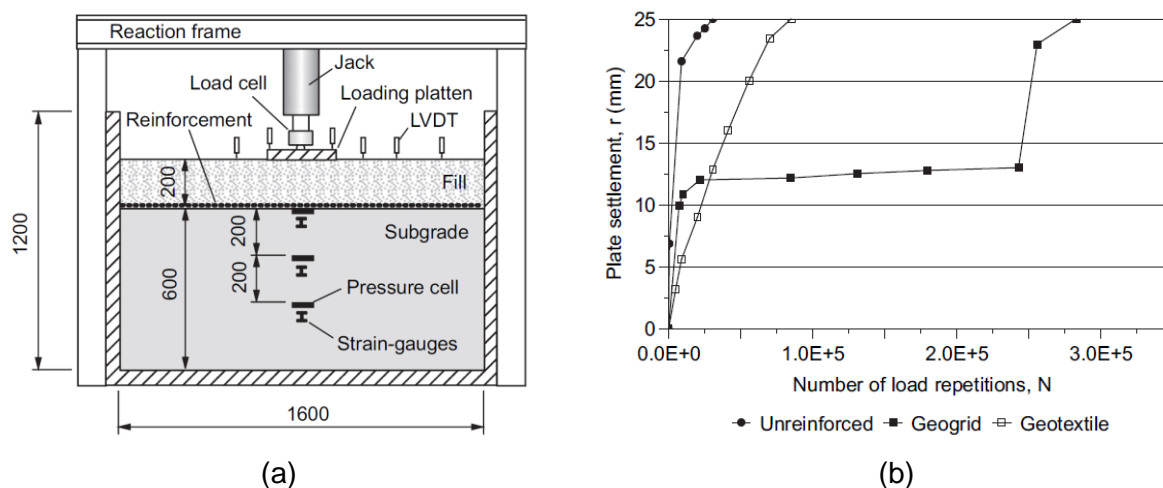


Figure 1.5-3: (a) Equipment used in the tests, (b) Plate settlement versus number of load repetitions-1<sup>st</sup> loading stage. (Palmeira & Antunes, 2010)

A comparison between monotonic plate and cyclic plate loading was performed by Palmeira & Antunes (2010). The used equipment and instrumentation are illustrated in Figure 1.5-3(a). The platform was placed in a box of 1.2 m in height, 1.6 m in width and 1.6 m in length. The load of 40 kN was applied on a plate of 300 mm diameter. The subgrade is a fine tropic soil with a State Of The Art

CBR of 8%. A fill material layer with a thickness of 200 mm was placed on the subgrade layer. A knitted biaxial geogrid and a woven geotextile were tested. The compaction and installation protocol was detailed, but the properties control tests are not mentioned. The instrumentation of the tests consists of: displacement transducers (LVDTs) in order to measure vertical displacements of the loading plate and the fill surface. A load cell attached to the jack measures the loads applied on the fill surface. Earth pressure cells set at different positions in the subgrade layer allow total vertical stress. Vertical strain measurement sensors were also placed at different depths in the subgrade soil. The comparison between the monotonic and cyclic plate load results showed that the tests under monotonic loading conditions underestimate the reinforcement benefits. Palmeira & Antunes (2010) compared the effect of the two GSY under cyclic plate load test under 566 kPa and 1 Hz frequency.

Figure 1.5-3(b) illustrates the developed rut at the surface with cycles. The performed cycles are over 10,000 cycles. The results show that 25 mm of rut was reached after 30,720 cycles for the reinforced platform and 5,000 cycles for the unreinforced platform. It is worth pointing out that the subgrade used in this application is fine-grained tropical soil and that its California Bearing Ratio is 8%, which is higher than 3% (the limit under which a geosynthetic reinforcement is recommended according to the FHWA (2008) Standard). Moreover, the installation procedure and the control of the soil layer properties are not detailed in the journal paper. The authors concluded that the geogrid provides a better overall performance than geotextile in this application due to the interlocking effect. This study addressed the performance of these reinforced platforms after the maintenance of the surface.

The large geotechnical test box (2 x 2.2 x 2 m) at the University of Kansas was used to perform various cyclic plate load tests at a frequency of 0.77 Hz.

Qian et al. (2011) used this apparatus to perform cyclic plate load tests and to investigate the efficiency of the triaxial geogrids with triangular aperture shape. The weak subgrade was an artificial soil composed of a mixture of 75 % Kansas River sand and 25 % of kaolinite by weight with a target CBR of 2%. Well graded aggregate was used for the fill material layer with 300 mm of thickness. The dynamic cone penetrometer test was used to control the layer properties and a correlation between CBR was made. The platform was instrumented with earth pressure cells at the subgrade surface and displacement transducers (LVDTs) at the base course surface. The setup of the cyclic plate load test is illustrated in Figure 1.5-4. The maximum applied load is 40 kN which is the half of a truck axle load regarding the AASHTO (1993) Standard. The base course thickness was settled on 300 mm. The cycles load were applied until the maximum allowed rut was reached, which is equal to 75 mm in this study according to the FHWA (2008) Standard. An unreinforced platform and three reinforced platform using three Triangular-Aperture Geogrids were tested. The three Triangular-Aperture Geogrids differ with their radial stiffness and aperture stability.

The maximum applied cycles were of 1600 cycles for the performing geogrid reinforcement (Figure 1.5-5). As for the unreinforced case, 100 cycles were enough to reach the allowable rut of 75 mm (Figure 1.5-5). It is worth noting that these structures are designed to be subjected to 10,000 cycles of heavy trucks load according to the FHWA (2008) Standard, and that 1600 cycles is a very small number regarding the maximum cycles that the structure should support. This experimental study

showed that the triangular aperture geogrid improves the performance of the structure, reduces the maximum vertical stress at the subgrade centre surface, and decreases the fill material deterioration with the cycles.

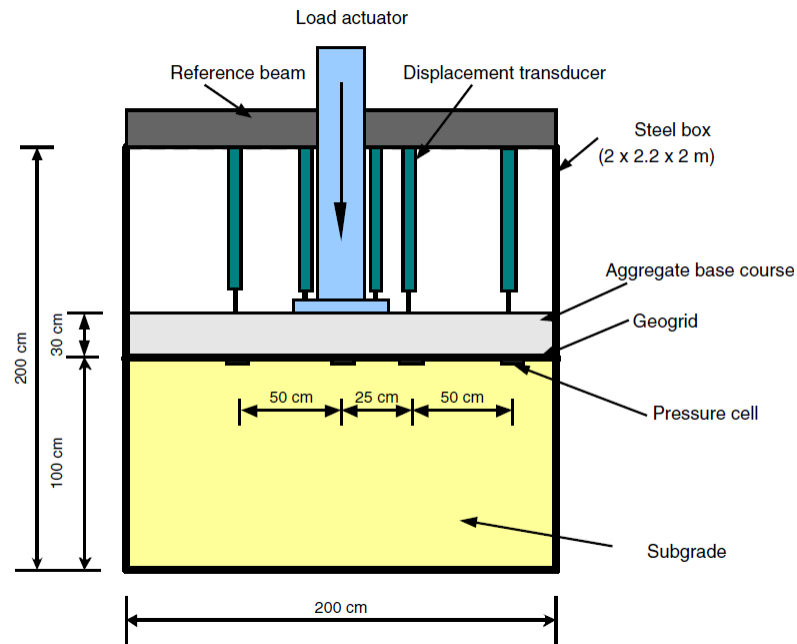


Figure 1.5-4: Setup of the cyclic plate load test. (Qian et al., 2011)

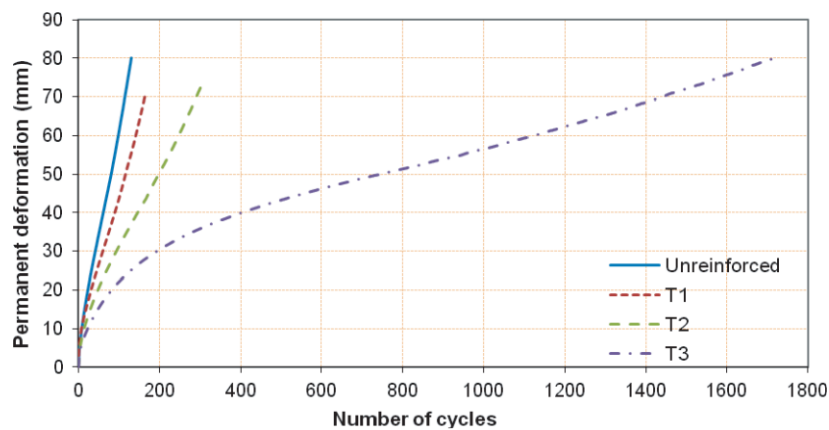


Figure 1.5-5: Permanent deformations of loading plate versus the number of cycles. (Qian et al., 2011)

Qian et al. (2013) used the same device and the same protocol to compare the effect of base course thickness. Three different thicknesses were tested (150 mm, 230 mm and 300 mm). However, as seen before the maximum performed cycles were of 1600 cycles for the reinforced 300 mm base course. The experimental results showed the effect of the reinforcement on the reduction of the maximum vertical stress on the subgrade surface for the three different base course thicknesses. Moreover, the authors concluded that the more robust and thicker the GSY is the more important the benefit in the platform behaviour improvement. In addition, the authors highlighted the effect of the confinement mechanism in improving the reinforced base course behaviour, and pointed out that the tension membrane effect was recognised when the permanent surface deformation was higher than 33% of the base course thicknesses. A similar cyclic plate load test is performed in this study on different GSY types and different fill material properties and thicknesses.

Sun et al. (2015) performed the same test procedure, in order to investigate the effect of load amplitude on the unpaved road response. The same materials and control protocols were used. The authors added earth pressure cells in the vertical plane in order to measure the radial stress propagation. In this test, with every 100 cycles, the load intensity increased by 5 kN from 5 kN to 50 kN. Three base course thicknesses were tested (150 mm, 230 mm and 300 mm). Extruded triaxial aperture geogrid with two different stiffness were tested. The test stopped when 75 mm of permanent surface deformation was reached. 1,000 cycles were the maximum performed cycles number, in the case of the reinforced 300 mm base course thickness. Based on the results the authors highlighted the effect of the geosynthetic in reducing the vertical stress on the subgrade, and related this improvement to the confinement mechanism that increased the radial stress in the reinforcement platforms.

More recently, Satyal et al. (2018) used this device to test the performance of geocells in improving the railways on soft subgrade. In fact, the soft soil part remained the same, and this time it was covered by 300 mm of ballast layer reinforced by geocells. The platform was subjected to 6,000 cycles, and the load amplitude increased by 10 kN every 1,000 cycles, starting from 10 kN and reaching 60 kN. The results showed that the geocell reinforcement decrease the surface settlement, and the applied vertical stress on the subgrade surface in the railways platforms.

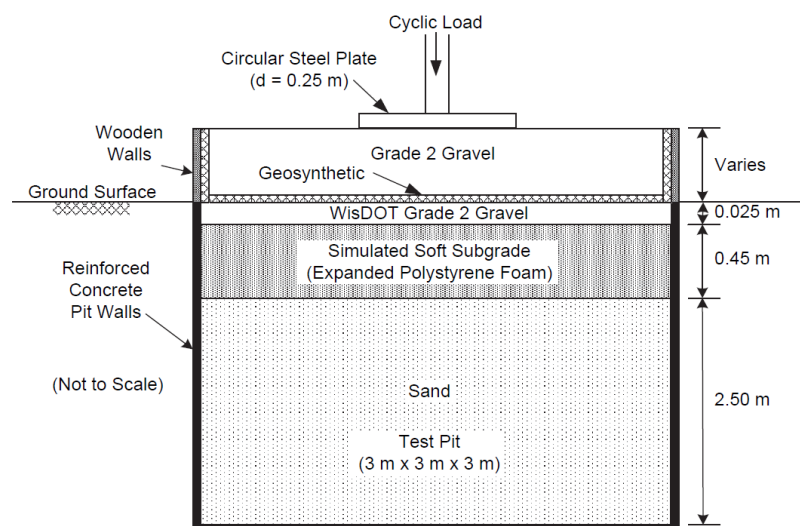


Figure 1.5-6: Schematic of large-scale model experiment (LSME). (Kim et al., 2006).

Kim et al. (2006) conducted cyclic plate load tests on a reinforced and unreinforced platform (Figure 1.5-6). The authors replaced the soft subgrade with an expanded polystyrene foam. Two granular materials were used in this study: the WisDOT (Wisconsin Department Of Transportation) grade 2, and the breaker run stone. Two base course thicknesses were studied: 300 mm and 460 mm. Four different GSY types were tested: biaxial polypropylene geogrid, polypropylene slit-punched geotextile, polypropylene woven needle-punched geotextile, and drainage geocomposite. No quality control tests were mentioned in the article. Moreover, the platform was not instrumented so the results were based on the surface rut development only. The 35 kN load was applied on the plate load 250 mm of diameter. An applied load pulse consisted on a load period of 0.1 s followed by a rest period of 0.9 s. Based on the results, the authors observed a linear relation between the

equivalent base course thickness and the GSY-Base course interaction modulus, obtained from a pull-out test.

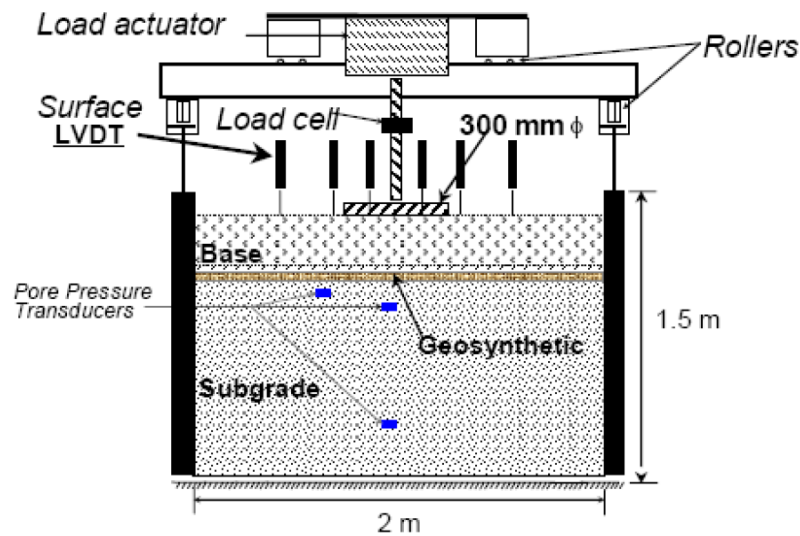


Figure 1.5-7: Schematic diagram of the pavement test facility. (Christopher & Perkins, 2008).

Christopher & Perkins (2008) performed a cyclic plate load test regarding the AASHTO 4E-SR method to evaluate the GSY drainage function in this application (Figure 1.5-7). The subgrade used in this study is a piedmont silt from Georgia with a CBR of 1%. A graded aggregate was used for the base course layer with a thickness of 300 mm. Two geosynthetics were used in this study: a welded polypropylene biaxial geogrid and a geogrid/geotextile geocomposite. The CBR was controlled during the placement, by using moisture content and hand held Pilcon vane shear strength.

On one hand the platform was instrumented using displacement transducers (LVDT's), calibrated load cell, pore pressure sensors and wire extensometers on the geosynthetics, on the other hand measurements were made on geosynthetics at the front of the box to control their movement on the edge of the box. A 40 kN initial load was applied to a 300 mm diameter plate. The cycles were applied with a load pulse frequency of 0.67 Hz. The authors concluded that the non-woven geotextile due to its drainage capacity could reduce the pore pressure in the subgrade. Moreover, they stated that the rutting is highly related to the pore pressure development in the subgrade.

Sarici et al., (2016) performed a large-scale laboratory cyclic plate load test (Figure 1.5-8). The base course thickness varied between 300 mm, 400 mm and 450 mm. The platform was placed in a box of 2 m in length, 2 m in width and 2 m in height. The weak subgrade was installed in order to get a CBR of 4%. No quality control tests were executed. The geogrid used in this study is an extruded triaxial geogrid. 40 kN of load was applied on the base course surface on a plate load of 300 mm diameter. The frequency of the cyclic load pulse was 0.77 Hz. The platform was not instrumented and the results were based on the plate displacement with cycles. The geogrid position depth was changed from 0.33D, 0.67D to 1D with 450 mm base course thickness, where D is the plate load diameter. The authors showed that the geogrid placed at 0.33D depth was more efficient than the other positions.

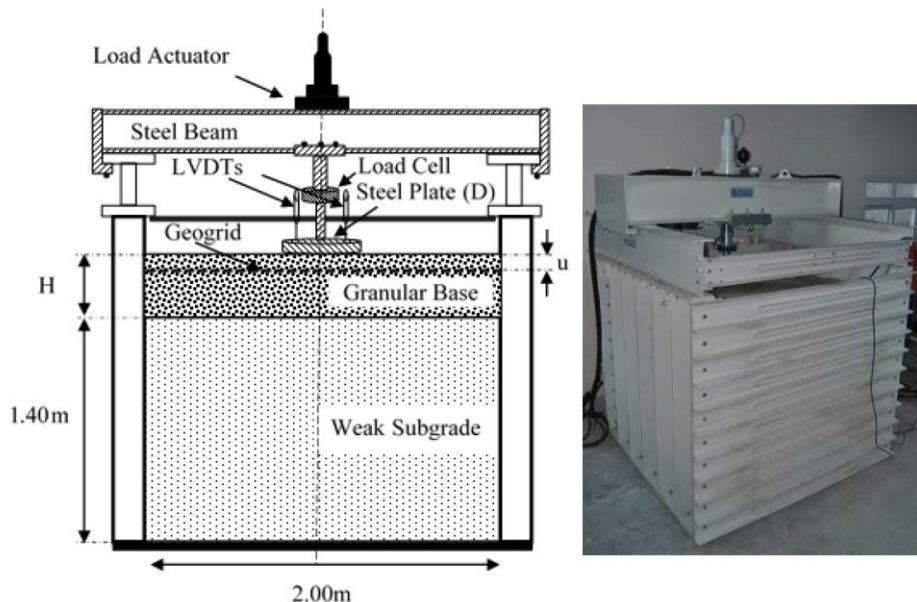


Figure 1.5-8: Schematic sketch and photograph of the large-scale cyclic plate loading test setup. (Sarici et al., 2016).

Gabr (2001) performed a cyclic plate load test. The platform is placed in a box of 1.5 m in length, 1.5 m in width and 1.35 m in height. The subgrade soil is a mixture of 85% Lillington sand and 15% kaolinite with a target CBR of 3%. The aggregate base course used in this testing is classified as GW according to the USCS. Two base course thicknesses were tested: 152 mm and 24 mm. Nuclear density/moisture gage were used to control the soil layer compaction procedures. Earth pressure cells were placed at the subgrade surface and LVDTs were used to determine the surface displacement. Different extruded biaxial geogrid were tested in this study. Forty kN were applied on a 300 mm diameter plate with load pulse frequency of 0.67 Hz. Based on the results of this study two analytical methods were developed to design the reinforced unpaved roads (Giroud & Han, 2004 and Leng & Gabr, 2006). However, these analytical methods were calibrated for the specific GSYs types used in Gabr (2001) testing.

As seen in this literature revue on the plate load tests various tests with different configurations were performed. The comparison between the monotonic plate load test and the cyclic plate load tests in literature showed that the monotonic load underestimates the effect of GSYs (Palmeira & Antunes, 2010b). Moreover, the performed tests showed the evolution of vertical stress on the subgrade surface with cycles due to base course deterioration, and it showed the influence of the reinforcement on this mechanism developed with cycles. However, in many studies the maximum displacement criteria was reached after a relatively small number of cycles even with reinforcement, in comparison with the 10,000 cycles proposed for the design of these structures. Furthermore, the installation procedures and the control of the soil layer properties are rarely considered in the above presented works. In general, and according to the above presented work, the tested GSYs had the same manufacturing types.

However, these tests aimed to simulate circulation traffic on unpaved roads by cyclic load on a plate. In literature, authors proposed in situ tests to simulate better the real applied load. Some of these studies are summarized in the following section.

## 1.5.2. Large-scale in situ tests

In the previous laboratory testing the loading conditions do not simulate perfectly the real trafficking conditions on site, many research projects aim to develop an in-situ testing protocol with real traffic load.

Maxwell et al. (2005) performed full-scale in-situ tests on different sections of a platform with different reinforcement types. Three types of geosynthetics were used: woven geotextile, knitted biaxial geogrid, and punched sheet drawn geogrid. The geosynthetics were equipped with strain gages to monitor the geosynthetics strain. A falling weight reflectometer test (FWD) was performed on the different reinforced and unreinforced sections.

Hufenus et al. (2006) proposed full-scale field tests in order to evaluate the effect of the GSY reinforcement on the bearing capacity of an unpaved road supported by a soft subgrade. The soft soil is consisted of a relatively homogeneous clayey silt existing on the site field. The testing area was divided into 12 sections of 8 m in length and 5 m in width each; in which different types of GSYs were placed. Seven different GSYs were used, with different types of manufacturing processes. Each platform was tested under a state plate load test and the young modulus  $E_{v1}$  and  $E_{v2}$  were calculated. The platforms were trafficked with a loaded and unloaded truck. Based on the results the authors concluded that the effect of the reinforcement is significant regarding the bearing capacity of a thin base course layer ( $h < 0.5$  m). Moreover, they noted that the reinforcement has reduced the rut development as well as the number of trafficking before reaching the allowable rut depth even for a thicker base course layer  $h > 0.5$  m. In this study, the soil installation and the soil compaction were controlled.

Cuelho & Perkins (2009) proposed as well a full-scale test on site (Figure 1.5-9). The tested pit was 4 m in width, 195 m in length and 1 m in depth, in which 12 different sections were tested with 10 different GSY types. The subgrade is consisted of artificial soil, which is the site soil, treated and compacted in order to have a small strength. The traffic load was applied using a three-axle truck. The trafficking was applied until it reached 100 mm of rut in each section. A total 40 truck passes were applied. The results of this test permitted the comparison between different GSY types and manufacturing processes. The authors provided a correlation between the materials properties and the rut development, and proved that the stiffness of the GSY was the most important material property that dominates the behaviour of the GSY under relatively high rut development. Moreover, they compared the experimental results to the Giroud & Han (2004) analytical design method and they concluded that this method underestimates the base course thickness. Cuelho et al. (2014) performed an additional work on the same experimental field and with the same soil materials and installation protocol. Three control sections with different base course thicknesses, three sections with the same reinforcement but different subgrade strength and eleven more sections with the same base course thickness and subgrade strength but different GSY types. The trafficking was applied with the same truck as the one in the previous experimental test, but this time 700 truck passes were applied. Based on the results, the authors established a correlation between the GSY junction strength, the GSY stiffness, the ultimate strength and the cyclic stiffness in the cross-machine direction with the rut development.



(a)



(b)

Figure 1.5-9: (a) Delivery and distribution of the artificial subgrade in the test pit, (b) Installation of geosynthetics. (Cuelho & Perkins, 2009)

Cuelho & Perkins (2017) performed in-situ test in the same pit with the same configuration. The authors changed the base course thickness for the controlled area from 270 mm to 410 mm and to 630 mm. Moreover, they changed the subgrade strength for a given section with a given reinforcement from 1.79% in CBR to 2.17% and 1.64%. The results show the effect of the reinforcement on the platform performance improvement, and they show a relation between the reinforcement junction stiffness and the performance indicator. The authors used the experimental results to calibrate the analytical method given by Giroud & Han (2004). They proposed as well a new analytical solution to enhance the factor that depend on the geosynthetics properties based on the junction stiffness.

Mekkawy et al. (2011) conducted an in-situ testing; 310 m of section with different reinforcements were prepared (Figure 1.5-11). The in-situ soft subgrade was characterised and classified as SC (A - 4). A crushed limestone was used for the base course layer. Three biaxial geogrid types were used to stabilize the platforms. The authors performed a dynamic cone penetrometer test and showed the effect of the reinforcement on the CBR of the granular layer. The sections were continuously monitored using in situ for a period of about one year. After one month from construction, an edge rut of about 127 mm was measured at the control section. The reinforced sections showed no rutting. It is worth noting that in this full-scale test, the load magnitude and the number of cycles were not controlled. Moreover, the sections were not instrumented; the results are based on surface rut development.

On one hand, Mekkawy et al. (2011) performed a laboratory plate load test in a box of 600 mm in width, 600 mm in length and 450 mm in depth. On the other hand, the load was applied on the surface using a plate of 150 mm diameter. The authors compared the effect of the anchored and unanchored reinforcement, and showed that effect of the anchored geogrid is more important than the effect of the unanchored geogrid. However, this experiment was performed in a reduced dimension box.





Figure 1.5-10: (a) Prepared testing sections, (b) 76 mm rut developed with few truck passes. (Mekkawy et al., 2011)

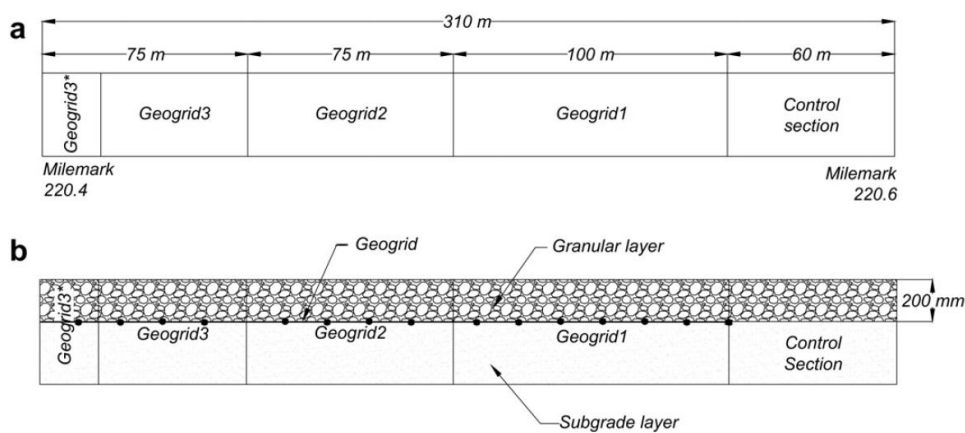


Figure 1.5-11: Schematic diagram of the test section, (a) plan view, (b) cross section. (Mekkawy et al., 2011)

These tests that have been performed in in-situ full-scale conditions simulate very closely the real conditions. However, the maximum truck axle passes were limited between 200 and 700 passes, which is a limitation, because as it is known based on the FHWA standard (2008), these structures should be designed to support 10,000 passes. Moreover, it is hard to control the soil conditions and the repeatability of the test in an outdoor environment. It is important to note that the platform installation procedure requires an important amount of time.

### 1.5.3. Reduced-scale laboratory cyclic Traffic load tests

In order to facilitate the platform installation procedure the scale reduction is a solution. Tang et al. (2008) proposed a laboratory test with a 1/3 scaling using the one-third scale model mobile load simulator (MMLS3). This test was performed on paved roads. Where the traffic speed was set to 7200 axles per hour; with a nominal speed of 9.4 km/h. The MMLS3 illustrated in Figure 1.5-12 applied a wheel load of 2.7 kN. The subgrade material was silty sand SW-SM, with 6.2% of fine particles. Two different subgrade CBRs were used in this test, a CBR of 3% and a CBR of 1.5%. Dense-graded Crushed stone is used for the pavement base course layer. The pavement subgrade soil was compacted in three layers with a vibratory plate compactor. Four different geogrid types

were used in this study: two biaxial geogrids with high tenacity polyester multifilament yarns coated, one biaxial grid made of woven polypropylene yarns, and one biaxial extruded polypropylene geogrid.

The end of the geogrid sections are folded against the pit walls to obtain necessary anchorage and slight pre-tensioning, in order to prevent the shifting of the geogrids out of their position.

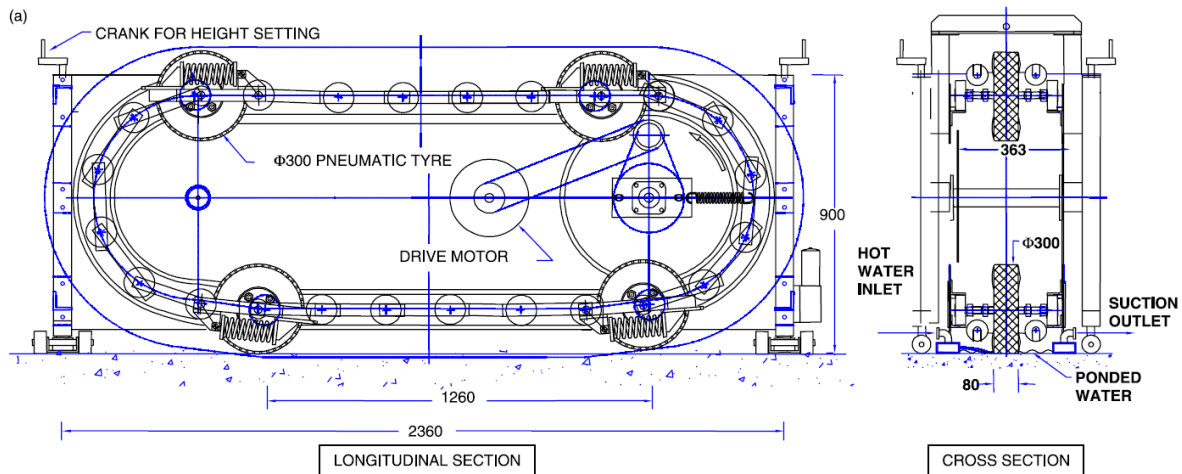


Figure 1.5-12: Schematic illustration of the One-third scale MMLS3. (Tang et al., 2008)

However, the structural thickness of the pavement is accordingly reduced; the gradation of the pavement materials is not scaled because it is not possible to scale the geogrid. Thus, the experimental results may be limited to the purpose of comparison among different geogrids.

Tang et al. (2016) performed more tests using the same machine. The authors proposed a simplified finite element (FE) analysis to predict the mechanistic pavement response that is needed as input to the mechanistic-empirical (ME) performance model of subgrade permanent deformation. The authors compared the experimental results to the results of the mechanistic empirical model developed and the ME model was calibrated using the results of this reduced scale test. The results showed that the developed model underestimates the permanent developed deformation. Nonetheless, it is worth pointing out that the model was based on a reduced scale physical model where the geogrid and the pavement materials gradation were not scaled.

Kareem et al. (2012) proposed a scaled laboratory test to compare the reinforced and unreinforced subbase over soft subgrade. The platform soil layers were placed in a box of 0.75 m in length, 0.5 m in width and 0.5 m in height. The base of the box is performed with holes in order to facilitate the saturated subgrade drainage. The soft subgrade material was white Kaolin Clay brought from Duitla, west of Baghdad. A Moisture-Density relationship was performed to characterise the subgrade. The kaolin was mixed with water by hands at moisture content equal to 37%. A weight of 375 kg, equivalent to a pressure of 10 kPa is applied and left for 4 days on the surface of the subgrade, so it reaches an undrained shear strength of about 15 kPa. Two base course thicknesses were tested: 100 mm and 125 mm. Two geogrids with two different aperture sizes were compared in this study. The geogrid layer is placed on the surface of the subgrade and folded in 90° against the long side of the steel container, in order to insure the anchorage and slight pre-tensioning. For the loading procedure, a new rubber tire is manufactured with 250 mm diameter and 100 mm in width. A total

load of 1.74 kN was applied which produces a contact pressure of 550 kPa. The load was applied with a speed equal to 3 km/h. The application of the load continues until 75 mm rut development. The comparison between the different tests is used on the comparison of the surface rut development with cycles. As mentioned previously the scaled laboratory tests can be used only for comparison since the geosynthetics cannot be scaled.

Based on the results, the authors showed the effect of the reinforcement on the rut development reduction. Moreover, the results showed that the efficiency of the reinforcement decreases with the increase of the base course thickness.



Figure 1.5-13: Test setup. (Farhan et al., 2012)

#### 1.5.4. Large-scale laboratory cyclic Traffic load tests

As mentioned before the restrictions of a large-scale test are in fact the load application, and the large number of cycles. Over the years, the full-scale Accelerated Pavement Testing (f-sAPT) facilities were used in transportation researches to apply the traffic circulation load on the tested platforms.

To avoid the inconvenient of the full-scale test on site, three f-sAPT facilities were used in literature to test the unpaved roads:

- U.K. Transport Research Laboratory (TRL) pavement test facility,
- U.S Army Corps Engineers (EDRC) waterways experimental station (WES),
- Accelerated Pavement Testing (APT) facility at Kansas State University,
- Accelerated Load Facility (ALF) of the Federal Highway Administration located in Mclean, Virginia.

The TRL is a fixed facility located in a big hangar in Crowthorne, United Kingdom. The facility simulates a linear unidirectional or bidirectional one-axle dual-tire traffic load. The applied load range varies between 46 and 200 kN depending on the tested platform type. The maximum speed range is 20 km/h. The tested platforms were placed in a 10 m width, 25 m long and 3 m depth pit.

Watts et al. (2004) and Cook et al. (2016) used this facility to characterise the effect of the reinforcement on unpaved roads.

Cook et al. (2016) presented the results of 8 tests carried by the TRL f-sAPT facility since 2000 (Figure 1.5-14). The platform tested in each of the 8 tests was divided into sections and panels with different reinforcement types. The subgrade layer was a natural grey silty London Clay. The subgrade strength was controlled by a correlation between the cone index and the CBR. The target subgrade CBR was 2% CBR. A crushed granite was used for the base course layer conforming to the requirements of 800 series of the specification for Highway Works (SHW). The base course thickness is about 300 mm. Prior to trafficking the platform stiffness was controlled by a Falling Weight Deflectometer (FWD) test. The platform was not instrumented; the results are limited to the surface rut development with cycles. The geosynthetics tested in this study are: geogrids made by punching and stretching a polymer sheet, a geogrids made by extrusion and stretching, welded geogrids, woven geogrids, woven geotextiles, geocomposites.

A bi-directional traffic was applied on the panels, using a dual-tire with a speed of 15 km/h and an applied load of 40 kN resulting in a contact pressure of 700 kPa. Based on the results, the authors highlighted the important contribution of the confinement mechanism in the behaviour of the reinforced platform.



*Figure 1.5-14: View of PTF carriage fitted with dual wheel assembly. (Cook et al., 2016)*

Watts et al. (2004) performed tests following the same protocol but with different GSY types (Figure 1.5-15). The testing pit had those dimensions 10 m in width, 25 m in length and 3 m in depth. The subgrade used in this testing is a local grey silty London Clay with a very high plasticity, and a CBR of 2%. A static penetrometer was used to control the clay installation and compaction protocol. A correlation between the cone index (CI) and the subgrade CBR was proposed. The sub-base material consisted of a crushed granite aggregate with a thickness of 320 mm for the first section and 300 mm for the second trial. The pit was divided into 12 different sections with one unreinforced reference section and different types of geosynthetics (woven geotextile, welded bonded grid, woven grid, extruded internal grid, punched and stretched integral grid). The stiffness of the pavement was assessed using a Falling Weight Deflectometer (FWD).

The platform was not instrumented, only the surface rutting was used to compare the results.

Which show that the reinforcement improves the road serviceability.

The authors compared the experimental results to the Giroud and Noiray (1981) design method, and concluded that the calculated base course thickness was overly conservative in some cases.



Figure 1.5-15: TRL pavement testing facility. (Watts et al., 2004)

The U.S. Army Corps of Engineers facility is a mobile machine, that applies a unidirectional or bidirectional linear load using a single or double axle. The load range varies between 10 and 440 kN, and the tire used can be super single tires, single axle or dual axle truck tire, and even an aircraft single tire. The speed range varies between 1 and 12 km/h.

This facility was used to characterise the effect of GSY reinforcement by Jersey et al. (2012), Norwood & Tingle (2014) and Robinson et al. (2017). These research programs were constructed at the Hangar No.4 pavement facility at ERDC 's Vicksburg, MS location. The platforms were placed in a pit of 9 m wide, 15 m long and 1 m deep. The pit was divided into 5 different test sections with different GSY types. The trafficking was applied using a dual-wheel single axle loaded to a nominal load of 40 kN. It is important to note that these applications were not for an unpaved road, they were for a flexible paved road on loose subgrade with a thin layer of asphalt, which reduces the developed rut at the surface. However, the authors highlighted the benefit of a specific manufacturing reinforcement product. It is worth pointing out that all these tests performed using the U.S. Army Corps of Engineers facility were executed on paved roads, which reduces the surface rut development and changes the mechanisms developed.

Jersey et al. (2012), performed large scale test on paved roads with geosynthetics placed at the interface between the subgrade and the base course (Figure 1.5-16). The subgrade used in this test is a local high-plasticity clay with a CBR of 3%. The aggregate base course was made of crushed limestone with a thickness of 200 mm. Dynamic cone penetrometer (DCP) tests were conducted to control the layers properties, and the results were correlated to the CBR. Moreover, falling weight deflectometer tests were performed on each test. The platform was not instrumented, and the results were explored in terms of surface rut development.

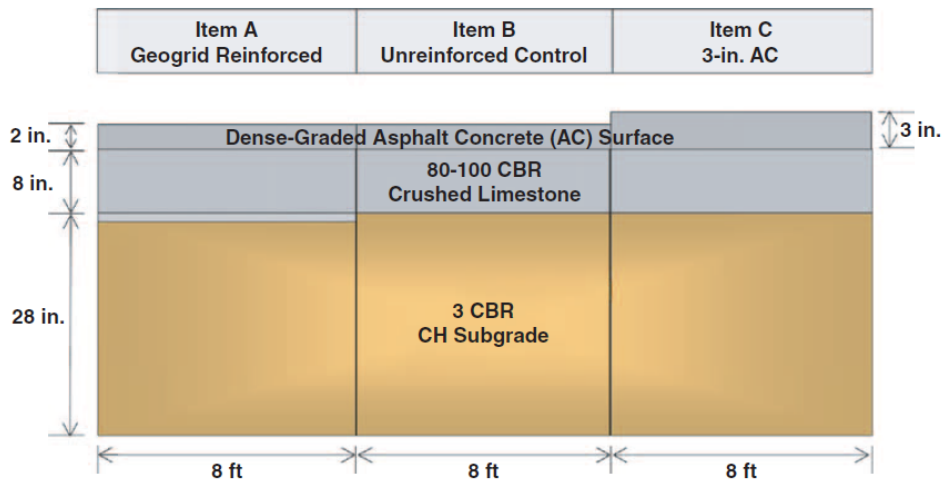


Figure 1.5-16: Profile of test section. (Jersey et al., 2012),

In the Robinson et al. (2017) study 150 mm of a crushed limestone were used as a base course layer (Figure 1.5-17). A locally sourced high-plasticity clay was used to construct the subgrade layer. A subgrade target CBR of 6% was fixed. The geogrids evaluated in this study are multi-axial geogrid products manufactured from a punched and drawn polypropylene sheet.

The platform was instrumented with the following sensors: earth pressure cells, single-depth deflectometers, asphalt strain gauges, moisture sensors, pore pressure and temperature sensors (Figure 1.5-18). A dynamic cone penetrometer was used to control the soil layers properties. Moreover, Falling Weight Deflectometer tests were performed on the surface of both test items after construction and prior to trafficking.



Figure 1.5-17: Dual-wheel tandem axle configuration. (Robinson et al., 2017)

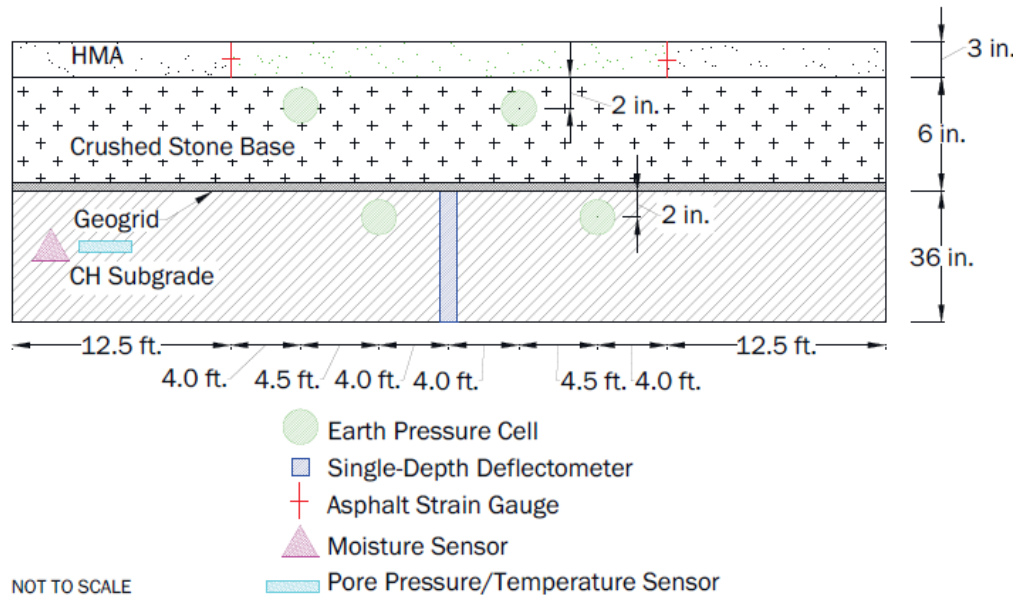


Figure 1.5-18: Profile view of instrumentation layout. (Robinson et al., 2017)

The Accelerated Pavement Testing (APT) facility at Kansas State University is an indoor fixed facility that applies a linear bi-directional traffic load using single or dual axles. The range of the applied load is between 5 and 22 kN for single axle and double in the case of dual axle. The circulation velocity range is between 8 and 11 km/h.

This facility was used by Yang et al. (2012) to evaluate the efficiency of the geocell reinforcement in unpaved roads on soft soil (Figure 1.5-20). The tested platform was placed in a pit of 6.1 m in length, 4.9 m in width and 1.8 m in height. This pit was divided into four sections with different geocell types. The trafficking was applied using a single axle dual wheel, with an applied load of 80 kN resulting in a tire pressure of 552 kPa. The subgrade clay used in this application was classified as A-7-6 Clay according to the AASHTO soil classification. The CBR of the subgrade is about 5%. Dynamic cone penetrometer (DCP) tests were performed as a quality control test. Two base course materials were used in this test: a well-graded aggregate and a poorly graded sand. The sand was placed in the geocell aperture and covered by a well compacted aggregate layer. The instrumentation in this study is limited to strain gauges in the geocell (Figure 1.5-19). The results of this study showed the efficiency of the geocell regarding the reduction of the permanent surface displacement subjected to a load of 40 kN under a dual wheel assembly.

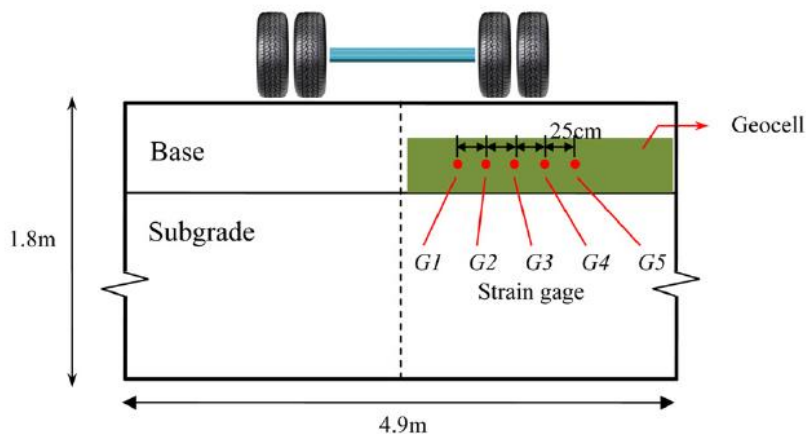


Figure 1.5-19: Tested platform section. (Yang et al., 2012)

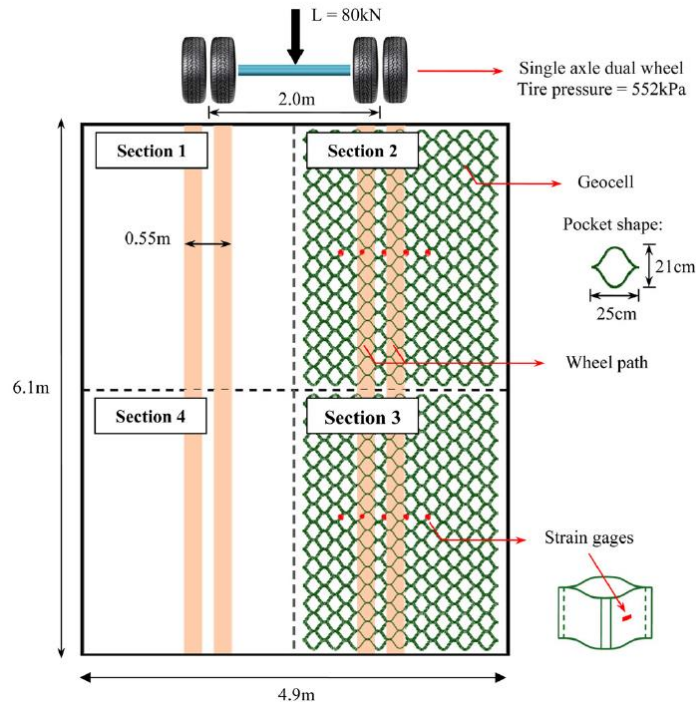


Figure 1.5-20: Tested platform top view. (Yang et al., 2012)

The full-Scale Accelerated Load Facility (ALF) of the Federal Highway Administration located in Mclean, Virginia, is a fixed testing device which applies a linear unidirectional trafficking to the tested section with a velocity of 16.8 km/h.

Tang et al. (2015) used this facility to perform full-scale tests on reinforced sections. Six lane sections were prepared over native soft subgrade soil (Figure 1.5-21 and Figure 1.5-22). These tests were performed in an outdoor environment. The size test pit is 24 m in length and 4 m in width. The subgrade used in this study is classified as heavy clay. The aggregate used in this study is a dense-graded crushed limestone. A triaxial geogrid and a high-strength woven geotextile were used in the reinforced sections. The tested sections were instrumented by:

- Earth pressure cells placed at the subgrade surface in the wheelpath,
- Piezometers placed at the wheel path in the subgrade,
- LVDT (Linear Variable Differential Transformers) placed and connected to the subgrade surface in order to measure the subgrade total deformation,
- Customized potentiometers placed at mid-height of the aggregate layer in order to measure the base course layer deformation,
- Strain gauges placed at the geogrids to measure the geogrid strain.

Quality control tests were performed in order to control and characterize the native in-situ subgrade: nuclear density gauge, Light Weight Deflectometer (LWD), Geogauge, dynamic cone penetrometer (DCP) and vane shear device. The load was applied on a dual wheel assembly with 43.4 kN axle load. The load was applied with a normal speed of 16.8 km/h. The journal paper shows no quality control nor layer property curves or results. The results showed a decrease in the vertical stress at the subgrade surface with cycles. The authors explained this decrease as the result of the base



course increase in stiffness under the applied load. The results of the circulation tests showed the effect of both GSYs in the permanent deformation reduction. The strain gauges showed that the developed strain in the geogrid was around 0.2%. Moreover, the geogrid installed at the upper one-third of the aggregate base course layer showed twice the tensile of the geogrid installed at the base course/subgrade interface.



Figure 1.5-21: ALF with insertion of dual-wheel assembly. (Tang et al., 2015)

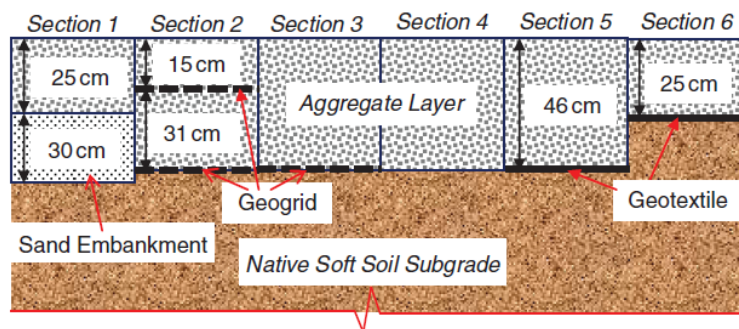


Figure 1.5-22: Testing platforms cross section. (Tang et al., 2015)

Abu-Farsakh, & Chen (2012) used this same facility with the same protocol to compare the effect of the reinforcement on paved platforms. The authors noticed an important permanent displacement for the same platform under cyclic circulation wheel load in comparison with to the plate load test. They assigned these differences to the lack of stress rotation in the cyclic plate load test. However, they noticed that the friction between the tire and pavement during the rolling wheel load results in a tangential force that induces primarily shear stress on the surface. In addition, the authors explained that the particles in the base layer experienced lateral movements, which resulted in the reduction of their bearing capacity of the base layer, and thus caused the shear failure of the base layer.

The authors in this study compared the behaviour of the pavement platform under cyclic and rolling load, and showed the differences in the behaviour that is due to the load application method.

These tests performed in full-scale simulate very closely the real conditions, and the fact that these facilities are indoor facilities allows the control of parameters and avoid the environment variables. Moreover, the fact that the applied load is automatic permits the application of large cycle numbers. Nevertheless, the large pits dimensions involve important platform preparation works. Therefore, in this research work f-sAPT facility fits the most this application, reduces the amount of work regarding the soil preparation and develops its installation.

## 1.6. Unpaved roads tests synthesis:

References	Type of test	Loading type	Platform size (m) Length, Weight, Height	Subgrade	Base course
<a href="#">Akond (2012)</a>	Small-scale laboratory test	Monotonic plate load (ASTM D 1196-93)	1.5 x 0.91 x 0.91	Silty saturated clay soil	Kentucky limestone with 300 mm, 450 mm and 200 mm in thickness
<a href="#">Demir et al. (2013)</a>	Field plate load test	Monotonic plate load test : variable plate diameter (300, 450, 600, 900 mm) ASTM D 1196-93	2.8 x 2.8 x 2	In situ saturated Clay	Variable Base course thicknesses
<a href="#">Abu-Farsakh et al. (2016)</a>	Laboratory plate load test	Monotonic plate load ASTM D 1196-93	1.5 x 0.91 x 0.91	Silty saturated clay with a CBR of 1%	Crushed limestone
<a href="#">Palmeira &amp; Antunes (2010)</a>	Laboratory plate load test	Monotonic and cyclic plate load, Plate diameter: 300 mm Max load: 40 kN Frequency: 1Hz	1.2 x 1.6 x 1.6	Fine tropic soil with a CBR of 8%	200 mm of thickness










Qian et al. (2011)	Laboratory plate load test	Cyclic plate load, Plate diameter: 300 mm Max load: 40 kN Frequency: 0.77Hz	2 x 2.2 x 2	25% kaolinite and 75% of Kansas river sand with CBR 2%	Well graded aggregate with 300 mm
Qian et al. (2013)	Laboratory plate load test	Cyclic plate load, Plate diameter: 300 mm Max load: 40 kN Frequency: 0.77Hz	2 x 2.2 x 2	25% kaolinite and 75% of Kansas river sand with CBR 2%	Variable thickness: 150 mm, 230 mm and 300 mm
Sun et al. (2015)	Laboratory plate load test	Cyclic plate load, Plate diameter: 300 mm Max load: 5 kN to 50 kN Frequency: 0.77Hz	2 x 2.2 x 2	25% kaolinite and 75% of Kansas river sand with CBR 2%	230 mm of base course thickness
Satyal et al. (2018)	Laboratory plate load test	Cyclic plate load, Plate diameter: 300 mm Max load: 10 kN to 60 kN Frequency: 0.77Hz	2 x 2.2 x 2	25% kaolinite and 75% of Kansas river sand with CBR 2%	300 mm of ballast
Kim et al. (2006)	Laboratory plate load test	Cyclic plate load, Plate diameter: 250 mm Max load: 35 kN Frequency: 1Hz	3 x 3 x 3	Polystyrene foam	Two types of base course fill material : 300 mm and 460 mm of thickness
Christopher & Perkins (2008)	Laboratory plate load test	Cyclic plate load, Plate diameter: 300 mm Max load: 40 kN Frequency: 0.65Hz	2 x 2 x 1.5	Saturated silt from Georgia with a CBR of 1%	300 mm of fill material

Sarici et al. (2016)	Laboratory plate load test	Cyclic plate load, Plate diameter: 300 mm Max load: 40 kN Frequency: 0.77Hz	2 x 2 x 2	Soft subgrade with a CBR of 4%	A variable thickness: 300 mm, 400 mm and 450 mm
Gabr (2001)	Laboratory plate load test	Cyclic plate load, Plate diameter: 300 mm Max load: 40 kN Frequency: 0.67Hz	1.5 x 1.5 x 1.35	15% of kaolinite and 85% Lillington sand with a CBR of 3%	Two base course thicknesses: 152 mm and 254 mm
Hufenus et al. (2006)	Full-scale in-situ test	Uncontrolled full and empty truck passes	12 x (8 x 5 x Variable) (12 is the number of sections)	In situ silty clay with a variable CBR	Relatively poorly compactable recycled rubble with variable thicknesses
Cuelho & Perkins (2009)	Full-scale in situ test	A fully loaded three-axle dump truck ( with a tire pressure of 690 kPa)	12 x (15 x 4 x 1)	A saturated subgrade classified as A-2-6 according to the AASHTO with a CBR between 1.5 and 2%	200 mm of crushed gravel grade 6A
Cuelho & Perkins (2017)	Full-scale in situ test	A fully loaded three-axle dump truck ( with a tire pressure of 690 kPa)	17 x (15 x 4.9 x 0.9)	A saturated subgrade classified as A-2-6 according to the AASHTO with a CBR around 2%	277 mm of crushed gravel grade 6A, with two unreinforced section with 414 mm and 632 mm






Mekkawy et al. (2011)	Full-scale in situ test	Opened for vehicle trafficking	4 x (19 x 2.4 x in situ soil)	In-situ soil classified as SC(A-4) with a CBR between 6 and 5%	A crushed limestone classified as GW (A-1-a) with 200 mm of thickness
Tang et al. (2008 & 2016)	1/3 scaled laboratory test	Circulation with reduced wheel and a load of 2.7 kN	4 x (2.06 x 3.64 x 1.2)	Silty sand with 3 and 1.5% of CBR	Crushed stone with an asphalt layer
Farhan et al. (2012)	Reduced scale laboratory test	Circulation with reduced wheel and a load of 1.74 kN and an applied pressure of 550 kPa	( 0.75 x 0.5 x 0.5)	Subgrade is a saturated kaolin clay	Classified as GP according to the USCS with a variable thickness (100 mm and 125 mm)
Cook et al. (2016)	Large scale circulation laboratory test	TRL f-SAPT facility Applied load : 40 kN Velocity: 15 km/h/applied pressure: 700 kPa	Variable numbers and dimensions of the pit sections with 3 m in depth	Silty London Clay CBR 2%	Crushed granite with 300 mm of thickness
Watts et al. (2004)	Large scale circulation laboratory test	TRL f-SAPT facility Applied load : 40 kN Velocity: 15 km/h/applied pressure: 700 kPa	12 x ( 6 x 3 x 3)	Silty London Clay CBR 2%	Crushed granite with 300 mm and 320 mm of thicknesses
Jersey et al. (2012)	Large scale circulation laboratory test	U.S. Army of engineers facility with an applied load of 40 kN	5 x (7 x 2.5 x 1)	Subgrade with high-plasticity with a CBR of 3%	Crushed limestone with 200 mm of thickness with an asphalt layer
Robinson et al. (2017)	Large scale circulation laboratory test	U.S. Army of engineers facility with an applied load of 40 kN	5 x (7 x 2.5 x 1)	Subgrade with high-plasticity with a CBR of 6%	Crushed limestone with 150 mm of thickness with an asphalt layer

Yang et al. (2012)	Large scale circulation laboratory test	Kansas state university accelerated pavement-testing facility. Single axle dual wheel with an applied load of 820 kN and a resulted pressure of 552 kPa	2 x ( 3 x 4.9 x 1.8 )	Subgrade clay classified as A-7-6 clay according to the AASHTO with a CBR of 5%	Two base course material are used: well-graded aggregate and a poorly graded sand
Tang et al. (2015)	Large scale circulation laboratory test	The Federal Highway Administration Accelerated Load Facility (ALF) with an applied load of 43.4 kN with a velocity of 16.8 km/h	6 x ( 4 x 24 x in situ soil)	Subgrade clay classified as A-7-6 in AASHTO	Crushed limestone with variable thicknesses

## Quality Control tests

 1-Nuclear density gauge	 2-Geogauge stiffness device	 3- Dynamic cone penetrometer
 4-Light falling weight / falling weight deflectometer	 5-Pressuremeter test	 6-Static cone penetrometer
 7-Moisture content	 8-Vane shear strength	 9-In-situ unconfined compression tests / In-field CBR test / plate load

## Instrumentation









 1-Surface displacement	 2-Pore pressure measurements	 3-Subgrade strain measurements
 4-Vertical stress measurements	 5-GSY strain measurements	

References	Geosynthetics	Quality control tests	Instrumentation																												
Akond (2012)	Extruded triaxial and biaxial geogrids and geotextile placed at the interface	<table border="1"> <tr><td>1</td><td>2</td><td>3</td><td>4</td><td>5</td><td>6</td><td>7</td><td>8</td><td>9</td></tr> <tr><td></td><td></td><td></td><td></td><td></td><td></td><td></td><td></td><td></td></tr> </table>	1	2	3	4	5	6	7	8	9										<table border="1"> <tr><td>1</td><td>2</td><td>3</td><td>4</td><td>5</td></tr> <tr><td></td><td></td><td></td><td></td><td></td></tr> </table>	1	2	3	4	5					
1	2	3	4	5	6	7	8	9																							
1	2	3	4	5																											
Demir et al. (2013)	Secugrid Q type Geogrid, placed at variable positions	<table border="1"> <tr><td>1</td><td>2</td><td>3</td><td>4</td><td>5</td><td>6</td><td>7</td><td>8</td><td>9</td></tr> <tr><td></td><td></td><td></td><td></td><td></td><td></td><td></td><td></td><td></td></tr> </table>	1	2	3	4	5	6	7	8	9										<table border="1"> <tr><td>1</td><td>2</td><td>3</td><td>4</td><td>5</td></tr> <tr><td></td><td></td><td></td><td></td><td></td></tr> </table>	1	2	3	4	5					
1	2	3	4	5	6	7	8	9																							
1	2	3	4	5																											
Abu-Farsakh et al. (2016)	Extruded biaxial and triaxial geogrids and geotextiles placed at the interface	<table border="1"> <tr><td>1</td><td>2</td><td>3</td><td>4</td><td>5</td><td>6</td><td>7</td><td>8</td><td>9</td></tr> <tr><td></td><td></td><td></td><td></td><td></td><td></td><td></td><td></td><td></td></tr> </table>	1	2	3	4	5	6	7	8	9										<table border="1"> <tr><td>1</td><td>2</td><td>3</td><td>4</td><td>5</td></tr> <tr><td></td><td></td><td></td><td></td><td></td></tr> </table>	1	2	3	4	5					
1	2	3	4	5	6	7	8	9																							
1	2	3	4	5																											
Palmeira & Antunes (2010)	Knitted biaxial geogrid Woven geotextile placed at the interface	<table border="1"> <tr><td>1</td><td>2</td><td>3</td><td>4</td><td>5</td><td>6</td><td>7</td><td>8</td><td>9</td></tr> <tr><td></td><td></td><td></td><td></td><td></td><td></td><td></td><td></td><td></td></tr> </table>	1	2	3	4	5	6	7	8	9										<table border="1"> <tr><td>1</td><td>2</td><td>3</td><td>4</td><td>5</td></tr> <tr><td></td><td></td><td></td><td></td><td></td></tr> </table>	1	2	3	4	5					
1	2	3	4	5	6	7	8	9																							
1	2	3	4	5																											

Qian et al. (2011)	Three different extruded triaxial geogrid placed at the interface		
Qian et al. (2013)	Extruded triaxial geogrid placed at the interface		
Sun et al. (2015)	Two extruded multi-axial geogrids Extruded triaxial geogrid placed at the interface		
Satyal et al. (2008)	Geocell placed at the interface		
Kim et al. (2006)	Extruded triaxial geogrid Two types of geotextile Geocomposite placed at the interface		
Christopher & Perkins, (2008)	Welded biaxial geogrid Geocomposite placed at the interface		
Sarici et al. (2016)	The geogrid position varied between, 0.33D, 0.67D and 1D were D is the plate diameter		
Gabr (2001)	Extruded biaxial geogrids placed at the interface		



Hufenus et al. (2006)	Biaxial extruded PP grid, PVC coated knitted PET grid.... and different geotextile types with variable positions		
Cuelho & Perkins (2009)	Biaxial welded geogrid, biaxial integrally-formed geogrid..... geocomposite, different geotextile types placed at the interface		
Cuelho & Perkins (2017)	Different types of welded, integrally-formed and coated geogrids, a woven and non-woven geotextile placed at the interface		
Mekawy et al. (2011)	Three biaxial geogrids placed at the interface		
Tang et al. (2008 & 2016)	Biaxial geogrids with different types of manufacturing and joints placed at the interface		
Farhan et al. (2012)	Two biaxial geogrids with different apertures size placed at the interface		
Cook et al. (2016)	Geogrids with different manufacturing types, geotextile and geocomposite placed at the interface		
Watts et al. (2004)	Welded geogrid Woven geogrid Extruded geogrid Punched and stretched integral geogrid		

Jersey et al. (2012)	Extruded geogrid placed at the interface		
Robinson et al. (2017)	Multi-axial extruded geogrid placed at the interface		
Yang et al. (2012)	Different geocell types placed at the interface		
Tang et al. (2015)	Triaxial extruded geogrid and high-strength woven geotextile placed at different positions		

## 1.7. Analytical and Empirical design methods

Since 1970, various empirical design methods and analytical methods have been developed in order to determine the base course thickness by considering the GSY effect.

Based on a large testing program proposed by Corps and Engineer, Hammitt & Iii (1970) suggested an empirical design method for an unreinforced unpaved road. This method consists of calculating the aggregate thickness for a rutting criterion of 75 mm.

$$h_{os} = (0.0236 \log N + 0.0161) \sqrt{\frac{P}{CBR} - 17.8A} \quad \text{Eq. 1.7-1}$$

$h_{os}$  = design thickness of the base course (m)

$N$  = passages number;  $P$  = wheel load (kN)

$CBR$  = California bearing Ratio of the subgrade

$A$  = tire contact area (m<sup>2</sup>)

Giroud & Noiray (1981) proposed another empirical formula for an unreinforced unpaved road with other rutting criteria.

$$h_{os} = \frac{(0.190 \log N + 0.445(r - 0.075))}{CBR^{0.63}} \quad \text{Eq. 1.7-2}$$

$h_{os}$  = design thickness of the base course (m)

$r$  = rutting criteria (m)

$N$  = passages number of standard axle load 80 kN

This method is not recommended for  $N$  higher than 10,000 cycles or less than 20 cycles.

Moreover, Giroud & Noiray (1981) proposed a theoretical design method for reinforced unpaved roads based on the large displacement mechanism. This design method was further elaborated by Giroud (1984). The reinforcement was included in the equations as stress distribution improvement and normal stress difference due to the tension membrane effect.

This approach has become the basis of many design methods. It includes a tensioned membrane effect and incorporates, for the reinforced system, a bearing capacity failure in the subgrade that is one of the general shear failure, rather than a local shear failure.

$$q_u = (\pi + 2)C_u + \gamma h = p - p_g \quad \text{Eq. 1.7-3}$$

$q_u$  = ultimate bearing capacity of the subgrade (kPa)

$C_u$  = subgrade undrained cohesion (kPa)

$\gamma$  = base course volumetric weight (kN/m<sup>3</sup>)

$h$  = base course thickness (m)

$p$  = subgrade pressure (kPa)

$p_g$  = reduction of the pressure due to the tension-membrane effect (kPa)

The failure of the unpaved road can occur in the subgrade or in the geotextile. The base course material is assumed to have sufficient friction to ensure mechanical stability of the layer and to prevent sliding over the geotextile.

A pyramidal load distribution is presumed (Figure 1.7-1). For base course thickness of  $h_0$  without geotextile, the base course's layer pressure at the base is calculated as below:

$$p_0 = \frac{2LBp_{ec}}{2(B + 2h_0 \tan \alpha_0)(L + 2h_0 \tan \alpha_0)} + \gamma h_0 \quad \text{Eq. 1.7-4}$$

A base course thickness of  $h$  in the reinforced case yields a stress in the subgrade as below:

$$p = \frac{2LBp_{ec}}{2(B + 2h \tan \alpha)(L + 2h \tan \alpha)} + \gamma h \quad \text{Eq. 1.7-5}$$

$L$  &  $B$  = dimensions of the wheels – base course contact area (m) (Figure 1.7-1)

$p_{ec}$  = applied stress at the base course surface (kPa) (Figure 1.7-1)

$p_0$  &  $p$  = applied load at the subgrade surface (kPa) (Figure 1.7-1)

$\alpha$  &  $\alpha_0$  = distribution stress angle ( $^\circ$ ) (Figure 1.7-1); this values were assumed equal and taken equal  $\pi/4 - \varphi/2$

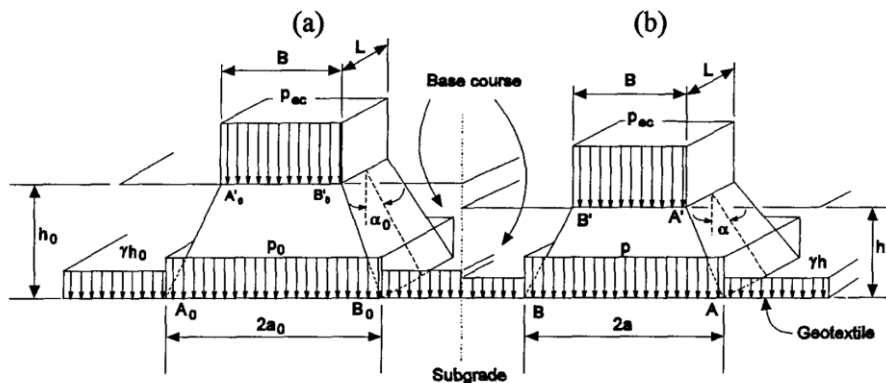


Figure 1.7-1: Load distribution by base course layer: (a) case without geotextile; and (b) case with geotextile. (Giroud & Noiray, 1981).

Strain in the geotextile is calculated, for an assumed parabolic deformed shape (Figure 1.7-2), as it is shown in the following:

$$\varepsilon = \frac{b + b'}{a + a'} - 1 \quad \text{for } a' > a \quad \text{Eq. 1.7-6}$$

$$\varepsilon = \frac{b}{a} - 1 \quad \text{for } a' < a \quad \text{Eq. 1.7-7}$$

Where  $b$  and  $b'$  are respectively the half-length of  $(P)$  and  $(P')$  (Figure 1.7-2), and the widths  $a$  and  $a'$  are obtained from Figure 1.7-1 and Figure 1.7-2.

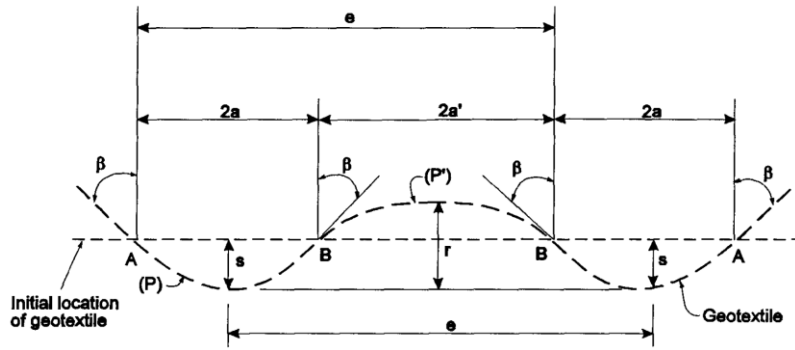


Figure 1.7-2: Assumed parabolic shape of deformed geotextile. (Giroud & Noiray, 1981).

The reduction in pressure due to the tensioned-membrane effect  $p_g$  is considered a uniformly distributed pressure on AB (Figure 1.7-2) and is equal to the vertical component of the tension  $T$  in the geotextile at points A and B:

$$p_g = \frac{E_g \varepsilon}{a \sqrt{1 + \left(\frac{a}{2s}\right)^2}} \quad \text{Eq. 1.7-8}$$

$E_g$  = geotextile elastic modulus

$\varepsilon$  = geotextile strain determined in Eq. 1.7-6 and Eq. 1.7-7

$a$  &  $s$  = geometric parameters determined from Figure 1.7-1 and Figure 1.7-1

The thickness of the base course layer in the reinforced case is then determined from Eq. 1.7-3, Eq. 1.7-5 and Eq. 1.7-8:

$$(\pi + 2)C_u = \frac{P}{2(B + 2h \tan \alpha)(L + 2h \tan \alpha)} - \frac{E_g \varepsilon}{a \sqrt{1 + \left(\frac{a}{2s}\right)^2}} \quad \text{Eq. 1.7-9}$$

Giroud (1984), modified the above design approach for geogrids use, in order to take into account the interlocking of the geogrid and base course material. Progressive deterioration of the subgrade shear strength is explained. The design is performed according to the same procedure described by Giroud & Noiray (1981), while pointing out that the tensioned-membrane effect should be neglected.

Milligan et al. (1989) developed analytical design method based on small displacement mechanism of reinforced unpaved roads. This method allows the calculation of tension developed in GSY established on stress analysis at the base and subgrade shear interface.

Their method does not follow the conventional tensioned-membrane approach, but emphasizes the role of shear stresses at the subgrade surface. When load is applied to the base course layer, it produces vertical and horizontal stresses in the subgrade layer. The base course material outside the loaded area resists some of the horizontal stress, and the remainder develops outward acting shear stresses on the subgrade surface. This acting shear reduces the subgrade bearing capacity significantly. If a GSY is installed at the subgrade surface, the outward acting shear stresses will be taken up by tension in the GSY. The method, that is developed to be used in the design of unpaved roads at small rut depths, does not consider a tensioned-membrane effect. Although, anchorage is

considered to be less important than other procedures. However, the stiffness of the GSY is important if small ruts are expected. The authors recognize the importance of the tensioned-membrane effect, but only at considerable rut depth. The bearing capacity of a strip footing is predicted by using upper and lower bound theorems of plasticity theory.

$$N_{Ca} = 1 + \frac{\pi}{2} + \arccos\left(\frac{\tau_r}{S_u}\right) + \sqrt{1 - \left(\frac{\tau_r}{S_u}\right)^2} \quad \text{Eq. 1.7-10}$$

Where

$$N_{Ca} = \frac{\sigma_{va} - \sigma_{v0}}{S_u} \quad \text{Eq. 1.7-11}$$

$\sigma_{va}$  = the vertical stress distribution on the subgrade surface (kPa)

$\sigma_{v0}$  = the vertical stress distribution on the subgrade surface by the base course layer weight (kPa)

$S_u$  = the subgrade undrained shear strength (kPa)

The vertical stress developed at the subgrade surface depends on the load spread angle  $\beta$ .

Underneath the footing the base course is pushed outwards, developing active pressures. However, passive pressures are developed outside the influence zone of loading. Based on the horizontal equilibrium of the rectangular area (Figure 1.7-3) between the base course surface and the subgrade surface the stress developed in the GSY can be calculated based on the following formula:

$$\tau_r = \frac{1}{2}(K_a - K_p) \left(\frac{1}{B'}\right) \gamma h^2 + \frac{K_a p}{\tan \beta} \left(\frac{B}{B'}\right) \cdot \log\left(\frac{B}{B'}\right) - p \left(\frac{B}{B'}\right) \tan \delta \quad \text{Eq. 1.7-12}$$

$\tau_r$  = the minimum average shear stress required on the subgrade surface for stability is determined by solving the horizontal equilibrium of the rectangular area (kPa)

$B$  = the half footing width (m)

$B'$  = the half loaded width on the subgrade surface (m)

$\gamma$  = base course volumetric weight (kN/m<sup>3</sup>)

$h$  = base course thickness (m)

$p$  = subgrade pressure (kPa)

$\delta$  = the base course friction angle (°)

$K_a$  &  $K_p$  = the earth pressure active and passive coefficient

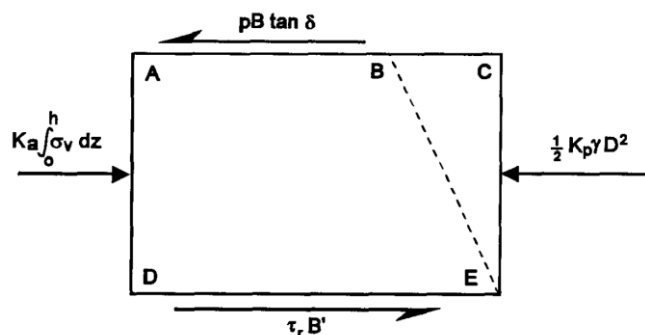


Figure 1.7-3: Soil block in equilibrium analysis. (Milligan et al., 1989).

In order to create a design using this method, it requires half-width of loaded area, base course thickness, load spread angle value, base course friction angle and unit weight, and subgrade undrained shear strength (kN/m<sup>3</sup>) knowledge. The required reinforcement force in the GSY is determined by  $T = \tau_r \times B'$

More recent researches have been carried in this field and more analytical methods were developed (Giroud & Han, 2004; Leng & Gabr, 2006). In fact, Giroud & Han (2004) improved the methods developed earlier to determine the aggregate thickness of unreinforced and GSY-reinforced unpaved roads. This design method was developed for geogrid-reinforced unpaved roads, and takes interlocking between aggregates and geogrids into account, in-plane aperture stability modulus of the geogrid and stress distribution angle degradation with cycles. This design method has been included in the "GSY Design and Construction Guidelines" manual by the FHWA (2008).

Giroud & Han, (2004) proposed the following equation:

$$h = \frac{(0.868 + (0.661 - 1.006 \cdot J_{ASM}^2)) \cdot \left(\frac{r}{h}\right)^{1.5} \cdot \log N}{1 - 0.204 \cdot (R_E - 1)} \cdot \left( \sqrt{\frac{\frac{P}{\pi r^2}}{\left(\frac{s}{fs}\right) \cdot \left(1 - 0.9e^{-\left(\frac{r}{h}\right)^2}\right) \cdot N_c \cdot C_u}} - 1 \right) \cdot r \quad \text{Eq. 1.7-13}$$

$h$  = base course thickness (m)

$J_{ASM}$  = aperture stability modulus of geogrid (mN/°)

$r$  = radius of the equivalent tire contact area (m)

$N$  = passages number;  $P$  = wheel load (kN);  $s$  = allowable rut depth (mm);  $fs$  = factor equal 75 mm.

$N_c$  = bearing capacity factor ( $N_c = 3.14$  (unreinforced unpaved roads),  $N_c = 5.14$  (geotextile-reinforced unpaved road),  $N_c = 5.71$  (geogrid-reinforced unpaved road))

$$C_u = f_c \cdot CBR_{sg} \quad \text{Eq. 1.7-14}$$

$$R_E = \min\left(\frac{E_{bc}}{E_{sg}}, 5\right) = \min\left(\frac{3.48 CBR_{bc}^{0.3}}{CBR_{sg}}, 5\right) \quad \text{Eq. 1.7-15}$$

$C_u$  = subgrade undrained cohesion (kPa)

$CBR_{sg}$  = California bearing ratio of the subgrade soil

$CBR_{bc}$  = California bearing ratio of the base course soil

$f_c$  = factor equal to 30 kPa

$R_E$  = limited modulus ratio

$E_{bc}$  = the base course Young modulus (kPa)

$E_{sg}$  = the subgrade Young modulus (kPa)

Leng & Gabr (2006) provided a further development in the geogrid-reinforcement unpaved roads design. This method is based on Odemark's method, which is an approximate method to transform a two-layer system with different modulus into an equivalent one-layer system. This method takes the stress distribution angle, the base course and the subgrade modulus degradation with cycles into account.

$$h = \frac{(1 + \left(\frac{r}{h}\right)^{0.81} (0.58 - 0.000046 J_t^{4.5})) \cdot \log N}{\tan \alpha_1} \cdot \left( \sqrt{\frac{p_c}{\left(\frac{s}{f_s}\right) \cdot \left(1 - e^{-0.78 \frac{r}{h}}\right) \cdot N_c \cdot C_u}} - 1 \right) \cdot a \quad \text{Eq. 1.7-16}$$

$h$  = base course thickness (m)

$J_t$  = average geogrid tensile strength at 2% of strain (kN/m)

$r$  = radius of the equivalent tire contact area (m)

$N$  = passages number;  $p_c$  = tire contact pressure (kPa)

$s$  = design rutting criterion (mm)

$f_s$  = critical subgrade deformation (mm)

$N_c$  = bearing capacity factor ( $N_c = 3.8$  (unreinforced unpaved roads),  $N_c = 6$  (geogrid-reinforced unpaved road))

$C_u$  = subgrade undrained cohesion (kPa) with the same formula as before

$\alpha_1$  = initial stress distribution angle.

The design methods proposed in literature allow the aggregate thickness determination based on the rutting development, the cycle number, the subgrade and base course stiffness and the GSY reinforcement contribution. As previously seen various theories were proposed and different analytical methods were developed. In fact, depending on the displacement range Giroud & Noiray (1981) and Milligan et al. (1989) have proposed two different theoretical methods with different dominant reinforcement mechanisms. More recently, Giroud & Han (2004) and Leng & Gabr (2006) have proposed two analytical methods that were calibrated based on the results of a laboratory plate load tests performed by Gabr (2001). It is worth pointing out that these tests were performed using a specific GSY manufacturing type, and under the same conditions of base course and subgrade stiffness. Watts et al., (2004) compared the results of the large-scale performed tests with the expected base course thicknesses given by Giroud & Noiray (1981) and concluded that this design method was overly conservative. Cuelho & Perkins (2017) based on the results of the large-scale in situ performed tests calibrated Giroud & Han (2004) method and proposed other analytical formulas to calculate the parameter based on the geosynthetics junction stiffness. Calvarano et al. (2016) has concluded after comparing , Giroud & Han (2004) and Leng & Gabr (2006) analytical methods and the estimated base course thicknesses given by these two, that the method proposed by Leng & Gabr (2006) is more conservative than the method of Giroud & Han (2004). Moreover, the authors noted that these methods were calibrated using one type of geosynthetic.

Therefore, more investigations are needed to clarify the dominant mechanism and to develop an analytical method that will cover more cases that are general. Moreover, in literature authors proposed numerical methods to try to understand the behaviour of the reinforcement in the structure, these developed numerical methods are presented in the next paragraph.



## 1.8. Numerical Approaches

In literature, many authors proposed numerical simulations to estimate the rut development in the reinforced unpaved roads under monotonic or cyclic loadings. Several numerical methods and tools were used. Miura et al (1990) developed a finite element model to simulate the behaviour of geogrid in unpaved roads over soft subgrade. In this model, the geogrid is simulated as a continuous membrane with a shear interface model to simulate the interaction with the soil layer. The authors observed no reinforcement effect in the simulation results regarding the displacement and stress distribution. They concluded that the reinforcement effect is not important because the analysis only takes into consideration the membrane tension effect but not the interlocking.

Burd et al. (1986) developed a finite element formulation of large displacement analysis for one-dimensional elastic membrane in plan strain condition. This formulation was used in reinforcement of fill material in unpaved roads application since it is an application where large displacements are imposed.

Calvarano et al. (2017) proposed a finite element model, using the ABAQUS software, to simulate the behaviour of the geosynthetic in unpaved roads. The soil layers behaviour was modelled using an extended Drucker-Prager model and the geogrid behaviour was model using a linear elastic constitutive model. The geosynthetic was modelled as a membrane. A monotonic load was applied at the surface of the subgrade. Two reinforced and unreinforced models were performed with two different base course thicknesses. The numerical results show the benefits of the reinforcement in improving the bearing capacity.

More recent works were proposed by Hussein et al. (2016) using the ABAQUS software. A 3D finite element model that is capable of simulating the real geometry of the geogrid with the apertures and the interaction between the geogrid ribs and the surrounding soil (Figure 1.8-1). The geogrid-soil interaction method introduced in this work was calibrated based on the plate load laboratory test performed on reinforced crushed limestone and performed by Chen et al., (2009). The Mohr-Coulomb constitutive model was used for the crushed limestone layers. The authors simulated two geogrid reinforcement configurations under footing loading: one layer placed at the interface, and two layers at the reinforcement. The load-settlement results given by the numerical simulations and the experimental tests fits well up to a footing displacement of about 25 mm. Close to the failure state the reinforced model underestimates the footing bearing capacity. Based on the simulations results, the authors concluded that the increase of the geogrid number results in an increase of the ultimate bearing capacity. However, the presented models above simulate monotonic load and are limited to simple constitutive models for the soil layers and the GSY.

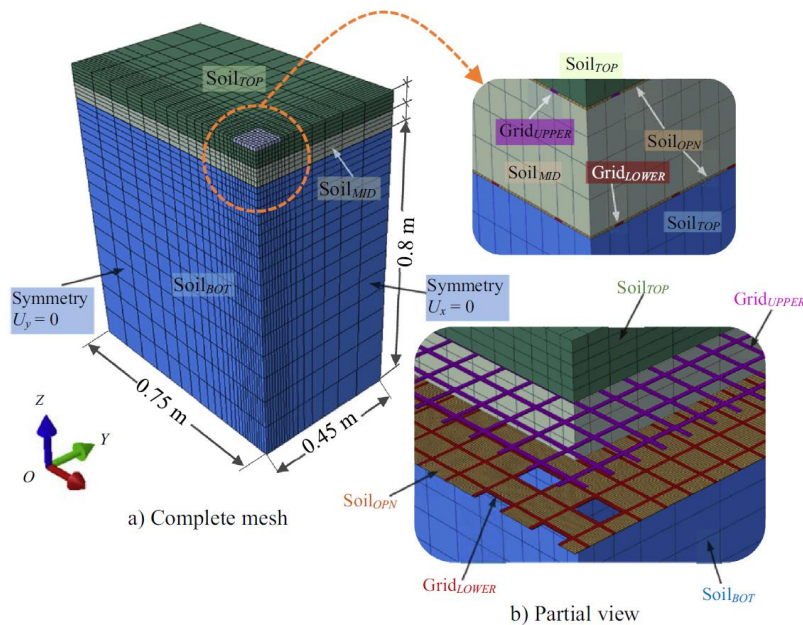


Figure 1.8-1: Complete and partial 3D mesh geometry of the in-soil FE model. (Hussein et al., 2016)

Studies were proposed to develop more advanced constitutive models to simulate the GSYs behaviour. Perkins (2000) described the finite element formulation of a constitutive model that incorporates direction-dependent elastic, plastic and time dependent creep properties. The performance of this model was tested under monotonic and cyclic tension loading, and the results were compared to experimental tension tests. However, the limitation of this model is the fact that this model does not take into account normal stress and temperature dependent. More recently, Liu et al. (2007) proposed an isothermal constitutive model within the framework of elasto-plasticity finite element formulation to simulate the time-dependent monotonic and cyclic behaviour of GSYs. This model was developed to simulate the time-dependent and cyclic behaviour of the GSY. This constitutive model was verified using simple tension test on GSYs. Nevertheless, this model needs to be calibrated with additional GSY types, and it needs to be verified with field full-scale tests. Dong et al. (2010, 2011) investigated the stress–strain responses of uniaxial tension numerical test with different GSYs aperture shapes, using FLAC Software. Beam elements were used in this study to simulate the ribs of an extruded geogrid (Figure 1.8-2). The geogrid ribs were modelled as beams with rigid connection at the nodes, and linearly elastic-perfectly plastic material. The model was validated by comparing the numerical and test results of geogrid with rectangular apertures. Based on the results the authors pointed out that the triangular geogrid aperture has a more uniform stress and strain distributions in the different ribs than the rectangular geogrid apertures.

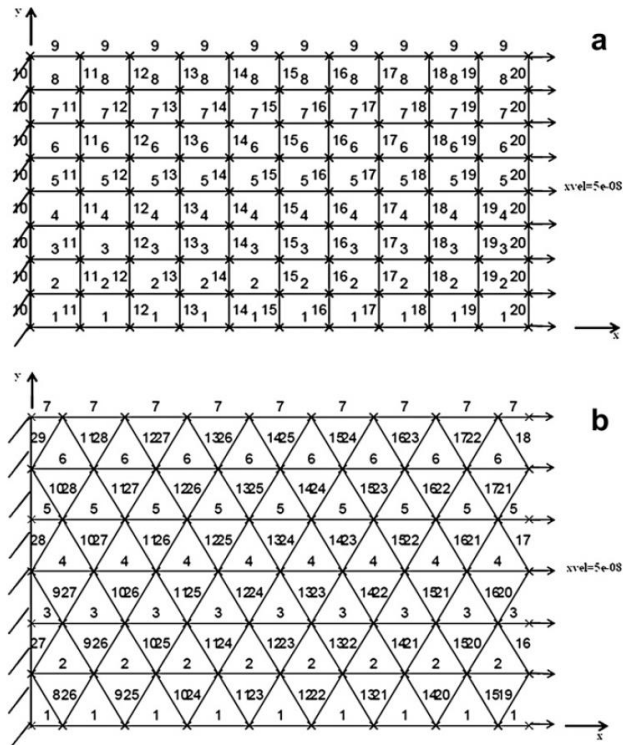


Figure 1.8-2: Meshes with beam elements. (a) Geogrid with rectangular apertures. (b) Geogrid with triangular apertures. (Dong et al., 2011)

As seen in the previous studies the continuum-based finite element or finite difference method reduces the interaction between the aggregate particles and the geogrid apertures to a constitutive law. Moreover, advanced constitutive models should be used to replicate the response of the system and simulate the micro-scale responses.

The discrete element method (DEM) based on the discrete approach is used to better simulate the GSY-particles interaction. In fact, the discrete approach handle the problem at a micro-scale, force-displacement relation is applied to each particle and very few parameters are required to simulate the response of the granular medium. Bhandari & Han (2010) investigated the behaviour of GSY reinforced and unreinforced bases using a 2D discrete element method model (Particle Flow Code (PFC2D) software). The main objective of this study was to characterise the mechanisms involved, and the importance of the depth and stiffness of the GSY under cyclic wheel load. The DEM analysis was based on the experimental work done by Han et al. (2008). In their tests, the authors used a reduced scale test using the Asphalt Pavement Analyser (APA) machine and a box of 0.38 m x 0.45 m x 0.1 m where the soil was placed. In this test, a poorly graded, subrounded river sand with a mean grain size of 2.6 mm was used. Spheres were used to simulate the sand particles, and microscopic particle properties were calibrated based on a biaxial test simulation. The comparison between the numerical and experimental deformation versus cycles showed differences. The authors noted that the reason for this difference might be due to the number and dimensions of particles. The geotextile was modelled using bounded particles, and the microscopic properties were calibrated using a tensile test. The authors highlighted the effect of the GSY in improving the behaviour of the reinforced section. The results of the simulations showed the impact of the GSY position on the mechanism developed on the interface. However, the limitation of this method is the

simulation of the subgrade, which is a cohesive soil and the simulation of a granular material with high friction angle. Moreover, they require significant computation time.

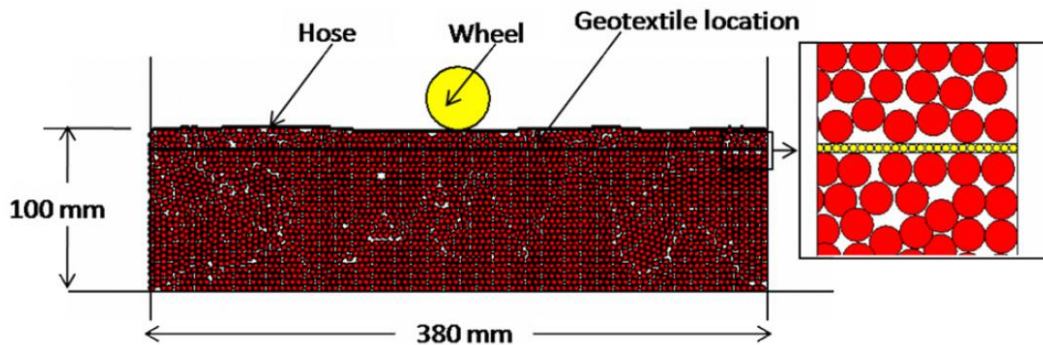
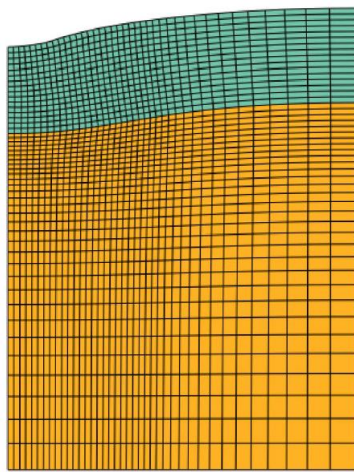


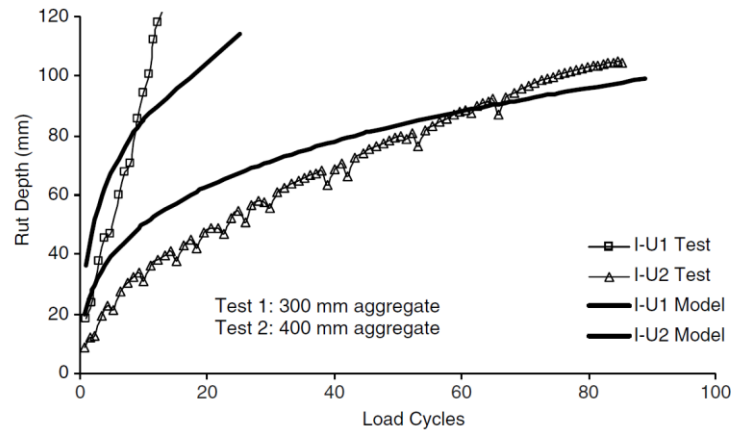
Figure 1.8-3: DEM model of Asphalt Pavement Analyser (APA) machine test simulation. (Bhandari & Han, 2010)

The mechanistic-empirical method has been frequently used to estimate the long-term behaviour of flexible roads under cyclic load. This method consists of an empirical part that takes information from a mechanistic response model and extends this information by taking into consideration the damage to predict the long-term behaviour in terms of rut developed. To simulate the cyclic response of the structure in a purely mechanistic model advanced constitutive models of soil are needed. In mechanistic-empirical method, the empirical part predicts the long-term performance based on calibrated empirical formulas.

Perkins et al. (2012) developed a mechanistic-empirical model for unpaved roads based on a model previously developed for paved roads by Perkins et al. (2009). This method consists of an axisymmetric finite element model, with a nonlinear elastic model for base course and subgrade and an elastic model for the membrane simulating the geogrid with a shear interface model between the membrane and the base course (Figure 1.9-4 (a)). In addition, an empirical damage model for the base course and the subgrade layers is included. Perkins et al. (2012) calibrated, based on the results of an instrumented unpaved road test section, a mechanistic-empirical method that takes into consideration the reinforcement effect. The reference tests used to calibrate the model are large-scale plate load tests. Nine sections were tested: four unreinforced sections with different base course thicknesses varying between 400 and 200 mm, two sections reinforced with geotextile with different base course thicknesses, and three sections reinforced with two different geogrids. Limited details about the performed large-scale tests were given, regarding the installation protocol and, the GSY types. The finite-element model developed in this study is a two dimensional axisymmetric model. An isotropic elastic model was used for the base aggregate layer; a simple linear elastic model was used for the reinforcement behaviour, a contact shear interaction model for the interface between the reinforcement and base aggregate and a linear elastic model was used for the subgrade. Moreover, a damage model for permanent deformation was used for the base and subgrade layer to determine the rut during load cycle. However, the limitation of this method is the prediction of a quick rut development especially for unreinforced cases (Figure 1.8-4 (b)); in fact, the damage models used for rutting were unable to predict a linear rut development with cycles.



(a)



(b)

Figure 1.8-4: (a) Axisymmetric FE model deformed mesh of an unpaved road. (b) Model prediction of rutting curves for unreinforced Test Section I Georgia aggregate and subgrade. (Perkins et al., 2012)

More recently, Tang et al. (2016) used the small-scale test on paved roads using the MMLS3 machine detailed in section 1.5.3 to calibrate a mechanical-empirical design method. The developed finite element model over which the empirical method is based to predict the behaviour with cycles is illustrated in Figure 1.8-5. In this model, an asphalt layer is placed at the surface as in the experimental tests. For simplicity, the FE model is assumed to be elastic and the focus in this model is on the interface geogrid-pavement behaviour. In order to take into account the initial tension in the geogrid due to the construction in the model, an initial decrease in the geogrid temperature that creates a shrinkage in the membrane was applied. In this study, a permanent deformation model for unbound pavement layers was adopted and calibrated based on the experimental results of the APT I, and the results of the model were compared to the experimental results of the APT II (Figure 1.8-5). However, this model was calibrated using a 1/3 reduced scale experimental test. Based on the comparison between the numerical and experimental results, the authors concluded that the ME method underestimates the geogrid-modified subgrade permanent deformation.

As mentioned before the use of continuum-based finite or differential element method reduces the interaction between the geogrid apertures and the aggregates to a simple elastoplastic shear law at the interface. Moreover, large deformation formulation is in need to model the behaviour of the unpaved reinforced road. In addition, complex constitutive models are also in need to simulate the cyclic behaviour of the reinforcement and the soil layers. Therefore, still no reliable continuum-based model and clear calibrated parameters can simulate the reinforcement effect in this application under monotonic and cyclic loads.

Hence, in order to simulate the cyclic behaviour of these structures the ME method is frequently used, but the results of mechanistic model under monotonic load is an input for the empirical method. Therefore, more studies are in need to simulate better the effect of the reinforcement using the continuum-based finite approaches at least under monotonic load.

The discrete element method is more used to simulate the micro-scale interaction between the GSY apertures and the aggregates. In fact, this approach requires less of the complex interaction law and

calibrated parameters than of the continuum-based approaches to simulate the cyclic behaviour. The limitation of this approach is the simulation of a cohesive soft soil and a granular material with a high friction angle.

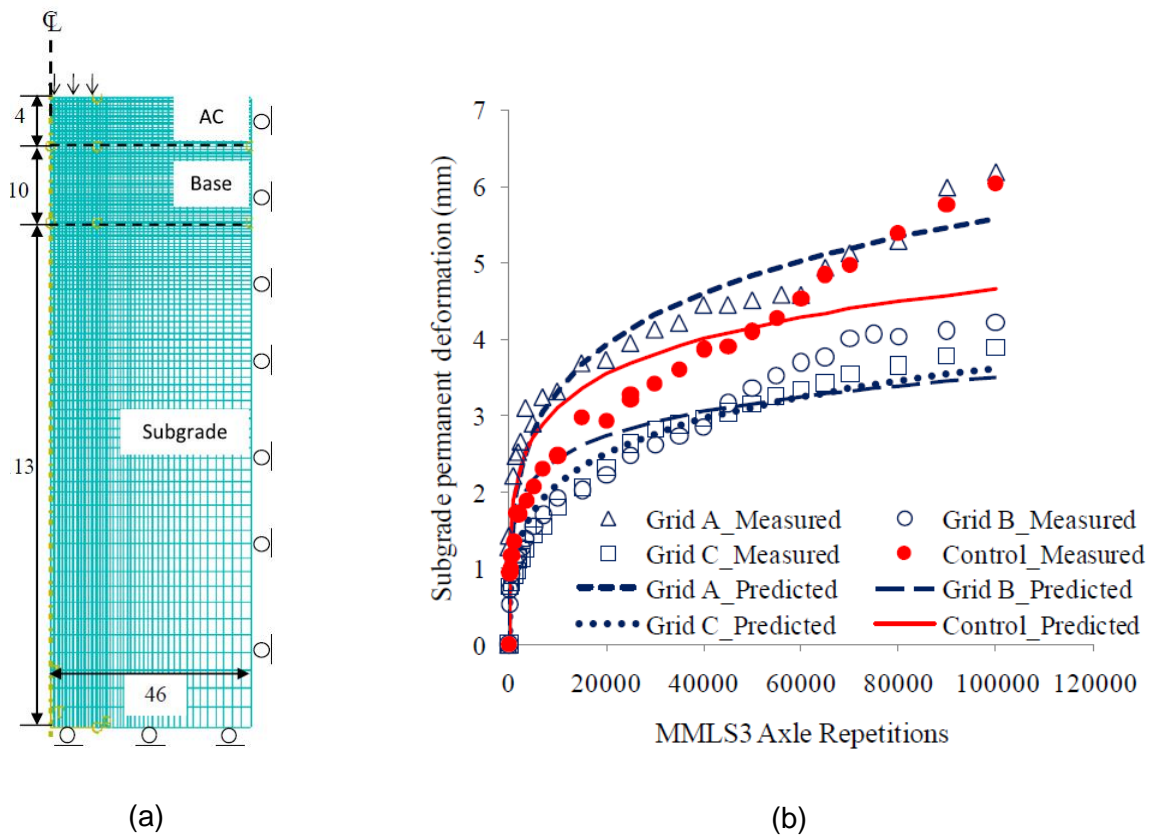


Figure 1.8-5: (a) Geometry of the axisymmetric finite element model for the test section. (b) Measured and modelled subgrade permanent deformation for sections in APT II. (Tang et al., 2016)

## 1.9. GSY installation damage

The GSYs were used during the last decades to provide the filtration, damage, separation, reinforcement and protection functions. Between the large application numbers, we can mention a few cases where the GSYs failed in providing its function, due to the installation mechanical damage. In fact, the GSYs may be subjected to the highest service mechanical stresses during installation.

To avoid that kind of failure cases, the GSYs manufacture focused on this phenomenon.

A wide number of studies covers by literature, carries the GSYs installation damage topic, (Bathurst et al., 2011; Hufenus et al., 2005; Watn et al., 2002; Müller-Rochholz, 1996; Allen & Bathurst, 1994).

The installation damage magnitude depends on different parameters. Watn & Chew (2002) cited these parameters: the GSYs characteristics, the aggregate diameters, the angularity and thickness of the aggregates layer, the construction equipment, and the climatic conditions. The GSY characteristics not only influence the magnitude, but also the mode of installation damage.

Six different installation damage modes were identified:

- Abrasion (Figure 1.9-1): a repetitive sliding of the GSY on an abrasive material causes the abrasion. That kind of damage appears in general when the geotextile is placed on the top of the structure (Channel coating, embankment...).

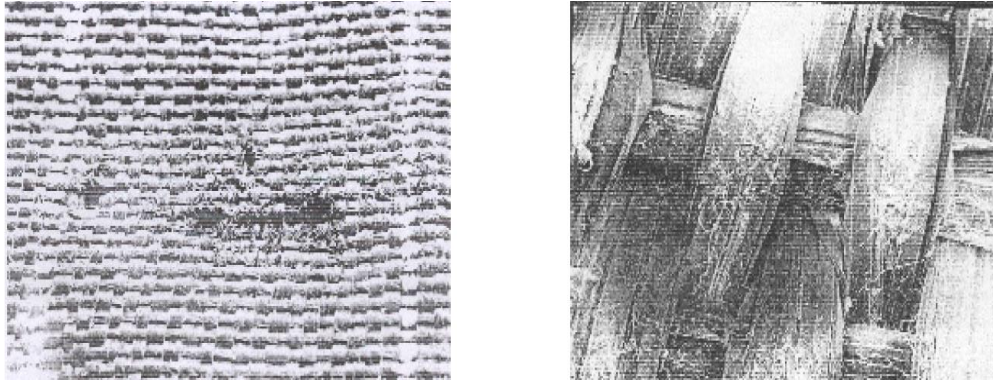


Figure 1.9-1: Example of a woven geotextile abrasion surface. (Brady et al., 1994)

- Notches (Figure 1.9-2): the notches damage mode is observed when a cutting material is in contact with the geotextile, especially if this contact is combined with a vibration equipment.

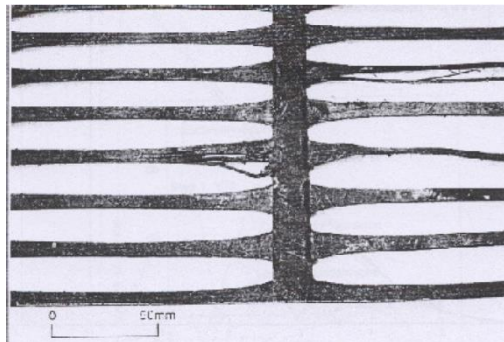


Figure 1.9-2: Example of notches on extruded polyethylene grid. (Brady et al. 1994)

- Punching (Figure 1.9-3): the punching damage mode appears when an angular and cutting material is poured directly on the geotextile, or if an aggressive compaction equipment is used on a thin aggregate layer over the geotextile. In general, the non woven geotextile with a low flexibility is the most sensitive product on that kind of damage.



Figure 1.9-3: Example of geotextile punching. (Brady et al. 1994)

- Failure under stress (Figure 1.9-4): the failure of geotextile under stress occurs generally when the geotextile is subjected to excessive stresses or deformations. That kind of damage is observed frequently when the geotextile is used for separation over soft soil.

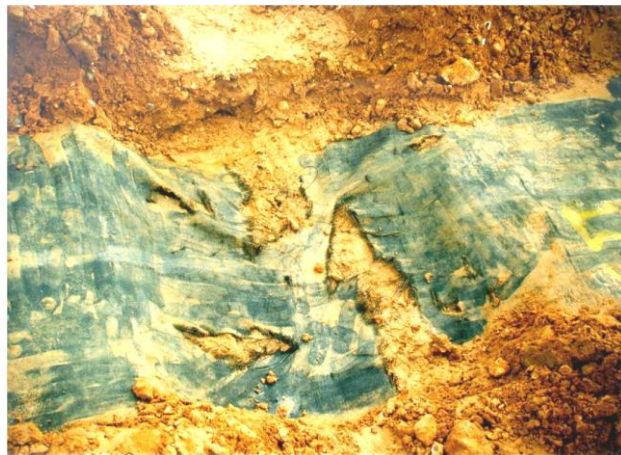


Figure 1.9-4: Deformation failure of geotextile due to traffic load.

The failure of geotextile under stress occurs as well when a bounded load of heavy equipment is applied on a thin aggregate layer over a soil with low bearing capacity.

- Fibres failure (Figure 1.9-5): the geotextile fibres failure occurs when an aggressive material acts as a knife, cutting the geotextile fibres. This mechanism is more likely to occur in the case of a woven geotextile.



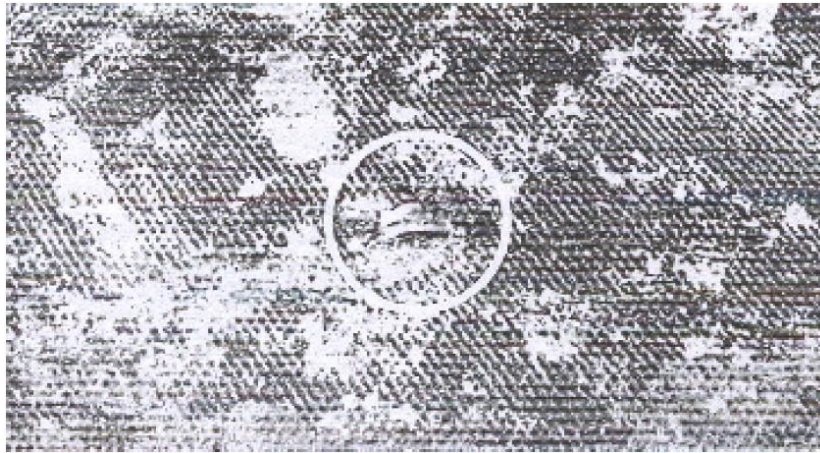


Figure 1.9-5: Fibres failure of a non-woven polyester geogrid. (Brady et al. 1994)

- Tear failure (Figure 1.5-6): The Tear failure occurs when the geotextile is subjected to a propagation of tear forces due to a preliminary damage. In fact, that kind of damage occurs when the geotextile is already damaged by another damage mode as the failure under stress, the fibres failure...



Figure 1.9-6: Geotextile damage by tear failure.

Most of GSY-reinforced soil structure have a long service period, which implies that the reinforcement will last accordingly. The GSY properties generally depend on time. In fact, at the installation phase the GSY is subjected to a damage that reduces its maximum tensile strength. Moreover, during its service period, the GSY is affected by the creep, aging, oxidation and abrasion effects.

The current design approach proposes the reduction of the ultimate tension strength by three reduction factors to calculate the allowable tension strength used for structure design:

$$T_{al} = \frac{T_{ult}}{RF_{CR}RF_{ID}RF_D}, \quad RF_{CR}, RF_{ID}, RF_D \geq 1 \quad \text{Eq. 1.9-1}$$

$RF_{ID}$  The installation damage factor,  $RF_{CR}$  the creep reduction factor and  $RF_D$  the durability reduction factor.

During the last decades, numerous authors studied the GSYs installation damage approach. Koemer & Koemer (1990) presented the results of installation damage on 75 different geotextiles and geogrids from 48 construction sites and found tremendous variation in tensile strength after

installation and excavation. Watts & Brady (1990) proved that the tensile strength and the elongation at failure were subjected to a reduction after installation damage, but the Young's modulus was largely unaffected. Hufenus et al. (2005) proposed a matrix to calculate the maximum expected installation damage. This matrix depends on the type of GSYs, the fill material, the compaction energies and the number of passes.

The NF EN ISO 10722 Standard presents a laboratory test procedure, to determine the installation damage due to a cyclic load. Moreover, most field installation tests are already normalised (EBGEO, GT7 and ISO 13437). However, in literature various studies showed unconformity between the site damage and the estimated damage in the laboratory based on the procedure proposed by the NF EN ISO 10722 standard (Greenwood, 1998; Orsat & Khay, 1998).

In spite of all the efforts put in this field, generalised installation damage factor does not always lead to a well damage prediction. Therefore, more investigations are in need to better estimate the installation damage, especially in the unpaved road application.

## 1.10. Conclusion

Over the years, the GSY reinforcement base course layers over soft subgrade support in unpaved roads application proved a significant improvement in the structure bearing capacity. However, as showed in this background Chapter, the physical quantification of this improvement is not yet fully understood. The fact that the load applied is in the vertical direction and the reinforcement is placed in the horizontal plan creates a confusion in explaining the mechanisms that happen in the structure and the dominance of mechanisms. Three types of mechanisms take place in the reinforced structure: the lateral restraint mechanism, the membrane effect and the separation. For more than thirty years of research in this field, authors proposed empirical and analytical methods to estimate the base course thickness needed to design the structure by taking into consideration the reinforcement effect. In fact, based on a supposed dominant mechanism, different theories were suggested. The more recent developed analytical method gives the privilege to the lateral restraint mechanism. This method was adopted by the "GSY Design and Construction Guidelines" manual by the FHWA (2008). However, this method was calibrated for one geogrid manufacturing type. The lack of knowledge and the various factors and parameters that affect the response of the structure result in the fact that there are no clear and general design method for this structure. This highlights clearly the need of further investigations in this field.

Moreover, experimental investigations were performed to help understand the structural behaviour under cyclic vertical load. Different types of tests were performed: large-scale laboratory cyclic plate load tests, in situ tests, large-scale laboratory circulation load tests and reduced scale circulation laboratory tests. The large-scale cyclic plate load tests are one of the most used tests that characterise the behaviour of roads under traffic load in general, and since it is a laboratory test, the parameters can be controlled. However, it is clearly known that in situ tests simulate better the real applied load, but it is difficult to control the influencing parameters especially for the shallow depths of the soft subgrade. In addition, the number of axle passes causes problems for in-situ tests while such structure is normally designed to support more than 10,000 cycles.

Accelerated pavement tests facility were used in Large scale laboratory tests to simulate traffic load. These facilities are normally designed to simulate traffic on paved roads and specially to explore the behaviour of the asphalt superficial layer. Therefore, large facilities with long circulation length exist in the Transportation Research Departments, usually as large containers, these facilities are used to characterise the effects of the reinforcement in unpaved roads on soft subgrade. Hence, this kind of test requests important preparation and installation works especially for the soft subgrade soil layer regarding the pits large dimensions. More importantly, all these tests proposed in literature, investigated the effect of specific manufacturing GSY types.

The aim of our work is to provide more knowledge regarding the mechanisms that take place within the reinforced structure, the influencing parameters, the overall structure behaviour and response. Therefore, an experimental protocol has been developed to test the unpaved roads under two loading types: the plate load and the circulation traffic load. In this experimental protocol, a special attention to the soil layer preparations and installations have been considered to insure the repeatability of the tests. Moreover, an Accelerator Simulator of Traffic has been developed for the unpaved road under soft subgrade structure testing. In fact, this facility has been designed to simulate circulation traffic load by taking into consideration the large settlement development at the surface of this flexible structure. In addition, the dimensions of the facility have been optimised in a way to reduce the installation and preparation soil works. More importantly, an advanced soil instrumentation has been considered in order to provide the maximum number and the best quality of measurements.

This developed facility was used in this study to compare the effect of different GSY types and quantify the effect of the reinforcement in improving the structural bearing capacity. Moreover, a comparison between the plate load test and the circulation load test has been performed in this work to identify the effect of the load type. The installation damage of the product under the specific laboratory condition developed in this experimental study has been investigated as well.

Many studies aimed to develop a numerical model to simulate the behaviour of these structures under monotone or cyclic load. However, these developed models showed several limitations. In fact, the use of the continuum – based finite or differential methods require the use of complex constitutive models to simulate the behaviour of the reinforcement and the soil layers especially under cyclic load. Moreover, these methods limit the geogrid and base course material interface to a perfect shear elastic plastic constitutive model. In addition, the discrete-based method simulates a more realistic interaction between the geogrid aperture and the base course aggregates, but the limitation of this method is the simulation of a cohesive soft subgrade, aggregates with high friction angle and the simulation of the complex behaviour of the GSY.

In our present work, a continuum-based differential method using FLAC 3D® software has been developed to simulate the behaviour of the structure under monotonic and cyclic load. This model has been calibrated based on geotechnical laboratory testing and the numerical results were compared to the experimental results. The main objective of this numerical work is to develop a reliable model as a design tool. So this latest model can be used to predict the base course layer thickness and the tension developed in the reinforcement.

# Chapter 2. Experimentation

---

## 2.1. Introduction

In this Chapter, the developed experimental protocol is explained. In fact a large-scale laboratory experimental protocol has been developed.

Two types of tests were performed:

- A cyclic plate load test using a circular plate performed on the unpaved road platform and placed in a box of 1.8 m large, 1.9 m in length and 1.1 m in height.
- A Traffic load test using a traffic Simulator Accelerator of Traffic (SAT), developed during this project and especially for this application. The tested platform was placed in a box of 1.8 m large, 5 m in length and 1.1 m in height. The same platform was subjected throughout this test using different loading types: a cyclic traffic load and a cyclic plate load using a special plate, in order to have a similar load contact area as in the Traffic load.

The aim of the experimental protocol developed is firstly and more importantly, the comparison of different GSY types reinforcement benefits. In this research work, three geogrids were tested, two knitted coated geogrid with two different stiffness and an extruded geogrid. Other than the GSY type effect, the base course thickness effect has been studied, in fact two base course thickness were tested (350 mm and 220 mm).

In order to have comparable results, a special attention was given to the unpaved structure layer preparations, installations and the quality control tests. Actually, a preparation protocol was established and controlled for each tested platform. Moreover, several tests have been performed to check the installation protocol and its repeatability.

In this Chapter, the experimental devices and configurations are presented. The tested platform constitution and used materials are detailed too. More importantly, in order to have the same platform with the same properties for each test the developed installation protocol and the quality control tests are presented. Furthermore, the platform instrumentation for the two test types are detailed.

## 2.2. Experimental configurations and devices

### 2.2.1. Tests benches

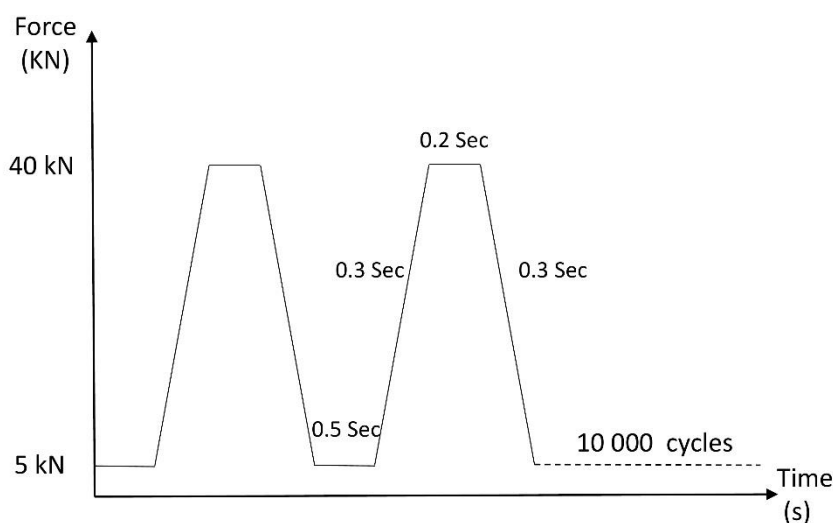
The cyclic plate load tests were performed on an unpaved platform placed in a box of 1.8 m large, 1.9 m in length and 1.1 m in height. The platform was constituted of 350 or 220 mm of base course overcoming 600 mm of soft soil.

The traffic load test was performed on a platform placed in a box of 1.8 m large, 5 m in length and 1.1 m in height. The tested platform had the same constitution of 220 mm of base course overcoming 600 mm of soft subgrade. In this test, the Traffic circulation load was performed on a 3 m length and a plate load test was performed on the remaining 2 m in order to compare the solicitation type effect. The CBR of the soft subgrade should be less than 3%, and so a GSY reinforcement is needed according to the FHWA (2008) standard. The soft soil composition, installation and quality control are presented in the next sections. The CBR required for the granular platform is about 20% (FHWA, 2008). In the plate load test, two granular platform thicknesses were tested, 350 mm and 220 mm. A light non-woven geotextile was placed at the interface between the soft subgrade layer and the base course layer in order to reduce the pollution of the two different layers, especially that the same soils are reused in the different constitutive tests. The geotextile used is very light and is free of any mechanical resistance so it does not affect the behaviour of the structure.

The tested geogrid in most tests is placed at the interface since it is the most common position. However, in order to evaluate the GSY position effect a test was performed with geogrids placed at the base course middle thickness position.

The borders of the box were covered with plastic films to prevent the water content variation. At the bottom of the box 200 mm of well-compacted aggregates were placed and covered with anti-vibration mat to limit the vibration propagation.

## 2.2.2. Cyclic plate load test



(a)

(b)

Figure 2.2-1: (a) Load waves diagram, (b) Hydraulic Jack.

The test consists on applying a cyclic load using a 300 mm diameter rigid plate on the surface of an unpaved road supported by soft subgrade (Figure 2.2-1(b)). The maximum applied load on the surface of the platform was 40 kN equal to the half-axle load (ESAL : Equivalent Single Axle Loads) according to the American standard AASHTO (1993), with an applied pressure of 566 kPa.

The cyclic load was applied at a constant frequency no greater than 1 Hz as specified in the published document of the AASHTO standard (Berg, 2000). The cycle load waves were generated by a hydraulic loading system. The maximum load was held for about 0.2 seconds, the unload phase was maintained for 0.5 seconds, and the loading-unloading phase was done in 0.6 seconds (Figure 2.2-1(a)). Each cycle of pavement load will be considered to be one ESAL pass. The unpaved roads tested with this facility are supposed to support 10,000 ESAL passes, with a maximum rutting of 75 mm regarding the FHWA (2008) standard. Therefore, 10,000 cycles are applied on the tested platform.



Figure 2.2-2: Test setup.

### 2.2.3. Traffic load test

The apparatus Simulator Accelerator of Traffic (SAT) was designed to apply accelerated heavy traffic load on different road structures. The mechanical design of the apparatus is complicated because of the load magnitude and the allowable displacement of 100 – 75 mm in some tested structure cases. Regarding the mechanical concept, two chains carry the tire axle movement, and an electrical motor controls their movement. The motor velocity can be controlled by a velocity controller. The main piece of the machine is the central metallic beam of 3.3 m in length, which carries the two chains. In order to apply unidirectional traffic load, the central beam is raised up when the tire drops in the opposite direction, the beam is put down again and applies the load on the main load direction. This option can be deactivated, when bidirectional traffic is requested. The load is applied on the tire by the apparatus self-weight, and then controlled by two air pneumatic jacks (Figure 2.2-3). The main beam is attached to a deformable parallelogram in order to apply the same force at every tire position, and to insure the application of the same load magnitude on the platform surface even after excessive rut development. The total circulated platform length is 2.5 m, with an effective length of 2 m far from the contact impact zone. Another central beam configuration can increase the circulated platform length to 4.5 m. The overall dimensions of the SAT are 5 m in length, 1.8 m large and 3.2 m in height. The total weight of the apparatus is 8,400 kg. The apparatus reduced dimensions and weight facilitates the mobility of the machine in the laboratory or even on site.

The SAT can apply load on a platform placed in a geotechnical box with a specific altitude, or even apply load with a zero altitude platform, due to its adjustable support.

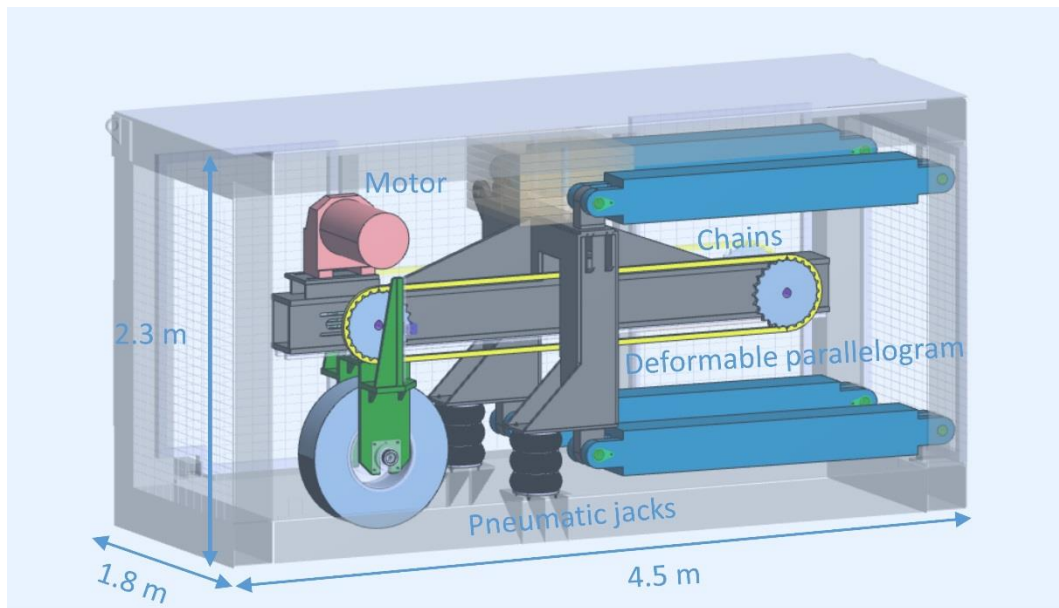


Figure 2.2-3: SAT plan.

The principal parameters of the SAT can be adjusted depending on the application. Table 2.2-1 resumes its main characteristics. Noting that the SAT was firstly designed for the specified application of the unpaved roads, as for the reduced dimension regarding the effective circulated length it aims at reducing the subgrade and base course preparation and installation. Moreover, all concepts that resulted in the control of the load are applied on the unpaved road surfaces even after the excessive rut development.

Table 2.2-1: The SAT facility principal characteristics.

Parameter	Selection
Mobile / fixed	Mobile / can be used for elevated platform
Linear / nonlinear(circular, elliptical)	Linear
Uni / bi-directional	Both
Number of axles	1
Field site/fixed site	Both
Roads/airfields	Roads
Load range	28 kN and more / can increase depending on the application
Tire details	Single filled Tire- L = 210 mm, D=821 mm, W=86 kg Can be modified for dual Tires configuration
Speed range	2-10 km/h / Variable depending on the application
Suspension	Yes, can be stopped in a specific position, with load application
Maximum vertical displacement	100 mm

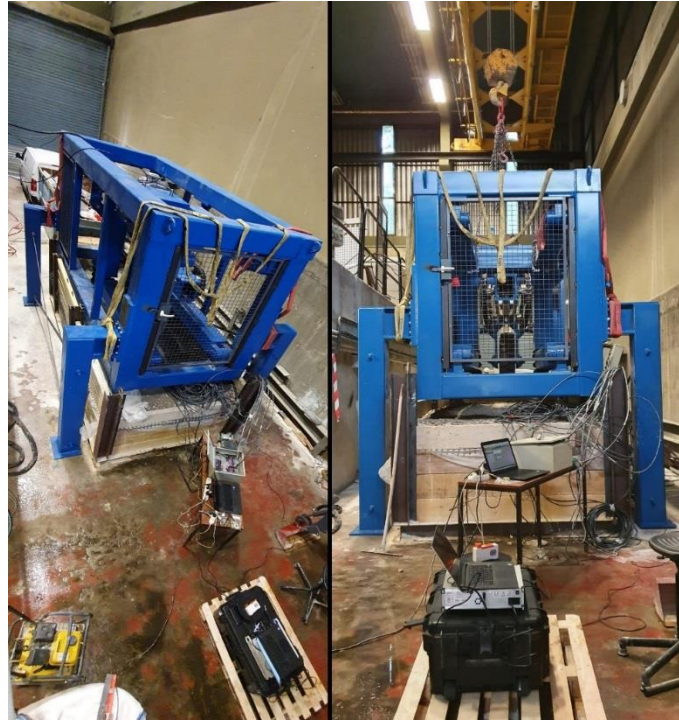


Figure 2.2-4: SAT placed over the tested platform.

The specifications of the load were modified and adapted to this application. In fact, the load magnitude was determined based on the tire contact area in order to have a resulting contact pressure of about 560 kPa. The tire contact area was measured using the simple method of colour application as seen in Figure 2.2-5. The result showed a square central area with a dimension of 180 mm, completed with two arcs at the borders with an area of 0.042994 m<sup>2</sup>. The minimum load that can SAT can applied under its own weight is 28 kN, which results in a contact pressure of 650 kPa > 560 kPa applied above with the plate load test. The Traffic circulation velocity was fixed for 4 km/h. The applied load is bidirectional and the load is being applied until the maximum rut depth is reached.



Figure 2.2-5: Tire contact area.

A plate load test was performed on the 2 m non-circulated part of the platform in order to compare the load application effect. The used plate in this test was not a circular plate but a plate with the same measured tire contact area (Figure 2.2-6). The applied load diagram was the same as the plate load test described above but with a maximum of 28 kN (Figure 2.2-1(a)), to compare the



results of the Traffic circulation and the plate load tests. This platform was instrumented in two areas, the first one is at the middle of the Traffic circulation area and the second one is under the plate load test.

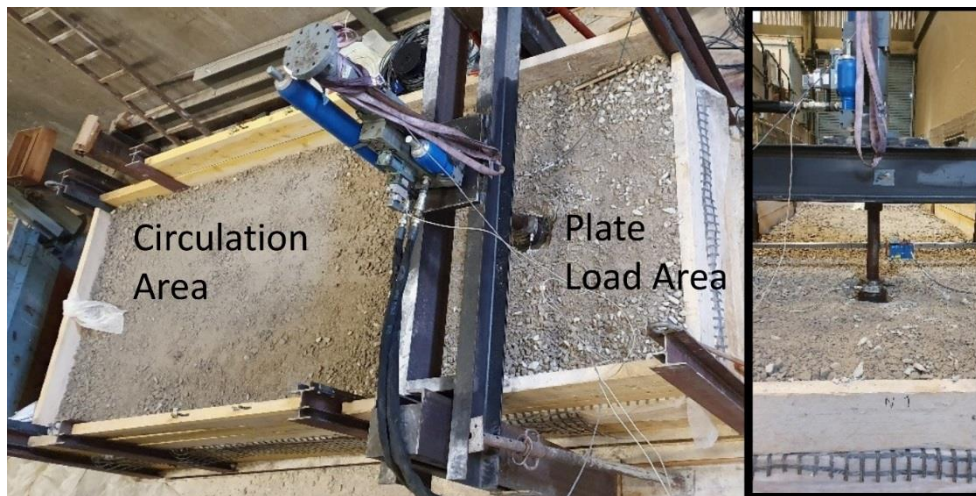


Figure 2.2-6: Illustration of the circulation and plate load platform test.

## 2.3. Materials

The unpaved road platform was set up in the laboratory at a large-scale. In fact, the dimensions of the box where the platform was placed, were optimised in order to reduce the work related to the soil installation and at the same time limit the border's effects, this was proved later in the experimental results. The Figure 2.3-1 illustrates a section of the soil layers constitution and the position of the GSY in the plate load test.

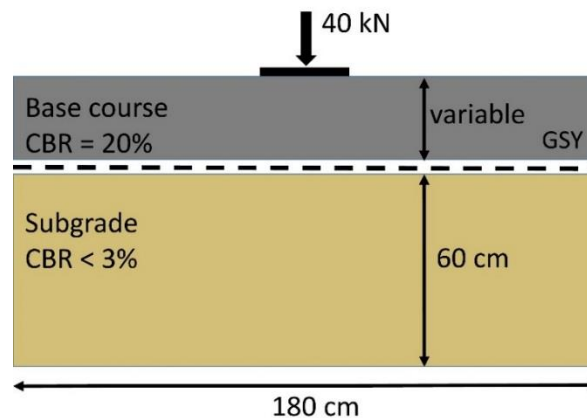


Figure 2.3-1: Platform soil layers constitution.

The tested platform consisted of 600 mm of soft subgrade and a variable base course thickness between 350 and 220 mm in the plate load test. The base course thickness was fixed to 220 mm in the Traffic circulation load tests. An artificial subgrade was used in order to simulate a soft subgrade in the laboratory and to reconstitute for every test the same subgrade properties.

### 2.3.1. Soft subgrade

Regarding the FHWA (2008) standard a base course reinforcement is necessary when the CBR ratio of the subgrade layer is less than 3%, being in mind that the CBR ratio is determined according to the ASTM - D4429 standard.

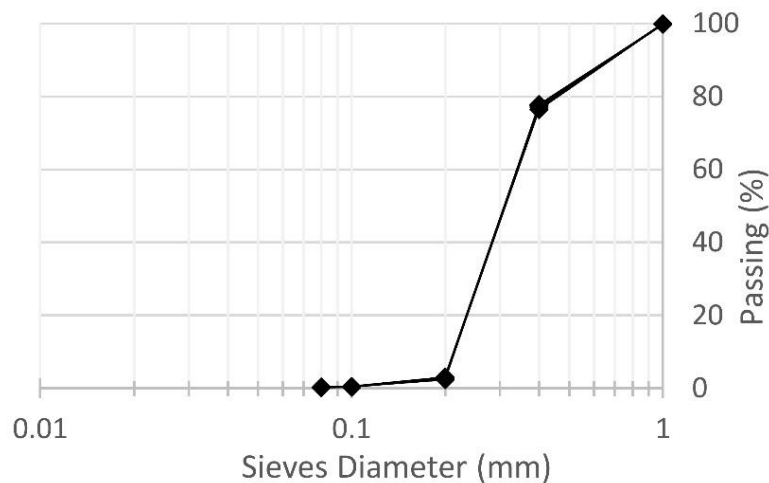
In order to simulate the same subgrade with the same properties for each prepared laboratory test an artificial subgrade was constituted of clay and sand mixture.

#### 2.3.1.a. Subgrade constitution

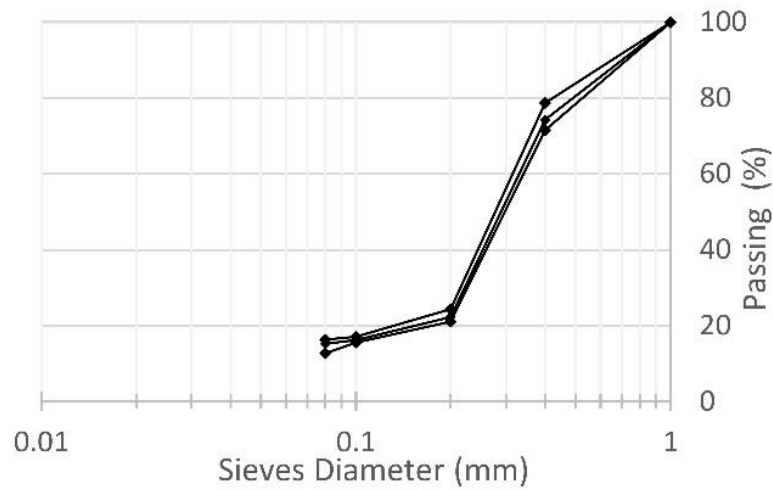
Seven different mixtures were tested to get the mixture constitution that will give a CBR ratio of 2% at the right side of the proctor optimum ( $w > w_{OPN}$ ), within the unsaturated situation.

Two clay types were tested: the calcium bentonite and the kaolinite. The Hostun sand (HN 34) was used in all the mixtures. Three different mixture percentages were tested for the bentonite clay: M2 (25% Clay, 75% Sand), M3 (30% Clay, 70% of sand), M4 (40% Clay, 60% of sand).

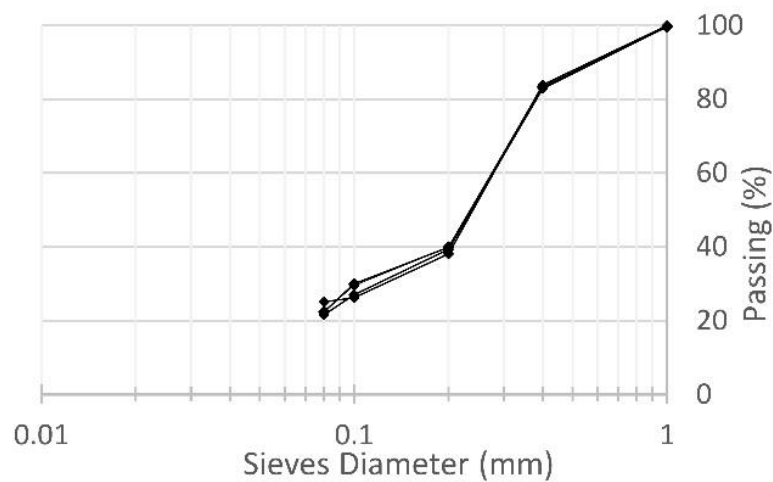
Moreover, for the kaolinite clay four different mixture percentages were tested for the kaolinite clay: M1 (20% Clay, 80% Sand), M2 (25% Clay, 75% Sand), M3 (30% Clay, 70% of sand), M4 (40% Clay, 60% of sand). For every mixture a particle size distribution was drawn to verify that the two materials can be well mixed. In fact, we have the same particle distribution curves for different specimens taken from the same mixture percentage, this shows that the two soil materials can be well mixed (Figure 2.3-2). Furthermore. It is shown that the percentage of fine particles is close to the percentage of clay added. However, because of the chemical reaction between the sand particles and the clay not all the fine clay particles could pass the 0.1 mm diameter sieve. Actually, to distinguish more clearly this portion of particles diameters a wet particle size distribution is needed.



(a)



(b)



(c)

Figure 2.3-2: (a) Particles size distribution of the used Hostun sand, (b) Particles size distribution of the mixture 20% kaolinite Clay and 80% Hostun sand, (c) Particles size distribution of the mixture 40% kaolinite Clay and 60% Hostun sand.

This artificial soil mixture will be used to physically simulate the soft subgrade in the laboratory, under which the reinforced granular platform will be placed. A CBR value less than 3% is needed. On site, the groundwater level is usually under the first superficial meter. Therefore, to simulate in a better way the site conditions an unsaturated soil is needed. Moreover, to avoid the saturation of the soil under the load and the accumulation of deformation an unsaturated soil far from the saturation water with a CBR of 2% is needed.

For each mixture combination, the Proctor and CBR curves were drawn (Figure 2.2-2, Figure 2.2-3). Based on the curves, the water content over which the mixture was compacted to get a CBR of 2% was determined.

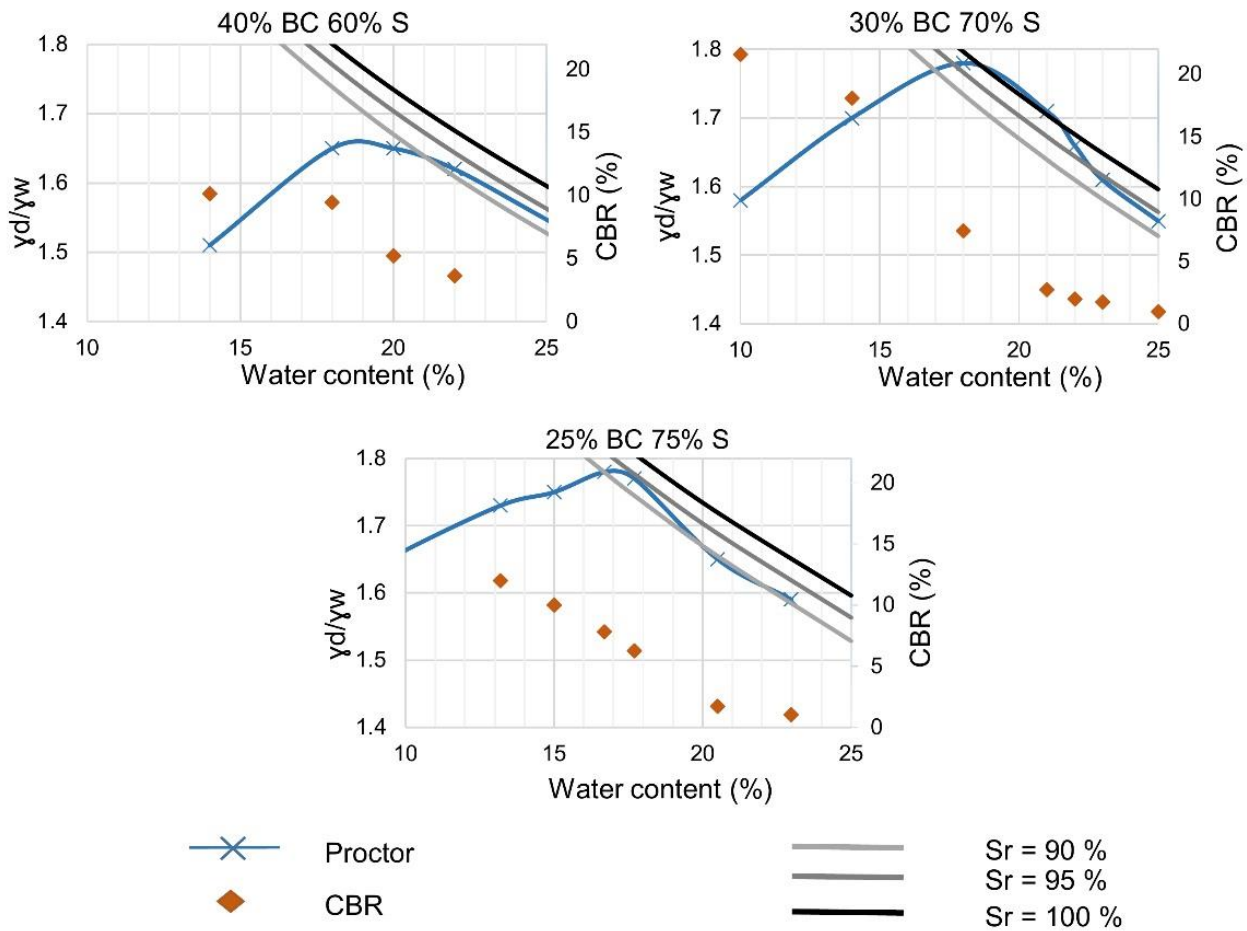


Figure 2.3-3: Calcium bentonite and Hostun sand mixtures proctor and CBR curves.

Figure 2.3-3 illustrates the proctor and CBR curves of the three mixtures of calcium bentonite clay and hostun sand. It shows that the water content value that gives the maximum dry density decreases with the decreasing percentage of the clay in the mixture. The maximum dry density and the maximum CBR reached are made of 30% clay in the mixture.

More importantly, the curves show that in order to reach a CBR of 2% bentonite clay and sand mixtures the percentage of saturation needed is around 95% and 90% which is a high number. In fact, with this percentage of saturation the risk of reaching 100% of saturation during the loading does exist, and this could change the behaviour of the soil. Therefore, the type of clay was changed and the kaolinite clay was used, which has a water reactivity lower than the bentonite clay.

Figure 2.3-4 illustrates the proctor and CBR curves of the four kaolinite and hostun sand mixtures. As for the bentonite mixtures, the clay percentage of 30% presents a very high dry density, and the maximum reached density decreases for the 40% and 25% of clay percentage.

The comparison between the bentonite and kaolinite mixture proctor curves, shows that the optimum proctor for the bentonite is reached at around 18% of water content, as for the kaolinite the optimum proctor is reached at around 11% of water content.

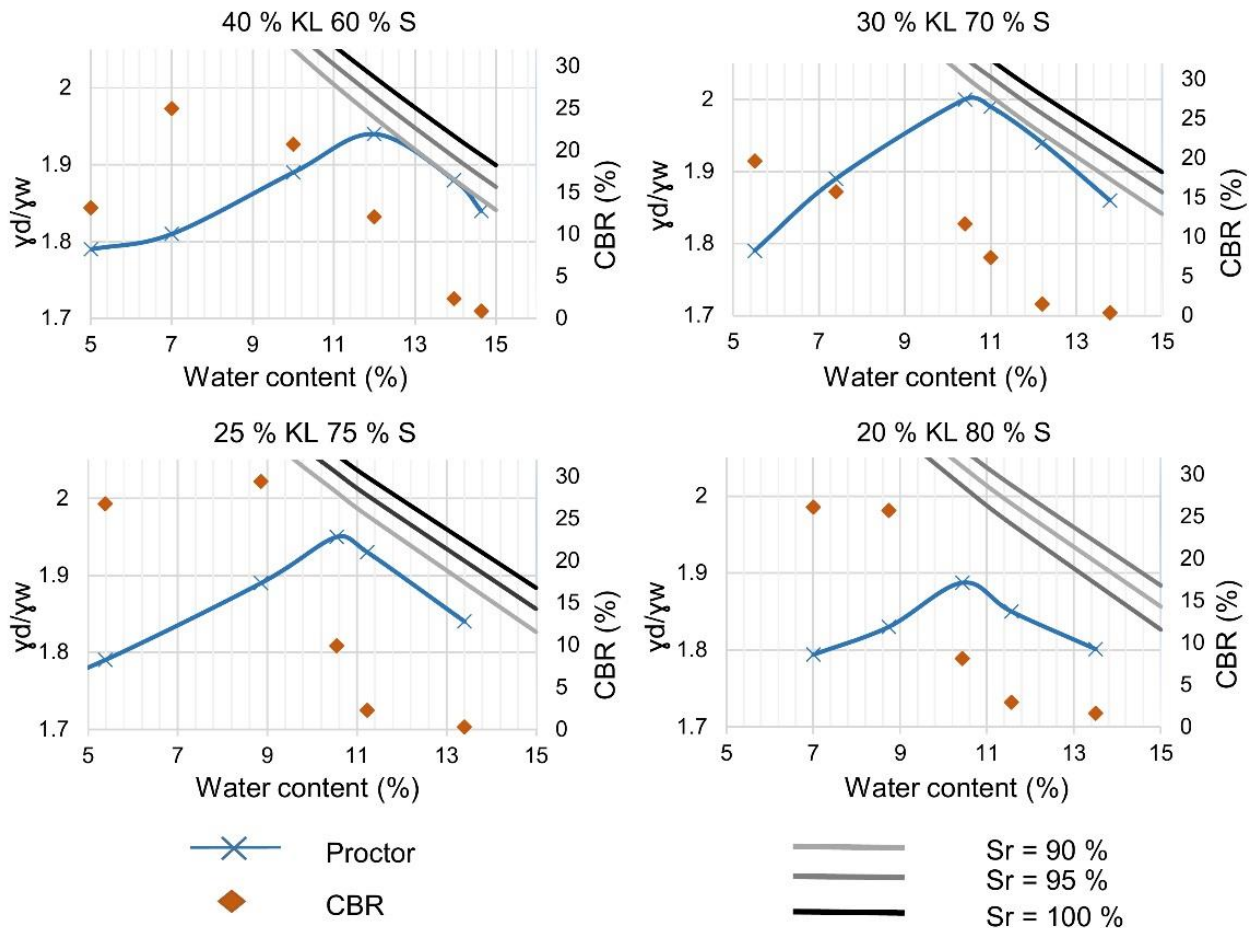


Figure 2.3-4: Kaolinite and Hostun sand mixtures proctor and CBR curves.

Moreover, it is shown that the percentage of saturation at which the mixture CBR is 2% decreases with the clay percentage decrease (Table 2.3-1). Consequently, the mixture M1 (20% clay and 80% sand) with the kaolinite clay was chosen to simulate the subgrade soil, since the degree of saturation of this mixture at the point giving a CBR of 2% is 75%, far enough from the 100% of saturation.

Table 2.3-1 : Mixtures degree of saturation at the water content giving a CBR of 2% under proctor compaction conditions.

Mixture	20% Clay 80% Sand	25% Clay 75% Sand	30% Clay 70% Sand	40% Clay 60% Sand
<b>Kaolinite</b>	$S_r$ (CBR 2%) = 75%	$S_r$ (CBR 2%) = 80%	$S_r$ (CBR 2%) = 90%	$S_r$ (CBR 2%) = 95%
<b>Calcium Bentonite</b>	---	$S_r$ (CBR 2%) = 90%	$S_r$ (CBR 2%) = 95%	$S_r$ (CBR 2%) = 95%

The used mixture of 20% of kaolinite clay and 80% of Hostun sand was compacted at 11.5% of water content to give a CBR ratio of 2% and a dry density of 18.5 kN/m<sup>3</sup>. The challenge was the preparation and compaction procedure in the large laboratory box in order to have a homogenous soil layer with the same CBR value of 2% over the depth and the area. The developed installation procedure will be explained in the next section.

### 2.3.1.b. Subgrade characterization

The triaxial specimens were taken from the installed large-scale subgrade in the laboratory box. A cylindrical corer was used to withdraw the specimens from the prepared subgrade. A specimen has a diameter of 35 mm and a length of 70 mm (Figure 2.3-5). On one hand, an undrained unconsolidated test was performed on an unsaturated specimen. In fact, the soil was under the same conditions as in the large-scale test. On the other hand, three tests with three different confinement stresses were performed (50 kPa, 100 kPa and 200 kPa).



Figure 2.3-5: Triaxial prepared specimens.

These tests give apparent cohesion ( $C_{UU}$ ) and friction angle ( $\phi_{UU}$ ) since they are performed on an unsaturated soil. These cohesions and frictions have no physical meaning, but they were used to calibrate the dry soil parameters applied in the numerical simulations in Chapter 4.

Figure 2.3-6 shows the deviatoric stress versus the axial strain, as for Figure 2.3-7 it shows the volumetric strain versus the axial strain. Figure 2.3-7 was used later in the numerical Chapter to calibrate the soft soil dilatancy properties. With Mohr-Coulomb method in the total stress analysis, we can determine an apparent cohesion of 19 kPa and an apparent friction of  $28^\circ$ .

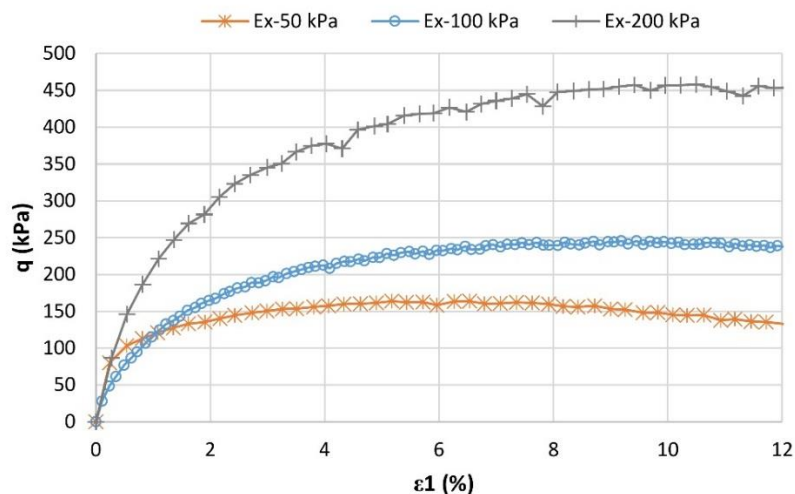


Figure 2.3-6: Deviatoric stress versus the axial strain.

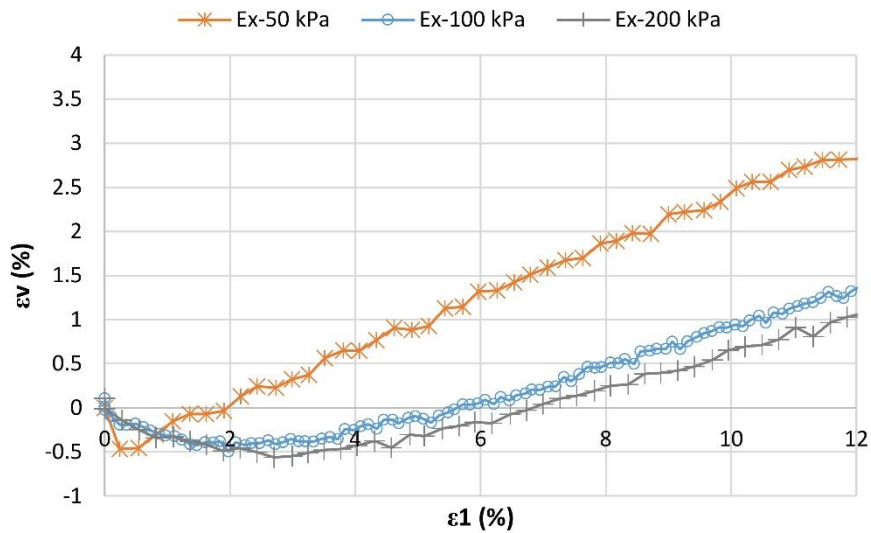


Figure 2.3-7: Volumetric strain versus the axial strain.

Moreover, a cyclic triaxial test was executed under a confining stress of 100 kPa and the cycles were performed between a deviatoric stress of 0 and 150 kPa. Ten cycles were performed while the shearing test continued until the soil plasticity occurred. The results of this test were used to determine the soft soil reloading stiffness modulus in order to calibrate the numerical soft soil that used a constitutive model in Chapter 4.

The curve in Figure 2.3-8 shows a reloading stiffness modulus of about 60 MPa. In addition, it is observed according to the graph that this modulus does not change between the first and the tenth cycle.

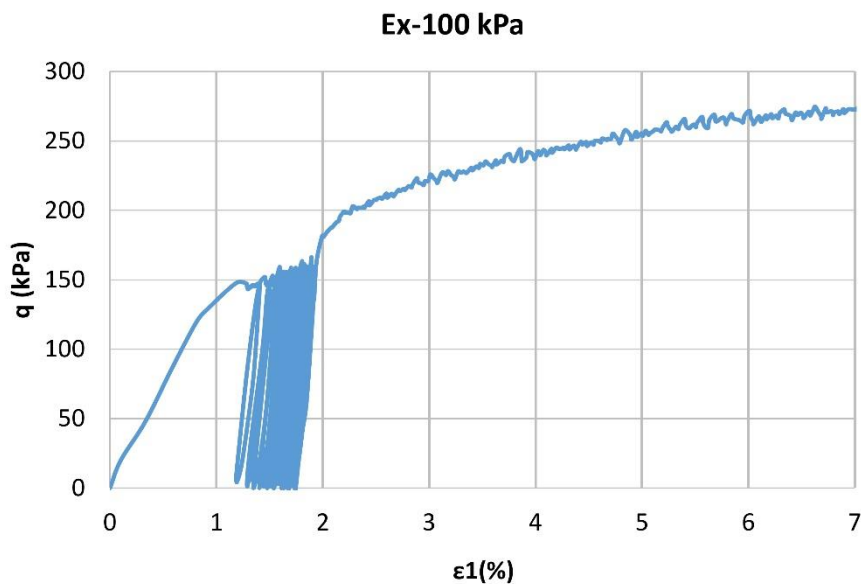


Figure 2.3-8: Deviatoric stress versus the axial strain under cyclic loading.

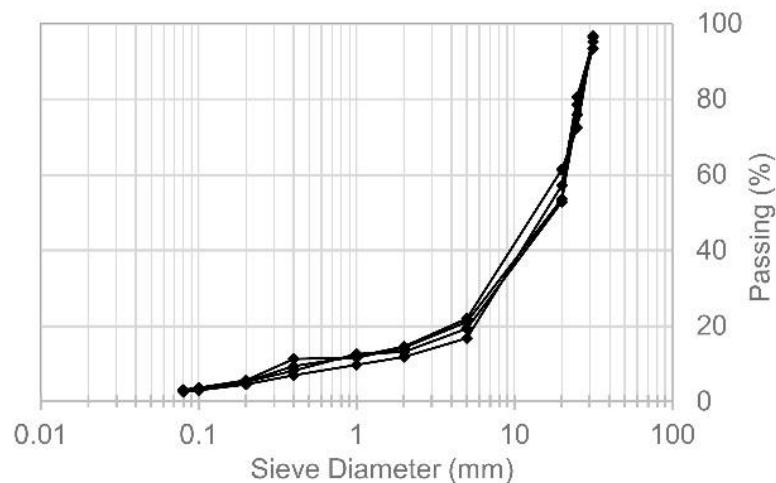
## 2.3.2. Base course

### 2.3.2.a. Base course identification

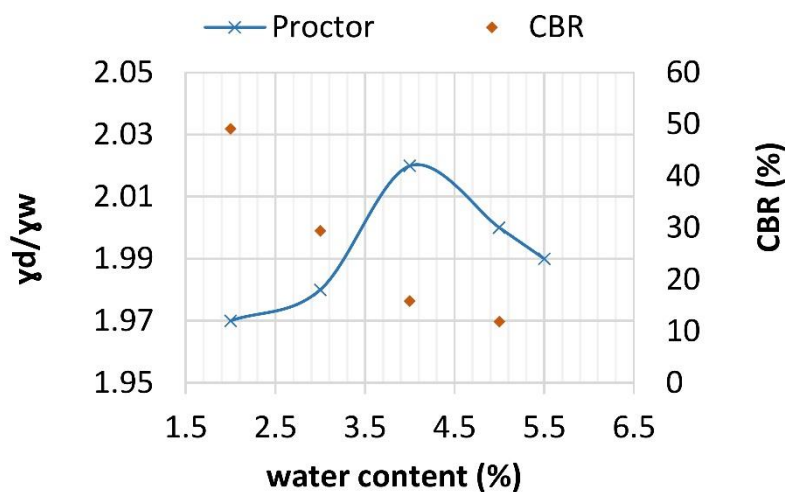
The aggregates used in these tests are non-treated aggregates with particle diameters ranging between 0 and 31.5 mm (GNT 0/31.5), which is the most commonly used material for road constructions in France.

Figure 2.3-9 (a) illustrates the aggregates size distribution. Based on the curve the  $C_u$  and  $C_c$  factors are respectively equal to 20 and 5. This soil is classified as a GP (poorly graded gravel) soil regarding the USCS standard ( $C_u = 11$ ,  $C_c = 4.45$ ) and the LPC standard.

The CBR required for the base course layer is 20% regarding the FHWA (2008) standard. Figure 2.3-9 (b) illustrates the proctor and CBR curves of the aggregates. Since the plate vibrator used to compact this layer is not qualified for the compaction of this material, we will test on a large scale the compaction of the aggregates at 4% of water content and fix the compaction protocol that will give us the 20% CBR.



(a)



(b)

Figure 2.3-9: (a) GNT particles size distribution, (b) The GNT Proctor and CBR curves.



### 2.3.2.b. Base course characterization

A large shear box test was performed, in order to characterize the aggregates and determine its friction angle. The shear box is composed of a large lower box of 450 mm in length, 200 mm in large and 200 mm in depth and of a smaller upper box of 200 mm in length, 200 mm in large and 180 mm in depth (Figure 2.3-10). The geometrical advantage of this box is that the shear plane does not change with the displacement. The shearing was performed under three normal stresses: 66 kPa, 120 kPa and 200 kPa. This same box was used to characterize the aggregates and to characterize the base course and the geogrid interface. For the shearing, the upper box is fixed and the displacement is applied on the lower box with a velocity of 1 mm/min. The aggregates were placed in the box with a water content of 4% and compacted in six layers. The Proctor hammer was used for the compaction, with two drops per position. This compaction protocol was fixed so we have the same soil with the same density around 17 kN/m<sup>3</sup> for each test.

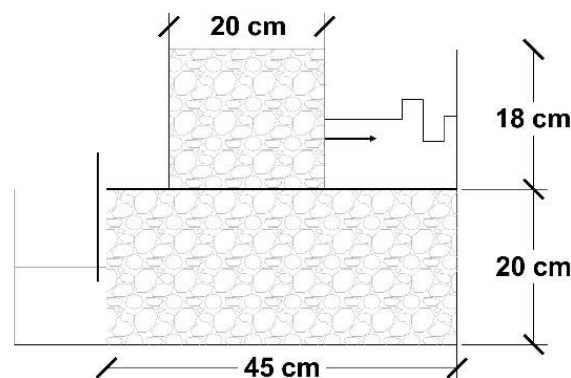
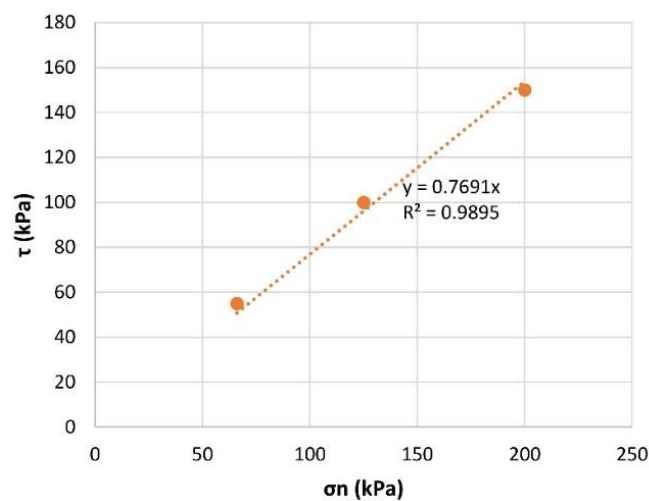


Figure 2.3-10: Configuration of the large shear box for soil test.

Figure 2.3-11 (b) shows the shear stress versus the horizontal displacement. The analysis of these results gives a friction angle of 37° and a cohesion of 0 kPa (Figure 2.3-11(a)). The curves given by this test were used to calibrate the base course parameters in the numerical simulations.



(a)

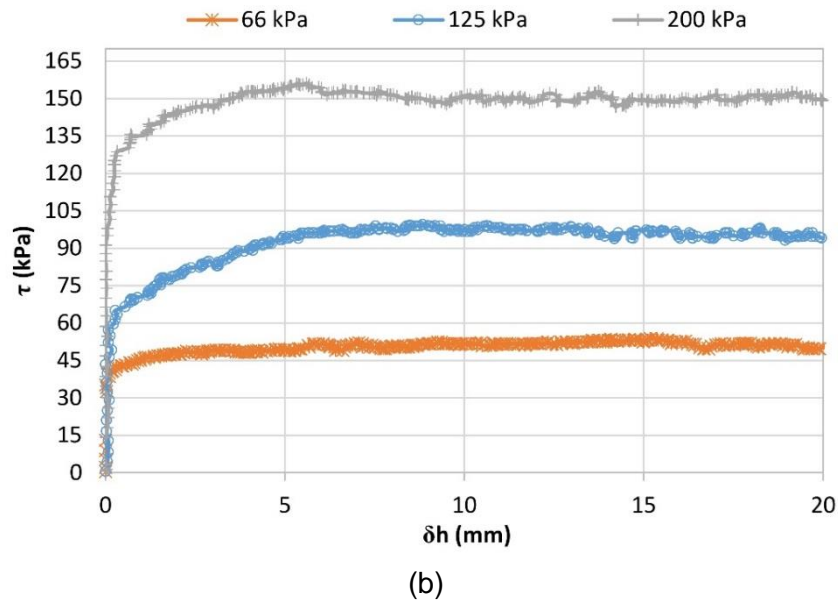


Figure 2.3-11: (a) Maximum shear versus the normal stress of the reinforced and unreinforced interface, (b) Shear stress versus horizontal displacement at different normal stresses.

Moreover, a cyclic load was performed to investigate the aggregates response to the unloading-reloading under 200 kPa of normal stress. Five cycles were performed when 100 kPa of shear stress was reached, and then five more cycles were performed at 135 kPa of shear stress, and an additional five were performed as well when the plasticity was reached at 9.5 mm of displacement.

It can be seen in the Figure 2.3-12 that the reloading stiffness is close to the initial loading stiffness with a high rigidity. However, the comparison between the curves without cycles and the curves with cycles demonstrates that the cycles reduce the maximum shear stress from 150 kPa to 135 kPa. Furthermore, in this Chapter a comparison between sgravel and gravel reinforced with geosynthetic shear plane will be discussed under the same shear box test protocol.

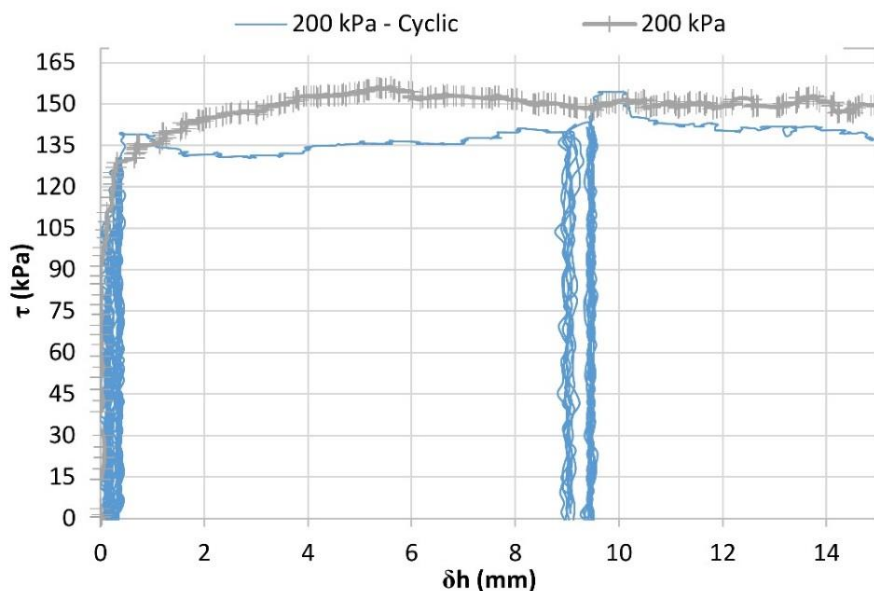


Figure 2.3-12: Shear stress versus horizontal displacement for cyclic solicitation at a normal stress of 200 kPa.

### 2.3.3. GSYs

A layer of a light non-woven geotextile (17 g/m<sup>2</sup>) was placed under the geogrid layer to separate the soil layers, and prevent the base course pollution by the soft soil. Two different GSY manufacturing types were tested: a knitted coated geogrid and an extruded geogrid. Moreover, in order to investigate the effect of the geogrid stiffness two different knitted coated geogrid were tested.

Table 2.3-2 : Geogrid properties.

Name	Type	Stiffness at 2% of strain (kN/m)	Rectangular aperture (mm)	Ultimate tension strength (kN/m)	
				PD*	TD*
GSY 1	Knitted coated - PET* fibres-	1,000	40	100	100
GSY 2	Knitted coated - PVA* fibres-	2,500	40	200	200
Name	Type	Radial stiffness at 2% of strain (kN/m)	Hexagon aperture (mm)	Nodes stability (kg-cm/°)	
GSY 3	Extruded geogrid -PP* fibres-	360	80	6.1	

\*PET: Polyester, \*PP: Polypropylene, \*PVA: Polyvinyl Alcohol

\*PD: Production Direction, \*TD: Transversal Direction

The tested GSY 1 and 2 products have a special manufacturing process (Figure 2.3-16). In fact, the bands are joined with a special knitting technology that keeps it in a straight position. These straight bands initial positions allow the development of tension in the product after a relatively small strain, which is not the case when the initial manufacturing bands state present some curves (Figure 2.3-13). The product apertures have a square shape, with a dimension of 40 mm. The maximum tension strength is equal in both directions. More importantly, the manufacturing technology allows the implementation of fibre optics in the product bands during the production.

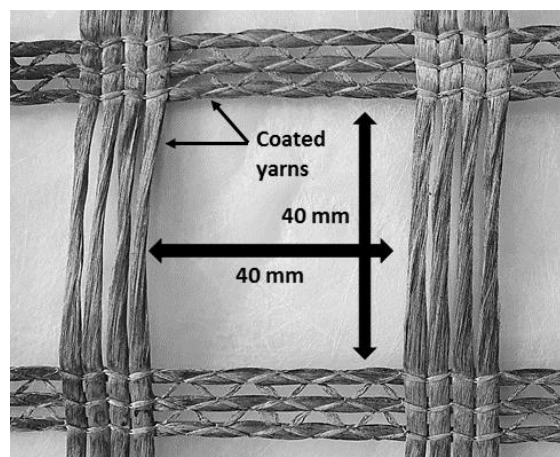


Figure 2.3-13: Geometry of the Geosynthetic GSY 1.

The stiffness of this product changes by changing the yarns material (PET, PVA...) or the number of yarns per band.

However, the nodes' connections and stabilities are not characteristics of this product. In fact, the bands in both directions are connected using connection yarns.

Figure 2.3-14 presents the tensile curves of the GSY 1 and the GSY 2. It shows that the GSY 2 is about twice the stiffness of the GSY 1. A cyclic tension test was performed on the GSY 1 with a load of 20 kN/m. Figure 2.3-15 shows that the GSY 1 presents under tension an imperfect elastic behaviour. In fact, the first loading and unloading cycle shows 0.7% plastic strain and 2.6% elastic strain. This plastic strain can be due to the yarns straightening and the structures' geometry. After a 1,000 cycle, the unloaded strain becomes equal to 3.13% due to the material damage.

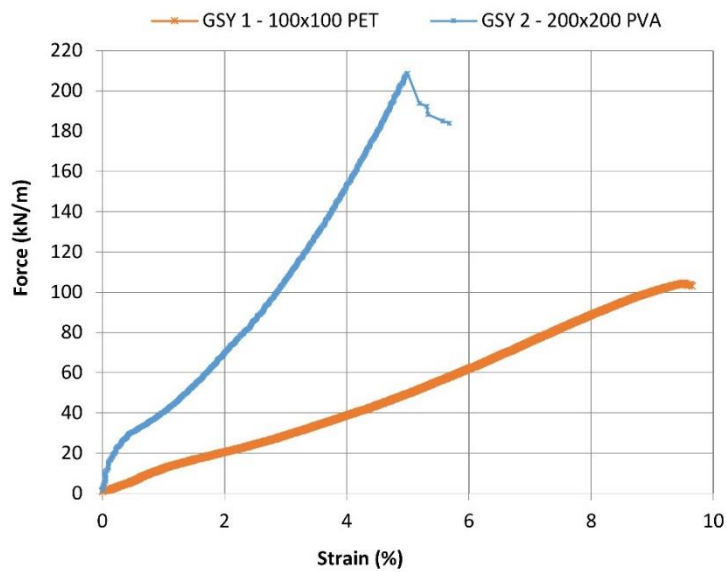


Figure 2.3-14: GSY 1 and GSY 2 tensile curves.

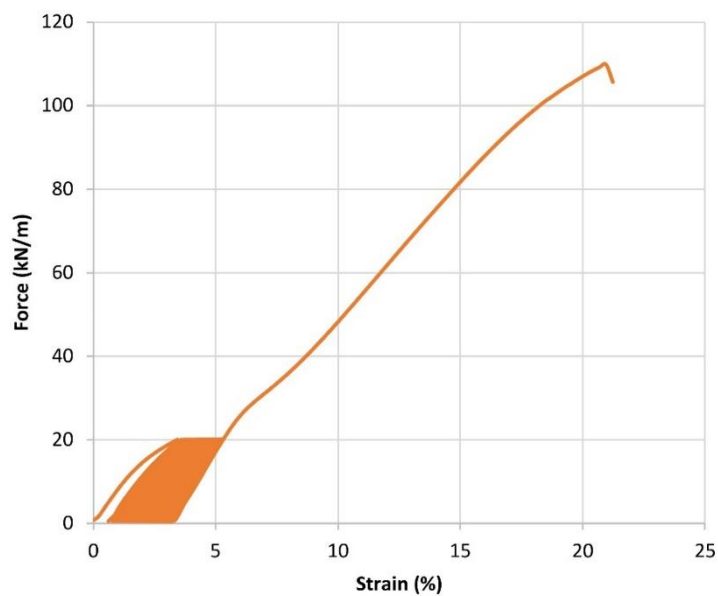


Figure 2.3-15: GSY 1 tensile curve under cyclic load.

The GSY 3 is an extruded polypropylene geogrid, with a hexagonal structure forming a series of triangular apertures (Figure 2.3-17). This geogrid is tested under a radial tensile load and the special

extruded manufacturing of this product gives a stability to the nodes. In fact, integral junctions are formed during the drawing of punched sheets, and the nodes' stabilities are measured and given by the nodes' stabilities. In the analytical method given by Giroud & Han (2004) to design these structures the geosynthetic effect is taken by considering the node's stability. In literature, many studies tested this geogrid type with different radial stiffness and nodes ratio stabilities and showed the efficiency in increasing the platform bearing stability with the confinement mechanism (Gabr, 2001; Qian et al. 2013 & 2011; al. Farhan et al., 2012; Jersey et al., 2012; Tang et al., 2015).



Figure 2.3-16: Installation of the GSY 1 and aggregates.



Figure 2.3-17: Installation of the GSY 3 and aggregates.

#### 2.3.4. Geosynthetic / Base course interface characterization

The same large shear box presented in section 2.3.2.b, and used to characterize the aggregates, was used to characterize the aggregate and geosynthetic interface. At the interface between the upper box and the lower box, the geosynthetic GSY 1 was placed and fixed at the front edge of the box (Figure 2.3-18).

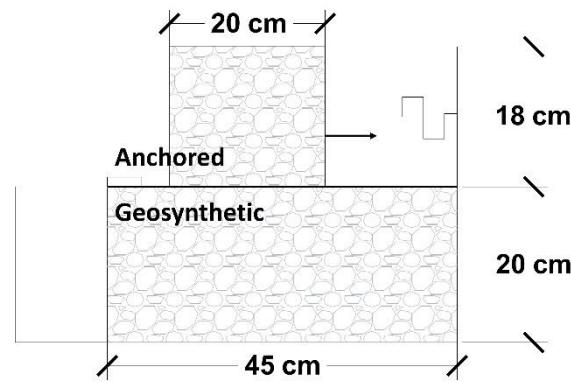


Figure 2.3-18: Configuration of the large shear box for GSY tests.

The aggregates were placed in the box using the same protocol as the tests without reinforcement in order to have the same density of material. Three different tests with three different normal stresses were performed (66 kPa, 125 kPa and 200 kPa). The shear stress versus the horizontal displacement for the reinforced and unreinforced tests are plotted in Figure 2.3-19.

The GSY 1 geogrid does not affect the curve shape and the elastic part. In fact, this part is mostly dominated by the aggregates-aggregates interface behaviour which is interlocked in the geogrid apertures. However, the geogrid at the interface increased the maximum shear strength of the interface. In fact, the maximum shear strength at 66 kPa of normal stress increases from 55 kPa to 75 kPa with the geogrid. Figure 2.3-20 shows the intrinsic curves of the reinforced and unreinforced interface. The unreinforced interface demonstrates no cohesion on the contrary to the reinforced interface that demonstrates an apparent cohesion of 15 kPa. Moreover, the reinforcements increase the friction's interface from 37° to 39°.

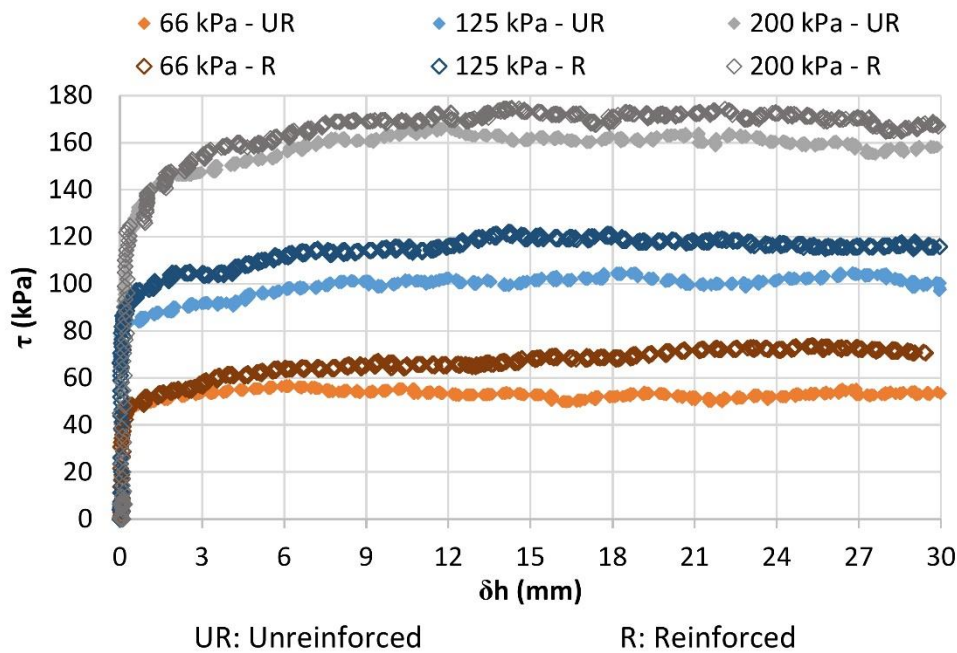


Figure 2.3-19: Shear stress versus horizontal displacement at different normal stresses for the reinforced and unreinforced interface.

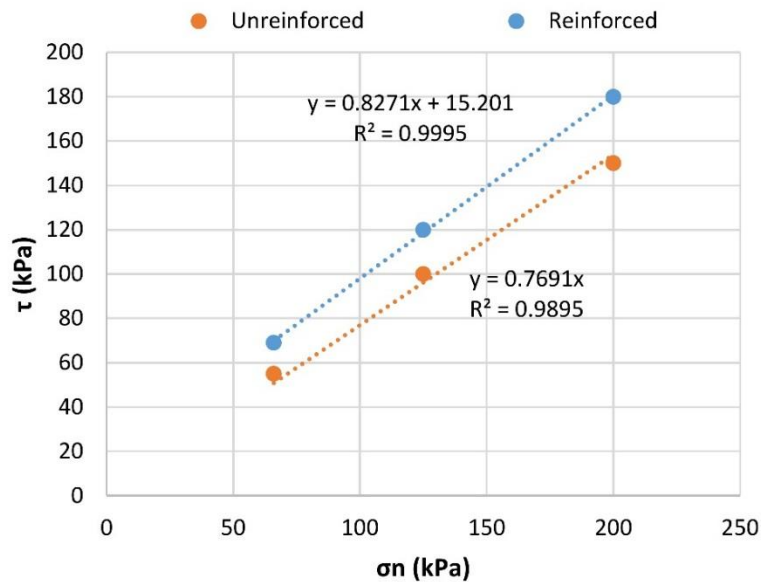


Figure 2.3-20: Maximum shear stress versus the normal stress of the reinforced and unreinforced interface.

Furthermore, a cyclic test was performed on the interface under 200 kPa of normal stress. Five cycles were performed when 135 kPa of deviatoric stress was reached, and 15 additional cycles were performed in the plastic state at 9 mm of displacement. Figure 2.3-21 shows that the reloading stiffness is close to the initial loading stiffness and it shows a high rigidity. It is seen in the graph that the cycles reduce the maximum shear strength from 170 to 160 kPa. However, compared to the unreinforced cyclic load test, the reinforcement reduces the damage of the interface due to the cycles.

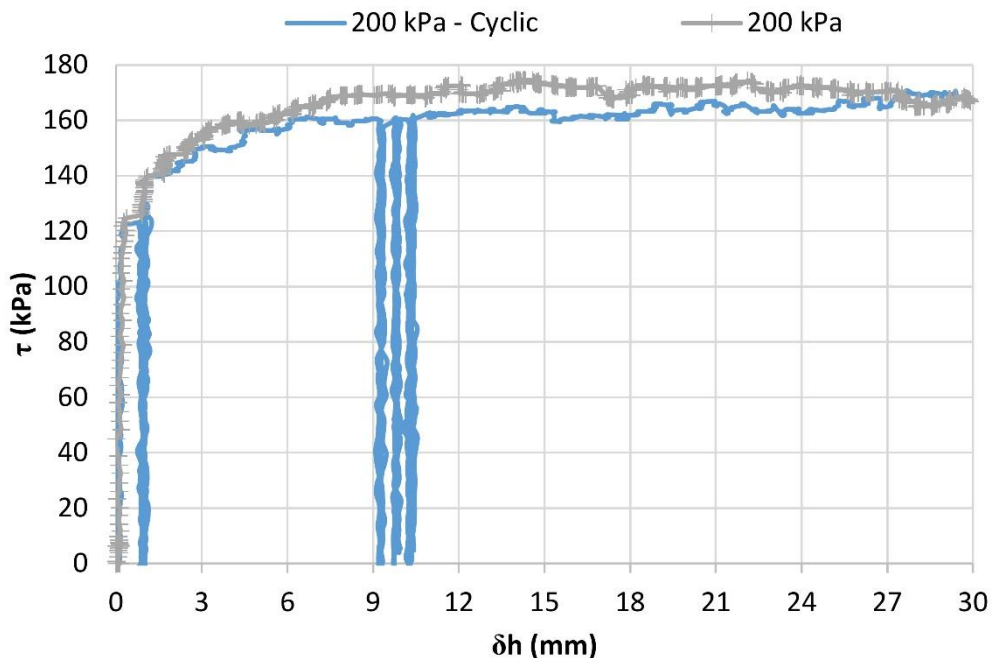


Figure 2.3-21: Shear stress versus horizontal displacement for cyclic solicitation at a normal stress of 200 kPa with reinforcement.

## 2.4. Installation procedure

A special grout mixer (EIRICH R08) was used to mix the two soil materials that constitute the subgrade soil at 11.5% of water content. To fill the 600 mm of the large box where the cyclic plate load tests were performed, 4 Tonnes of dry soil were mixed per steps of 65 kg, the maximum mixer capacity.

The soil compaction was performed using a plate compactor (DQ-0139). Moreover, the aggregate installation was made using a mini excavator (K65 V2) to simulate better the real site installation.

The main aim in this stage was to find a good installation protocol in order to obtain a homogeneous layer in depth and over the whole area with a CBR ratio of 2% for the soft subgrade and 20% for the fill material. Therefore, a series of installation tests were presented, and for each test, the quality control tests were performed to control the installed soil properties and homogeneity. The quality control tests performed will be presented in the section below.


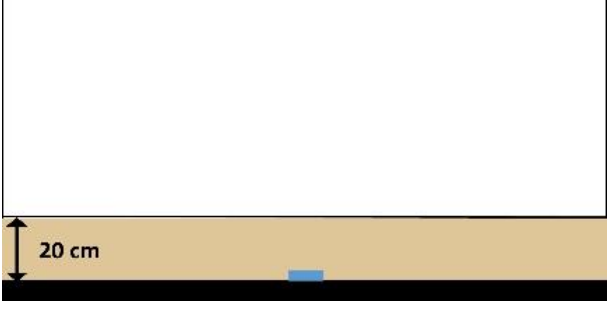
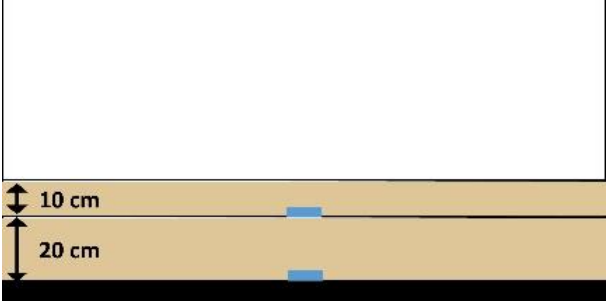



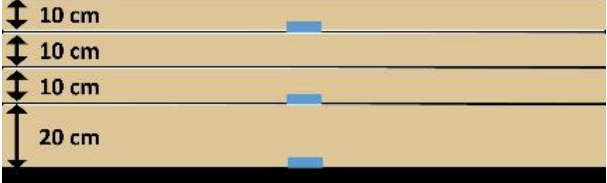
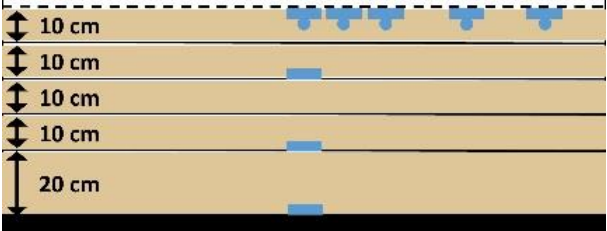
*Figure 2.4-1: The mixer, plate compactor and mini excavator used for the soil installation.*

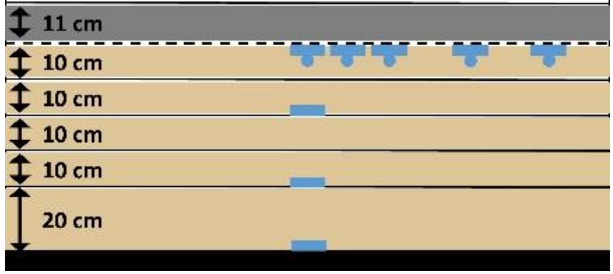
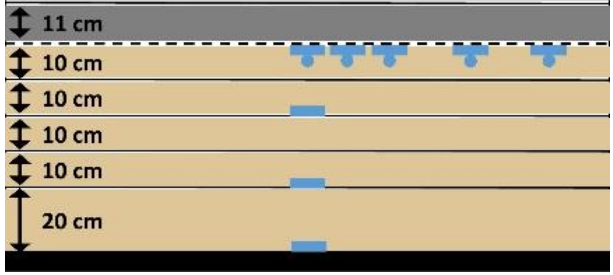
A final installation protocol was fixed, and it was applied on all the steps of each test preparation. The same protocol was used for the preparation of the platform's plate load test and the Traffic circulation load test, but with different soil quantities per layer since the platform dimensions are different. This protocol is presented with all its details in Table 2.4-1. The instrumentation illustrated in this table is specific for the plate load test.

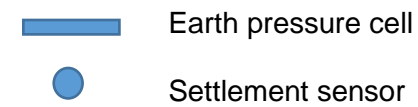


Table 2.4-1 : Installation Protocol details.

Stage	Stage description	Compaction	Figure
1	Anti-vibration mats were placed at the bottom of the box to limit the vibration.	--	
2	<p>At first an earth pressure sensor was placed at the base.</p> <p>The first 1400 kg in the plate load test platform preparation (3800 kg in the case of the Traffic test platform preparation) of subgrade that correspond to 200 mm were not compacted since they will be subjected to the compaction of the layers above.</p>	No compaction	
3	One more earth pressure sensor was placed at the surface centre. In addition, 700 kg in the plate load test platform preparation (1900 kg in the case of the Traffic test platform preparation) that correspond to 100 mm of subgrade were placed and compacted.	One compactor pass	

4	<p>An additional 100 mm (700 kg in the plate load test platform preparation and 1900 kg in the case of the Traffic test platform preparation) of subgrade was placed and compacted.</p>	<p>One compactor pass</p>	
5	<p>One more earth pressure cell was placed at the centre of the surface. An additional 100 mm (700 kg in the plate load test platform preparation and 1900 kg in the case of the Traffic test platform preparation) of subgrade was placed and compacted.</p>	<p>One compactor pass</p>	
6	<p>An extra 100 mm of subgrade was placed without any compaction since it will be subjected to the base course compaction. Moreover, 5 earth pressure and settlement sensors were placed at the surface. At this stage the non woven geotextile and the geogrid are placed.</p>	<p>No compaction</p>	

7	800 kg plate load test platform preparation (2200 kg in the case of the Traffic test platform preparation) of dry base course at 4% of water content were placed and compacted with four compactor passes. This quantity corresponds to 110 mm of layer thickness.	Four compactor passes	
8	An additional 800 kg in the plate load test platform preparation (2200 kg in the case of the Traffic test platform preparation) was placed and compacted with 4 compactor passes.	Four compactor passes	



## 2.5. Quality control tests

In order to compare the effect of different GSY reinforcement in this test, the variation in the soils properties is not allowed. Therefore, a series of quality control tests was performed on each soil layer prepared for testing. The quality control tests consist of a water content profile, a shear vane test, a static test and a dynamic penetrometer test (Figure 2.5-1).

### 2.5.1. The water content profile

The water content profile along the subgrade depth was plotted before and after each test to make sure that the subgrade water content does not change during the test and to make sure that there is no water migration from the upper layer to the bottom layer. The results will be presented in the next sections. However, it shows that the subgrade water content remains constant during the test and that there is no water migration.

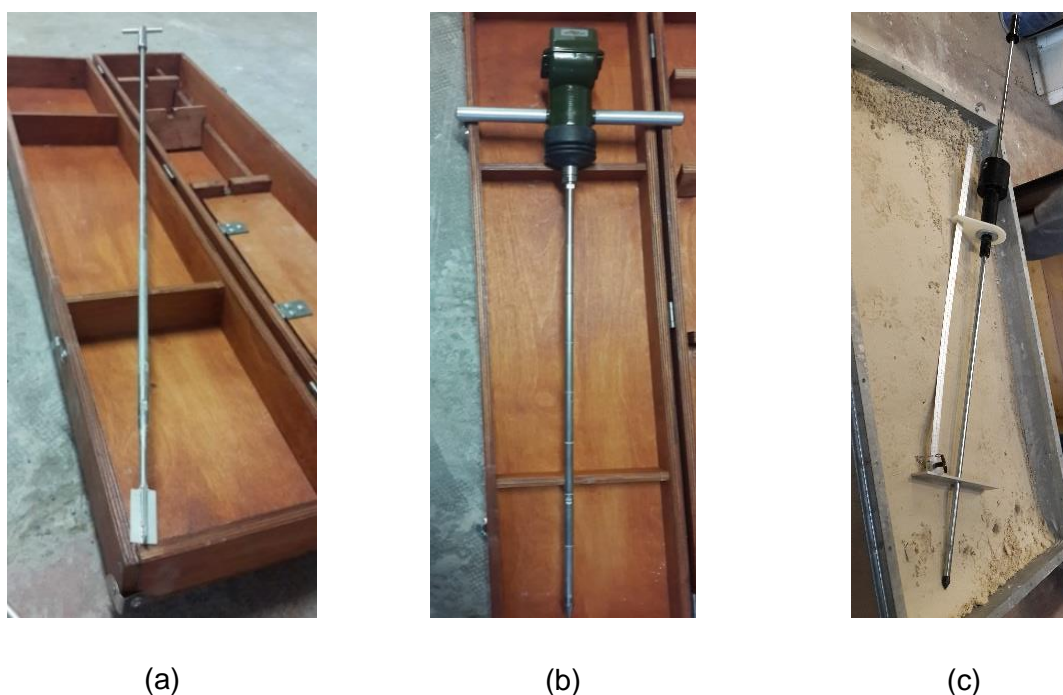


Figure 2.5-1: Instrument used for the quality control tests : (a) Shear vane test instrument, (b) Static penetrometer instrument, (c) Dynamic penetrometer instrument.

### 2.5.2. Shear vane test

The shear vane test consists of introducing a vane in the soil, and applying a rotation moment on it to establish a relation between the moment applied and the soil shear resistance.

The shear vane test was used to compare the maximum shear values along the subgrade depth and to verify the homogeneity of the soil. In fact, in a fully saturated clay soil the maximum shear value correspond to the undrained cohesion  $S_u$ .

However, since it is not the case in the subgrade used for this test, the maximum shear value is not the soil characterisation value; it is used only for comparison.

Two values are determined at the same vane position:

The maximum shear resistance, which is the value determined at the first applied rotation moment:

$\tau_u$

The residual shear resistance, which is the value determined after 25 rotation tours:  $\tau_r$

The value used for the comparison at different vane positions is the soil sensibility, which is the ratio between  $\tau_u$  and  $\tau_r$ .

### 2.5.3. Static penetrometer test

The static penetrometer was used by in-situ to determine the penetration resistance of the soil. A lightweight rapidity measurement instrument for in-depth resistance to penetration was used. The penetration resistance is indicated in a dial in terms of in-situ CBR (California Bearing Ratio) value and the cone index value (CI). The CBR value range in the dial is between 0% and 15%. The CI value range is between 0 and 300 with a 60 division in a linear scale.

The test consists of applying a force onto the instrument handles until a steady downward movement occurs into the soil layer. The instrument should stay in a perfectly vertical position. During the penetration at a steady rate, the cone is flush with the surface of the test area and the dial indicates the corresponding CI and CBR values. The measurements are taken all over the depth with an interval of 75 mm. This test was used only in the subgrade soil, since the penetration into the well-compacted fill material is not possible with this instrument. Therefore, a dynamic penetrometer was used to characterise the base course and the subgrade layer.

### 2.5.4. Dynamic penetrometer test

The TRRL DCP (Dynamic Cone Penetrometer A 2465) was used in this application. It is a lightweight instrument designed for the rapid in-situ measurement of the structural properties for existing road pavements constructed with unbounded materials.

The test consists of introducing a cone into the soil by a weight drop. Under each weight drop the cone penetration is noted and a correlation between the penetration and the CBR ratio is done. The used instrument has an 8 kg weight dropping through a height of 575 mm and a 60° cone having a diameter of 20 mm.

The dynamic penetrometer test was performed in the subgrade and the base course layer, and the results were as far as correlated to the CBR value using Kleyn and Van Heerden formula given by the manufacturer technical file:

$$\text{Log}_{10}(\text{CBR})=2.632-1.28 \text{Log}_{10}(\text{DCP}) \quad \text{Eq. 2.5-1}$$

DCP= depression per blow (mm/blow).

By comparing the results of the static and the dynamic penetrometers in the subgrade layer, we have the same CBR correlated value, which confirmed the correlation reliability.

## 2.6. Instrumentation

The aim of these tests is to improve the knowledge regarding the mechanisms developed at the base course and soft subgrade interface with geosynthetic reinforcement.

Based on that, the test was instrumented with Earth Pressure Cells (EPC), settlement sensors (S), displacement laser sensors, inclination sensors (I), and fibre optic sensors.

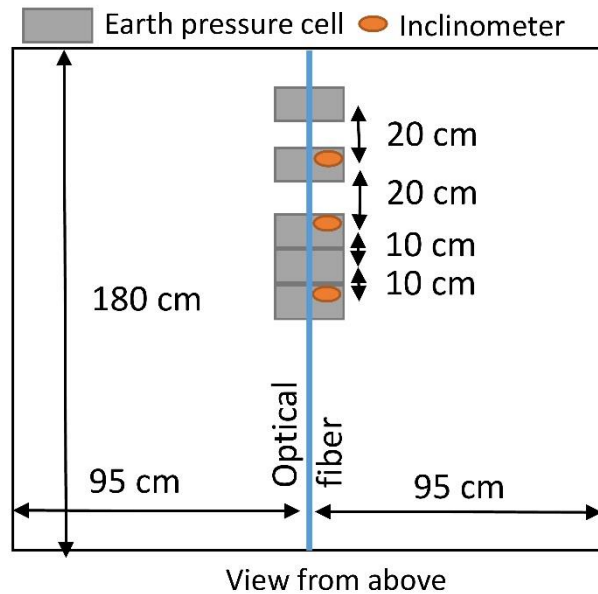


Figure 2.6-1: Platform instrumentation in the plate load test, view from above.

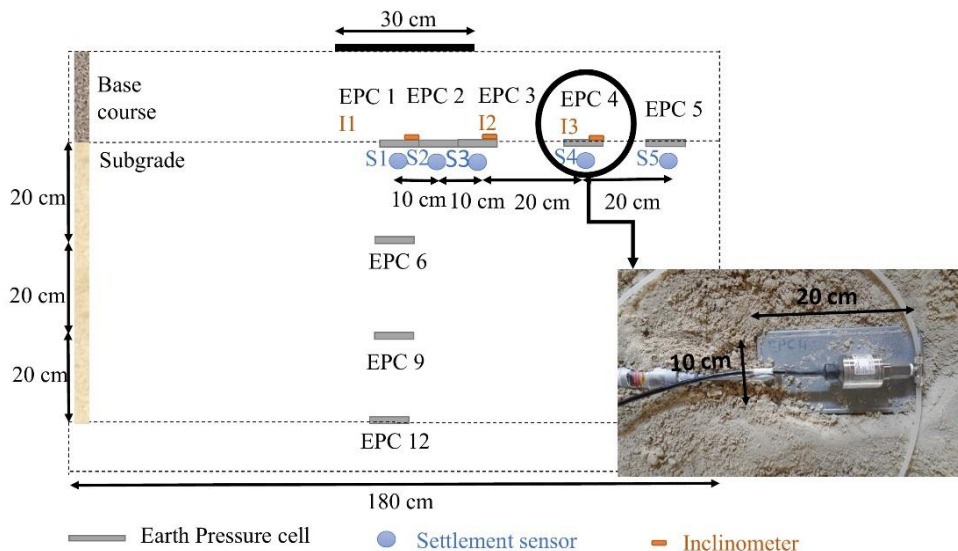


Figure 2.6-2: Sensors installation plan for the plate load test, a section.

In order to monitor the vertical stress distribution on the subgrade surface of the plate load test, five earth pressure cells were placed in different locations from the plate load centre (Figure 2.6-1 and Figure 2.6-2). On one hand, earth pressure cells were placed in different depth positions under the plate load centre. On the other hand, five settlement sensors were placed in different positions at

the subgrade surface to monitor the surface displacement during cycles. In addition, a fibre optic sensor was placed at the centre under the plate load in the geosynthetic in order to measure its strain.

Moreover, inclination sensors were placed on the earth pressure cells at the subgrade surface in order to monitor the sensors horizontality and check the reliability of the measured vertical stresses during the cycles.

In the traffic load test, two areas were instrumented: the area under the plate load test and the area under the traffic test. The same sensors repartition was considered in the two areas. For additional precision two earth pressure cells were added at 300 mm and 600 mm from the centre (Figure 2.6-3, Figure 2.6-4 and Figure 2.6-5). In addition, two fibre optic sensors were added in the traffic circulation load area in the GSY, and two more earth pressure cells were placed around the circulation line in order to control the load magnitude along the circulation line.

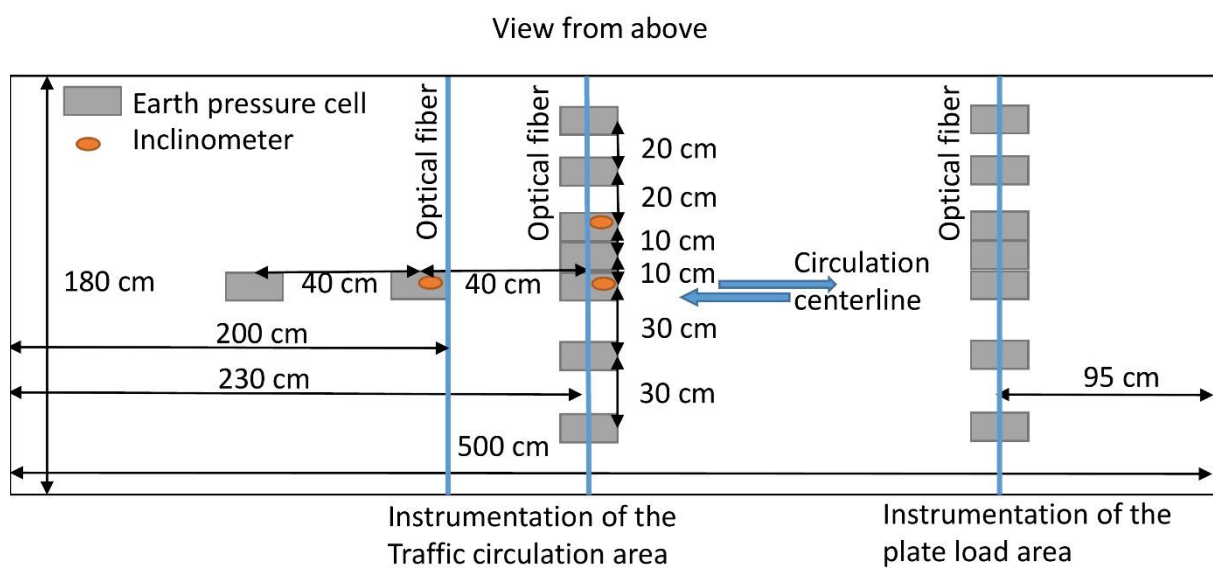


Figure 2.6-3: Platform instrumentation plan in the traffic load test, view from above.

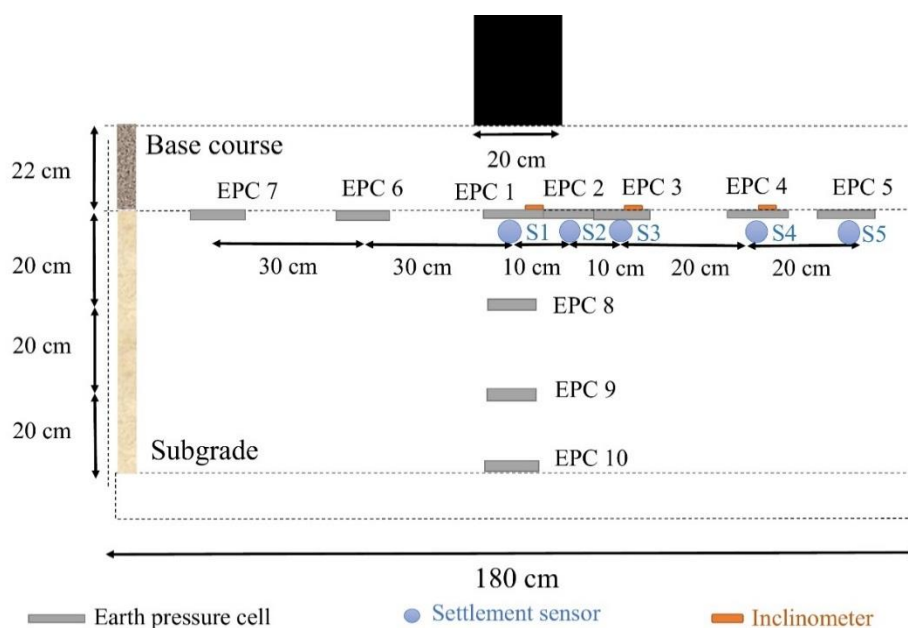


Figure 2.6-4: Sensors installation plan in the Traffic load test, a section.

A load sensor was used on the plate to control the load magnitude. Moreover, a laser sensor was used to monitor the plate displacement during the test, and to draw the settlement curve at the platform surface after the 10,000 cycles.



Figure 2.6-5: Illustration of the sensors installation in the traffic load test.

### 2.6.1. Earth pressure cell

The vertical stress distribution in the subgrade was measured using the earth pressure cells. These cells measure the normal stress increment applied on the sensor area filled with oil. In fact, the sensor area is composed of two plates welded on the borders and field with oil and connected to a pressure sensor. The sensors dimensions are adapted to the application and to the box's dimensions: 100 mm large and 200 mm length. The used sensor pressure ranges between 0-500 kPa with an accuracy of  $\pm 0.5\%$  of the full scale.

The sensor output signal measures currently 4-20 mA, it is the most used signal because of its technical and economic advantages. Unlike the tension signal, the current signal is not affected by the electromagnetic perturbation, nor by the alimentation tension variation or the cable length. The sensor alimentation and output signal are combined in the same cables.

The measurement of the cycles pressure with this kind of sensors is possible as long as the sensor is alimented continuously.

### 2.6.2. Hydraulic settlement sensor

The technology of this sensor consists of measuring the displacement based on the measurement of the hydraulic pressure variation. The transmitters placed at the same level are connected to each other's in series and connected to a tank placed on a fixed support out of the tested structure. The water tank keeps the sensors' circuits at a saturated state and a constant water pressure. The transmitter measures the pressure variation between its position and the tank's position. When the position of the sensor changes the measured pressure changes as well. An electrical cable connects each transmitter to the data logger. Like the earth pressure cells, the output signal is about 4-20 mA



as for the alimentation and the output, they are combined using the same cable. The transmitters have 50 mm diameter and 62 mm height. The measurements range of these sensors is between 0 and 300 mm with an accuracy of  $\pm 0.014\%$  of the full scale.

A transmitter was placed at a fixed position near the tank in order to control the variation of the water level in the tank, and insure that there are no measurement errors due to the water evaporation. It is worth noting that the measurement of the settlement during the cycles with that kind of sensors is not possible because of the vibrations' perturbation.



Fig. 2.6-1: Earth pressure cells and the settlement sensors.

### 2.6.3. Inclination sensor

Inclination sensors were placed at the surface of the earth pressure cells in order to check the horizontality of the sensors during the loading and unloading procedure. In fact, two directional sensors were used: x direction and y direction. Sensors with small dimensions were used to prevent the change of the pressure measurements: 45 mm in length and 22 mm in width. The output signal is a current 4-20 mA signal. The alimentation of these sensors is an external alimentation of 24 V. The measurements range is between  $-15$  and  $+15$  degrees with an accuracy of  $\pm 0.5^\circ$ .

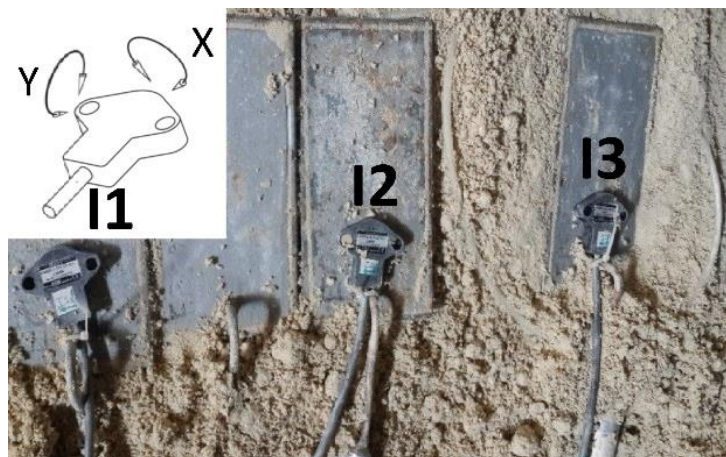


Fig. 2.6-2: Inclinometers placed on the earth pressure cells.

### 2.6.4. Displacement laser sensor

The displacement laser sensor was used in order to monitor the plate and wheel displacements over the cycles. This sensor was placed on a fixed bar. The measurements range is between 200

mm and 700 mm with an accuracy of  $\pm 0.07\%$  of the full scale. An external generator of 24 V was used to aliment the sensors. The tension output signal was connected to the acquisition centre. However, the sensor was used to measure the base course surface displacement over the cycles and the surface deformation after 10,000 cycles as seen in Figure 2.6-5. Moreover, this sensor was used to control the base course thickness. In fact, the subgrade and the base course surface elevation after the installation were plotted.



Figure 2.6-6: Laser sensor installation and measurements.

### 2.6.5. Data recording equipment

The sensors data collection and more importantly the optimisation of this system are described in this section. In fact, this is a cyclic loading system where an important number of sensors was used and it is worth mentioning that the optimisation of the recording data system is important as well. Two kinds of data acquisition loggers were used: Data-Taker logger, and Scaimé measurements acquisition instrument.

### 2.6.5.a. Data-Taker logger

The ST80's used in this application, are tools to measure and record a wide variety of quantities and values. This data logger can measure analogue, digital or serial output signals. In fact, it includes a powerful programming language, which allows complex systems to be developed and monitored. The limitation of this logger lies at the measurement of continuous values with high frequencies. Therefore, this logger was used to measure the static values of settlement given by hydraulic settlement sensors, and the static vertical pressures given by earth pressure cells placed in depth in the subgrade soil.

Although, to measure static values with an acquisition time of 1 min, loading and unloading static periods were taken between each series of loading. In order to connect all the sensors to the logger with five entries, two extensions were needed with 16 entries each.

The static measurement periods were taken between 100; 200; 300; 400; 500; 1,000; 2,000; 3,000; 4,000; 5,000; 6,000; 7,000; 8,000; 9,000; 10,000 cycles.



Fig. 2.6-3: Data Taker setup and interface.

### 2.6.5.b. Scaime measurements acquisition instrument

The scaime measurements acquisition instrument was used for continuous measurements during cycles. In fact, the advantage of this data logger is that it aliments all the channels at the same time and it can read continuous output values. This system can be used for different output types; the entry modulus should be changed based on the sensor circuits type.

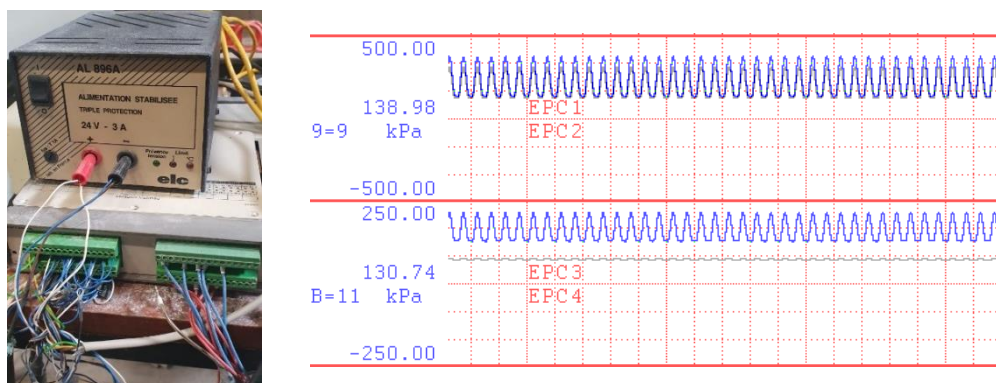


Figure 2.6-7: Scaime measurements acquisition setup and interface.

The used sensors connected to this logger are the earth pressure cells placed at the subgrade surface, the laser sensors and the inclination sensors.

The logger has an acquisition frequency of 8 Hz > 0.77 Hz of the load application frequency.

### 2.6.6. Optical fibre

Fibre optic sensors were placed in the GSY to measure the strain developed in the reinforcement during the loading. The spread sensor technology was used in this application, and the results analysis is based on the Retrodiffusion Rayleigh OFDR (Optical Frequency Domain Reflectometry) principle. The ODiSI-B optical centre was used to read the measurement values given by the optical fibre sensor. The ODiSI-B is able to measure the strain or temperature throughout the length of the fibre, and at intervals as low as 0.65 mm with an acquisition frequency of 62.5 Hz. It uses fibre optic sensors ranging from 1m to 20m in length.



Fig. 2.6-4: Optical acquisition software.

## 2.7. Conclusion

In this Chapter, the two performed tests were detailed: the devices used, the platform constitution, materials preparation, quality control and the instrumentation. In fact, the performed tests were presented:

- The plate load test in the square box using the circular plate,
- The traffic load test performed using the developed machine SAT and compared to the plate load test using a specific plate form, performed in the same prepared platform placed in the large box.

The unpaved road prepared in the laboratory using a specific material was presented. A presentation of the material used in the platform and its characterisation was detailed. A special attention was given to the developed installation protocol and the quality control tests. A heavy installation was used in these tests in order to collect the maximum of useful data and measurements. The instrumentation and acquisition systems were detailed in this Chapter as well.

The results presentation and analysis of the plate load tests are presented in Chapter 3. The results of the traffic load test and its comparison with the plate load performed on the same prepared platform are presented in Chapter 4.

# Chapter 3. Plate Load Test

---

## 3.1. Introduction

In Chapter 2, the developed experimental protocol was fully explained. The platform preparation, installation and the tests performed to control the layers' properties were presented as well. Moreover, the instrumentation and the data acquisition system were explained.

As mentioned in the previous Chapter, two types of solicitation were performed in two different experimental tests: the plate load test and the circulation load test.

In this Chapter, the plate load tests results are presented and analysed. The plate load tests were performed on an unpaved platform placed in a box of 1.9 m in length, 1.8 m in large and 1.1 m in height. A cyclic load was applied on the circular plate with 300 mm of diameter. The load is applied using a hydraulic jack with a frequency of 0.77 Hz with a maximum applied load magnitude of 40 kN resulting in a contact vertical pressure of 560 kPa.

Ten tests were performed under these loading conditions: with three different geogrid types, two base course thicknesses (350 mm and 220 mm), and one test with the reinforcement placed at the base course middle depth.

The results are presented in terms of developed vertical stresses at the subgrade surface and in the subgrade depth, the subgrade surface settlements, the base course surface settlements and the strain developed in the geogrid. Moreover, the aggregate damage under the applied 10,000 cycles was tested and analysed. In addition, the GSY damage under the plate load and the installation was tested and characterised. The experimental results were compared to the calculated base course thickness determined from the empirical and analytical design methods.

## 3.2. Performed tests

The base course thickness effect was studied by performing tests with reinforced and unreinforced platforms and two base course thicknesses (350 and 220 mm). In addition, the geosynthetic types were tested: two coated knitted geogrids with different stiffness' the GSY 1 and the GSY 2 (1,000 kN/m and 2,500 kN/m at 2% of strain) and an extruded triangular aperture geogrid the GSY 3. The main aim of these tests is to compare the geogrids' platform improvement effect. In order to allow the comparison, the test repeatability should be insured. Therefore, two identical tests were performed for the unreinforced platform, and for the reinforced platform with the GSY 1 and GSY 3.

Table 3.2-1: Performed tests details.

Test number	Base course thickness (mm)	Reinforcement	GSY position	Test status
Test 1	350	Unreinforced		Reference test
Test 2	350	GSY1	Interface	GSY improvement test
Test 3	220	Unreinforced		Reference test
Test 4	220	Unreinforced		Repeatability test
Test 5	220	GSY 1	Interface	GSY improvement test
Test 6	220	GSY 1	Interface	Repeatability test
Test 7	220	GSY 3	Interface	Reference test
Test 8	220	GSY 3	Interface	Repeatability test
Test 9	220	GSY 1	At the base course middle depth	
Test 10	220	GSY 2	Interface	

The platform thickness was controlled using the laser sensor; however, the subgrade elevation and the base course elevation were measured during the installation. In addition, the settlement sensors measured the subgrade settlement using the base course installation, which allowed the base course thickness control. The measured thickness' results are as follow:

$H_{\text{test 4}} = 230 \text{ mm}$ ,  $H_{\text{test 6}} = 233 \text{ mm}$ ,  $H_{\text{test 7}} = 221 \text{ mm}$ ,  $H_{\text{test 8}} = 222 \text{ mm}$ ,  $H_{\text{test 9}} = 225 \text{ mm}$ ,  $H_{\text{test 10}} = 221 \text{ mm}$ . These values show that it is not possible to control and to have the exact base course thickness for each test, the thickness varies between  $220 \pm 10 \text{ mm}$ .

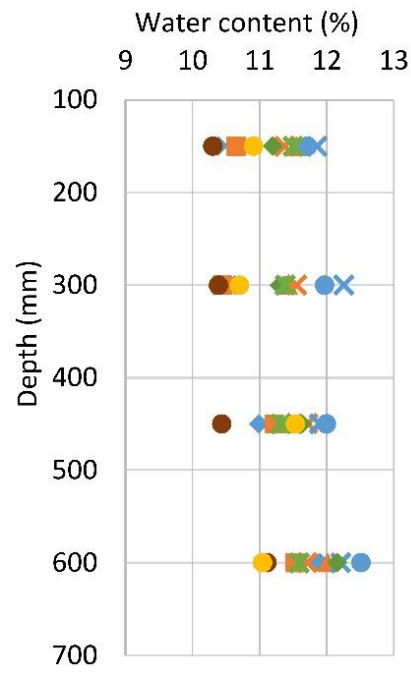
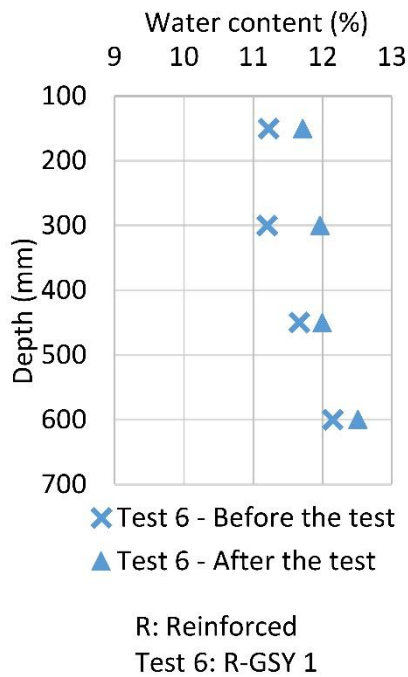
### 3.3. Quality control tests results

The quality control tests are performed on each prepared platform, in order to make sure that for each performed test the soil layers have the same properties and are under the same conditions. These tests were detailed in Chapter 2; however, in this section, the results of the performed quality control tests are presented:

#### 3.3.1.a. Water content

The water content was measured in depth for each prepared subgrade. Figure 3.3-1 (a) shows the water content profile before and after the test was performed. The profiles show that the water content in depth varies between 11% and 12%. In addition, it shows that there are no water variation or migration in depth before and after the test. In fact, the conditions of the subgrade water content are constant during the test.

Figure 3.3-1 (b) shows a cloud of water content points over the subgrade depth for each prepared layer. It shows a cloud of points between 10.5% and 12%, so the water content of the soil varies in an acceptable range.



(a)

(b)

Figure 3.3-1: (a) Water content profile before and after the test for the reinforced test 6, (b) Cloud of water content points of all the performed tests before the test.

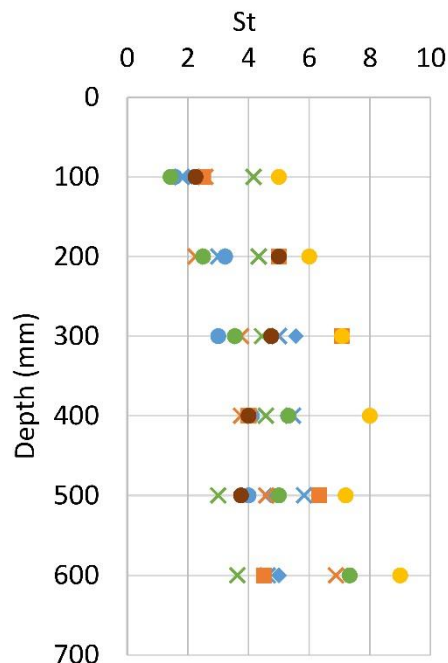
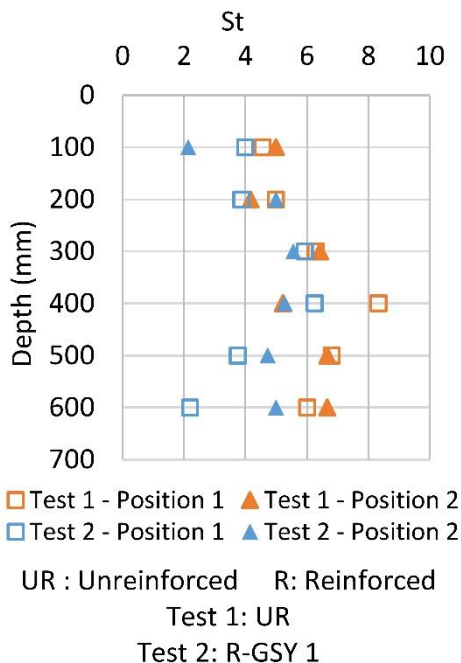
### 3.3.1.b. Shear vane test

The shear vane test is usually performed in a saturated soil to determine the undrained cohesion ( $C_u$ ). In this application, the prepared subgrade was an unsaturated soil. However, the shear vane test was performed in order to have comparison values. The soil sensibility  $S_t$  that is the ratio between  $\tau_u$  and  $\tau_r$  was used to compare in depth and between the prepared platform the soil homogeneity.

Figure 3.3-2 (a) shows the  $S_t$  profile in depth in two different positions for the reinforced (GSY 1) and unreinforced platforms with 350 mm of base course thickness tests. The graph shows a homogeneity over the subgrade depth and between the different positions. In fact, a concentration of the soil sensibility values ( $S_t$ ) is between 4 and 6. It shows a consistency between the values for the two prepared platforms, which verifies the repeatability of the same installation protocol.

Figure 3.3-2 (b) shows the  $S_t$  cloud of points over the depth of each prepared platform. The graph shows a soil sensibility concentration between 4 and 6 as in the Figure 3.3-2 (a). Based on the results of the shear vane test and the soil sensibility comparison, the soil homogeneity was verified over the depth and in the area, and it was the main characteristic to fix the right installation and compaction protocol.





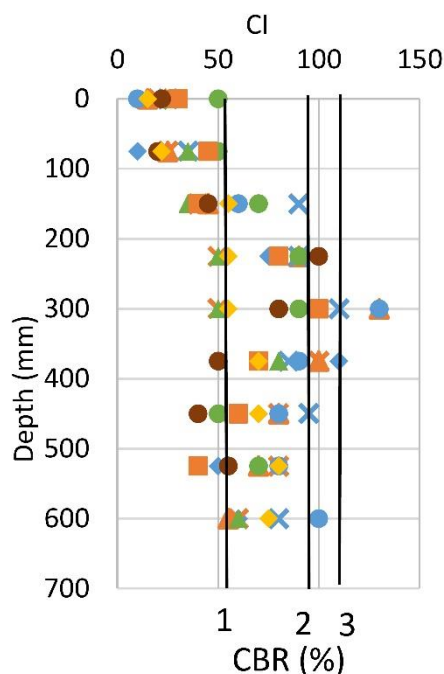
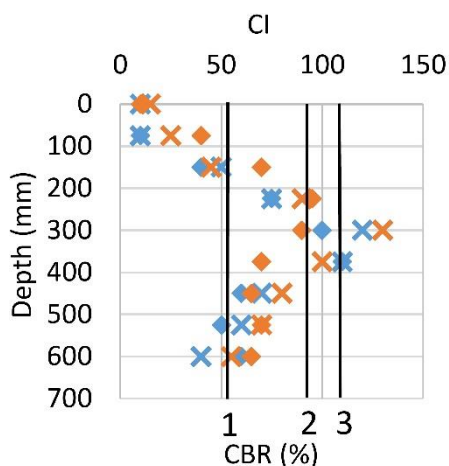
(a)

(b)

Figure 3.3-2: (a)  $S_t$  profile in two different positions for the Test 1 and Test 2, (b) Cloud of  $S_t$  points of all the performed tests.

### 3.3.1.c. Static penetrometer test

The static penetrometer was used too in the subgrade soil to determine the cone index, which is correlated to the CBR (%) by the apparatus manufacturer. Figure 3.3-3 (a) shows the profile in depth with regard to the cone index and the CBR (%).



(a)

(b)

Figure 3.3-3: (a) The CI/CBR (%) profile in two different positions for the Test 1 and Test 2, (b) Cloud of the CI/CBR (%) points of all the performed tests.

Figure 3.3-3 (a) shows the CI/CBR (%) profile in depth for the reinforced (GSY 1) and the unreinforced platforms 350 mm base course thickness tests. The profile shows homogeneous soil from 200 mm in depth with a CBR between 1% and 2%. At the surface a null CBR is seen, which is because the static penetrometer is performed before the base course installation, and in the subgrade compaction protocol the last 100 mm are not compacted since they will be subjected to the base course compaction.

Figure 3.3-3 (b) shows the CI/CBR (%) profile in depth of all the prepared platforms. It shows a CBR concentration between 1% and 2% from 200 mm in depth, as for the Figure 3.3-3 (a), the CBR at the surface is very low because of the compaction procedure.

### 3.3.1.d. Dynamic penetrometer test

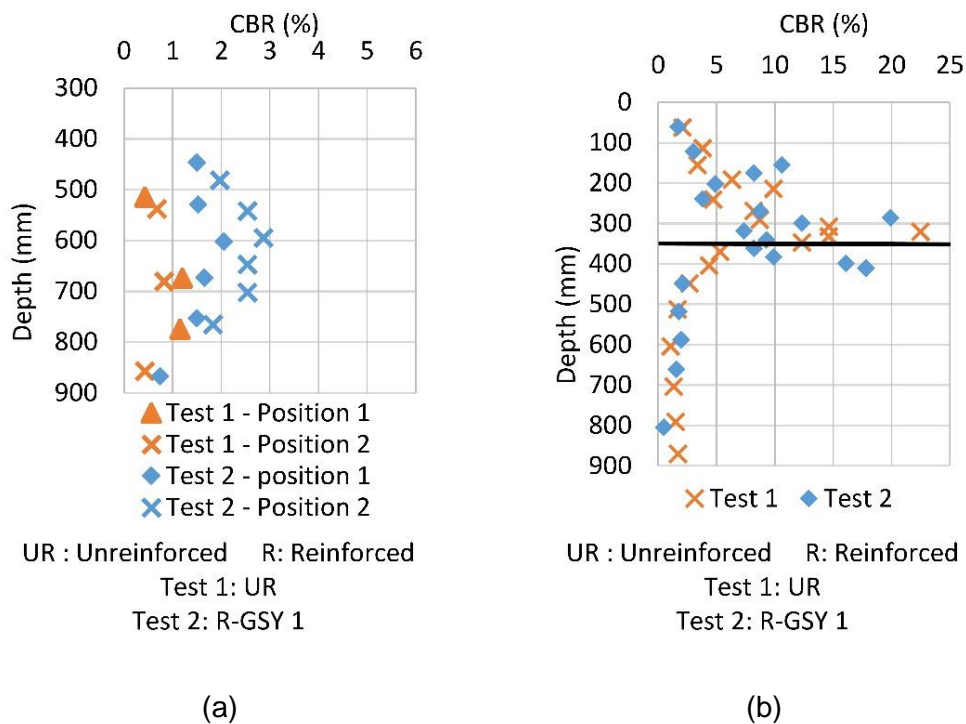


Figure 3.3-4: (a) CBR (%) profile in two different positions for the Test 1 and Test 2 with  $H = 350$  mm, before the base course installation, (b) CBR (%) profile in two different positions for the Test 1 and Test 2 with  $H = 350$  mm, after the base course installation.

The dynamic cone penetrometer was performed on the subgrade soil before the base course installation and after the base course installation in order to control the base course and the subgrade CBR (%). In fact, the results were correlated with the CBR (%) based on formulas given by the manufactural, and detailed in Chapter 2.

Figure 3.3-4 shows the dynamic penetrometer tests performed on the prepared reinforced and unreinforced platforms with 350 mm of base course thickness. Figure 3.3-4 (a) shows the CBR profile before the base course installation and Figure 3.3-4 (b) shows it after the installation and with the base course CBR values.

Figure 3.3-4 (a) shows the variation of the base course between 1% and 2% as seen before in the graph given by the static penetrometer Figure 3.3-3 (a), which confirms the CBR correlation reliability in both static and dynamic penetrometers.

Figure 3.3-4 (b) shows the base course CBR between 0 and 350 mm in depth. At the base course surface, the CBR value was about 5% due the soil repulsion on the surface. However, more in depth the CBR varies between 10% and 15% and it reaches 20% on some of the points. The CBR is at approximately 2% at the subgrade depth.

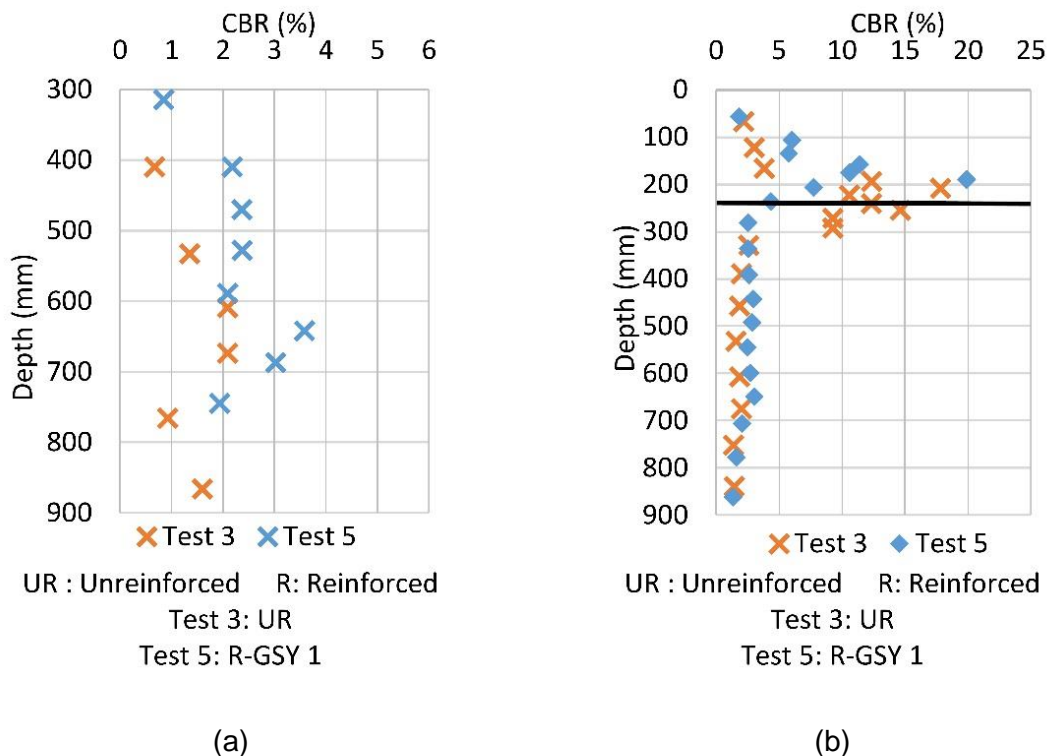


Figure 3.3-5: (a) CBR (%) profile in two different positions for the Test 3 and Test 5 with  $H = 220$  mm, before the base course installation, (b) CBR (%) profile in two different positions for the Test 3 and Test 5 with  $H = 220$  mm, after the base course installation.

Figure 3.3-5 show the dynamic penetrometer tests performed on the prepared reinforced (GSY 1) and unreinforced platforms with 220 mm of base course thickness. Figure 3.3-5 (a) shows the CBR profile before the base course installation, and Figure 3.3-5 (b) shows the CBR all platform depth after the base course installation. The CBR profile in Figure 3.3-5 (b) shows the base course CBR in the first 220 mm in depth, which is between 10% and 15% and reaches 20% on some points. The CBR is at approximately 2% at the subgrade depth and this was demonstrated in Figure 3.3-5 (a). Figure 3.3-6 show the CBR cloud points for all the prepared platforms with 220 mm of base course thickness. Figure 3.3-6 (a) shows the subgrade CBR before the base course installation and Figure 3.3-6 (b) shows the CBR after the base course installation. The graphs show the superposition of the CBR profile, which confirms the soil repeatability for the different performed tests. In addition, it shows an average base course CBR of 15% and an average subgrade CBR of 2%.

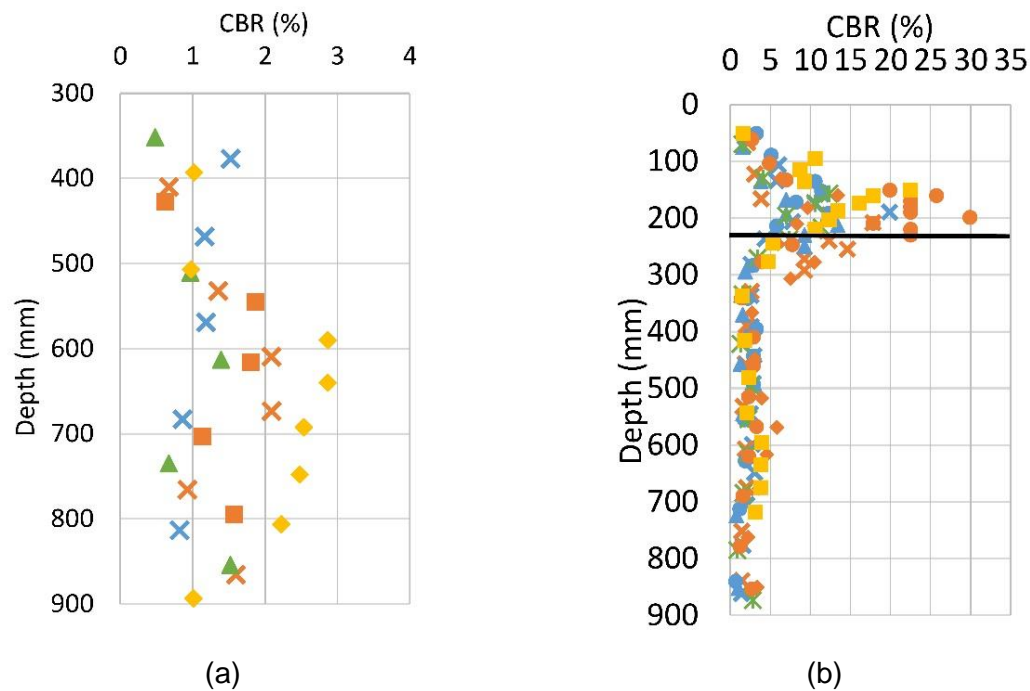


Figure 3.3-6: (a) CBR (%) profile of all the performed tests with 220 mm of base course thickness before the base course installation, (b) CBR (%) profile of all the performed tests with 220 mm of base course thickness after the base course installation.

The quality control tests were used first to define an installation and compaction protocol and to check that, under the defined protocol, the soil layers are homogeneous in depth and over the area and to confirm the soil properties.

Moreover, they were used to control the soil properties for each prepared platform. The results presented in this section showed the efficiency of the installation protocol. In fact, the superposition of the results given by the different tests showed the soil properties repeatability and homogeneity.

### 3.4. Results and analysis

During the tests, the subgrade, the base course surface displacement and the vertical stress distribution on the subgrade were monitored. The platforms were subjected to 10,000 cycles. The rut development at the platform surface is an important criterion in the results analysis, since it is the base of the design process. There are two rutting definition, the “elevation rut” and the “apparent rut” (Cuelho and Perkins, 2009). The rut depth was measured using a laser sensor, and the rut was the difference in the elevation of the measurement points over time which is referred to the “elevation rut”.

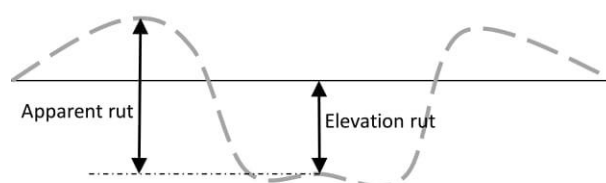


Figure 3.4-1: Illustration of rut measurement.

### 3.4.1. Measurements verifications

During the first performed tests, earth pressure cells were placed vertically on the box's borders in order to check the boundary effects. In fact, these sensors measured no stress on the borders during the loading, which insured that there are no boundary effects, and specified the box's dimensions. Moreover, in order to check the measurements reliability, a verification of the sensors effect on the subgrade behaviour was performed, noting that the sensors have relatively important dimensions. Figure 3.4-2 shows the subgrade surface settlement profile after 10,000 cycles. The curve shows no great differences between the monitored the unmonitored sides. This shows that the presented sensors do not disturb the subgrade behaviour.

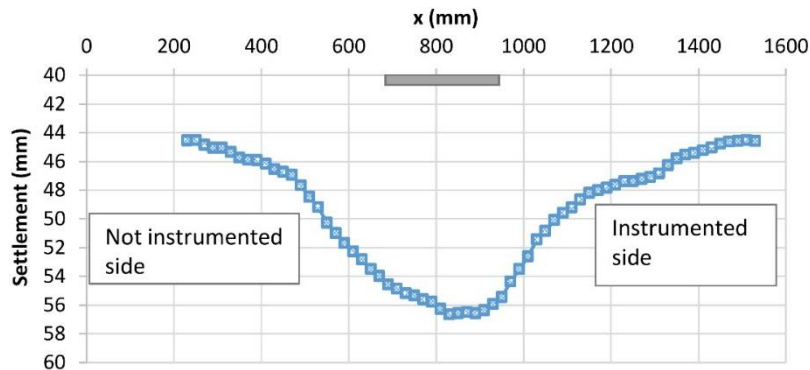


Figure 3.4-2: Subgrade settlement profile after 10,000 cycles.

The stress measurements in a soft soil can present some uncertainties related to the sensor movement and rotation during the loading, or to the arch effect that can occur around the earth pressure cells. In order to limit these uncertainties inclinometers were placed on the earth pressure cells to measure the sensor rotation and its evolution with cycles.

In fact, the earth pressure cell rotation was monitored for the ones placed at the surface centre, at 200 mm and 400 mm from the plate centre.

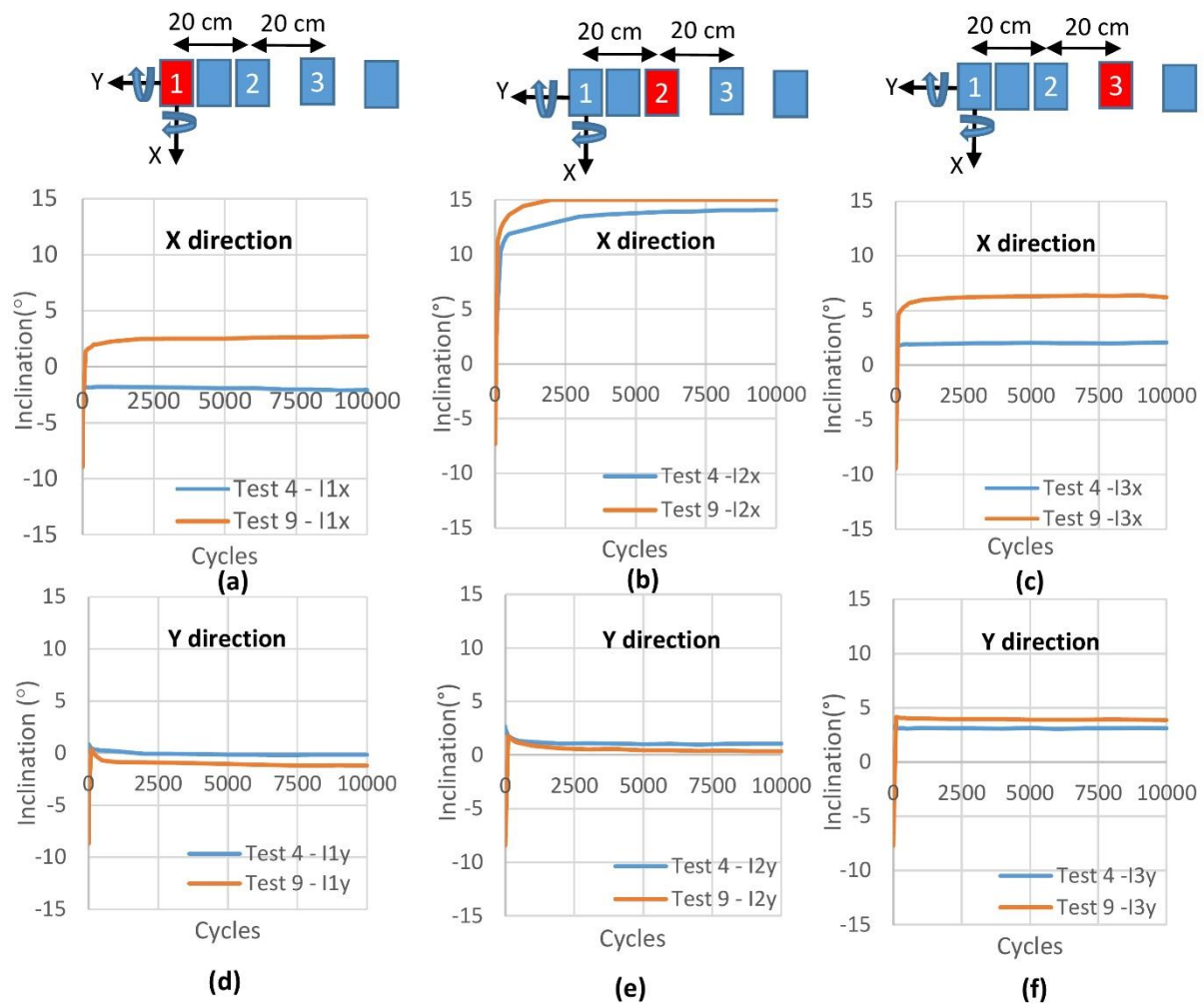
Figure 3.4-3 presents the sensors inclinations at three surface positions and around two different axes (x and y) for two performed tests.

All curves in both directions show an important inclination at the first loading; this can be due to the imperfections in the setup, or to the vertical stress non-uniform distribution on one earth pressure cell.

Figure 3.4-3 (a) and (d) show the central sensor inclination respectively around the x and y directions. The curves show a constant inclination of this central sensor around 0° and 2° in both directions. This shows that the values of the central sensor correspond to the vertical stress.

Figure 3.4-3 (b) and (e) show the inclination of the sensor placed at 200 mm from the plate sensor, this sensor was placed at the surface, it must curve the zone around the x axe. The inclinometer shows an important inclination in both tests that occur in the first cycles. In fact, in the 9<sup>th</sup> test, the inclination around the x axe reaches 11 degrees after 100 cycles and it continues to increase until it reaches the upper limit of the inclinometer which is 15 degrees after 2,000 cycles. In the 4<sup>th</sup> test, the inclination reaches 11 degrees after 2,000 cycles and increase into a constant value of 14° after 3,000 cycles. This shows that the values measured by the sensor present uncertainties related to the

inclination of the sensor. However, around the y direction the sensor shows a constant value around zero degrees after the first cycle. Figure 3.4-3 (c) and (f) show an inclination of 5 degrees during the first 1,000 cycles and then a constant value over the cycles around the x direction and a constant value in the y-direction. This shows that there are uncertainties related to the sensor inclination especially in the x direction and for the sensors placed at 200 mm from the plate's centre. Therefore, the stress measurements are analysed in a qualitative way in the following sections.



Test 4: Unreinforced

Test 9: Reinforced with GSY 1 - At the base course middle depth

Figure 3.4-3: (a) Centre earth pressure cell inclination over the X direction, (b) Earth pressure cell placed at 200 mm from the load centre inclination over the X direction, (c) Earth pressure cell placed at 400 mm from the load centre inclination over the X direction, (d) Centre earth pressure cell inclination over the Y direction, (e) Earth pressure cell placed at 200 mm from the load centre inclination over the Y direction, (f) Earth pressure cell placed at 400 mm from the load centre inclination over the Y direction.

### 3.4.2. Repeatability tests

Identical tests were performed to check the experimentation repeatability. In fact, in order to compare the results the test repeatability should be checked especially in such a large-scale test. Three repeatability tests were performed on an unreinforced platform and a reinforced platform with GSY 1 and GSY 3. The 3<sup>rd</sup> and the 4<sup>th</sup> tests are the identical unreinforced tests, however, the 5<sup>th</sup> and the 6<sup>th</sup>

are the identical reinforced tests with GSY 1 as for the 7<sup>th</sup> and the 8<sup>th</sup>, they are identical reinforced with GSY 3. All the repeatability tests were performed with 220 mm of base course thickness. The maximum central subgrade settlement evolution with cycles for the identical performed tests is shown in Figure 3.4-4. It shows as well close displacement results given by each two identical tests. For the first cycle, the unreinforced platforms displacement is 30 mm for both identical tests. The displacement at the first cycle for the reinforced with GSY 1 platforms is 24 mm (Test 5) and 26 mm (Test 6), with the GSY 3 platforms it is 13 mm (Test 7) and 9 mm (Test 8). It shows close results given by the identical tests at this specific point. With these cycles, the settlement evolves in the same way for each identical test. Figure 3.4-4 shows the subgrade settlement reduction also given by the reinforcement. However, the reinforcement effect will be discussed later in section 3.4.1, in this section the focus is only on the repeatability.

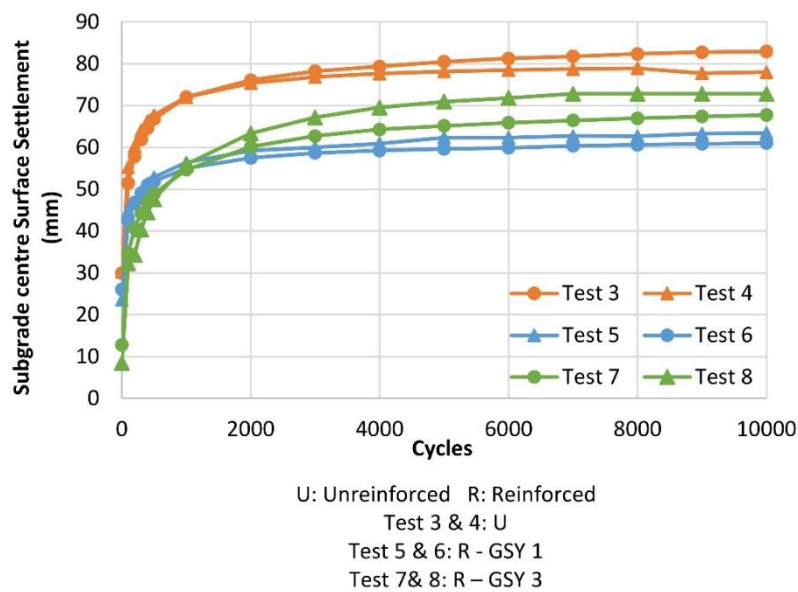


Figure 3.4-4: Subgrade surface centre settlement evolution with cycles.

Figure 3.4-5 below shows the maximum vertical stress at the subgrade surface centre evolution with cycles. It shows as well that the maximum stress of the unreinforced platform starts at 300 kPa (Test 3) and 270 kPa (Test 4) and decreases in the first 100 cycles. It then shows a constant curve of 300 kPa (Test 3) and 270 kPa (Test 4). The reinforced platform with GSY 1 shows a stress at the first cycle of 200 kPa (Test 5 & 6), which increases with the cycles until it reaches a constant value of 250 kPa (Test 5) and 230 kPa (Test 6). The reinforced platform with GSY 3 shows a stress at the first cycle as well of 200 kPa (Test 7 & 8), which increases with the cycles until it reaches a constant value of 321 kPa (Test 7) and 350 kPa (Test 8).

Three different stress categories can be noticed between the three identical cases. More importantly, differences between the identical tests are observed in stress terms. This can be due to the uncertainties related to the stress measurements.

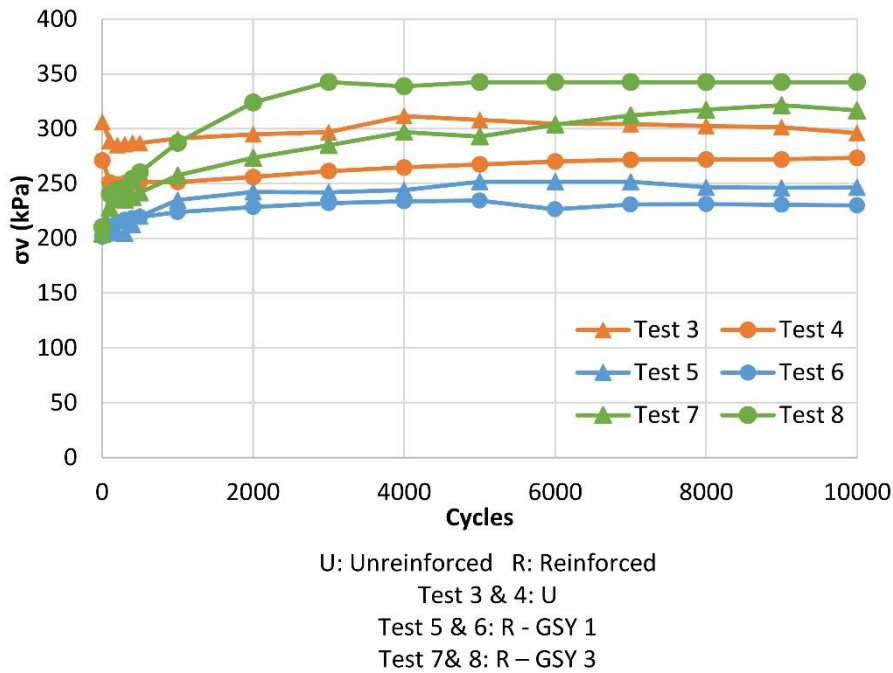


Figure 3.4-5: Subgrade surface centre vertical stress evolution with cycles.

Figure 3.4-6 presents the stress evolution with settlement at the same position, which is the subgrade surface centre. This graph demonstrates first the functionality of the earth pressure cells and settlement sensors. In fact, it shows that a higher stress level causes a higher settlement especially for the first points on a virgin subgrade.

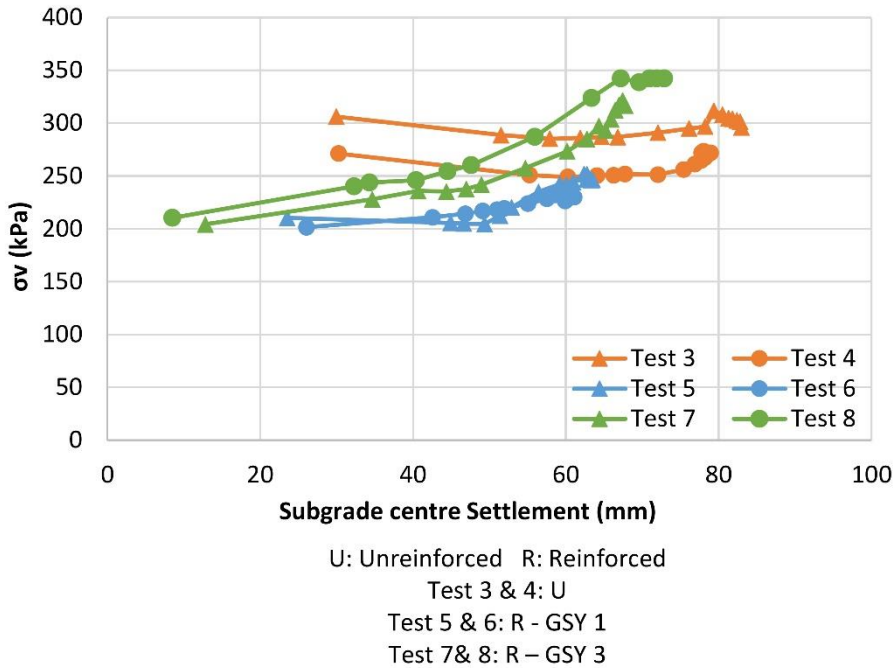


Figure 3.4-6: Subgrade surface central vertical stress evolution with settlement.

The graph demonstrates three different categories given by the three identical performed tests. In fact, each test category starts at a given point and evolve differently depending on the reinforcement type. The graph also demonstrates that the two identical tests have the same behaviour and evolution with the cycles.



The results presented in this section proved the tests repeatability and the developed installation protocol. In section 3.4.1, the reinforcement effect will be discussed. Since the repeatability was already proven and presented, in the next analysis only one of the two identical tests will be presented: Test 3, Test 5 and Test 7.

### 3.4.3. Base course thickness influence

Two tests were performed with a base course thickness of 350 mm, one with reinforcement (Test 2) and the other without reinforcement (Test 1). Figure 3.4-2 shows a small difference in the final rutting for  $H = 350$  mm between a reinforced and an unreinforced platform. In fact, both curves for  $H = 350$  mm have the same shape with an average maximum rut of 44 mm for the unreinforced platform and 50 mm for the reinforced platform. The results show that the reinforcement effect can be negligible for a base course thickness of 350 mm. Moreover, this can be shown in the subgrade surface settlement Figure 3.4-13.

It is worth pointing out that the base course thickness has the most significant influence on the surface rut development. The two unreinforced tests' comparison for  $H=220$  mm and  $H=350$  mm shows an evident rut reduction (Figure 3.4-2). For 130 mm of base course thickness variation, the surface rut passes from 44 mm to 89 mm. Moreover, the subgrade surface stress distribution was illustrated in Figure 3.4-15 and Figure 3.4-16. Furthermore, Figure 3.4-15 shows that the central vertical stress in the unreinforced platform is 130 kPa and in the reinforced platform is 100 kPa at the first loading cycle. These values increased with the cycles until they have reached 140 kPa for the unreinforced platform and 120 kPa for the reinforced platform after 10,000 cycles (Figure 3.4-16). A small difference is shown between the reinforced and unreinforced platforms in terms of stress too. More importantly, the stress reduction due to 130 mm of base course thickness addition increases the maximum vertical stress on the subgrade of about 67%. In fact, on one hand the unreinforced platform with 350 mm of base course thickness presents a central vertical stress of 300 kPa while on the other hand, the unreinforced platform with 220 mm of base course presents 100 kPa of maximum stress.

### 3.4.4. GSY benefit

In this section the GSY reinforcement is discussed mainly for  $H = 220$  mm

Five tests will be compared in terms of settlement and stress:

- Test 3, one of the identical performed unreinforced tests
- Test 5, one of the identical performed reinforced tests with GSY 1
- Test 6, one of the identical performed reinforced tests with GSY 3
- Test 9, a reinforced platform with the GSY 1 placed at the base course middle depth
- Test 10, a reinforced platform with GSY 2, regarding this test, the subgrade settlement and the surface settlement profile after 10,000 cycles are missing because of technical issues during the test.

### 3.4.4.a. Settlement

The base course settlement profile was measured after 10,000 cycles using the laser sensor. Figure 3.4-7 shows the profiles measured for the reinforced and unreinforced platforms with 350 mm of base course thickness (Test 1 & 2) and three tests with 220 mm of base course.

The remarkable point regarding the profiles is the curves symmetry around the plate load centre, which explains the platform instrumentation on one-half.

Figure 3.4-7 shows a large displacement of the unreinforced platform (Test 3), which is 90 mm > 75 mm the allowable rutting according to the FHWA (2008) standard. The two reinforced platforms with GSY 1 and GSY 3 show the same surface displacement of 70 mm < 75 mm.

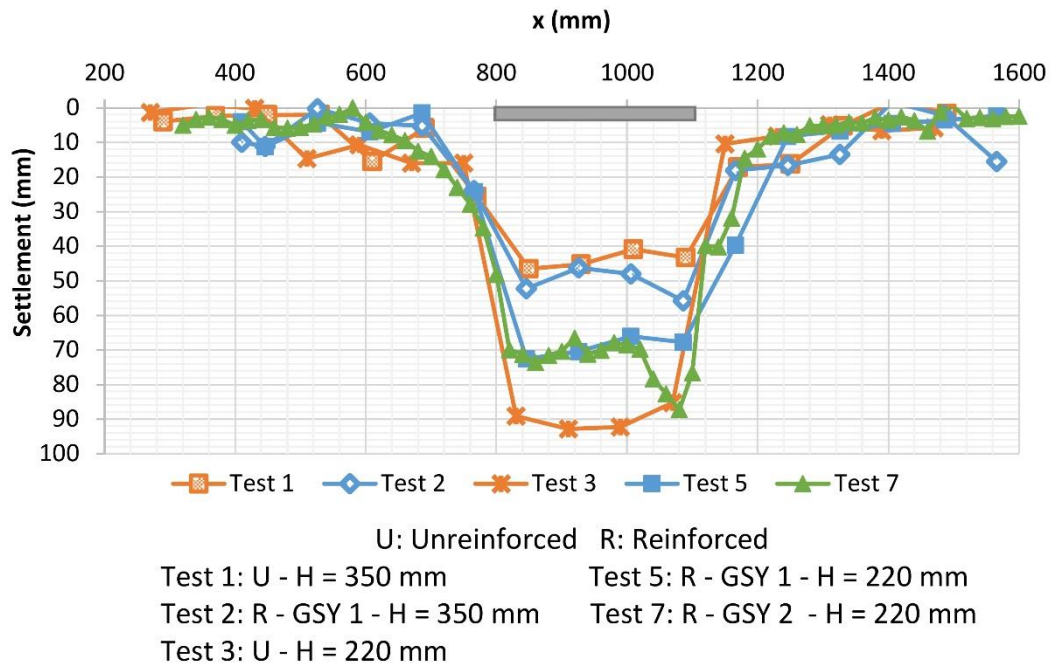


Figure 3.4-7: Base course surface settlement after 10,000 cycles.

This first graph shows the effect of the reinforcement on the surface settlement. It shows no difference between the two types of reinforcement used; this can be due to the imprecise measurements related to the unsmooth base course surface. In order to look more closely at the reinforcement behaviour, the subgrade settlements are presented later.

Figure 3.4-8 below shows the base course centre settlement evolution with cycles. The presented curves show an important displacement at the first loading and during the first 100 cycles. This settlement depends on the compaction method and can be eliminated on site by the heavy compaction machines. In this study, the behaviour of the platform under the first loading is different depending on the reinforcement, so the results of this first loading can be used for more explanations. However, another settlement evolution starting after 200 cycles was illustrated in order to eliminate the first settlements that can be removed on site by the compaction machines (Figure 3.4-9).

Figure 3.4-8 shows a displacement of about 36 mm (Test 3), 29 mm (Test 5 & 7 & 9) and 10 mm (Test 10). The reinforced platform with the geogrid GSY 2 (the coated and knitted geogrid with the stiffness higher than GSY 1) presents the lower first displacement. The unreinforced platform presented the biggest first displacement.

Under the cycles, the evolution of the displacement is different depending on the reinforcement type. After 2,000 cycles the curves presents a linear part with different inclinations. However, after 10,000 cycles Test 10 with GSY 2 presents the smaller displacement of 65 mm, followed by Test 5 with GSY 1 and a displacement of 76 mm. Test 7 with the extruded geogrid presents a maximum displacement of 88 mm. The remarkable point in this graph (Figure 3.4-8) is the platform reinforced with the GSY 1 placed at the base course middle depth, which presents a settlement behaviour close to the unreinforced platform behaviour.

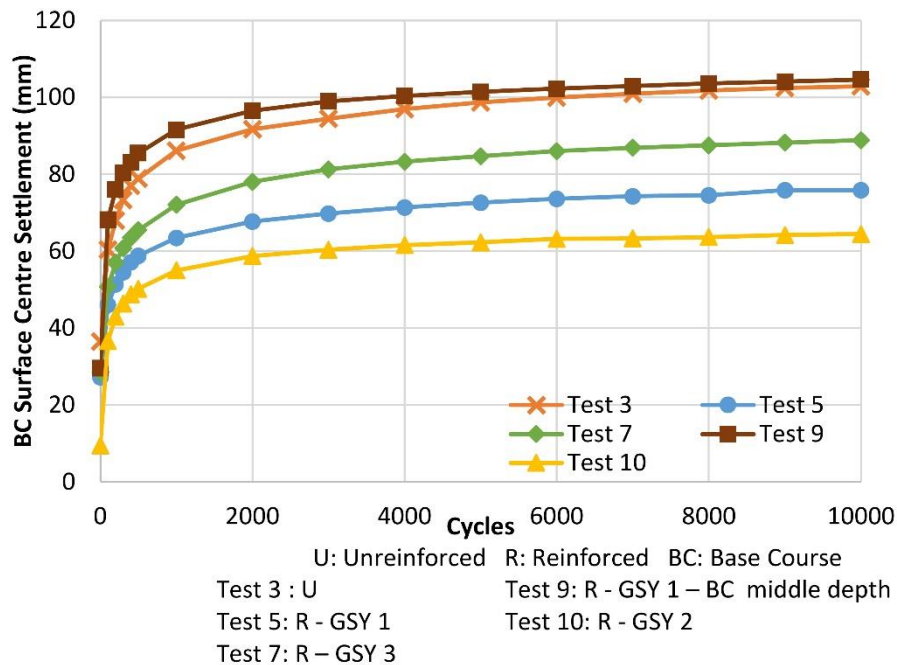
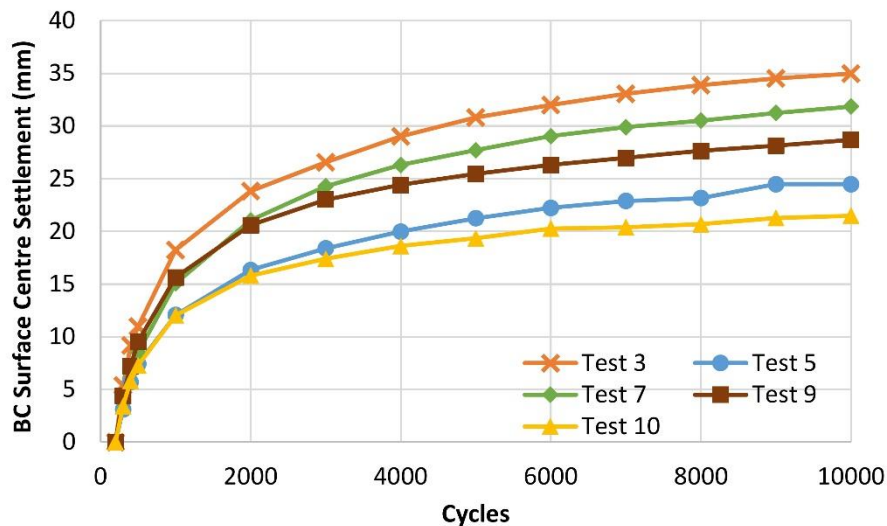


Figure 3.4-8: Base course surface centre settlement evolution with cycles (for  $H = 220$  mm).

In order to look at the reinforcement behaviour on the surface settlement evolution with cycles the settlements were plotted after 200 cycles (Figure 3.4-9).

In Figure 3.4-9, Test 10 and Test 5 present a close evolution curve until 3,000 cycles, after this point a small difference appears after 10,000 cycles with 5 mm of settlement difference. This shows that the most important efficiency is provided by the stiffer geogrid.



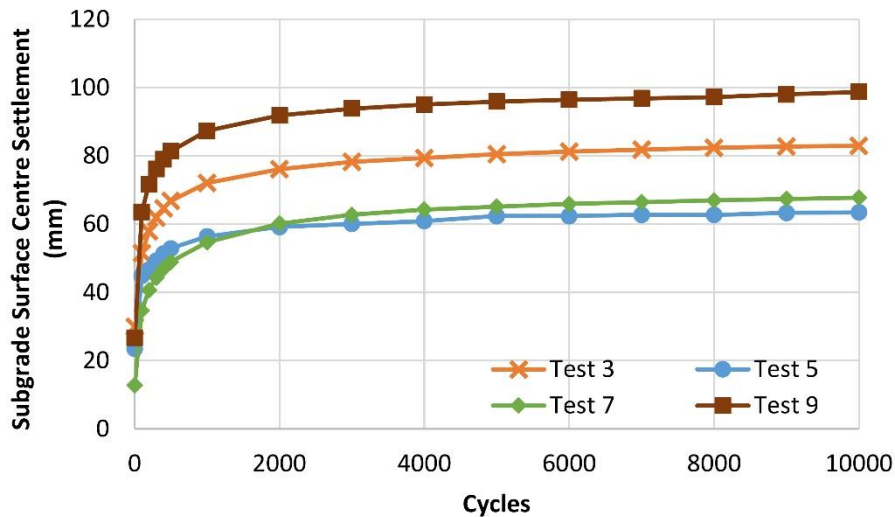
U: Unreinforced R: Reinforced BC: Base Course  
 Test 3 : U Test 9: R - GSY 1 – BC middle depth  
 Test 5: R - GSY 1 Test 10: R - GSY 2  
 Test 7: R – GSY 3

Figure 3.4-9: Base course surface centre settlement evolution after 200 cycles with cycles, (for  $H = 220$  mm).

More importantly, the reinforcement GSY 1 placed at the base course middle depth (Test 9) shows in Figure 3.4-9 a reinforcement effect on the settlement evolution with cycles. In fact, this platform presented an important settlement under the first cycles, but the reinforcement affected the platform behaviour over the cycles especially after 2,000 cycles.

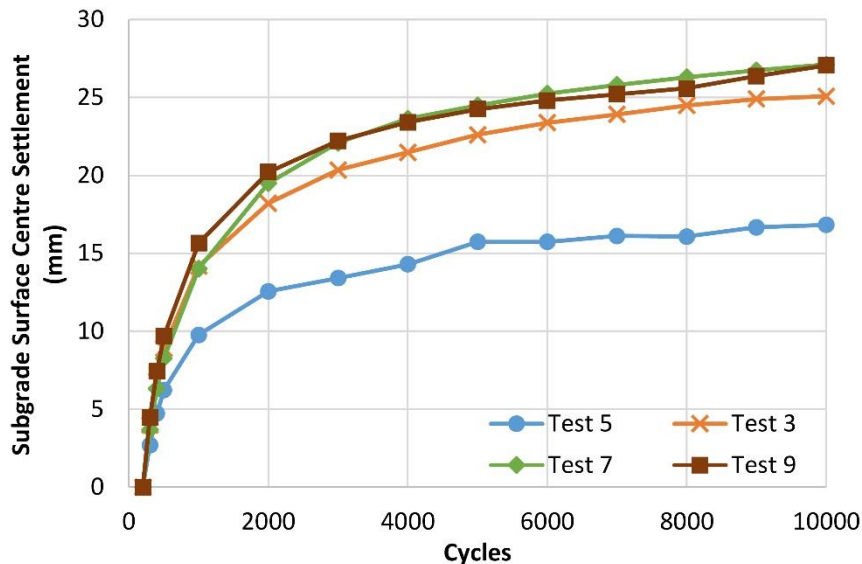
The extruded geogrid GSY 3 (Test 7) showed a reduced effect on the settlement evolution with cycles, in fact its behaviour after 200 cycles is the closest behaviour to the unreinforced platform.

Figure 3.4-10 shows the subgrade centre settlement evolution with cycles. Tests 5 and 7 show the most reduced settlement at the subgrade surface of 65 mm. The first cycles show that GSY 3 is more efficient in reducing the subgrade settlement than the GSY 1. However, GSY 1 performs better with the settlement evolution and after 2,000 cycles, and it presents a better performance than the GSY 3. In fact, the GSY 3 concept is based on the confinement mechanism, which performs better under small displacement. While the GSY 1 concept is based on the tension membrane mechanism, with a high stiffness and negligible nodes stiffness, and it performs better under large displacement. This phenomenon was more observed in the graph showing the subgrade settlement evolution after 200 cycles (Figure 3.4-11). In fact, the GSY 3's effect on the evolution of the settlement was close to the unreinforced platform, while GSY 1 shows a significant settlement reduction with cycles.



U: Unreinforced R: Reinforced  
 Test 3 : U Test 9: R - GSY 1 – BC middle depth  
 Test 5: R - GSY 1 Test 7: R – GSY 3

Figure 3.4-10: Subgrade surface centre settlement evolution with cycles (for H=220 mm).



U: Unreinforced R: Reinforced  
 Test 3 : U Test 9: R - GSY 1 – BC middle depth  
 Test 5: R - GSY 1 Test 7: R – GSY 3

Figure 3.4-11: Subgrade surface centre settlement evolution after 200 cycles with cycles (for H=220 mm).

In addition, Figure 3.4-10 above shows that Test 9 presents the highest settlement at the subgrade surface, noting that Test 9 is the reinforced test with GSY 1 placed at the base course middle depth. In the first 100 cycles, the settlement observed is about 40 mm; this can be due to some uncontrolled factors related to the installation and compaction. Therefore, Figure 3.4-11 is more reliable to compare with it this test behaviour. Figure 3.4-11, shows that the GSY 1 placed at the base course middle depth efficiency is limited and that the platform behaves as if there are no reinforcements.

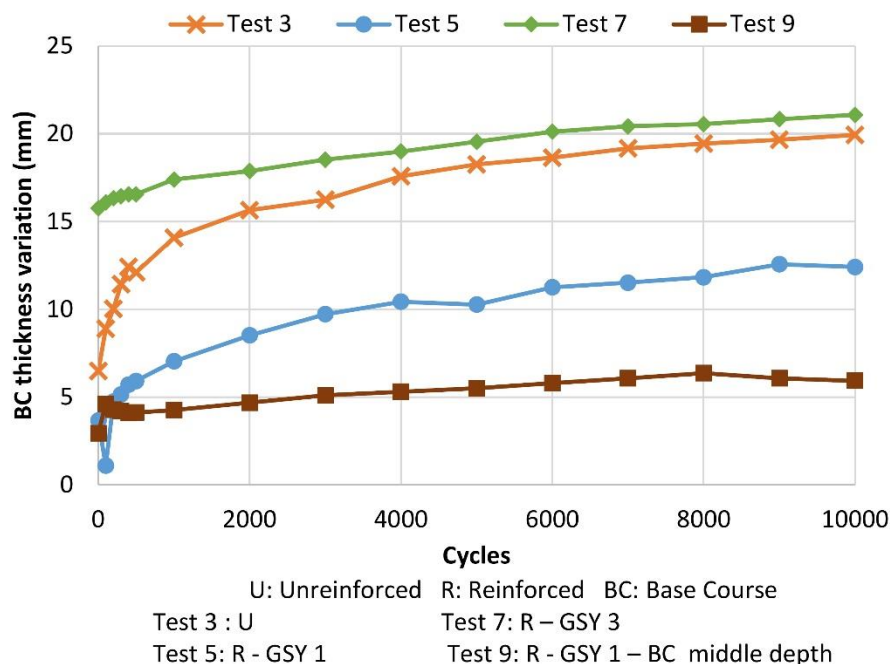


Figure 3.4-12: Base course thickness variation evolution with cycles (for H=220 mm).

A difference between the base course surface settlement and the subgrade surface settlement was observed above because of the base course thickness variation. Figure 3.4-12 shows the effect of the reinforcement on the base course thickness variation. The unreinforced platform and the reinforced platform with GSY 3 show the highest base course thickness variation of 20 mm. However, the unreinforced platform variation evolves with the cycles, while the reinforcement with GSY 3 platform shows an important variation of for the first cycle and then a very small variation during following cycles. The two reinforced platforms with GSY 1 show the smallest thickness variation, mainly the one placed at the base course middle depth.

Figure 3.4-13 shows the subgrade surface settlement profiles of the first cycle and after 10,000 cycles. The curves show that starting with 400 mm from the plate centre at the subgrade surface the settlement is null for the reinforced and unreinforced cases, which confirms again the boundary conditions respect.

The settlement curvature shows no differences between the reinforced and unreinforced platforms. It is worth pointing out that the same settlement rank was observed at the plate centre, as well as at 100 mm and at 200 mm from the plate centre.

By comparing and analysing the settlement results, the reinforcement efficiency was observed and quantified. The knitted geogrid GSY 1 shows a platform behaviour improvement especially with the large displacement development when the geogrid is mobilised. Moreover, the results show that the stiffer the geogrid is the more improvement on the surface settlement is observed specifically for the first cycles. The extruded geogrid GSY 3 shows a platform behaviour improvement for the first 2,000 cycles, but it shows a significant change in its behaviour after a large displacement development. In addition, these results showed that the geogrid GSY 1 placed at the base course middle depth has a reduced benefit on the platform behaviour. In order to explain better these mechanisms and observations the vertical stress is analysed in the next section.

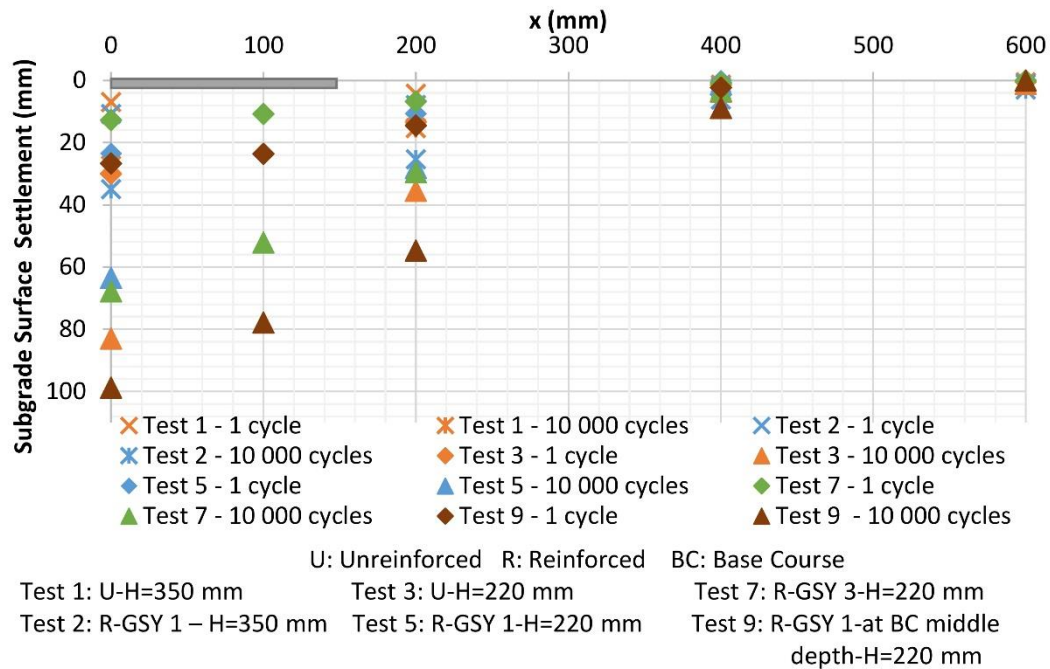
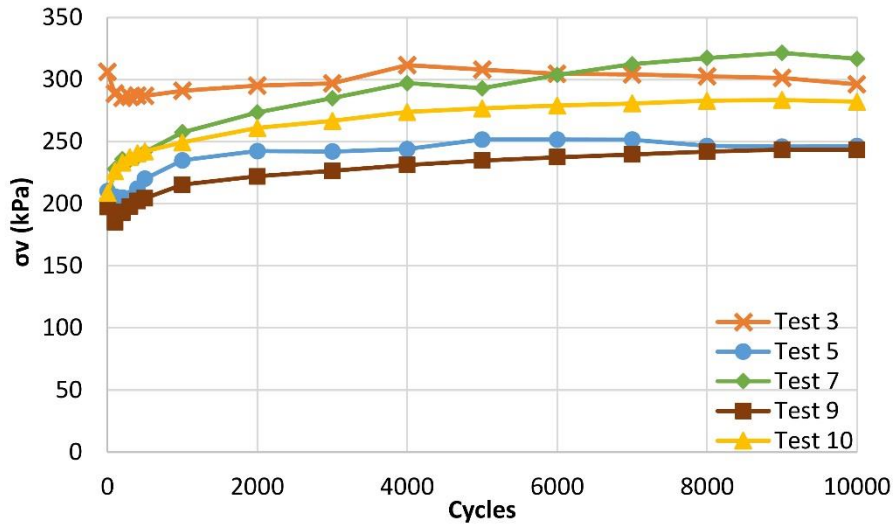


Figure 3.4-13: Subgrade surface settlement profile from the plate centre to the edge, at the first cycle and after 10,000 cycles.

### 3.4.4.b. Vertical stress

Figure 3.4-14 shows the maximum vertical stress applied on the subgrade surface and its evolution with cycles. The graph (Figure 3.4-14) shows that the unreinforced platform's first applied stress is 300 kPa while for all the reinforced platforms first applied stress is around 200 kPa. Moreover when the cycles increase, the reinforced platforms stress increases. However, after 10,000 cycles for Test 5 & 9 & (GSY 1 placed at the interface and at the middle depth) the maximum stress is still smaller than the unreinforced platform developed stress  $250 < 300$  kPa. The GSY 3 (Test 7) curve shows the most important stress evolution especially after 2,000 cycles. In fact, the curves show different stress evolution rates depending on the reinforcement type.

It is clear in the graph (Figure 3.4-14) that the reinforcement decreases the stress magnitude applied on the subgrade surface. This stress reduction can be due to the base course stress distribution angle or to the tension membrane resultant and developed with the reinforcement.

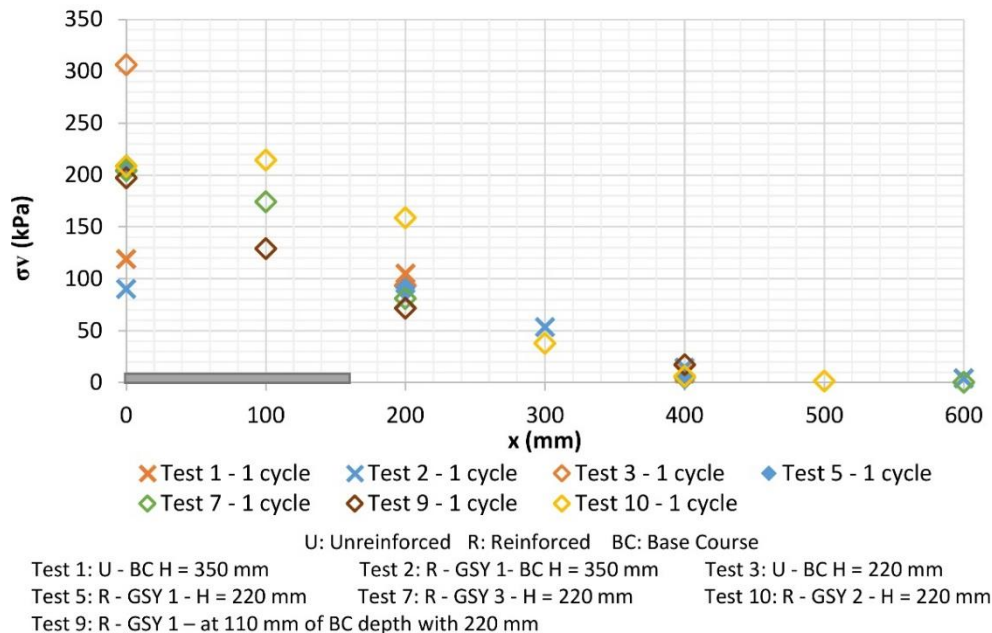


U: Unreinforced R: Reinforced BC: Base Course  
 Test 3 : U Test 9: R - GSY 1 – BC middle depth  
 Test 5: R - GSY 1 Test 10: R - GSY 2  
 Test 7: R – GSY 3

Figure 3.4-14: Subgrade surface central vertical stress evolution with cycles.

Figure 3.4-15 shows the vertical stress distribution on the subgrade surface for the first loading. The curves show that in all the tests the stress magnitude reaches zero at 400 mm from the plate centre, which was shown before by the subgrade settlement curves (Figure 3.4-13).

Figure 3.4-13 shows that the stress distribution curve shape changes depending on the case. In Fact, the unreinforced platform (Test 3) shows a high stress concentration at the centre with a maximum stress of 300 kPa and 100 kPa at 200 mm from the centre of the first cycle, and this distribution stayed constant during all the cycles (Figure 3.4-16).



U: Unreinforced R: Reinforced BC: Base Course  
 Test 1: U - BC H = 350 mm Test 2: R - GSY 1- BC H = 350 mm Test 3: U - BC H = 220 mm  
 Test 5: R - GSY 1 - H = 220 mm Test 7: R - GSY 3 - H = 220 mm Test 10: R - GSY 2 - H = 220 mm  
 Test 9: R - GSY 1 – at 110 mm of BC depth with 220 mm

Figure 3.4-15: Vertical stress distribution at the subgrade surface after 1 cycle.

Figure 3.4-15 shows the reinforcement insures a stress distribution on a larger area (GSY 3 - Test 7) or just decreases the stress intensity due to the tension membrane effect (GSY 1 - Test 9). However, this observation is not accurate because of the sensor's rotation.



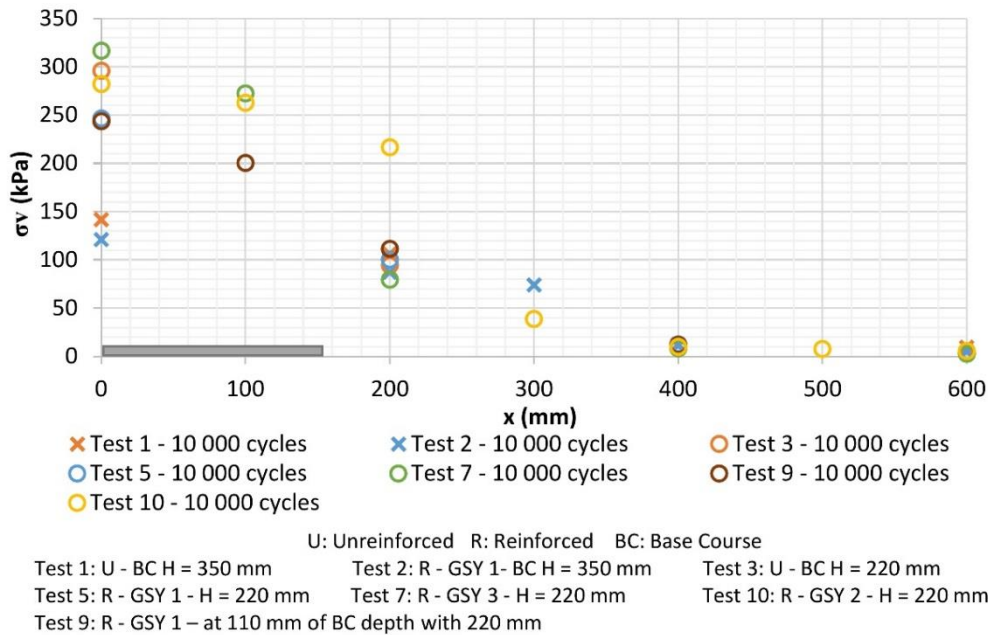


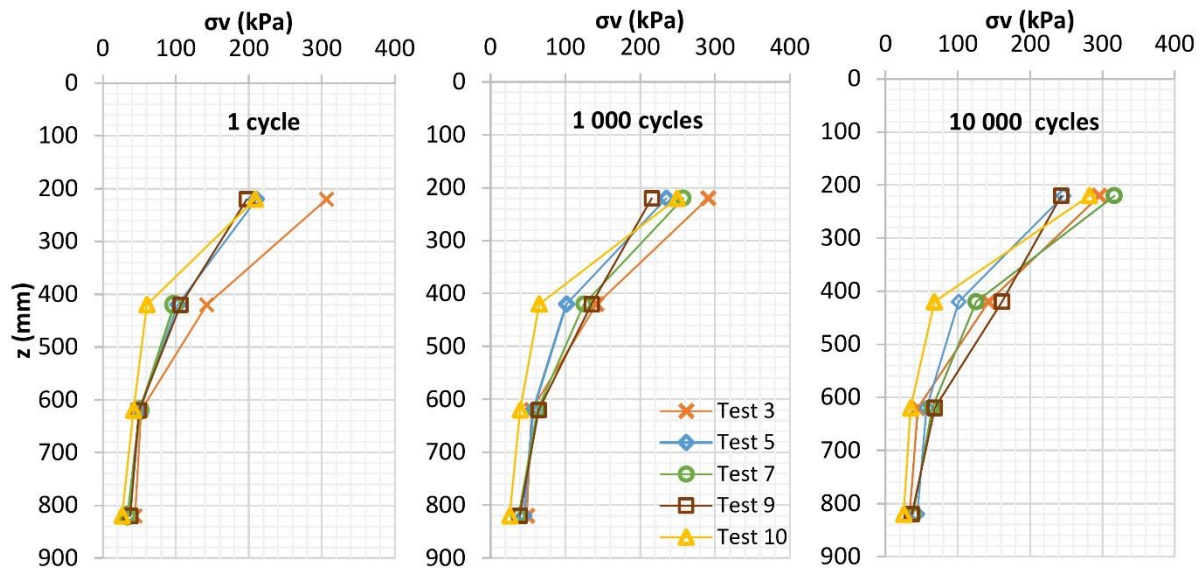
Figure 3.4-16: Vertical stress distribution at the subgrade surface after 10,000 cycles.

With the cycles, the stress of the reinforced platforms evolves, and this is clear in Figure 3.4-16. In fact, not only the central vertical stresses increase with the cycles but also the stresses at 100 mm from the plate centre. However, the stresses at a distance of 200 mm from the plate centre showed no evolution over the cycles and this can be due to the uncertainties related to the sensor's rotation with the cycles.

Figure 3.4-17 shows the stress distribution in depth under the plate centre line. The first cycle stress distribution confirms the fact that all the reinforced platforms start from the same point even at 200 mm of the subgrade depth, while the unreinforced platform presents a stress concentration under the plate centre. With the cycles, the stress at 200 mm of depth increases too, after 1,000 cycles and 10,000 cycles. Tests 7 & 9 (GSY 3 and GSY 1 at the BC middle depth) show vertical stress close to the unreinforced platform in depth while Tests 5 and 10 (GSY 1 and GSY 2) keeps the same stress value of 100 kPa.

More importantly, it can be seen in the graph (Figure 3.4-17) that at 400 mm of the subgrade depth the reinforcement effect decreases significantly and that at 600 mm of the subgrade depth the stress reaches to zero.

The stress analysis shows that the reinforcement decreases the vertical stress applied on the subgrade surface significantly. It shows that the stress evolves over the cycles and the evolution changes depending on the type of the reinforcement.



U: Unreinforced R: Reinforced BC: Base Course

Test 3: U - BC H = 220 mm      Test 5: R - GSY 1 - H = 220 mm      Test 7: R - GSY 3 - H = 220 mm  
 Test 10: R - GSY 2 - H = 220 mm      Test 9: R - GSY 1 – at 110 mm of BC depth with 220 mm

Figure 3.4-17: Vertical stress in subgrade depth evolution with cycles at the plate centre, (for H=220 mm).

In order to relate the stress analysis to the displacement, the graph in Figure 3.4-18 was plotted. In fact, Figure 3.4-18 shows the stress evolution with the settlement at the subgrade surface central point.

The unreinforced platform (Test 3) demonstrates a high settlement at the first cycles with the highest stress magnitude of 300 kPa, and over the cycles, the settlement increases at an important rate due to the subgrade damage under the cyclic load.

The GSY 1 reinforcement (Test 5) shows reduced settlement with a reduced stress regarding the unreinforced one, and with a reduced settlement rate evolution with the cycles.

The GSY 1 (Test 9) placed at the BC middle depth position showed an important settlement evolution especially in the first 100 cycles, which is not coherent with the stress values; it could be related to some installation uncertainties. However, its settlement rate evaluation with the cycles is more important than the GSY 1 placed at the interface case, this can be due to the loss of subgrade confinement that the GSY 1 in tension can provide when placed at the interface.

The GSY 3 (Test 7) showed a reduced stress and settlement in the first cycles, but with the following cycles, the stress evolved significantly provoking an important settlement increase.

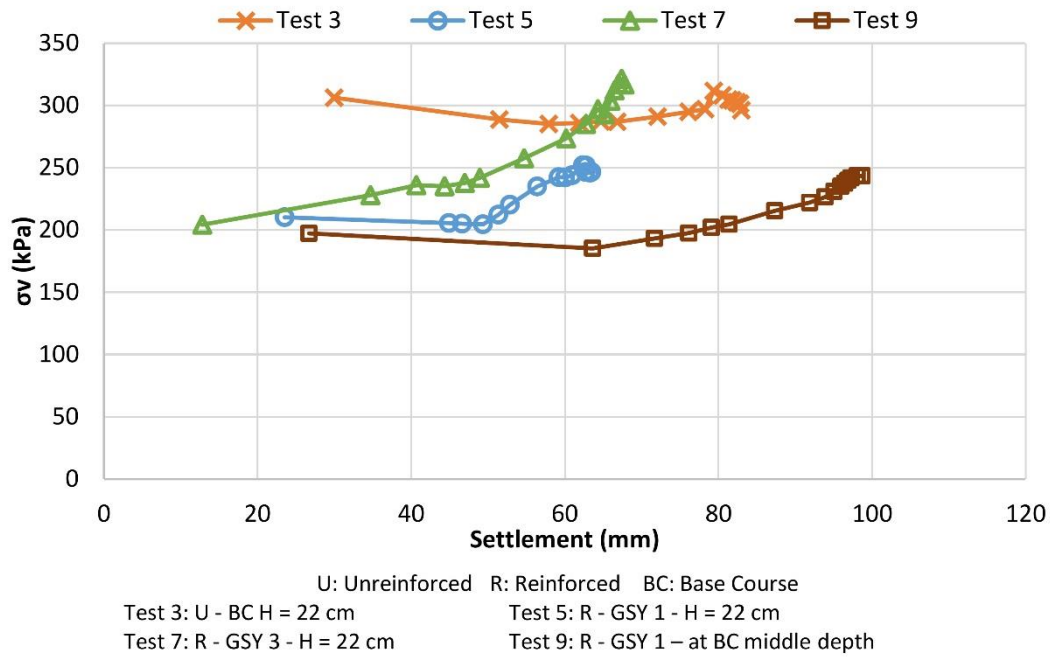


Figure 3.4-18: Subgrade surface central vertical stress evolution with settlement.

### 3.4.4.c. TBR comparison

In order to highlight the reinforcements, Traffic Benefit Ratio (TBR) was calculated, at 45 mm, 60 mm and 75 mm of surface rutting:

$$TBR = \frac{N_{reinforced}}{N_{unreinforced}} \quad \text{Eq.3.4-1}$$

$N_{reinforced}$  is equal to the load cycles' number of the reinforced base at a certain permanent deformation and  $N_{unreinforced}$  is equal to the load cycle's number of load cycles for the unreinforced base at the same permanent deformation.

Table 3.4-1 presents the load cycles' number of load cycles for the three different settlement values of the reinforced and the unreinforced platforms for the base course thickness of 220 mm, as for the TBR values they were presented in Table 3.4-2.

In fact, the base course settlement reaches 45 mm after 50 cycles of the unreinforced platform, while this settlement's value is reached after 75 cycles of the reinforced platform with GSY 3, 200 cycles with GSY 2, 100 cycles with GSY 1 placed at the interface and 50 cycles with GSY 1 placed at the base course middle depth. In order to verify these values kindly refer to Figure 3.4-8.

The highest the TBR is, the more efficient the GSY is. The GSY 2 followed by the GSY 1 placed at the interface gives the highest TBR. In fact, the TBR of 75 mm with the GSY 1 is 24.28 and with the GSY 2 is higher than 30. The coated knitted geogrid improved the platform's bearing capacity compared to the other used geogrids, and the reinforcement efficiency increased with the increasing of the stiffness from 1,000 kN/m at 2% of strain to 2,500 kN/m.

The extruded geogrid with the triaxle apertures showed a significant improvement at the first cycles, but with the settlement increasing, its efficiency was reduced. However, it is the geogrid GSY 1

placed at the base course that showed the smaller TBR values, because of the large displacement that occurred at the first cycles, which can be related to the installation and compaction uncertainties.

Table 3.4-1: Reinforced and unreinforced cycles number needed to reach the base course settlement of 45 mm, 60 mm, and 75 mm.

Base course Settlement (mm)	N GSY 1 Interface	N GSY 1 at BC middle depth	N GSY 2	N GSY 3	N Unreinforced
45	100	50	200	75	50
60	750	75	3,000	300	100
75	8,500	200	>10,000	1,500	350

Table 3.4-2: Reinforced TBR =  $N_{reinforced}/N_{unreinforced}$  for 45 mm, 60 mm, and 75 mm of the base course surface settlement.

Base course Settlement (mm)	TBR GSY 1 Interface	TBR GSY 1 at BC middle depth	TBR GSY 2	TBR GSY 3
45	2	1	4	1.5
60	7.5	0.75	30	3
75	24.2857	0.571429	>30	4.2857143

### 3.4.5. GSY strain

Optical fibre sensors were placed inside the geogrids. Due to the OFDR technology, the continuous strain developed in the GSY was measured even during the cycles. Measurements were taken even after the base course installation.

#### 3.4.5.a. After the base course installation

Figure 3.4-19 illustrates the developed strain in the GSY 1 during the base course installation. It shows that the developed strain is between 1,500 and 2,000  $\mu\epsilon$ . From the strain, the tension developed in the GSY is calculated knowing that the product stiffness is equal to 1,000 kN/m. The developed tension is around 1.5 kN/m, which represents 1.5% of the product ultimate tensile strength.

Figure 3.4-20 illustrates the developed strain in the geogrid GSY 2 during the installation; it shows it at different transversal positions in the box. The geogrid GSY 2 is more mobilised than the GSY 1, in fact, the developed strain in the GSY 2 during the base course installation is more important. It shows as well that the developed strain is between 2,500 and 3,000  $\mu\epsilon$ . From the strain, the tension developed in the GSY 2 is calculated knowing that the product stiffness is equal to 2,500 kN/m. The developed tension is around 7.5 kN/m, which is 3.75% of the product ultimate tensile strength.

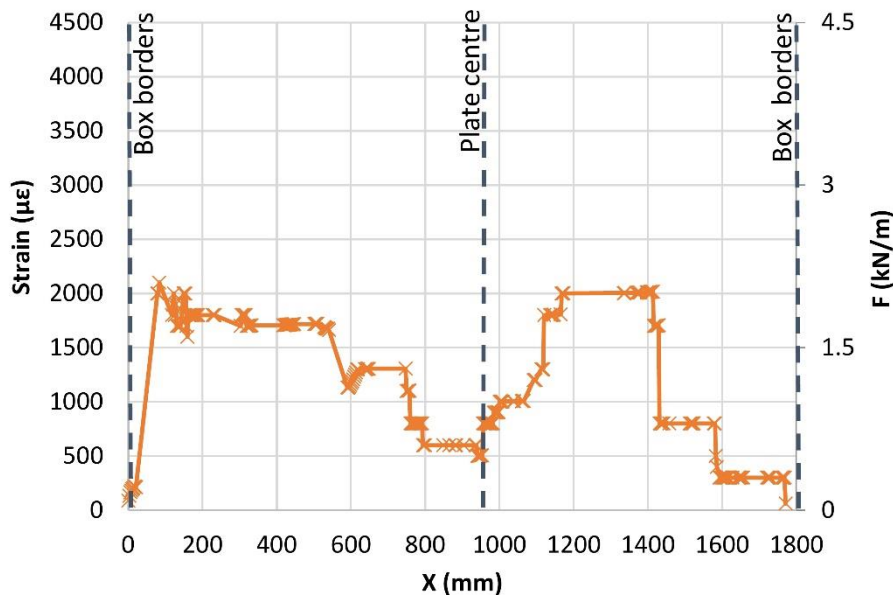


Figure 3.4-19: GSY 1 strain and equivalent force developed after the base course gravel installation.

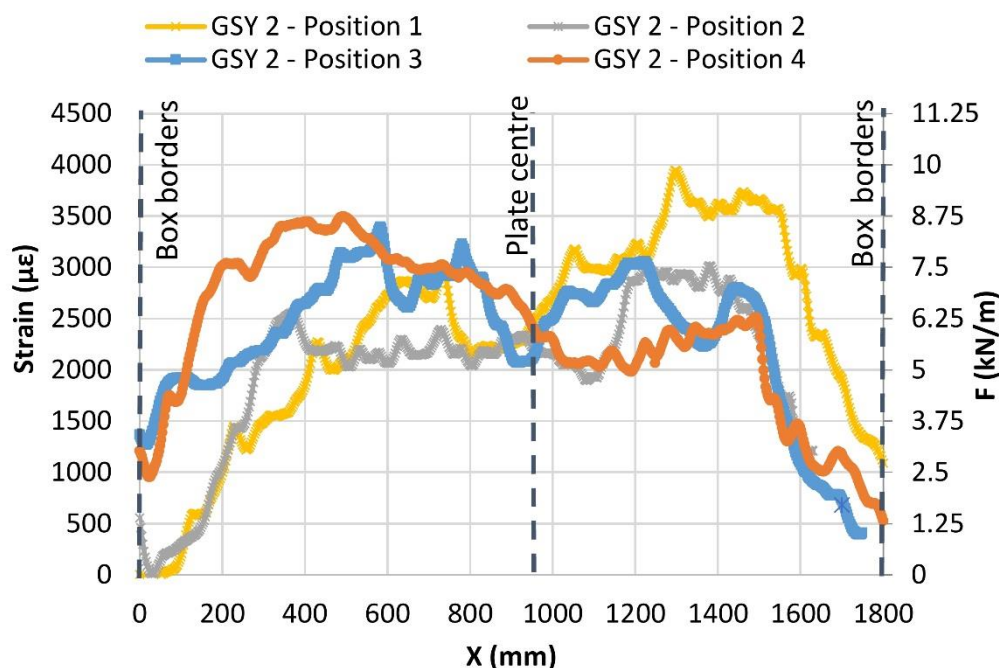


Figure 3.4-20: GSY 2 strain the equivalent force developed after the base course gravel installation in four different positions.

### 3.4.5.b. During the loading

After the base course installation, the strains were set at zero in order to measure the strain during the loading.

Figure 3.4-21 shows the developed strain in GSY 1 during the first loading. The maximum strain reached at the centre during the first loading is equal to 12,000  $\mu\epsilon$ . As mentioned before, knowing the GSY 1 stiffness, the developed force can be calculated, and it is equal to 12 kN/m (which represents 12% of the GSY maximum tensile strength).

Figure 3.4-22 shows the maximum developed strain at the first loading of the GSY 2, which is related to a tensile force of 23 kN/m (which represents 10% of the GSY maximum tensile strength). The

signal of the optical fibre was lost after the first loading; therefore, no further results were presented for the GSY 2.

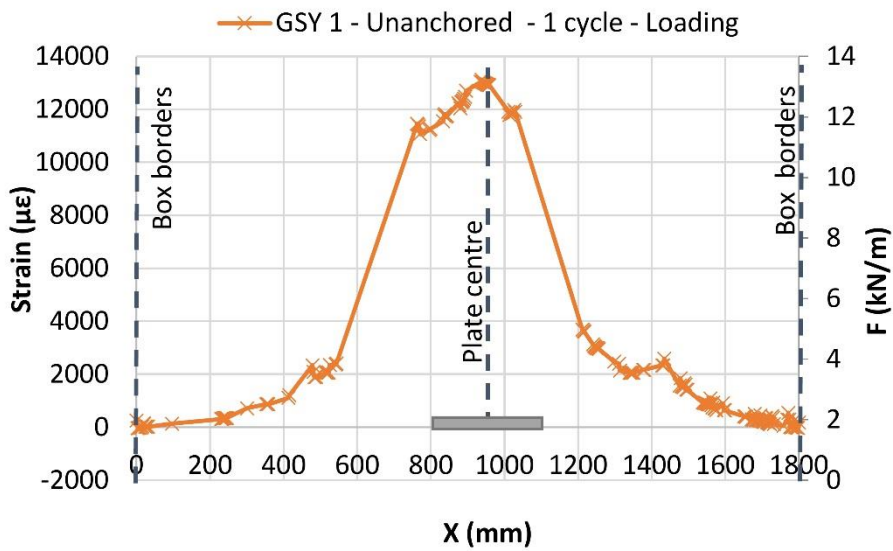


Figure 3.4-21: GSY 1 unanchored strain and equivalent force developed at the first loading cycle.

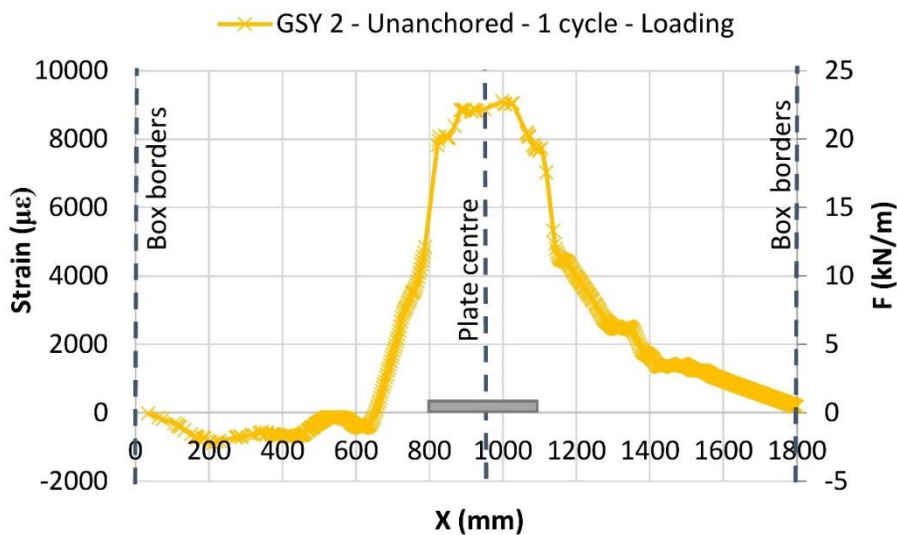


Figure 3.4-22: GSY 2 unanchored strain and equivalent force developed at the first loading cycle.

During all the tests the geogrid borders were placed between two wood plates without any additional anchorage system, this configuration is called later on in the text, an unanchored geogrid. Figure 3.4-21 and Figure 3.4-22 show the strain of unanchored geogrid. However, it is clear in both curves that the strain in the geogrid decreases respectively when moving away of the plate centre until it reaches zero near the box's borders. This proves that the distance from the plate centre to the box's borders is far from the geogrid solicitation area and that the geogrid anchor provided by the aggregates is enough.

In order, to look more closely at the anchorage's effect on the reinforcement mechanism, two different tests were performed with unanchored and anchored GSY1. Anchored means lifted around the box's borders, so the anchorage is provided by the aggregates weight on the borders.

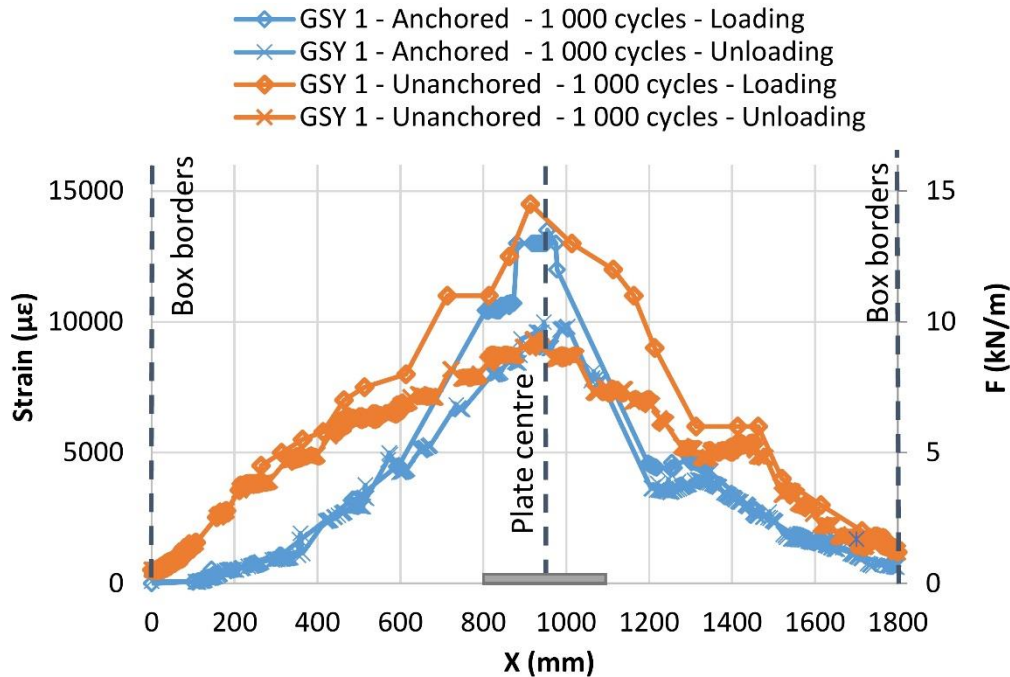


Figure 3.4-23: GSY 1 unanchored and anchored strain and equivalent force developed after 1,000 cycles at the loading and unloading stage.

Figure 3.4-23 shows the developed strain in the anchored and unanchored GSY 1 after 1,000 cycles during the loading and unloading phases. The curves show different shapes: the unanchored geogrid presents a larger strain curve, but this shape did not affect the maximum strain values developed in the GSY. However, both curve strains decrease respectively until reaching a negligible value near the borders. Moreover, both GSYs presented a maximum strain of 14,000  $\mu\epsilon$  during the loading and 10,000  $\mu\epsilon$  during the unloading phase. These showed that GSY anchorage has no effect on the results.

Moreover, Figure 3.4-23 shows the elastic and the plastic strain developed in the GSY during the loading and unloading phases. In fact, the plastic strain is about 60% of the total strain developed during the loading. Moreover, regarding the force developed in the GSY during the loading, it is equal to 15% of the ultimate tension strength. The maximum strain developed during the first applied load is about 9,000  $\mu\epsilon$  (Figure 3.4-21) and it increases after 1,000 cycles to reach 14,000  $\mu\epsilon$  (Figure 3.4-23).

In addition, at a distance of 200 mm from the box's edge, the strain due to the loading is null. This shows that there is no anchorage effect on the results and on the GSY behaviour and that the developed tension in the GSY is taken by the interaction with the base course layer before it reaches the box's edges.

### 3.5. Aggregates damage

The cycle effect on the aggregates was studied too. In fact, the virgin aggregate was already classified and characterized in Chapter 2. Gravel specimens were taken from the platform centre after it was subjected to 10,000 cycles, more precisely after Test 9.

Figure 3.5-1 shows the particle size distribution of the virgin and damaged aggregates. In fact, it is clear that the particles were smashed under the cycles. The particle's size distribution curve changed significantly after 10,000 cycles.

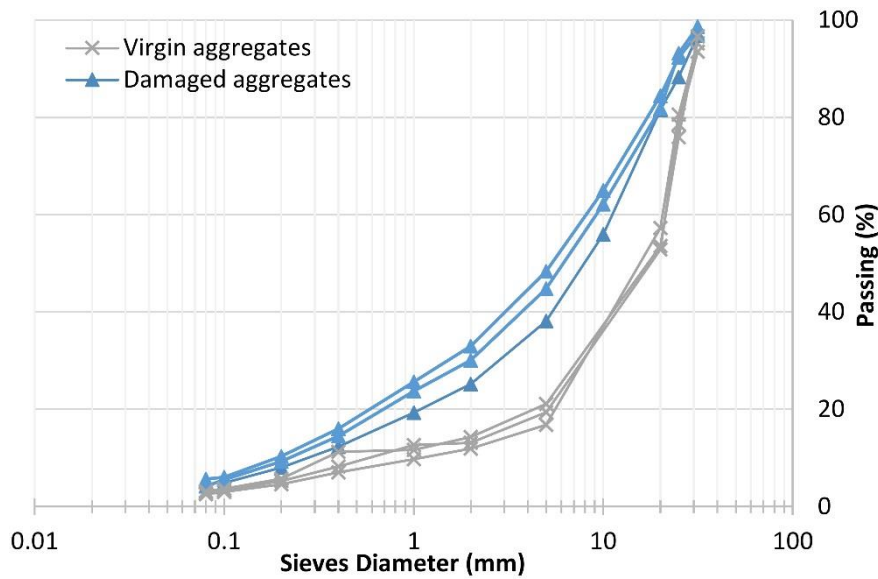


Figure 3.5-1: Particles size distribution of the virgin and damaged aggregates.

Table 3.5-1: The Virgin and damaged aggregates classification.

Virgin aggregates	Damaged aggregates
$D_{10} = 1 \text{ mm}$	$D_{10} = 0.2 \text{ mm}$
$D_{30} = 7 \text{ mm}$	$D_{30} = 2 \text{ mm}$
$D_{60} = 11 \text{ mm}$	$D_{60} = 10 \text{ mm}$
Particles with diameter $< 80 \mu\text{m} = 4\%$	Particles with diameter $< 80 \mu\text{m} = 4\%$
$Cu = \frac{D_{60}}{D_{10}} = 11$	$Cu = 50$
$Cc = \frac{D_{30}^2}{D_{10} \times D_{60}} = 4.45$	$Cc = 2$
<b>GP (LPC &amp; USCS standards)</b>	<b>GW (LPC &amp; USCS standards)</b>

The virgin and damaged classification factors are detailed in Table 3.5-1. The gravel passes from a poorly graded gravel to a well graded gravel according to the LPC and USCS standards.

In fact,  $D_{10}$  passes from 1 mm to 0.2 mm, and  $D_{30}$  passes from 7 mm to 2 mm.

Moreover, the damaged aggregates were characterized by the large shear box used in Chapter 3 to characterize the virgin aggregates. Figure 3.6-1 shows the shear stress evolution with the horizontal displacement for the virgin and damaged aggregates. The damaged aggregates show a reduction in the maximum shear stress at high normal stress of 200 kPa, it passes from 160 kPa to 140 kPa. In addition, the curves show that the plastic state starts earlier for the damaged aggregates and with a more curved beginning for the three different normal stresses.



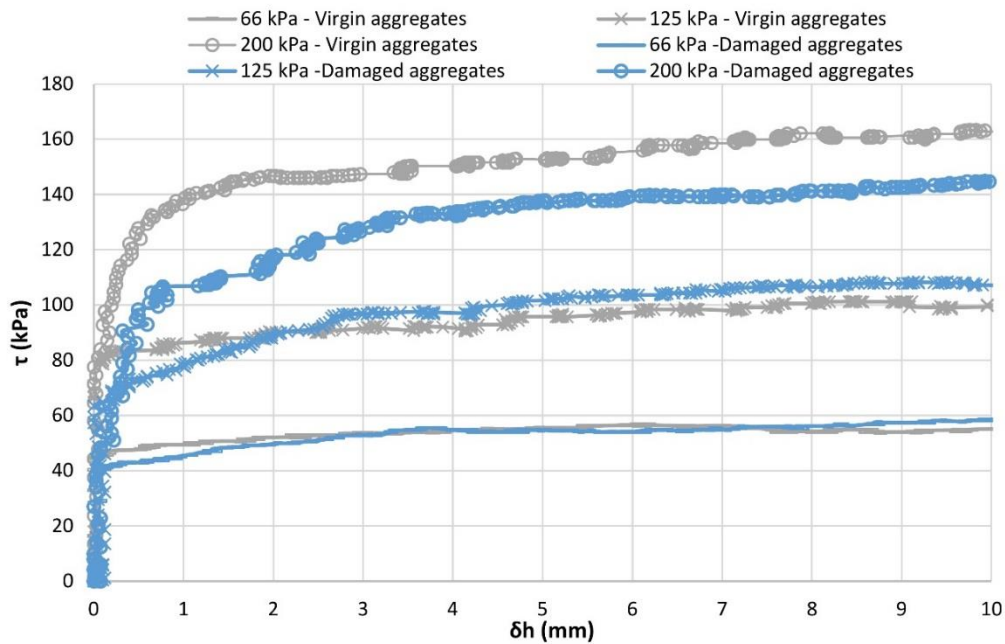


Figure 3.5-2: Shear stress versus horizontal displacement at different normal stresses for the virgin and damaged aggregates.

### 3.6. GSY damages

The geogrids were subjected to harsh installation conditions. It is true that the compaction machines are not heavy as the machines used on site, but the compaction was performed over 110 mm of base course thickness covering the geogrid, which is not recommended normally by the manufacturer to avoid the geogrid damage during installation.

Tensile tests were performed on virgin GSY 1 specimens, and later on, on the GSY 1 damaged specimens. Specimens were taken from the centre under the plate load and from the edges far from the load application. The aim was to separate between the damage only due to the installation and the damage due to the installation and the cycles.

Figure 3.6-1 shows the tensile curve of the virgin GSY 1, the central and the edged damaged specimens. The results show no differences between the edged and central specimens' tensile curves, which means that the installation damage is more important to the geogrid than to the 10,000 tensile cycles performed. In fact, the used gravel is an angular gravel that can create notches in the geogrid when it is poured over it and compacted.

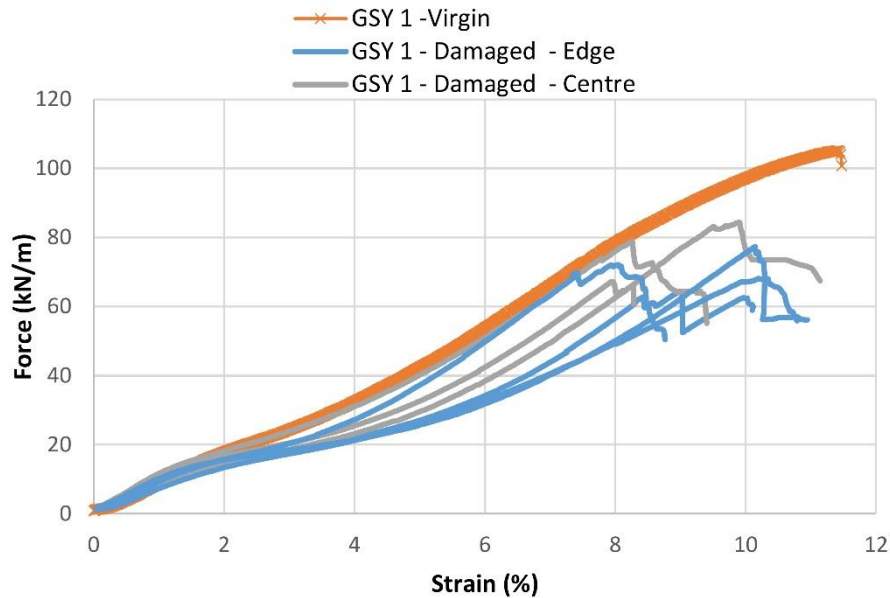


Figure 3.6-1: GSY 1 tensile curves for virgin specimen and damaged specimens under the plate load and at the box edges.

The curves (Figure 3.6-1) show a significant maximum tensile strength reduction from 100 kN/m to 70kN/m and 80 kN/m, which is about 20% and 30% of reduction.

More importantly, the geogrid stiffness presents a reduction too, but this reduction was not regular for all the specimens, it depends on the specimen's damage level. The stiffness at 2% of strain shows a reduction as well, from 1,000 kN/m to 650 kN/m for the most damaged specimens.

Unfortunately, the extruded GSY 3 geogrid could not be tested under one direction tensile test. In fact, this material with triangular aperture is tested under radial tensile test and the radial stiffness of this product is given.

### 3.7. Empirical and analytical design methods

The design methods proposed in literature allow the aggregate thickness determination based on the rutting development, the cycle number, the subgrade and base course stiffness and the GSY reinforcement contribution.

Hammitt and Iii (1970) proposed the following empirical formula for unreinforced unpaved road with rutting criteria of 75mm:

$$h_{os} = (0.0236 \log N + 0.0161) \sqrt{\frac{P}{CBR} - 17.8A} \quad \text{Eq. 3.7-1}$$

Where P is the wheel load (kN), and A the contact area (m<sup>2</sup>).

Giroud and Noiray (1981) proposed another empirical formula for unreinforced unpaved road with rutting criteria (r) other than 75 mm:

$$h_{os} = \frac{(0.190 \log N + 0.445(r - 0.075))}{CBR^{0.63}} \quad \text{Eq. 3.7-2}$$

Where,  $H$  and  $r$  are in meter;  $N$  = to the number of passages of the standard axle load 80 kN. This method is not recommended for  $N$  higher than 10,000 cycles or less than 20 cycles.

These empirical and analytical methods were used to design such structure in the case of an unreinforced platform. For the empirical method (Hammit and Iii, 1970), the  $CBR_{sg}$  calculated was equal to 2%, the platform was designed to support 10,000 load passes of 40 kN, noting that the rutting criteria in this method is 75 mm. The same parameters were used for the empirical method of Giroud and Noiray (1981), while the calculated  $N$  was taken equal to 10,000 cycles.

More recently, the analytical methods were developed to determine the aggregate thickness for reinforced unpaved roads on soft subgrade. Giroud and Han (2004) proposed the following equation:

$$h = \frac{(0.868 + (0.661 - 1.006 J_{ASM}^2)) \cdot \left(\frac{r}{h}\right)^{1.5} \cdot \log N}{1 - 0.204 \cdot (R_E - 1)} \cdot \left( \sqrt{\frac{\frac{P}{\pi r^2}}{\left(\frac{s}{f_s}\right) \left(1 - 0.9e^{-\left(\frac{r}{h}\right)^2}\right) \cdot N_c \cdot C_u}} - 1 \right) \cdot r \quad \text{Eq. 3.7-3}$$

For more details regarding this analytical method kindly refer to Chapter 1.

Also for unreinforced cases, the analytical method of Giroud and Han (2004) was used with the following parameters:  $N_c = 3.14$ ;  $CBR_{sg} = 2\%$ ;  $CBR_{bc} = 12\%$ ;  $P = 40$  kN;  $\pi = 560$  kPa;  $N = 10,000$  cycles;  $J_{ASM} = 0$  m.N<sup>o</sup>;  $s = 75$  mm;  $f_s = 75$  mm.

For this method the subgrade soil is assumed to be saturated and to have a low permeability, therefore its bearing capacity is equal  $m \cdot N_c \cdot C_u$ , where  $C_u$  is equal to  $30 CBR_{sg}$ , which is equal to 60 kPa in that case. The bearing capacity mobilization coefficient was determined based on the following equation:

$$m = \left(\frac{s}{f_s}\right) \cdot \left(1 - 0.9e^{-\left(\frac{r}{h}\right)^2}\right) \quad \text{Eq. 3.7-4}$$

With an assumed  $h$  of 390 mm the calculated  $m$  value is equal to 0.225 using Eq. 3.7-4.

This design method proposed a calculated  $h$  of 390 mm in the unreinforced case.

The same conditions were taken for the reinforced case using GSY 3, with a  $N_c = 5.71$  because it is a reinforced case using a geogrid, and  $J_{ASM} = 0.61$  m.N<sup>o</sup>.

For an assumed  $h$  of 100 mm the calculated  $m$  value is equal to 0.9456 using Eq. 3.7-4.

This design method proposed a calculated  $h$  of 100 mm in the reinforced case using GSY 3 the extruded geogrid.

This given analytical method could not be used to estimate the base course thickness in the reinforced case using GSY 1 and 2 since they are not characterised by a node stability factor.

Leng and Gabr (2006) developed the following analytical solution to calculate the aggregate thickness:

$$h = \frac{(1 + \left(\frac{r}{h}\right)^{0.81} (0.58 - 0.000046 J_t^{4.5})) \cdot \log N}{\tan \alpha_1} \cdot \left( \sqrt{\frac{p_c}{\left(\frac{s}{f_s}\right) \cdot (1 - e^{(-0.78 \frac{r}{h})}) \cdot N_c \cdot C_u}} - 1 \right) \cdot a \quad \text{Eq. 3.7-5}$$

In addition, the analytical method of Leng and Gabr (2006) was used with the same parameters as the above in Giroud and Han's (2004) method, only  $N_c$  is equal to 3.8 in the unreinforced case, and  $J_t$  which is the average geogrid tensile strength at 2% of strain is equal to 0 kN/m.

As in the previous method, the bearing capacity is equal to  $m \cdot N_c \cdot C_u$ , where  $C_u$  is equal to 30  $\text{CBR}_{\text{sg}}$ , which is equal to 60 kPa in that case. The bearing capacity mobilization coefficient was determined based on the following equation:

$$m = \left(\frac{s}{f_s}\right) \cdot \left(1 - 0.9 e^{(-0.78 \frac{r}{h})}\right) \quad \text{Eq. 3.7-6}$$

With an assumed  $h$  of 590 mm the calculated  $m$  value is equal to 0.271 using Eq. 3.7-4 and Eq. 3.7-6.

This design method proposed a calculated  $h$  of 590 mm in the unreinforced case, with a variation of the base course stress distribution angle  $\alpha$ , from  $\alpha_0$  of  $45.37^\circ$  to an  $\alpha_N$  of  $27.55^\circ$  after 10,000 cycles. In the analytical method of Leng and Gabr (2006), the expression involving the geogrid characteristics is negative for  $J_t > 8$  kN/m. Therefore, the comparison of the empirical and analytical methods was done only for the unreinforced conditions.

Table 3.7-1 resumes the design results of the empirical and analytical methods. Moreover, the designed base course thicknesses were compared with the experimental base course thickness equal to 350 mm, since the experimental surface rutting after 10,000 cycles is equal to 44 mm lower than the rutting criteria of 75 mm.

As shown in Table 3.7-1, the empirical methods propose a base course thickness of 460 mm (Hammit and Iii, 1970) and 500 mm (Giroud and Noiray, 1981) without reinforcement, which is higher than the experimental base course thickness for about 30%.

The highest required thickness is given by Leng and Gabr (2006) and it gives an overestimation of the thickness of about 40%, regarding the proposed experimental base course thickness. It is evident that the procedure proposed by Leng and Gabr (2006) is more conservative in comparison with the procedure of Giroud and Han (2004). In fact, the design dimension proposed by Giroud and Han (2004) is the lowest value and the closest one to the experimental proposed thickness. However, these conclusions are limited to the unreinforced platforms and to the experimental conditions applied throughout this study.

Moreover, the reinforced thickness determined by Giroud and Han (2004) using the reinforcement extruded geogrid GSY 3 is equal to 100 mm which is the minimum required thickness. Experimentally a 220 mm base course thickness was used with the GSY 3 and the design criteria of 75 mm was reached after 350 cycles. However, these design methods were calibrated under specific conditions and the subgrade soil is assumed to be saturated which is not the case in these experiments. Therefore, these comparisons and conclusions are limited to the experimental conditions and so more investigations are needed.

Table 3.7-1: Designed base course thicknesses estimation in the unreinforced case

The design methods	Designed base course thickness for the unreinforced case (mm)	Designed base course thickness for the reinforced case with GSY 3 (mm)	Experimental base course thickness (mm)
Hammit and Iii (1970)	460	---	< 350
Giroud and Noiray (1981)	500	---	
Giroud and Han (2004)	390	100	
Leng and Gabr (2006)	590	--	

### 3.8. Conclusions

In this Chapter the plate load tests results were presented and detailed. An installation and compaction protocol was developed in order to prepare the tested platforms and insure its constitution repeatability and homogeneity. The quality control tests were used first to define and fix the installation protocol and then to control the installed soil properties for each prepared platform. The subgrade soil water content was controlled before and after the performed tests, and it showed that the soil water content remains constant during the test and between each test. The shear vane test, and the static and dynamic penetrometer tests results were presented. These results showed the efficiency of this protocol. In fact, identical platforms with the same properties could be prepared for each test, and these soil layers showed homogeneous properties over the depth and the area. The test repeatability was checked by the performance of two identical tests on three different configurations: Unreinforced platforms and reinforced platforms with GSY 1 and GSY 3. The results proved the test repeatability in terms of settlement and stress distribution.

The reinforced and unreinforced tests performed on a base course thickness of 350 mm platforms showed that the reinforcement has a negligible effect on the platform behaviour. In addition, the results showed that an unreinforced platform with 350 mm of base course thickness is a well designed platform, and does not exceed the maximum allowable rut depth of 75 mm after 10,000 cycles. In order to characterize the reinforcement effects, the base course thickness was reduced in the following tests to 220 mm.

The results showed the different geogrid types and configurations efficiency in improving the platform bearing capacity and its durability:

- Regarding the base course surface settlement, GSY 2 showed the most important improvement on the platform behaviour. In fact, it reduced the maximum surface settlement after 10,000 cycles of 35%. While, GSY 1 reduced it of 25% and GSY 3 of 12%.
- The knitted geogrids GSY 1 and GSY 2 showed a significant platform improvement especially with the large displacement development (>50 mm) over the cycles when the

geogrids are mobilised. In fact, these geogrid types with a dominant mechanism are the tension membrane effect. Moreover, the most important platform improvement was provided by the stiffer geogrid (GSY 2).

- The extruded geogrid GSY 3, which behaves more as a confinement reinforcement due to its node significant strength, showed the most important platform improvement for the first 2,000 cycles. However, it showed a significant change in its performance after 2,000 cycles when large displacement (>50 mm) occurred.
- The GSY 1 placed at the base course middle depth showed a limited effect on the platform's improvement. Even though the stress on the subgrade presented a reduction, the subgrade showed more settlements than the GSY 1 placed at the interface. This can be due to the loss of the subgrade confinement provided by the GSY 1 in tension and placed at the interface.
- The stress analysis showed that the reinforcement decreases in a significant way the vertical stress applied on the subgrade surface. The central stress developed at the subgrade surface of the reinforced platforms showed there increase with the cycles. The stress evolution depends on the reinforcement type.
- The platform reinforced with the GSY 3 presented the most important stress rise. While GSY 1 and 2 presented a lower stress evolution rate with the cycles.
- After 10,000 cycles, the GSY 1 presents a maximum stress reduction of 16% while GSY 2 presents 10% of reduction, and GSY 3 presents no stress reduction after 10,000 cycles.

These results showed that the extruded geogrid contributed more to the platform's improvement by the lateral restrain mechanism under relatively small displacement in the first cycles. This is due to its special manufacturing type and rigid nodes. While the knitted geogrids showed no such contribution, however, they contributed with the tension membrane effect once mobilized after a certain developed displacement, due to their high stiffness.

The fibre optics placed in the geogrids GSY 1 and GSY 2 showed that after the base course installation the geogrid is subjected to a small strain about 0.3%. Moreover, under the first load,

both the GSY 1 and the GSY 2 were subjected to a total strain of 1%. This strain evolved with the cycles to reach 1.5% after 1,000 cycles. Moreover, 60% of this total strain is made of plastic.

On one hand these experimental results were compared to the empirical and analytical design methods. This showed that these design methods provided in literature overestimate the required base course thickness in the case of an unreinforced platform. On the other hand, Giroud and Han's (2004) method underestimated the base course thickness proposed for the reinforced GSY 3 platform. Moreover, the analytical design method proposed by Leng and Gabr (2006) is more conservative than the method proposed by Giroud and Han (2004) for the unreinforced case. However, these design methods could not be used with this specific GSY 1 and GSY 2 products in order to estimate the reinforced base course thickness.

# Chapter 4. Traffic Load Test

---

## 4.1. Introduction

In Chapter 3, the unpaved platform was subjected to a plate load test under a configuration commonly used in literature to simulate the traffic load in laboratory tests.

In order to better simulate the traffic load the Simulator Accelerator of Traffic (SAT) was developed. This apparatus has a special mechanical concept that allows the same load of magnitude application even after high rut depth (75 mm -100 mm), and at each circulation position. The applied wheel load magnitude was 28 kN resulting in a contact pressure of 650 kPa, used on an effective circulation length of 2 m with a velocity of 4 km/h. Moreover, on the same prepared platform a plate load test was performed too, with a plate shape similar to the wheel contact area and with the same maximum load magnitude of 28 kN. The aim of these two-load solicitation types is to compare between the plate load and the wheel circulation load. The tested platform was placed in a box of 1.8 m in large, 5 m in length and 1.1 m in height. The platform installation compaction and quality control tests were detailed in Chapter 2. The test repeatability was confirmed in Chapter 3 using the plate load test.

An unreinforced platform and a reinforced platform with GSY 2 and GSY 3 (Chapter 2) were tested under these loading conditions. The base course thickness was of 220 mm as in the plate load tests performed in Chapter 3.

Two platform areas were instrumented, the area under the plate load and the area under the circulation load. The instrumentation was detailed previously in Chapter 2. The results are presented in terms of displacement, stress and geogrid developed strain. These experimental large-scale tests allowed the reinforcement effect characterisation and quantification again under the plate load and circulation load. Moreover, the comparison between the circulation load and the plate load results are presented in this Chapter. In addition, the particular plate load tests given in this Chapter were compared to the circular plate load tests presented previously in Chapter 3.

## 4.2. Performed tests

A reference of an unreinforced platform (Test 1) and two reinforced platforms using the extruded triangular aperture geogrid (GSY 3 – Test 2) and the knitted geogrid (GSY 2 – Test 3) were performed.

The base course thickness was controlled like in the previous plate load tests. Moreover, the platform thickness was measured at two positions, under the plate load test and under the circulation load is 240 mm. The measured thickness for Test 1 is 216 mm under the plate load and 229 mm under the circulation load. For Test 2 the measured thickness under the plate load is 231 mm and under the circulation is 240 mm. As for Test 3 it presented 220 mm of base course thickness under the plate load and 240 mm under the circulation load. The measured thickness shows that the thickness variation over the area is between 5 and 10 mm and that the real thickness for this tests is  $220 \pm 20$  mm.

Table 4.2-1: Performed tests details.

Test number	Base course thickness (mm)	Reinforcement	GSY position
Test 1	220	Unreinforced	--
Test 2	220	GSY 3	Interface
Test 3	220	GSY 2	Interface

## 4.3. Quality control tests results

The platform layers installation and compaction protocol was defined and tested in the previous Chapters 2 & 3. The Traffic circulation tests were performed in a larger box of 5 m in length, 1.8 m in large and 1.1 m in height. More soil quantities were prepared to fill this large box (11.4 T of subgrade material and 4.4 T of base course material). The quality control tests were performed to control the soil homogeneity over this large area, and to verify that for each prepared platform the soil's properties remain the same. The quality control tests results are presented in below in this section.



### 4.3.1. Water content

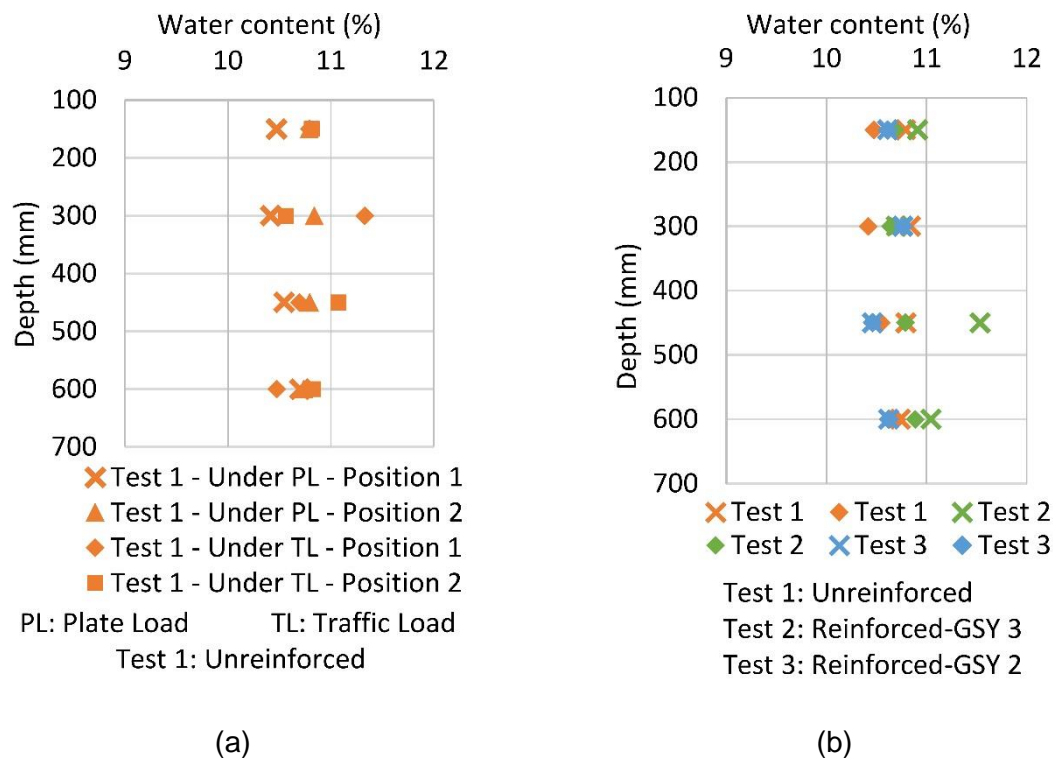


Figure 4.3-1: (a) Water content profile under the plate and Traffic load areas for Test 1, (b) Water content profile for Tests 1, 2 & 3.

More subgrade was made and added to the existing prepared material in order to fill the large box. The target water content is always 11.5%. Figure 4.3-1 (a) shows the water content profile over the depth of the unreinforced test (Test 1) at four different positions: positions 1 and 2 under the plate load area and positions 1 and 2 under the Traffic load area. Figure 4.3-1 (a) shows that the water content is in the same range over the area, between 10.5% and 11%. Moreover, this was demonstrated in Figure 4.3-1 (b) at two different positions of the three prepared platforms. The water content range is slightly under the target water content. This can be due to the fact that the soil was mixed and stocked during the summer. However, this did not affect the soil's properties in CBR terms (Section 4.3.3).

### 4.3.2. Shear vane test

The shear vane test was performed in order to check the prepared subgrade homogeneity over the area and depth. As mentioned before, this test was not performed to determine the undrained soil cohesion ( $C_u$ ), since the prepared soil is an unsaturated soil. The  $S_t$  is the soil's sensibility, which is the ratio between  $\tau_u$  and  $\tau_r$ , and was used in this section as a comparison factor.

In Chapter 3, the  $S_t$  graphs showed homogeneous values between 4 and 6. Figure 4.3-2 (a) shows the  $S_t$  profiles for the prepared unreinforced platform at two different positions under the plate load test area and under the traffic load test area. The graph shows a homogeneity between the profiles over the area and the depth. In fact, the  $S_t$  values are mainly concentrated between 4 and 6. Figure 4.3-2 (b) shows the  $S_t$  profiles at two different positions of the three prepared platforms. It shows

profiles matching between the three prepared platforms, and between the two positions of the same platform. These results present the prepared layers' homogeneity and repeatability even over a larger prepared area.

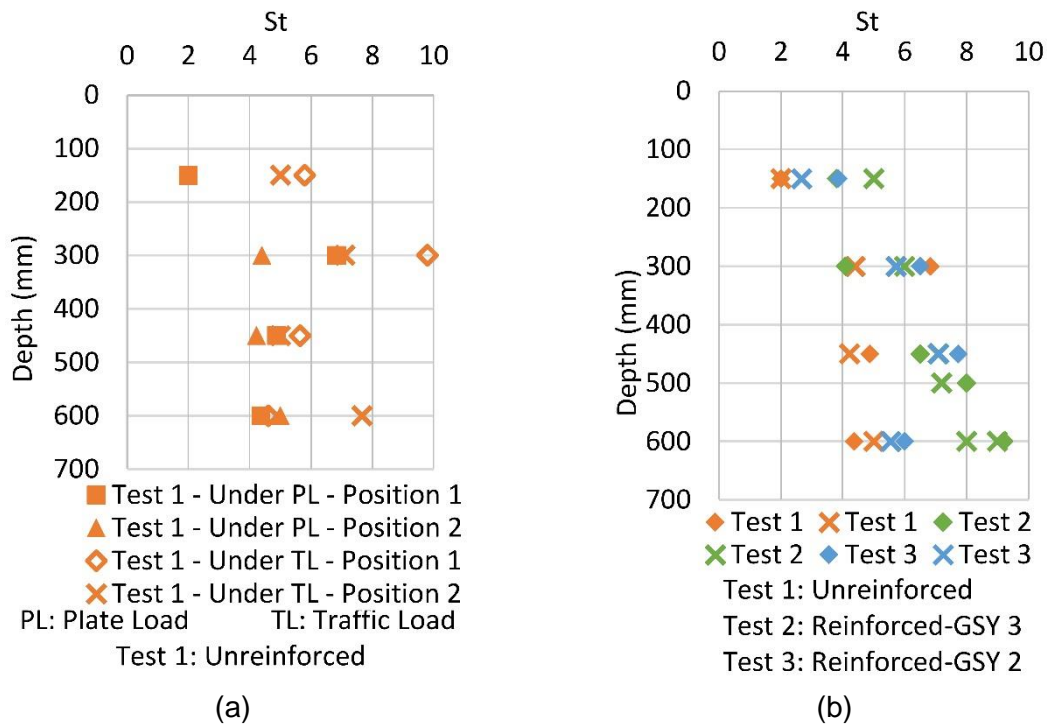


Figure 4.3-2: (a)  $S_t$  profile under the plate and Traffic load areas for Test 1, (b)  $S_t$  profile for Tests 1, 2 & 3.

### 4.3.3. Static penetrometer test

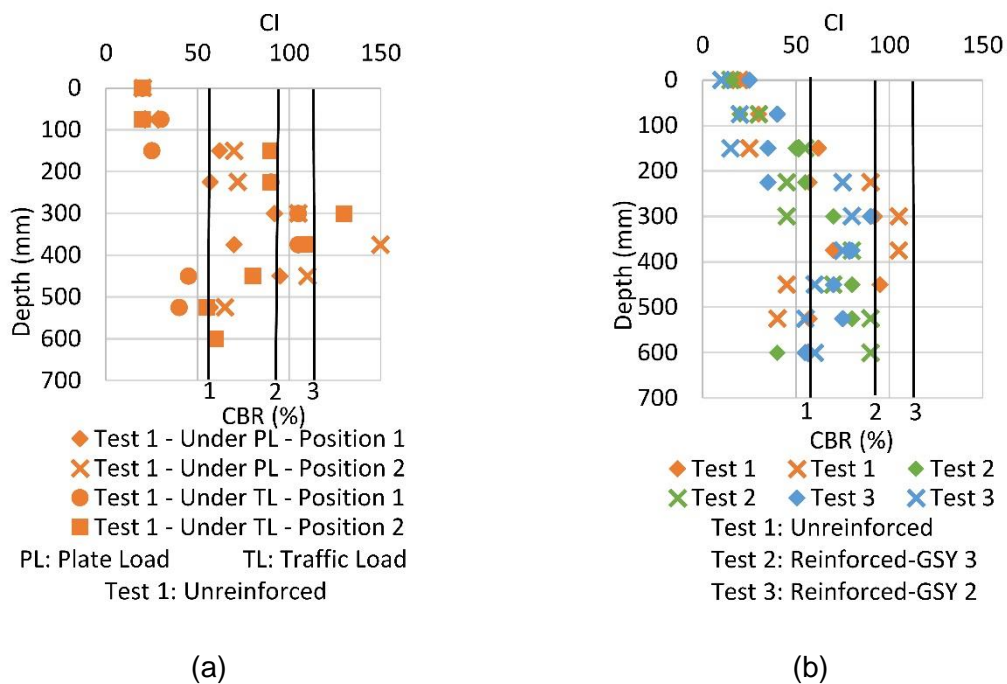


Figure 4.3-3: CI/CBR (%) profile under the plate and Traffic load areas for Test 1, (b) CI/CBR (%) profile for Tests 1, 2 & 3.

The static penetrometer test was performed in the subgrade, its results in term of cone index were correlated to CBR percentage, based on the apparatus manufactural proposed correlation. Figure 4.3-2 (a) presents the CI/CBR profiles over the depth at four different positions under the plate and Traffic load areas. It shows the CBR values concentration that varies between 1% and 2% in depth. The same is observed for the three prepared subgrades (Figure 4.3-2 (b)). At the subgrade's surface, null CBR values are observed. In fact, the first subgrades of 100 mm were not compacted because they will be subjected to the base course compaction.

#### 4.3.4. Dynamic penetrometer test

Moreover, the dynamic cone penetrometer was performed in the subgrade and in the base course layer. The results were correlated to the CBR percentage as well, based on a correlation formula given by the manufactural, and detailed in Chapter 2.

Figure 4.3-4 (a) shows the dynamic penetrometer results in CBR terms over the subgrade depth for the prepared unreinforced platform. The graph shows CBR values between 1% and 2%, which is seen too in Figure 4.3-4 (b) after the base course installation.

The base course CBR is around 10%, and at some point, it surpasses the 10%. At the surface, the CBR shows low values because of the soil repulsion. More in depth the subgrade CBR is around 2%.

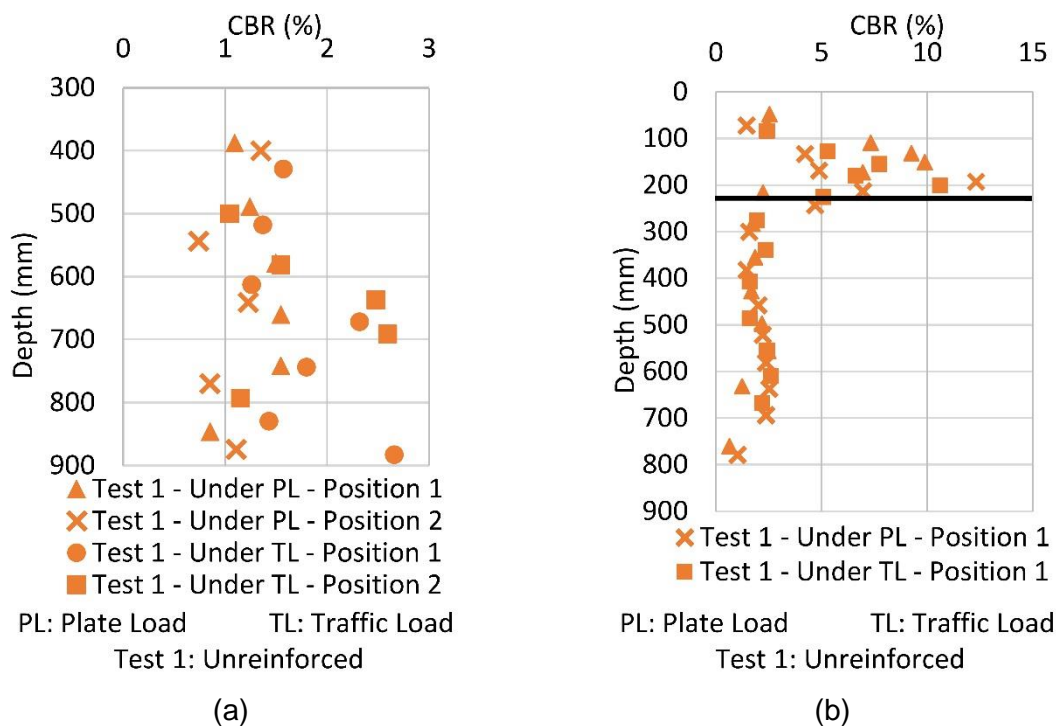


Figure 4.3-4: (a) CBR (%) profile under the plate and Traffic load areas for Test 1 before the base course installation, (b) CBR (%) profile under the plate and Traffic load areas for Test 1 after the base course installation.

Figure 4.3-5 (a) shows the subgrade CBR point cloud for the three prepared platforms. It shows a concentration between 1 and 2%. Figure 4.3-5 (b) shows the base course and subgrade CBR point cloud for the three prepared platforms. It shows a base course CBR concentration of around 10% and 12% close to the CBR seen in the platforms prepared for the plate load tests prepared in Chapter 3. In addition, as seen above at the base course surface the CBR is low because of the soil repulsion.

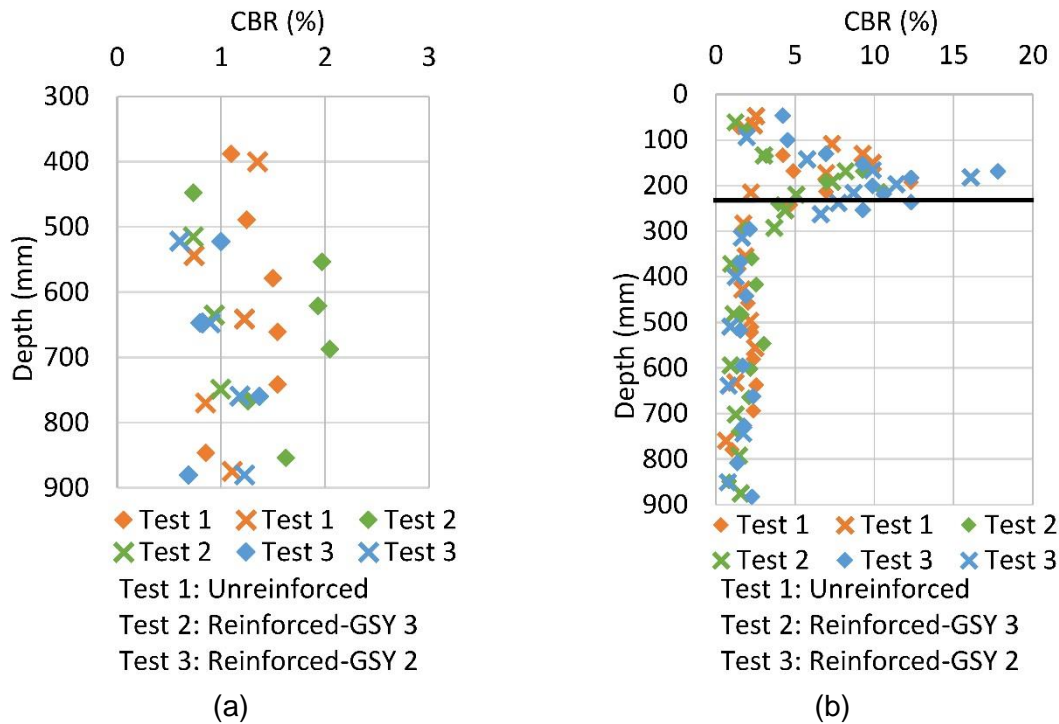


Figure 4.3-5: (a) CBR (%) profile under the plate and Traffic load areas for Tests 1, 2 & 3 before the base course installation, (b) CBR (%) profile under the plate and Traffic load areas for Tests 1, 2 & 3 after the base course installation.

The quality control tests showed that the prepared platforms present homogeneity over the depth and the area, and that the platform repeatability is insured. Moreover, it showed a coherent platform preparation repeatability, between the small box of the plate load test showed previously in Chapter 3, and the large box of the traffic tests.

## 4.4. Results and analysis

Two areas of the prepared platforms were instrumented: the area under the plate load and the area under the Traffic load. The instrumentation is detailed in Chapter 2. The subgrade stress and displacement were monitored during the cycles and under the static load. In fact, after a certain number of cycles, the wheel was placed over the sensors location, the load was used and the applied stress was measured. In the same way, the subgrade surface settlement was measured. After a number of cycles, the load of the plate load tests was applied and the measurements were taken. Regarding the surface rutting measurements, during the plate load test, the plate displacement was measured and the laser sensor was placed on a fixed support, which gave an elevation rut as seen in Figure 4.4-1. However, under the plate load test the soil repulsion on the plate edges was not observed, this is presented later in section 4.4.2.a.

During the Traffic load test the laser sensor was placed on the wheel, and the distance between its height and the base course surface was measured, which gives the apparent rut. Noting that under the Traffic load an important base course repulsion was observed on the wheel edges (section 4.4.2.a).

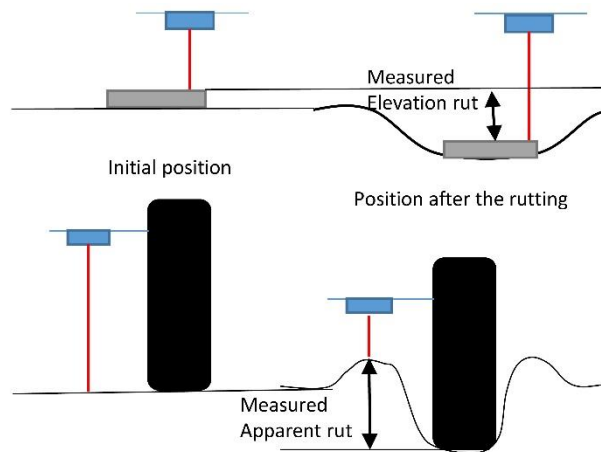


Figure 4.4-1: Rutting plate and Traffic load tests measurements.

The platform was subjected to 10,000 cycles under the plate load. While, it was subjected to 1,200 cycles under the Traffic load. In fact, under the Traffic load an important surface rutting was developed in the first 100 cycles, and the limits of the SAT machine were reached quickly. In order to continue the tests and compare the results, the base course rutting area were backfilled and the circulations were resumed. This procedure was to be held twice per test, one after 150 cycles and one after 500 cycles.

The performed plate load test using the particular shaped plate and the Traffic load results are presented in this section. A comparison between the same platforms subjected to the two different solicitations was presented in order to identify the loading type effect. Moreover, a comparison between the different platforms behaviour under the same solicitation was discussed.

#### 4.4.1. Measurements verifications

The stress measurements in a soft soil using earth pressure cells present uncertainties due to the cell displacement and rotation possibilities under the load or the arching effect that can occur around the cell. Moreover, the cells can create hard points in the soft soil and change the soft soil behaviour. In Chapter 3, the subgrade surface profile was measured after 10,000 cycles using the laser sensor. The settlement profile over the instrumented and the not instrumented sides presented the same shape and values, which proves that the earth pressure cells do not disturb the soft soil behaviour. Moreover, the inclinometers were placed on the earth pressure cells to check their rotation over the cycles.

In these tests, the inclinometers were placed under the Traffic load instrumented section. In this area, the sensors were located at the circulation middle length and distributed over the width. Additional earth pressure cells were placed along the circulated length, at 400 mm and 800 mm from the middle position of the sensors. The central inclinometer was placed on the earth pressure cell located at 400 mm from the circulation middle length and under the wheel centre. In addition, the other inclinometer was placed at the earth pressure cell located at the middle of the circulation length at 200 mm from the wheel centre line as illustrated in Figure 4.4-2.

Figure 4.4-2 (a) and (c) present the earth pressure cell located under the wheel centre line inclination in both X and Y direction. The inclination curves present an initial variation due to the installation imperfections. However, with the cycles, the inclination curves show a constant inclination between

0 and 2 degrees. This proves that in the three performed tests the central earth pressure cell stays in a horizontal position over the cycles.

Figure 4.4-2 (b) and (d) present the earth pressure cell placed at 200 mm from the wheel centre inclination in both X and Y direction. The curves show that the earth pressure inclination passes the sensor limits (15 degrees) in the first 10 cycles. In fact, this sensor presents an important inclination around the X axe. However, around the Y direction, it shows a small variation but it is still under 5 degrees. Compared to the circular plate load tests, in Chapter 3, the same sensor placed at 200 mm presented the same important rotation around this axe, but this rotation did not occur in the first 10 cycles.

The inclinometers' results show that during the Traffic load, and during the first cycles, the sensors placed between 200 mm and 300 mm present a high rotation around the X axe. This is due to the high curvature, that the subgrade surface settlement profile, presents between these two positions. The results given by these sensors do not represent the pure vertical stress applied on this position. Therefore, the stress measurements are analysed in a qualitative way in the following section.

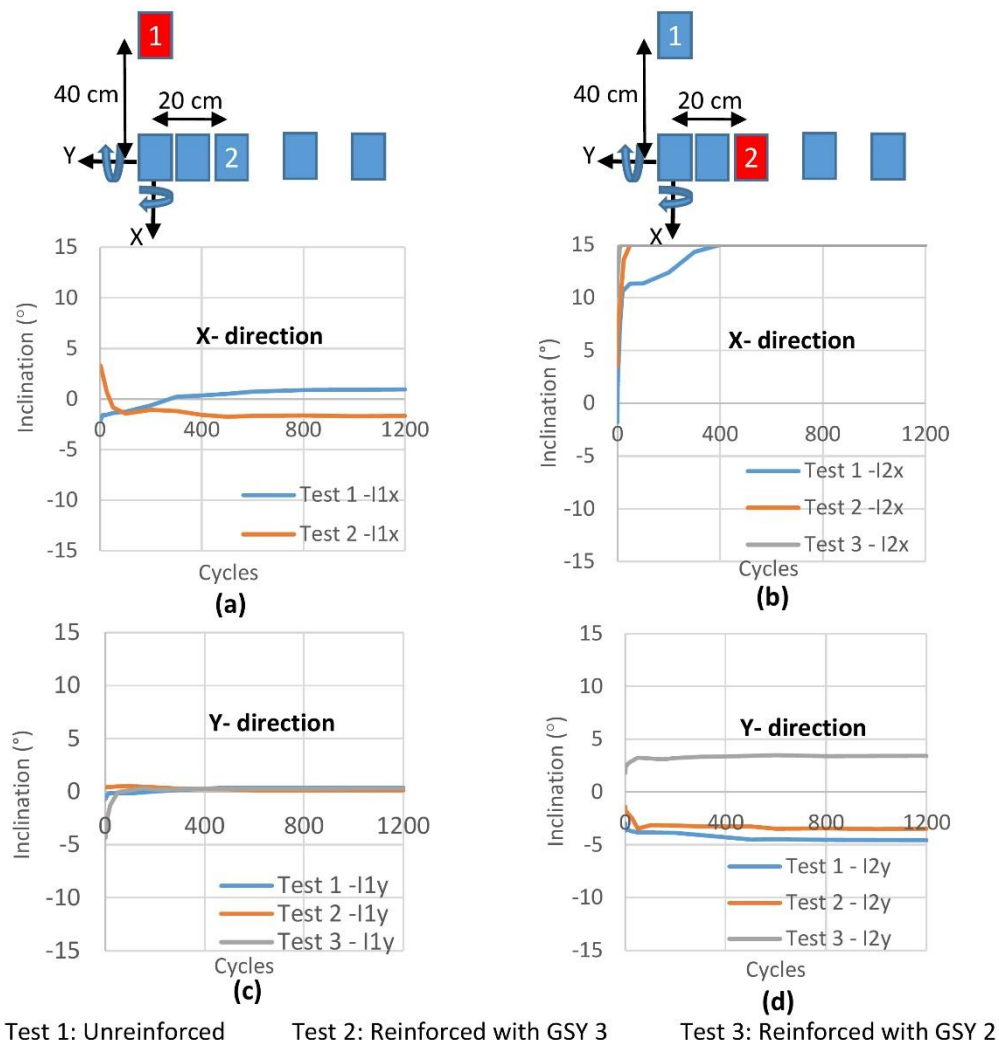


Figure 4.4-2: (a) Central earth pressure cell inclination over the X direction, (b) Earth pressure cell placed at 200 mm from the plate centre inclination over the X direction, (c) Central earth pressure cell inclination over the Y direction, (d) Earth pressure cell placed at 200 mm from the plate centre inclination over the Y direction.

## 4.4.2. GSY benefit

In this section, the unpaved road improvement provided by the reinforcement is studied. The reinforced and unreinforced platforms were subjected to two different solicitation types: particular plate and Traffic load using the SAT machine.

Three different platforms were tested and compared in this section in settlement and stress terms:

- Test 1, an unreinforced platform,
- Test 2, a reinforced platform using the GSY 3,
- Test 3, a reinforced platform using GSY 2.

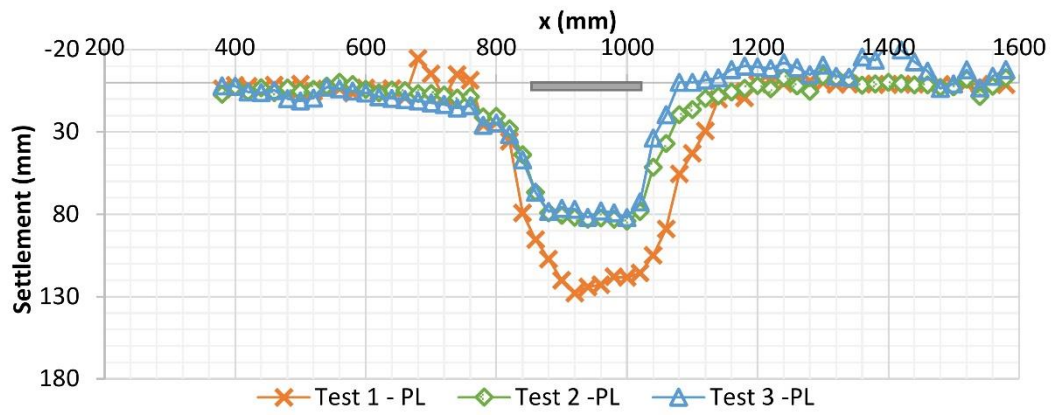
### 4.4.2.a. Settlement

The base course surface settlement profile after 10,000 cycles under the particular plate load was measured using the laser sensor. Figure 4.4-3 (a) shows the three performed tests settlement profiles. The unreinforced platform presents the highest settlement of 118 mm (Test 1) after 10,000 cycles. The two reinforced platforms present the same profiles with a maximum settlement of 79 mm (Tests 2 & 3). This graph demonstrates that under this loading condition the GSY 2 and GSY 3 performed identically with a maximum surface settlement reduction of 33%. More importantly, the curves show no surface lifting at the plate edges. In fact, under this loading condition the base course platform presents no repulsion mechanism.

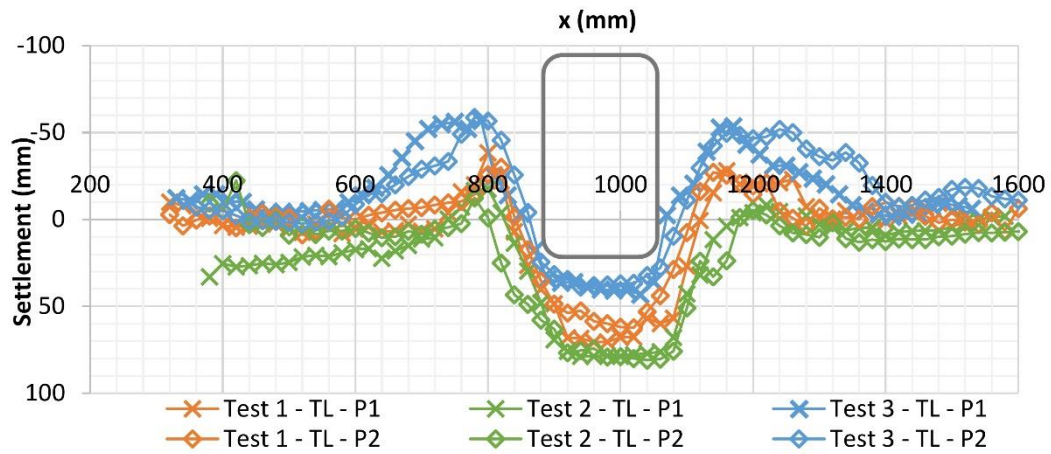
Figure 4.4-3 (b) presents the surface profile after 1,200 cycles of Traffic load. Two settlement profiles were plotted for the same test over two different positions: at the circulation middle length, and 300 mm further. The identical settlement profiles prove that the applied wheel load remains the same over the circulation length, and that the sensors placed under the middle length do not affect the platform behaviour.

The analysis of this graph (Figure 4.4-3 ) should be qualitative not quantitative, because of the rutting zone backfilling after 150 cycles and 500 cycles. In fact, the surface settlement after the backfilling depends on the filling material density.

The presented profiles show an important base course surface lifting on the wheel borders, which proves that under this load condition the base course layer presents important settlements due essentially to the aggregates lateral movement under the circulation loading.



(a)



(b)

PL: Plate Load      TL: Traffic Load  
 Test 1: Unreinforced      Test 2: Reinforced-GSY 3      Test 3: Reinforced-GSY 2

Figure 4.4-3: (a) Base course surface settlement after 10,000 cycles, under the plate load test, (b) after 1,200 cycles under the Traffic load test for two different positions.

Since under the plate load tests no base course surface lifting was observed, the apparent rut is equal to the elevation rut that was measured. Figure 4.4-4 (a) shows the apparent rut evolution with cycles under the plate centre. The unpaved platform presents a settlement of 40 mm (Test 1) at the first load, and this settlement increases during the cycles until it reaches 111 mm (Test 1) after 10,000 cycles. The reinforced platforms with GSY 3 and GSY 2 show an important rut reduction. The settlement under the first cycle is 26 mm for GSY 3 (Test 2) and 30 mm for GSY 2 (Test 3). It increases with the cycles until it reaches 79 mm for GSY 3 (Test 2) and 72 mm for GSY2 (Test 3).



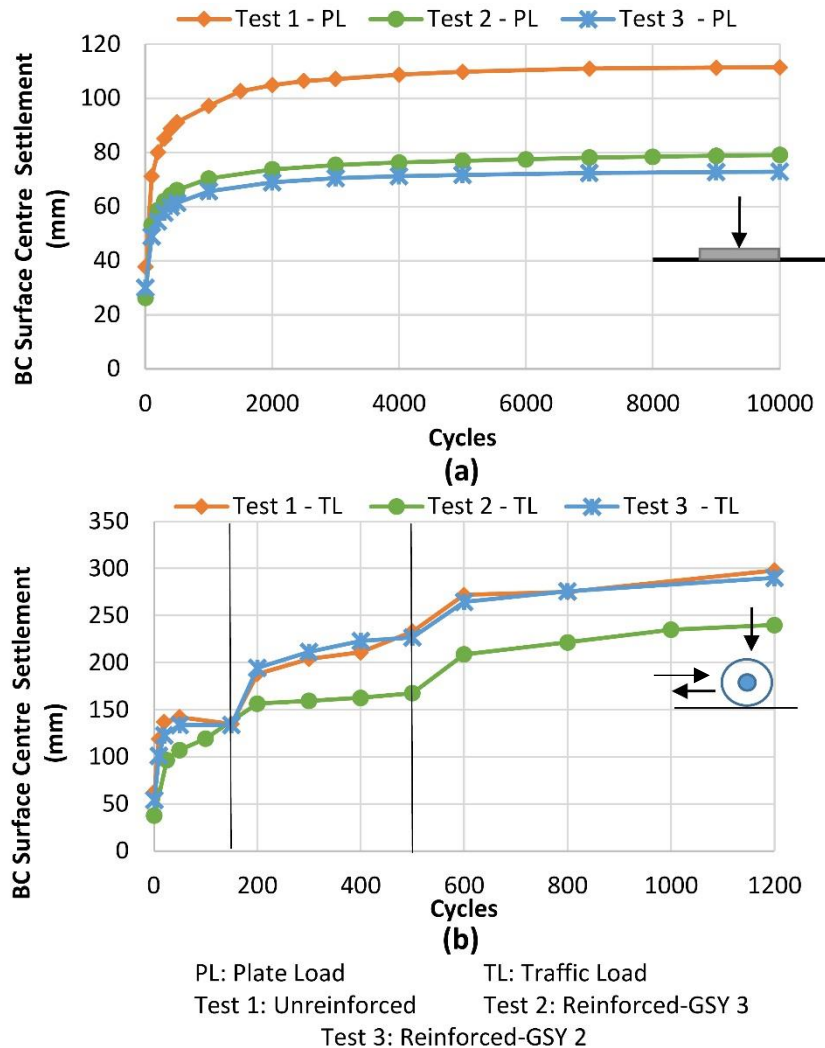


Figure 4.4-4: (a) Base course surface centre settlement evolution with cycles under the plate load test, (b) under the Traffic load test.

Figure 4.4-4 (b) presents the apparent rut evolution with cycles under the Traffic load. This apparent rut evolves very quickly under the Traffic load for the three platforms. In fact, even under the first loading the unreinforced platform presents a higher rut than the plate load (54 mm > 37 mm) (Test 1). Moreover, after 10 cycles, 100 mm of the surface apparent rut was exceeded in the three performed tests. This shows clearly that the circulation load is a more damaging load than the plate load. As mentioned before the SAT apparatus rutting limit was reached after 150 cycles. A rutting area backfilling was performed after 150 cycles and 500 cycles. Therefore, the base course rutting evolution data cannot be analysed in details. It can only show the high rate of rutting evolution with the cycles. In fact, all the test settlements reach 250 mm and more after 1,200 cycles. However, Figure 4.4-4 (b) shows, before the backfilling and post the 150 cycles, that the reinforced platform with GSY 3 (Test 2) presents the lowest surface settlements.

Figure 4.4-5 (a) shows the subgrade settlement under the plate load. Due to some technical issues, the subgrade surface settlement of Test 2 (GSY 3) is missing. Under the first cycle, the GSY 2 (Test 3) shows no significant settlement reduction; in fact, both platforms present an initial settlement of 20 mm (Tests 1 & 2). During the cycles, the reinforcement is in tension and its efficiency in the

settlement reduction appears after the first 100 cycles. After 10,000 cycles, the GSY 2 insures a subgrade settlement reduction of 20%.

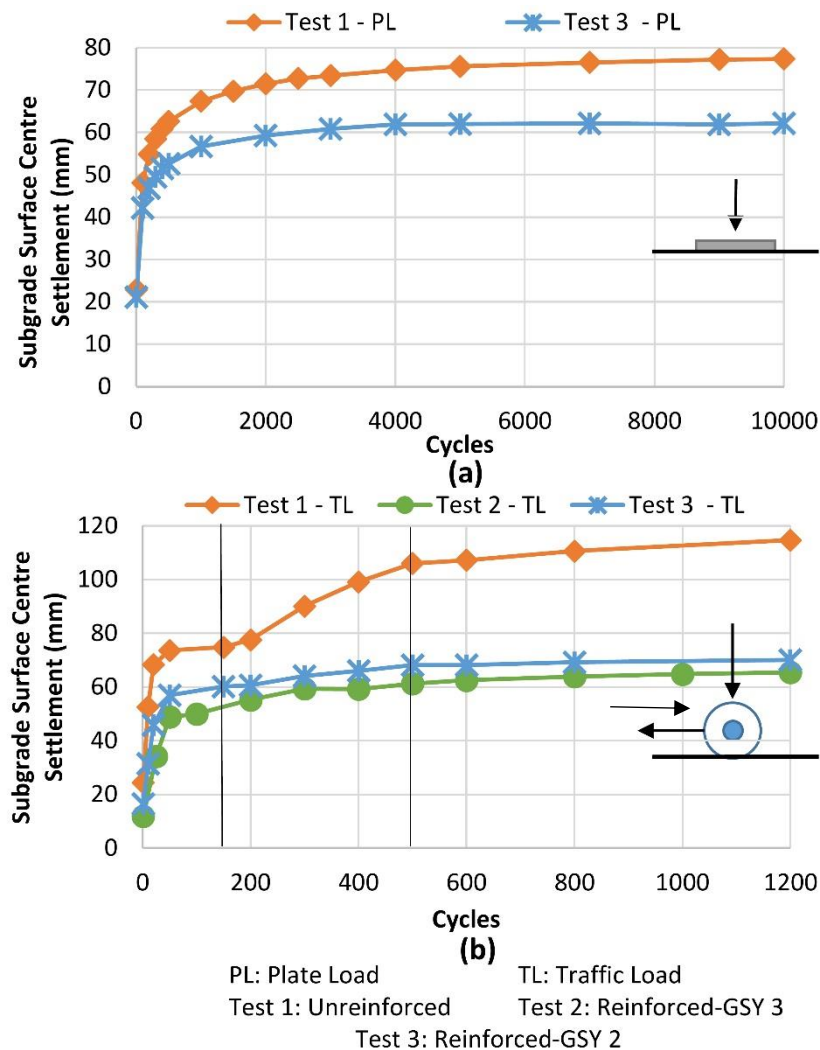


Figure 4.4-5: (a) Subgrade surface centre settlement evolution with cycles under the plate load test, (b) under the Traffic load test.

Figure 4.4-5 (b) shows the subgrade surface settlement evolution under the Traffic load. The unreinforced platform (Test 1) shows an initial subgrade settlement of around 20 mm, it evolves with the cycles to reach 120 mm after 1,200 cycles. Compared to the plate load, the unreinforced platform settlement evolves in a higher rate under the Traffic load. After 1,000 cycles the subgrade surface settlement reaches 67 mm, while the same platform reaches 120 mm after 1,200 cycles of Traffic load. This shows that the Traffic load is more damaging not only for the base course layer but for the subgrade layer too. As for the reinforced platform with GSY 2 (Test 3), under the plate load after 1,000 cycles, the subgrade surface settlement reaches 57 mm, while the same platform reaches 70 mm after 1,200 cycles of Traffic load. The Traffic presents less settlement on the reinforced platform, but still the platform still presents more settlements under the Traffic load than the plate load after the same number of the cycles.

Moreover, Figure 4.4-5 (b) shows the reinforcement efficiency under the Traffic load. Beneath the first load, the unreinforced platform shows a settlement of 30 mm (Test 1), while the reinforced platforms present 16 mm (GSY 2, Test 3) and 12 mm (GSY 3, Test 2).

The two tested geosynthetics present the same behaviour under this type of loading, which was shown previously for the plate load test too (Figure 4.4-4 (a)). It reduces the subgrade settlement from 120 mm to 70 mm (GSY 2) and 65 mm (GSY 3) after 1,200 cycles.

The Figure 4.4-4 and Figure 4.4-5 show an important difference of settlement between the base course surface and the subgrade surface, in particular under the Traffic load. After 1,200 cycles the unreinforced platform presents 120 mm at the subgrade surface and 300 mm at the base course surface which results in 200 mm of base course thickness reduction. It is worth pointing out again that the base course was backfilled twice during the test. The base course thickness variation is shown in Figure 4.4-6.

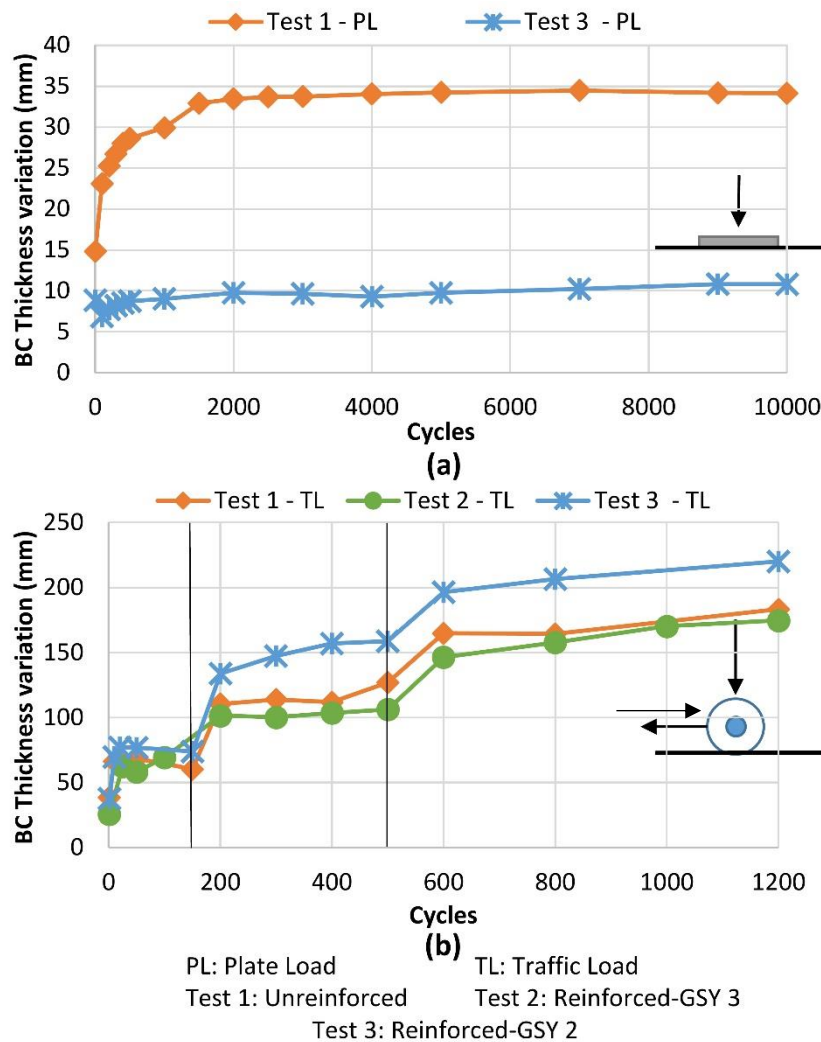


Figure 4.4-6: (a) Base course thickness variation evolution with cycles under the plate load test, (b) under the Traffic load test.

Figure 4.4-6 (a) presents the base course thickness variation under the plate load. The unreinforced platform (Test 1) shows a first thickness variation of 15 mm and it evolves with the cycles until it reaches 35 mm after 10,000 cycles. The reinforcement (GSY 2) reduces this thickness variation especially after the first loading, in fact the platform shows 10 mm (Test 3) at the first cycle and this value remains constant over the cycles.

Figure 4.4-6 (b) presents the base course variation under the Traffic load. It shows an important base course thickness variation under the three tests, and it starts under the first loading. The unreinforced platform (Test 1) shows a base course thickness reduction of 38 mm at the first loading, which increases to 68 mm after the first 10 cycles. The reinforced platform with GSY 3 (Test 2) presents a low base course thickness variation of 26 mm at the first loading and it reaches 62 mm after the 25 first cycles. The reinforced platform with GSY 2 (Test 3) presents 38 mm at the first loading and 77 mm after 20 cycles. These values show that the base course loses 30% of its thickness in the first 20 cycles of the Traffic load. These results showed that the Traffic circulation load induces an important gravel lateral movement and surface repulsion, which reduces the base course thickness. This phenomenon was not observed under the circular or the special plate load tests. However, this phenomenon can be more observed in these tests conditions, because of the loose base course compaction. In fact, the base course CBR in situ should be around 20%, but under the laboratory compaction conditions, the CBR obtained was around 12%.

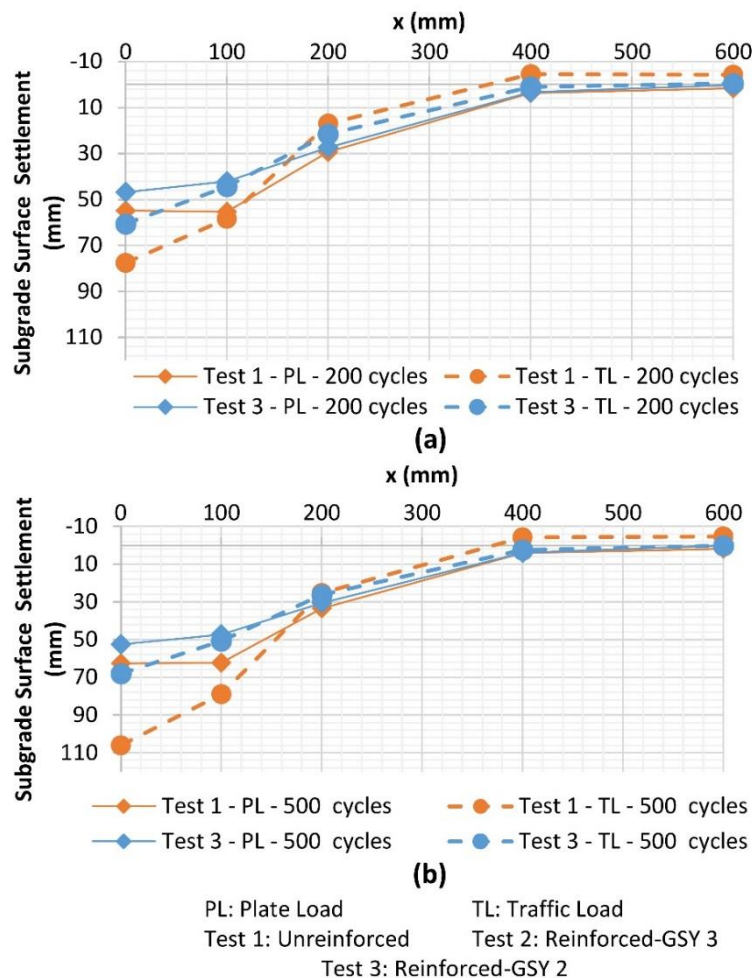


Figure 4.4-7: (a) Subgrade surface settlement profile from the load centre to the edge, for the plate load and Traffic load after 200 cycles, (b) after 500 cycles.

Figure 4.4-7 shows the subgrade surface settlement profile after 200 (a) and 500 cycles (b), for the reinforced platform with GSY 2 and the unreinforced platform, under the plate and Traffic load tests. The profiles' shapes are different under the Traffic and Plate load test. The graphs demonstrate that under the Traffic and plate load at 400 mm from the plate load centre line the settlement reaches

zero. Moreover, in both loading cases at 200 mm from the plate load for the reinforced and unreinforced platforms the settlement is around 30 mm.

The unreinforced platform presents a larger central settlement under the Traffic load than under the plate load after 200 cycles and 500 cycles. In fact, after 200 cycles under the Traffic load the central settlement is of 77 mm, while under the plate load it is only of 54 mm.

The reinforced platform with GSY 2 under the Traffic shows a central settlement after 200 cycles of 60 mm, while under the plate load, the central settlement is equal to 47 mm.

These results show that the same platform presents a higher settlement after many cycles under the Traffic load than under the plate load, and this higher settlement is mainly observed at the load centre. This results in a **profile** shape difference after the same performed cycles.

The settlements' results showed that the Traffic load is more damaging than the plate load, for the same platform. In fact, the Traffic load induced more gravel lateral movements and surface repulsions, which resulted in an important variation of the base course thickness. Moreover, the subgrade settlement presented a higher settlement under the Traffic load. The reinforcement presence reduced the subgrade settlement differences between the Traffic and plate load. However, under both solicitation types the reinforcement GSY 2 and GSY 3 presented an efficiency to reduce the surface settlement in subgrade and base course. Under the plate load test, both geogrid types showed the same base course settlement reduction efficiency of around 30% after 10,000 cycles. Under the Traffic load, both geogrid GSY 2 and GSY 3 reduced the subgrade surface settlement of about 40% after 1,200 cycles. In order to better understand the mechanisms the subgrade surface vertical stress is analysed in the following section.

#### 4.4.2.b. Vertical stress

Figure 4.4-8 shows the maximum vertical stress applied on the subgrade surface and its evolution with the cycles. The graph (Figure 4.4-8) demonstrates the maximum stress reduction due to the reinforcement presence. Under the plate load test, the unreinforced platform presents a maximum vertical pressure of 320 kPa. The reinforced platform with GSY 2 under the plate load presents a maximum subgrade stress of 250 kPa at the first loading, which decreases in the first 100 cycles until it reaches 220 kPa. Moreover, the platform reinforced with GSY 3 presents an initial maximum stress of 220 kPa, which decreases in the first 100 cycles until it reaches 172 kPa. This stress reduction due to the reinforcement presence explains the subgrade settlement reduction observed in the previous section (section 4.4.2.a). Moreover, it shows that the GSY 3 presents a stress reduction ratio higher than the GSY 2 geogrid.

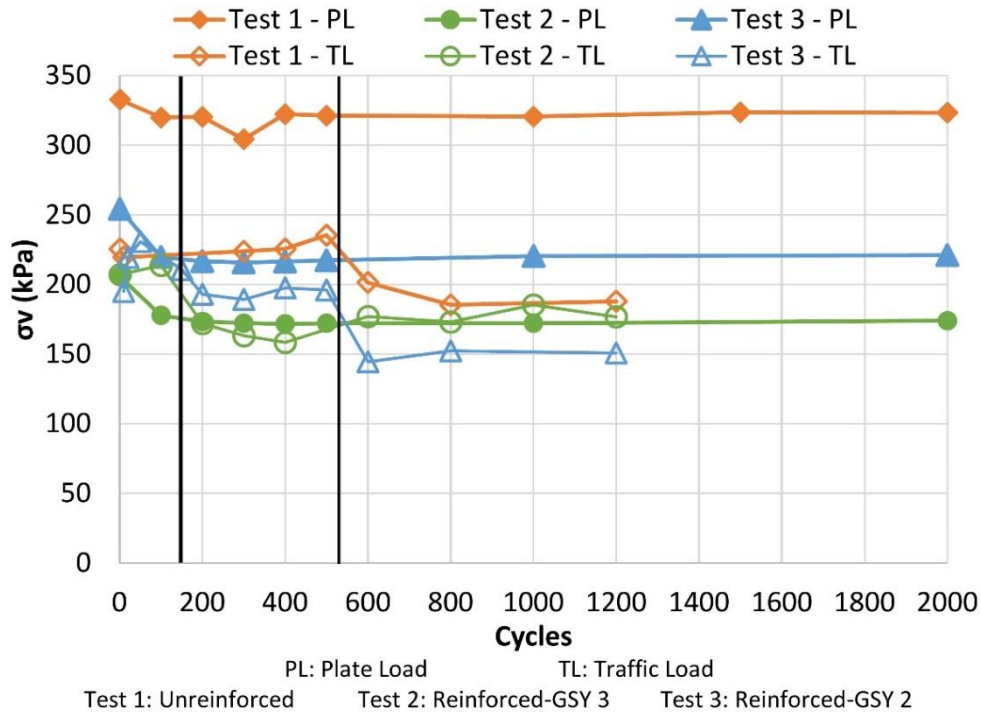


Figure 4.4-8: Subgrade surface central vertical stress evolution with cycles, under the plate and Traffic load.

Regarding the Traffic load stress measurements, there were some uncertainties around the measured values. The wheel position was set manually on the static load application after a certain number of cycles. In fact, sometimes the wheel could be placed a bit away from the sensors position. On one hand the stress measurements during the cycles were not precise because of the sensors measurement, the loading and the logger frequencies incoherence. On the other hand, when the base course surface was backfilled after 150 cycles and 500 cycles, the base course thickness changed, and so affected the stress applied on the subgrade.

However, Figure 4.4-8 shows the measured stress under the Traffic load too. Compared to the stress under the plate load, Figure 4.4-8 shows that the reinforced platforms present the same average stress applied on the subgrade. The unreinforced platforms' stress shows a difference between the plate and Traffic load tests, but the measured stress, during the cycles, of the unreinforced platform showed that the static measured stress in this test was probably wrong because of the wheel position during the static measurements. In fact, under the cyclic load the maximum values are around 300 kPa (Figure 4.4-9), which is the average stress under the plate load. As already mentioned the cyclic measurements do not always give the real applied maximum value because of the incoherence between the sensor, the load and the logger frequencies. However, the maximum given values for the first 22 cycles can give an idea about the average maximum value applied.

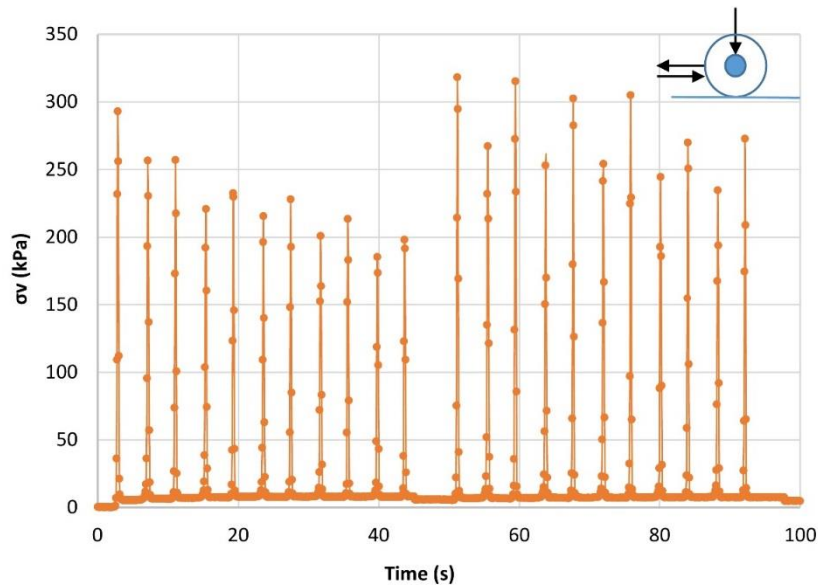


Figure 4.4-9: Subgrade surface central vertical stress cycles, for the unreinforced platform (Test 1).

Figure 4.4-10 shows the vertical stress distribution on the subgrade surface of the first loading and after 100 cycles, under the plate and Traffic load.

Figure 4.4-10 (a) shows the stress distribution under the first loading. Under the plate load, the profiles show a very concentrated stress at the plate centre line, for the reinforced and unreinforced platforms. Moreover, the same platforms under the Traffic load show the same stress concentration at the wheel centre line.

Figure 4.4-10 (b) shows the stress distribution after 100 cycles. The plate load test results show that after 100 cycles the stress presents a more distributed shape. In fact, the central high stress presented at the first load decreased. This high stress seen of the first loading could be due to an installation and compaction irregularity. On one hand, the platforms tested under the Traffic load showed again, after 100 cycles, a concentrated stress profile under the wheel centre line.

On the other hand, and regarding the unreinforced platform measured stress under the Traffic load, the profile presented in Figure 4.4-10 proves again that these measurements failed because of the wheel position while taking the static measurements.

In conclusion, the stress analysis showed clearly the reinforcement effect in reducing the applied stress on the subgrade under the plate load and the Traffic load. The GSY 3 showed a better reduction ratio than the GSY 2. The remarkable point in this study is that the reinforced platforms showed no stress increasing under the particular shaped plate of the maximum stress at the load centre line with the cycles like seen in Chapter 3 with the circular plate load. This can be due to the geogrid different behaviour depending on the load intensity and surface shape. However, the comparison between the particular shaped and the circular plate load results are discussed later in section 4.5.

Moreover, the stress distribution profile on the subgrade differs depending on the load type. In fact, the load is more localised on the load centre line under the Traffic load than under the plate load. Therefore, regarding all the uncertainties that affect the stress measurements, the overall stress analysis should be only qualitative.

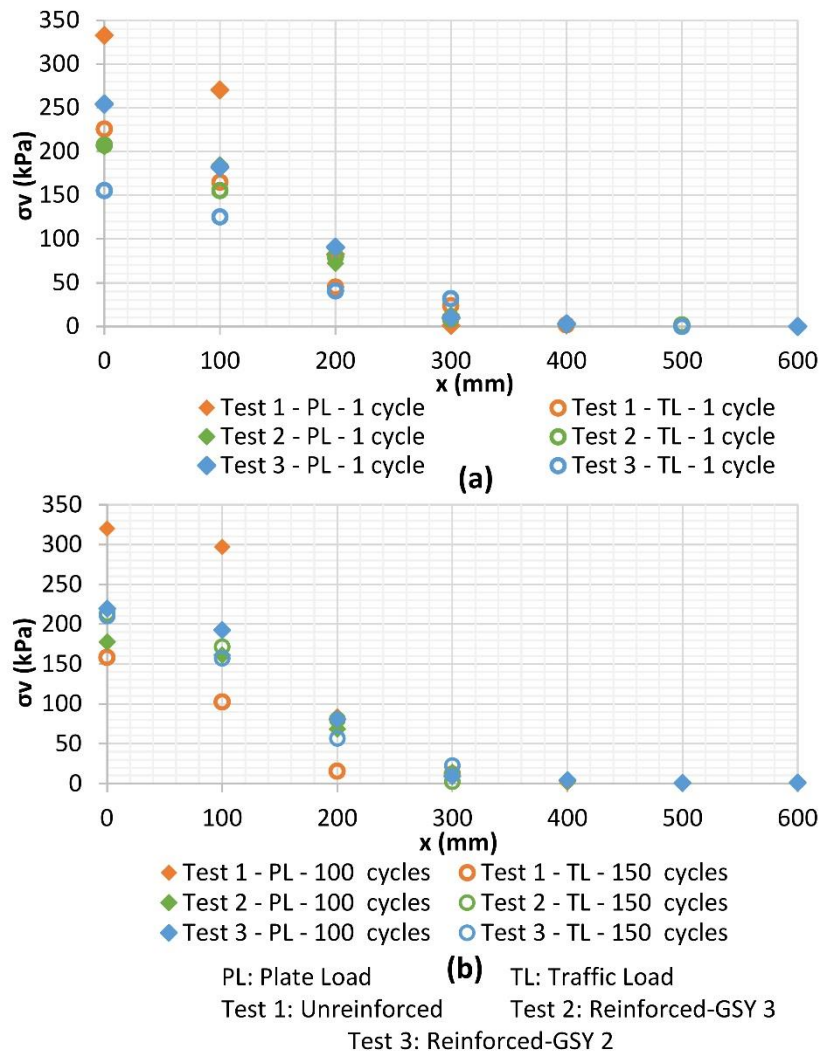


Figure 4.4-10: Vertical stress distribution at the subgrade surface, (a) after 1 cycle, (b) after 100 and 150 cycles.

### 4.4.3. GSY strain

The GSY 2 and GSY 3 are two different geogrid types. The GSY 2 is a knitted geogrid with a low node strength but a high band stiffness, while the GSY 3 is an extruded geogrid with triangular apertures' shapes and rigid nodes. The two geogrids' efficiency in reducing the settlement under the plate load and the Traffic load was shown in the previous section. The optical fibre sensors were placed inside the geogrids to monitor the GSY strain during the base course installation and during the loading and unloading stages.

#### 4.4.3.a. After the base course installation

Figure 4.4-11 illustrates the developed strain in the GSY 2 during the base course installation. The optical fibre was placed in three different positions over the box's length. The graphs (Figure 4.4-11) demonstrate an average strain developed in the geogrid of about  $2,500 \mu\epsilon$ , this was shown previously in Chapter 3. While the GSY 3 presents an average developed strain of  $3,500 \mu\epsilon$  (Figure 4.4-12).



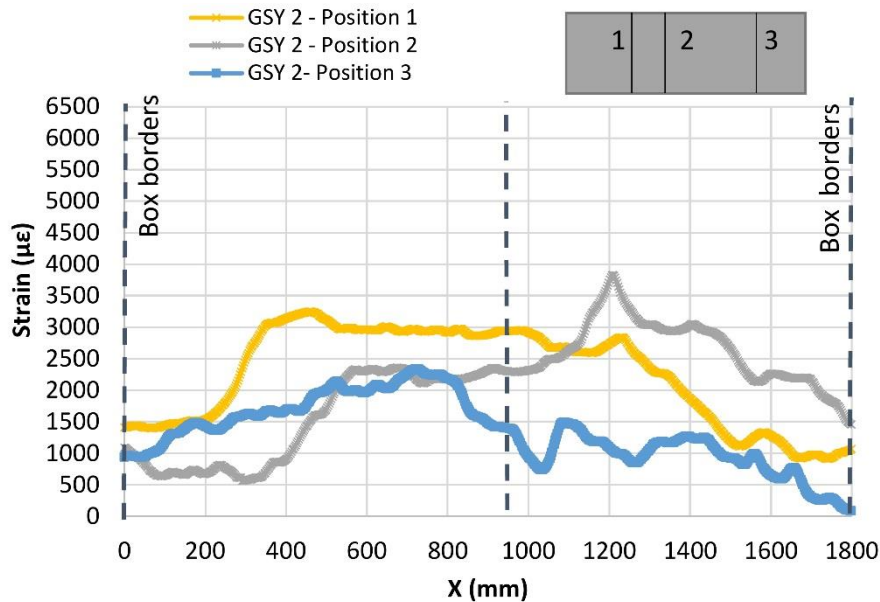


Figure 4.4-11: GSY 2 strain and the equivalent force developed after the base course installation in three different positions.

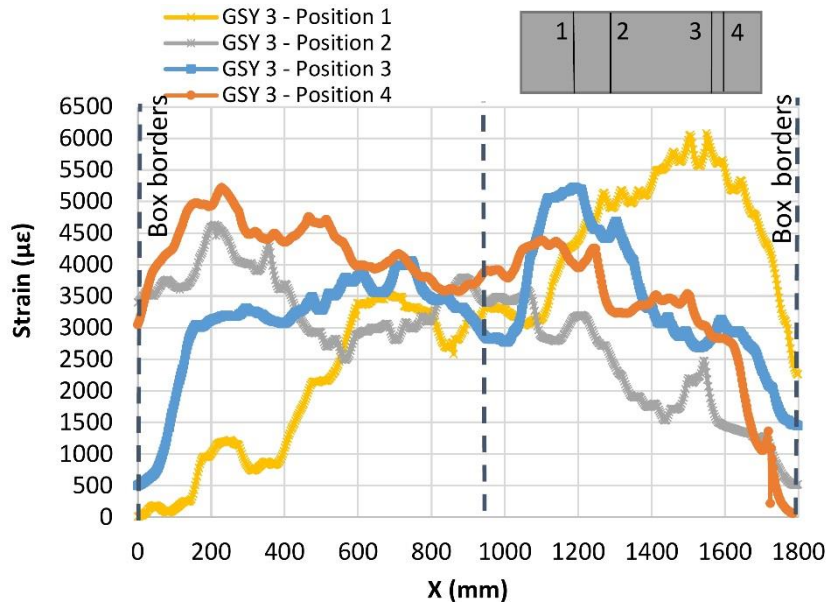


Figure 4.4-12: GSY 3 strain and the equivalent force developed after the base course installation in four different positions.

The GSY 3 presents a higher deformation under the gravel installation. This can be due to its special geometry and its nodes strength that gives privilege to the gravel and aperture interlocking. Moreover, this product presents a node stability strength, which mobilization cannot be measured by the optical fibre. In fact, the optical fibre measures the bands strain only. However, the GSY 2 was mobilized under the installation, next to the low nodes of stability factor, and to the large bands in comparison with the GSY 3.

In this case, the comparison in term of tensile strength is not possible, because the two products are characterized by two different stiffness. In fact, GSY 2 is characterized by a unidirectional I stiffness of 2,500 kN/m at 2% of strain, while GSY 3 is characterized by a radial stiffness of 360 kN/m at 2% of strain. In fact, both products were under tension after the gravel installation.

### 4.4.3.b. During the loading

After the installation, the measured strain of the optical fibre was put to zero, so only the strain due to the loading is measured in this section. In fact, to compare the geosynthetic strain with the subgrade settlement due to the loading, the reference state should be the state after the base course installation.

The geogrid strain was measured under the load and was monitored during the cycles.

Figure 4.4-13 shows the geogrids GSY 2 and GSY 3 strain under the first loading and unloading states, for the plate and Traffic load. Figure 4.4-13 (a) and (c) show the strain developed in the GSY 2 under the first plate and Traffic loading and unloading. It shows that the plate load induces more strain in the GSY 2 than the wheel load at the first cycle. In fact, under the loading, the plate load induces by 7,000  $\mu\epsilon$  in the reinforcement while the wheel's first load induces by 5,000  $\mu\epsilon$  in the GSY 2. After the loading, the remaining strain is about 5,000  $\mu\epsilon$  under the plate load and 2,000  $\mu\epsilon$  under the traffic load.

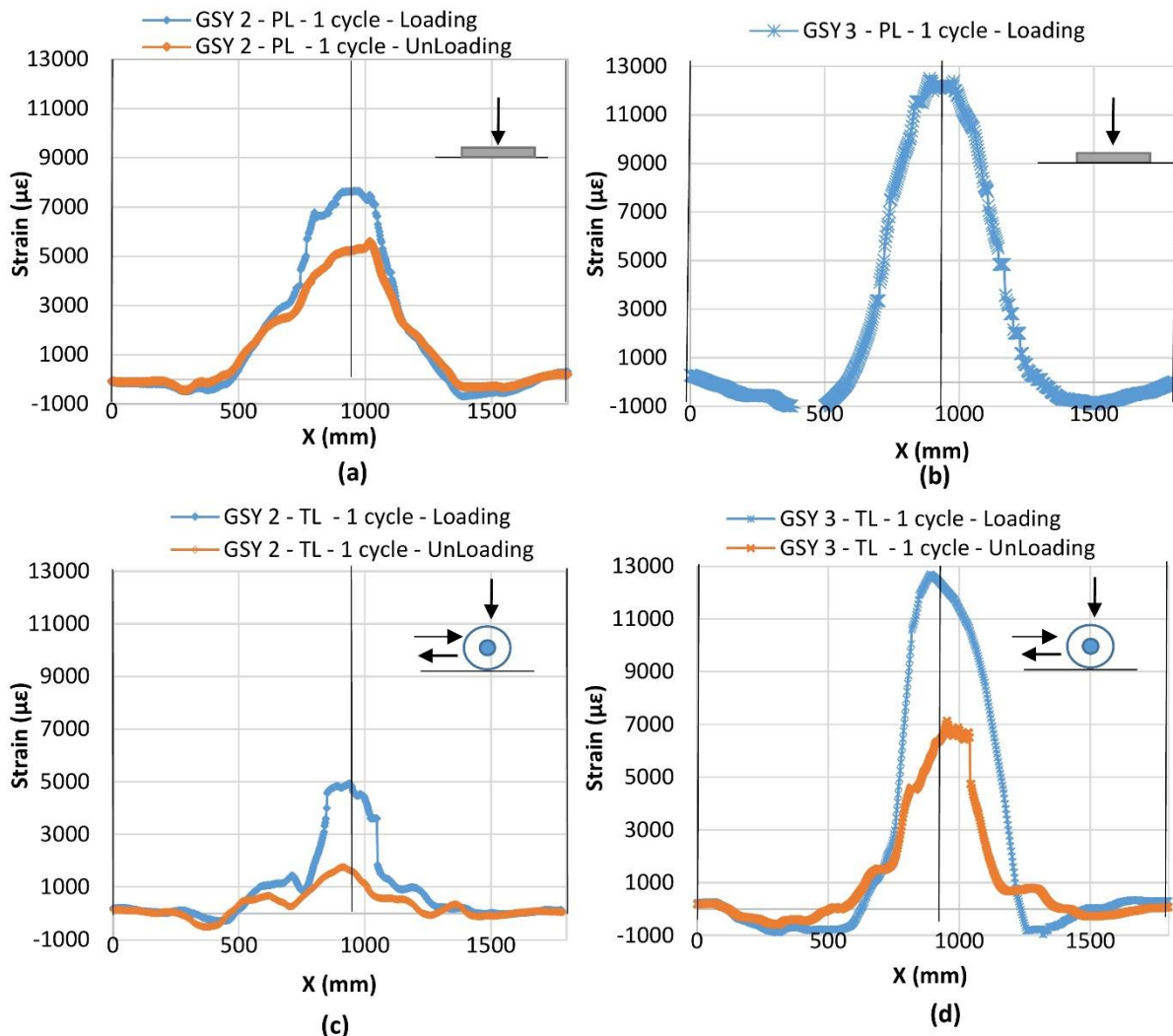


Figure 4.4-13: GSY 2 and GSY 3 strain developed at the first loading and after the unloading, (a) GSY 2 under the plate load, (b) GSY 3 under the plate load, (c) GSY 2 under the Traffic load, (d) GSY 3 under the Traffic load.

Figure 4.4-13 (b) and (d) present the GSY 3 strain under the first plate and Traffic load. The GSY 3 presents a higher strain than the one induced in the GSY 2 under the same load conditions. In fact, it reaches 13,000  $\mu\epsilon$  under both loading cases. After the loading, the remaining strain under the

traffic load is about 7,000  $\mu\epsilon$ . This shows the difference in the two geogrids behaviour under the same load and the same soil displacement following the first load, the two geogrids were mobilized differently. More importantly, these results showed that under a relatively small displacement the GSY 3 is mobilized under the lateral restrain mechanism. In fact, under a localized load as the wheel or the plate load the aggregates tend to move laterally, and the geogrid blocks this movement. This phenomenon mobilizes the geogrid in its horizontal plan in addition to the geogrid strain due to the soil settlement accumulation under the load.

With the cycles, the soil settlement increases and the geogrid strain too, which mobilize even more the geogrid and increases the tension membrane effect. In order to see this evolution, the geogrid strain was measured. However, some measurements were lost because the optical fibre strain limits were reached.

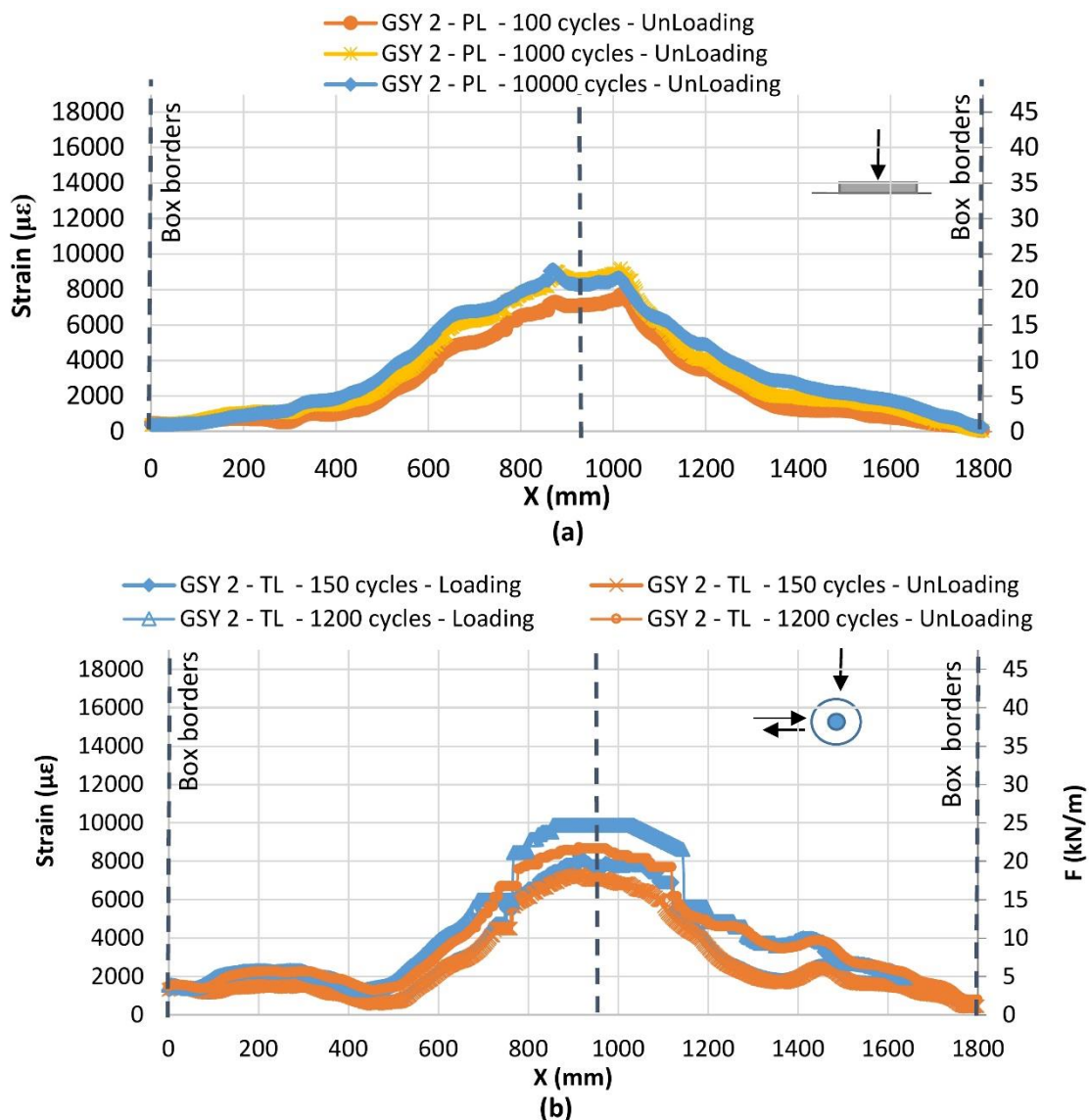


Figure 4.4-14: GSY 2 stain evolution with cycles. (a) Under the plate load, (b) Under the Traffic load.

Figure 4.4-14 illustrates the GSY 2 strain under the plate and traffic load. Under the plate load, the strain curves during the loading were lost, only the strain curves during the unloading were illustrated. The results show a coherence between the two loading types, in fact, the geogrid unloading strain after 1,000 cycles, under the plate load, is around 8,000  $\mu\epsilon$  and the GSY 2 presents 8,000  $\mu\epsilon$  of strain after 1,200 cycles under the Traffic load.

However, the loading strain presented in Figure 4.4-14 (b) shows that 80% of the strain is a plastic strain that remains during the unloading phase. In fact, after 1,200 cycles the maximum unloading strain is about 8,000  $\mu\epsilon$ , while the loading strain is around 10,000  $\mu\epsilon$ .

Moreover, Figure 4.4-14 (a) shows that the unloading strain curves remain the same between 1,000 and 10,000 cycles. In fact, after 1,000 cycles, the soil settlement shows an asymptotic evolution with cycles (Figure 4.4-4). In addition, the curves show again as seen in Chapter 3, that the geogrid anchorage is provided by the aggregates and that no addition of anchorage is needed. In fact, in all these tests the geogrid is placed between in the wooden plate box without any additional anchorage.

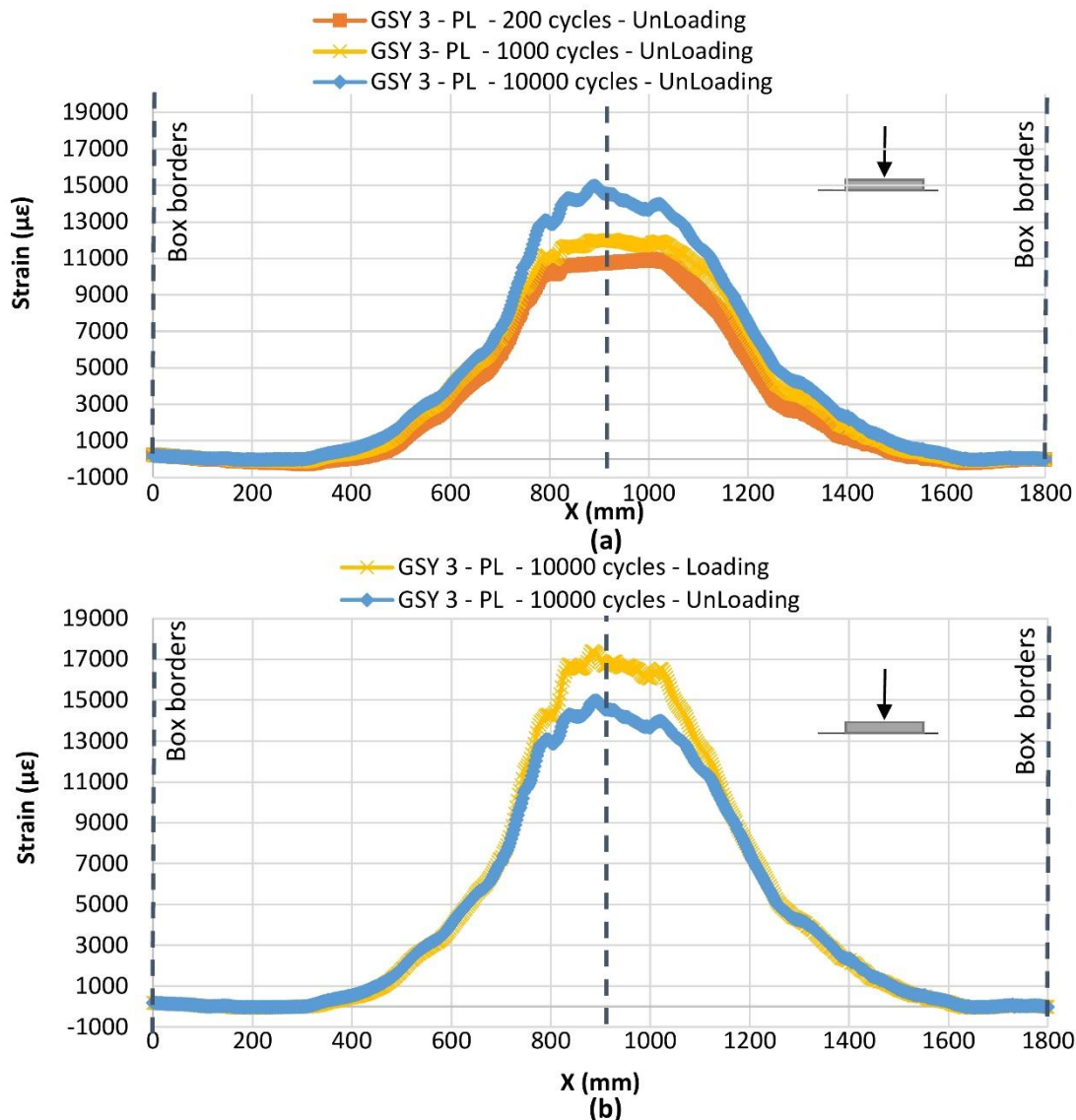


Figure 4.4-15: GSY 3 strain evolution under the plate load with cycles. (a) Evolution at the unloading stage, (b) after 10,000 cycles under the loading and unloading.

The evolution of the GSY 3 strain with the cycles under the traffic load could not be measured because of some technical issues. Therefore, only the curves of the GSY 3 strain under the plate load are illustrated in Figure 4.4-15. On one hand, Figure 4.4-15 (a) shows the GSY 3 strain curves evolution with cycles during the unloading phase. As seen under the first cycle the GSY 3 presents a more important strain than the GSY 2. In fact, even under the cycles the developed strain in the GSY 3 remains more important than the one developed in the GSY 2. After 1,000 cycles under the

unloading phase, the GSY 3 presents a maximum developed strain of 12,000  $\mu\epsilon$  while the GSY 2 presents 8,000  $\mu\epsilon$ . On the other hand, Figure 4.4-15 (b) presents the loading and unloading strain curves after 10,000 cycles. These curves show that the elastic strain's part forms only 12% of the total strain.

The measured strain in the geogrids showed different mechanisms developed in the geogrids regarding their manufacturing types. In fact, the relatively high strain developed under the first load in the GSY 3 proved its mobilization due to the lateral restrain mechanism, which was not seen in the GSY 2. However, due to its high stiffness a small strain developed in the GSY 2 induces an important force. Moreover, the strain curves showed that the GSY 2 and the GSY 3 strain evolved with the soil settlement evolution. Therefore, even if it is due to different mechanisms the benefits of the two geogrids provided benefits, are as close as it was seen in section 3.4.1.

More importantly, under the plate load and the traffic load, the natural geogrid anchor was enough, and the geogrids' strain reaches zero, which is close to the box's borders.

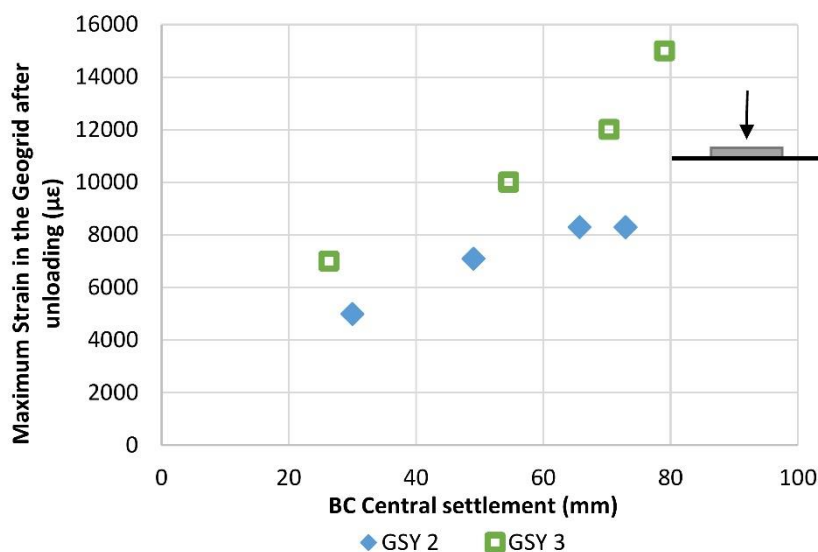


Figure 4.4-16: Geogrids Maximum strain evolution with the base course central settlement evolution.

In order to see better the geogrid developed strain due to the aggregate lateral restrain in the GSY 3, Figure 4.4-16 shows the developed geogrid maximum strain evolution with the base course central settlement. At the first cycle, the surface settlement is more or less the same for the two reinforcements, but the GSY3 is more mobilized. The additional strain developed in the GSY 3 can not be due to the soil settlement, it is due to the aggregates' lateral movement. Moreover, this was shown over the cycles, in fact for the same settlement state the GSY 3 is always more mobilized and shows more strain than the GSY 2.

## 4.5. Circular and particular plate shape tests results comparison

In Chapter 3, plate load tests were performed using a circular plate with 300 mm of diameter and 40 kN of applied load resulting in 560 kPa of pressure, and a cyclic load frequency of 1 Hz. This configuration with the circular plate load (CPL) is the most used in literature. In this Chapter, in order

to compare between the circulation and the plate load tests, a particular plate shape similar to the wheel contact area was used. The applied load under the particular plate load was chosen depending on the applied wheel load, which was equal to 28 kN resulting in a contact pressure of 650 kPa.

The particular plate load (PPL) applies a more localized pressure on the surface and this can mobilize differently the reinforcement. Therefore, in this section the circular and particular plate load tests results were presented and compared. In fact, as mentioned in Chapter 3, the unreinforced platform (Test 3 – CPL), the reinforced platform using the GSY 3 (Test 7 – CPL) and the reinforced platform using the GSY 2 (Test 10 – CPL) were compared to the unreinforced and reinforced platforms under the particular plate load ( Test 1 – PPL, Test 2 – PPL and Test 3 – PPL).

Figure 4.5-1 illustrates the base course surface centre settlement with the cycles. The unreinforced platform presents more settlement under the PPL than under the CPL. In fact, the unreinforced platform shows 111 mm after 10,000 cycles under the PPL, while under the CPL it shows 100 mm. This can be due to the more localized stress on the subgrade surface under the PPL. However, Figure 4.5-3 shows that under the PPL the stress applied on the subgrade for the unreinforced platform is around 330 kPa, while under the circular plate load it is around 300 kPa.

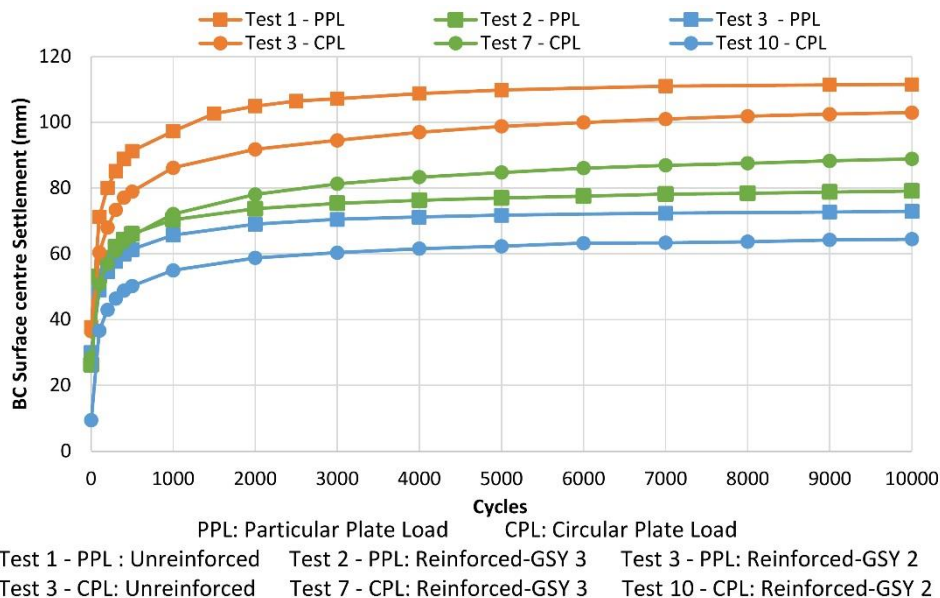


Figure 4.5-1: Base course surface centre settlement evolution with cycles, for the circular plate load tests (Test 3, 7 & 10); and the particular plate load tests (Test 1, 2 & 3).

Figure 4.5-1 shows that the GSY 3 presents a more important improvement under the PPL than under the CPL. In fact, under the first cycles the settlement curves are close until the reach of 1,000 cycles, while the settlement under the CPL continues to increase in a higher rate than under the PPL (Figure 4.5-1). Figure 4.5-2 presents the Base Course surface settlement evolution after 200 cycles. It shows that the platform reinforced with the GSY 3 differs the behaviour under the PPL and CPL after 1,000 cycles. In fact, under the CPL, the platform reinforced with the GSY 3 presents an important settlement evolution after 1,000 cycles, as if there are no reinforcement. This was due to the stress increase on the subgrade surface for this platform until it reaches the stress developed on the subgrade surface without any reinforcement (Figure 4.5-3). The stress under the PPL decreases under the first 100 cycles and then stays constant during the cycles (Figure 4.5-3). This proves that

under the PPL the GSY 3 behaves differently, this can be because under a localized stress the gravel lateral movement is more likely to happen and the GSY 3 is more mobilized in this case regarding its particular geometry and manufacturing type.

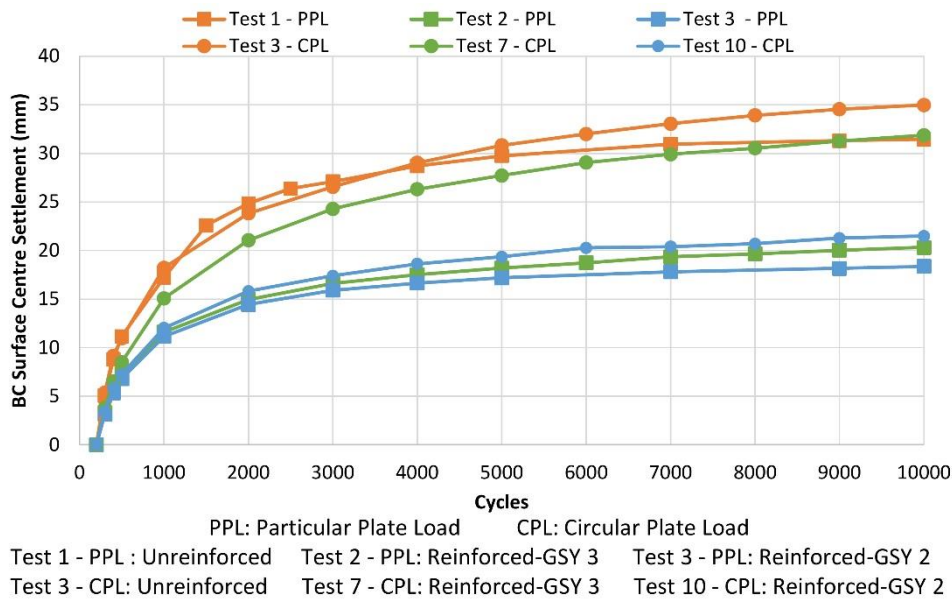


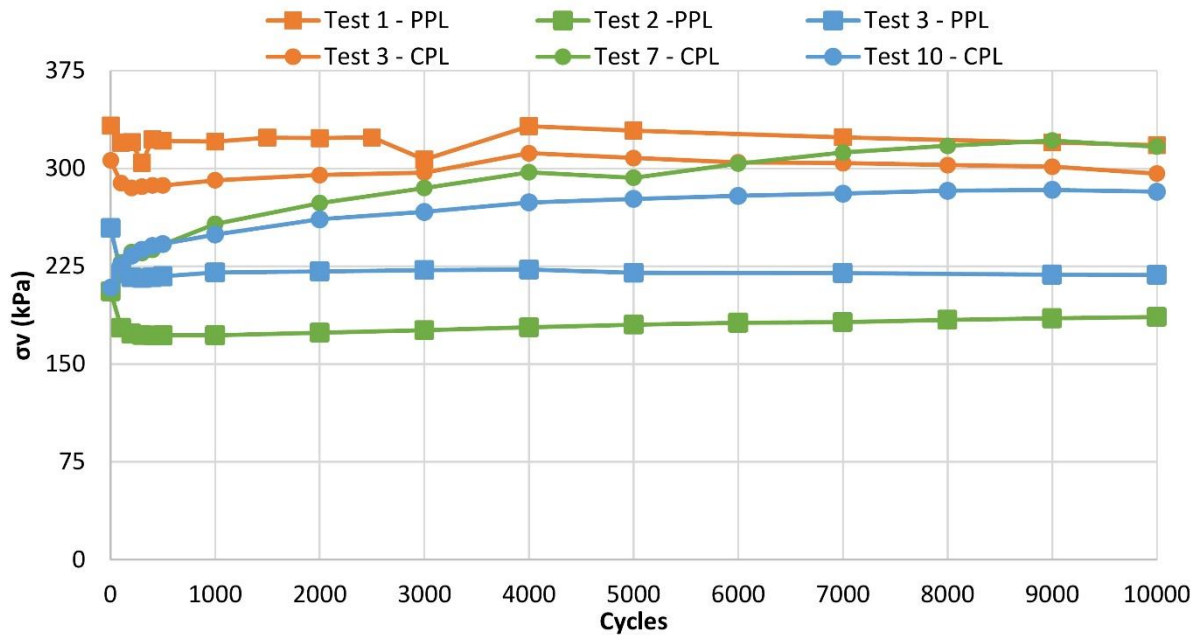
Figure 4.5-2: Base course surface centre settlement evolution with cycles after 200 cycles, for the circular plate load tests (Test 3, 7 & 10), and the particular plate load tests (Test 1, 2 & 3).

Figure 4.5-1 shows a difference between the platforms reinforced with GSY 2. This difference can be due to the first loading point. In fact, the stress applied on the subgrade surface under the first cycle is equal to 254 kPa under the PPL and 200 kPa under the CPL.

Moreover, Figure 4.5-4 shows the geogrid strain developed under the first loading for the PPL and the CPL. This graph demonstrates that under the CPL, the GSY 2 is more in tension than under the PPL. However, this difference under the first loading can be due to the installation uncertainties. To look more into the settlement evolution, Figure 4.5-2 shows that under the PPL and the CPL the platform reinforced with the GSY 2 presents the same evolution rate.

Figure 4.5-3 shows that the developed stress under the PPL shows no evolution with cycles contrarily to the stress developed under the CPL.

Figure 4.5-3 shows significant differences between the developed stress on the subgrade surface under the PPL and the CPL tests especially for the reinforced platforms. It is important to remember that the surface applied pressure has a different shape and a different magnitude, in fact under the PPL the applied pressure is equal to 650 kPa on a smaller area, under the CPL the applied pressure is equal to 560 kPa on a larger area.



PPL: Particular Plate Load      CPL: Circular Plate Load  
 Test 1 - PPL : Unreinforced    Test 2 - PPL: Reinforced-GSY 3    Test 3 - PPL: Reinforced-GSY 2  
 Test 3 - CPL: Unreinforced    Test 7 - CPL: Reinforced-GSY 3    Test 10 - CPL: Reinforced-GSY 2

Figure 4.5-3: Subgrade surface vertical stress evolution with cycles, for the circular plate load tests (Test 3, 7 & 10), and the particular plate load tests (Test 1, 2 & 3).

Under the CPL the reinforced platforms start from the same stress point equal to 200 kPa and evolves with the cycles differently depending on the geogrid type. While under the PPL the first loading presents a higher stress point that decreases in the first 100 cycles and stays relatively constant during the cycles.

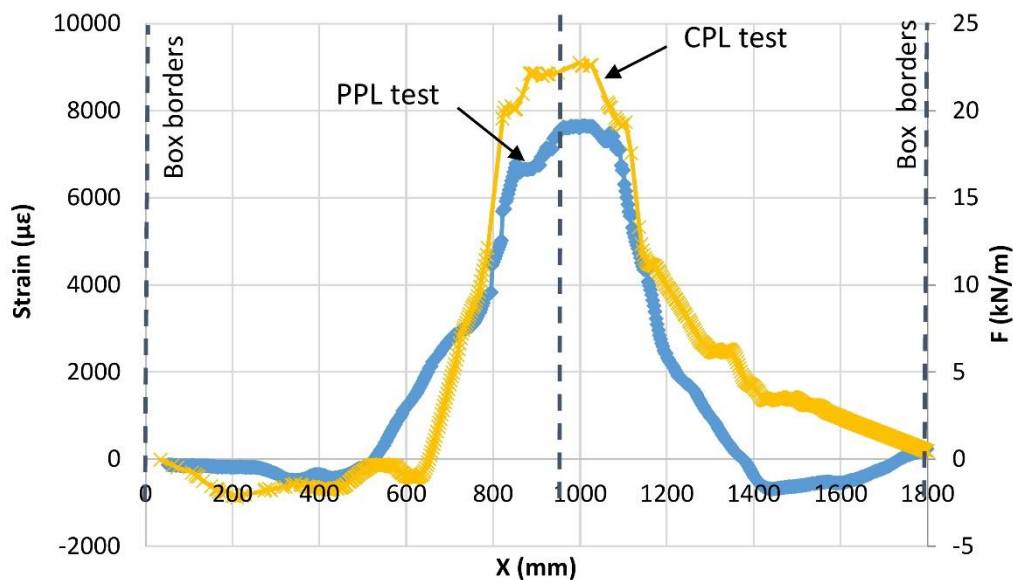


Figure 4.5-4: GSY 2 strain at the first loading cycle, under the circular and the particular plate load test.

However, the results show that under a more localised load the reinforced platform behaved differently, in fact the reinforcement was mobilized differently especially in the GSY3.



## 4.6. Conclusions

In this Chapter, the two different solicitation results were presented, the plate load and the traffic load. The same platform was subjected to two loading types, in order to compare the loading effect on the platform behaviour. Three platforms were tested: an unreinforced platform, a reinforced platform using the GSY 3 and a reinforced platform using GSY 2. During these tests, the base course thickness was fixed to 220 mm.

The SAT apparatus was used to perform the traffic load solicitation on the tested platforms. This machine applied 28 kN on the wheel resulting in 650 kPa on the platform surface. This traffic load was applied on an effective 2 m length with a velocity of 4 km/h. The plate load test was modified in order to match the traffic load. In fact, a plate with the same wheel contact area shape was used, with an applied load of 28 kN resulting in a contact stress of 650 kPa. The two loaded areas were instrumented separately. The results were presented in terms of settlement, stress distribution and strain developed in the geogrids.

The platform preparation and compaction protocol is the same protocol used in the plate load test and controlled previously in Chapter 3. The tests repeatability was proved previously in Chapter 3. The same quality control tests were performed on the prepared platforms under the plate load test area and the traffic load area. The results presented in this Chapter showed the platform homogeneity over the depth and over the large area. Moreover, the same soil layers properties were shown over the prepared platform area.

The comparison results between the plate and traffic load showed that the traffic load is a more damaging load:

- Under the first 10 cycles, the base course surface settlement under the traffic load reached more than 50 mm of apparent rut. In fact, under the traffic load the gravel lateral movement and surface repulsion was observed especially on the surface, which was not seen under the plate load test.
- In addition to the base course important thickness variation, the subgrade presented a higher settlement under the traffic load. However, the reinforced platform presented less subgrade settlement differences between the traffic and the plate load, than the unreinforced platform.

This base course thickness reduction under the circulation load was not taken into consideration in the analytical design methods; in fact, these analytical methods were calibrated based on circular plate load tests. Although, it was shown in the tests that the circulation load changes the platform behaviour and induces more settlement in the base course and on the subgrade surface.

Under both solicitation, the reinforcement showed an efficiency in reducing the platform rut development and in increasing the platform serviceability:

- The GSY 2 and GSY 3 under the plate load test showed a base course settlement reduction of 30% after 10,000 cycles. Under the traffic load test the GSY 2 and GSY 3 reduced the subgrade surface settlement of about 40%.

- The stress measurements under the traffic load tests were affected by many uncertainties, but the reinforced platform results showed that the average applied subgrade stress under the traffic load test were close to the applied stress under the plate load.
- The GSY 3 showed a better stress reduction ratio than GSY 2. In fact, the unreinforced platform presented a maximum subgrade stress of 330 kPa. The reinforced platform with GSY 3 showed a maximum subgrade stress of 180 kPa while the reinforced platform with GSY 2 presented 220 kPa.
- The developed strain in the geogrid under the gravel installation showed that the GSY 3 was more mobilized during the installation than the GSY 2. This can be due to its geometry and ability to interlock with the gravel particles.
- The developed strain in the geogrid under the first load showed that the GSY 3 was more mobilized under the first cycle than the GSY 2. Even over the cycles the GSY 3 showed a larger strain than the GSY2. This can be due to the fact that under the first cycles the gravel lateral movement is more blocked by the GSY 3. In fact, due to its nodes stability and special geometry the GSY 3 can limit more the aggregates lateral movement, and this resulted in a higher strain developed in GSY 3 than in GSY 2.

The comparison between the circular plate load tests presented in Chapter 3 and the particular plate load tests showed a difference in the reinforcement behaviour under a more localized load especially the GSY 3:

- In fact, under the particular plate load test the GSY 3 improved in a better way the platform behaviour, it reduced significantly the base course settlement and the subgrade developed stress compared to its performance under the circular plate load. This is because under a localized stress the extruded geogrid is more mobilized due to the more important aggregates lateral movement.
- The GSY 2 performance proved significant differences regarding the stress evolution with cycles, but these differences did not affect much the general settlement reduction compared to the circular plat load test.

These results showed that the efficiency of the reinforcement, and the developed mechanisms at the interface in the base course platform and in the subgrade depends on the loading mode, magnitude and applied area. Moreover, the circulation load is a more damaging load for the platform, especially on the base course layer. This base course thickness variation under the traffic load was probably amplified in the performed tests because of the laboratory base course compaction conditions.



# Chapter 5. Numerical Modelling

---

## 5.1. Introduction

The unpaved roads on soft subgrade are a complicated practical and research application, which involve various mechanisms. The GSY reinforcement addition at the interface complicates even more the mechanisms. In order to provide knowledge and better understand the complex mechanisms, the authors in literature used different numerical methods to simulate this application. In literature, the discrete element method based on the discrete approach proved its efficiency in simulating the behaviour of the interaction between the geogrid apertures and the base course particles. However, the limitation of this method in the unpaved roads supported by soft subgrade is mainly the simulation of a cohesive soft soil layer.

The continuous-based finite or differential element methods were used in literature to present a model that can simulate the behaviour of the structure under monotonic or cyclic load. In the continuous-based model, the geogrid is modelled as a continuous membrane with an equivalent stiffness. However, this approach reduces the geogrid apertures-aggregates interaction to a shear interface law. Moreover, in these methods a large deformation formulation is needed to deal with this application. In addition, complex constitutive models to simulate the materials behaviour especially under cyclic load are needed.

The mechanistic-empirical method is a very common method used in the traffic applications in order to determine the long-term behaviour of the structures under cyclic load. This method consists of taking the information from a mechanistic response model and extend it into a long-term behaviour based on empirical approaches. However, in order to introduce more this method in the unpaved roads reinforced with GSYs, reliable base information from the mechanistic model are required.

In this Chapter, a continuous three-dimensional model based on the finite differential method have been developed using the calculation Software FLAC 3D. This model simulates the plate load test performed experimentally, with the same configuration.

A special attention has been given to the soft soil constitutive model. Moreover, the material parameters have been calibrated based on the laboratory characterisation tests (triaxial test, direct shear test). A first model with a monotonic loading have been validated based on the experimental results. Finally, this model has been used to determine the influence of various parameters.

## 5.2. Soil constitutive models

The constitutive model of a material is the relation between its internal stresses and its strains. It is a specific law that depends on each material behaviour. The general formulation of this law is given by the following equation:

$$\sigma_{ij} = F(\varepsilon_{ij}) \quad \text{Eq. 5.2-1}$$

Where  $\varepsilon_{ij}$  is the strains tensor,  $\sigma_{ij}$  is the stresses tensor and  $F$  is the function.

### 5.2.1. Elasticity

The linear elasticity is characterized by reversible deformations upon unloading: the stress-strain laws are linear and path-independent. However, non-linear elasticity is divided into two main families: the hyper-elastic models and the hypo-elastic models. The hyper-elastic models are the first non-linear category and are characterized by their null intrinsic dissipation. The hypo-elastic models are the second non-linear category and are characterized by the fact that the stress depends not only on the strain increment but also on the stress state itself.

### 5.2.2. Elastoplasticity

The elastoplasticity models describe the non-linear and irreversible behaviour of the material. These models present a yield surface, a hardening/ softening function and a plastic flow rule. In fact, we assumed an additive decomposition of the total strains, an elastic part and a plastic part such as:

$$d\varepsilon_{ij} = d\varepsilon_{ij}^e + d\varepsilon_{ij}^p \quad \text{Eq. 5.2-2}$$

Where  $d\varepsilon_{ij}^e$  is the elastic strain increment and  $d\varepsilon_{ij}^p$  is the plastic strain increment.

The yield functions for each model define the stress combination for which plastic flow takes place. These functions or criteria are represented by one or more limiting surfaces in a generalized stress space with points below or on the surface being characterized by an incremental elastic or plastic behaviour, respectively. The yield function is a scalar that depends on the stress tensor  $f(\sigma_{ij})$ :

- If  $f(\sigma_{ij}) < 0$ , the stresses are in the elastic domain and no plastic strain occurs.
- If  $f(\sigma_{ij}) = 0$ , the stresses are at the elastic domain borders and plastic strain occurs only if  $\frac{\partial f}{\partial \sigma_{ij}} d\sigma_{ij} > 0$ , so it is the loading case.  $\frac{\partial f}{\partial \sigma_{ij}} d\sigma_{ij} < 0$  corresponds to an unloading condition where elastic strain occurs.
- If  $f(\sigma_{ij}) > 0$  is impossible to reach.

Figure 5.2-1 illustrates the general concept of the yield function in a deviatoric plane for loading and unloading cases.

One of the most used models in geotechnical is Mohr-Coulomb model. The shear yield function defined by Mohr-Coulomb model:

$$f(\sigma_{ij}) = (\sigma_1 - \sigma_3) - \sin \phi (\sigma_1 + \sigma_3) - 2c \cos \phi$$

Eq. 5.2-3

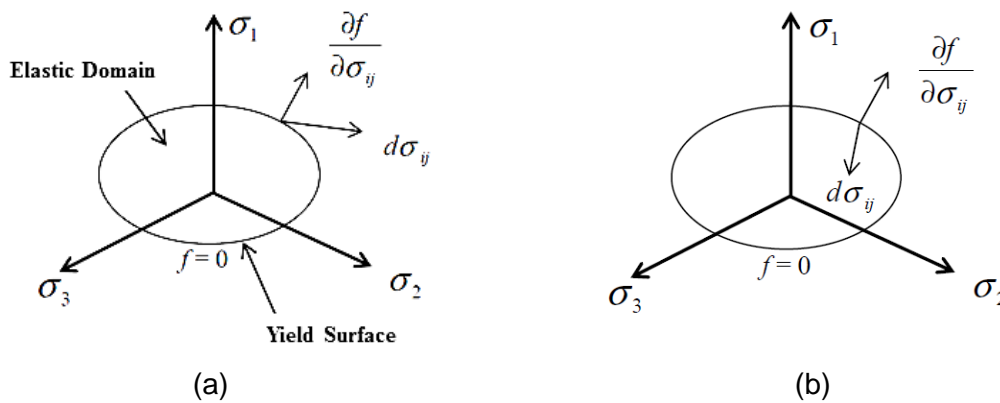


Figure 5.2-1: Yield function. (a) Loading case, (b) Unloading case.

The yield function can depend on the stress components only as seen before, in this case, the state is called “perfect plastic”, or it can depend on the stress and plastic strain, in this case, hardening occurs.

The hardening law gives the yield function evolution with the development of the plastic strain. Different hardening laws are distinguished:

- The isotropic hardening, the yield surface undergoes an expansion or a contraction during the deformation process (Figure 5.2-2).
- The cinematic hardening, the yield surface moves in stress space (Figure 5.2-2).
- The anisotropic hardening, the yield surface undergoes in addition to the expansion/contraction a translation, rotation and evolution.

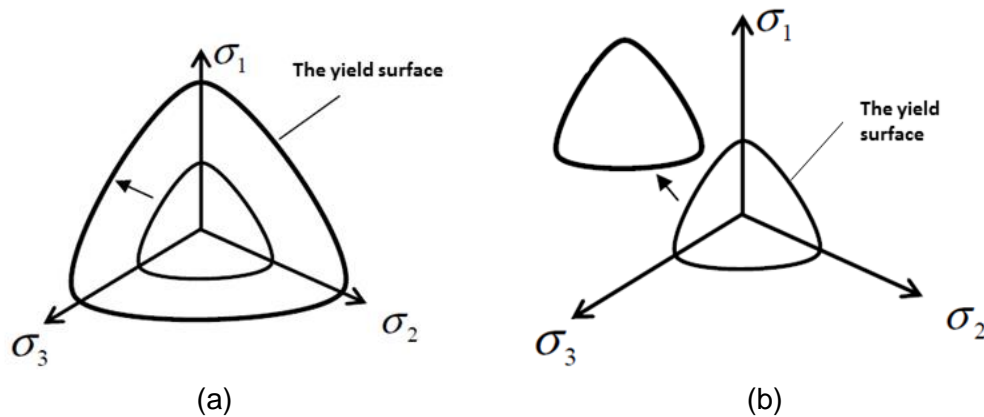


Figure 5.2-2: (a) isotropic hardening, (b) cinematic hardening.

In a constitutive model formulation, the hardening is introduced using a parameter in the yield function expression. In the case of an isotropic hardening, a scalar parameter is used, however, in a cinematic hardening a tensor is needed.

The plastic flow rule gives the accumulation of the plastic deformation regarding the stress state ( $\sigma_{ij}$ ) and ( $d \sigma_{ij}$ ) and the hardening ( $K$ ), using a plastic potential  $g$ . Non-associated flow rule is introduced if the plastic flow function  $g$  is different from the yield function  $f$ .

$$d\varepsilon_{ij}^p = d\lambda \cdot \frac{\partial g}{\partial \sigma_{ij}} \quad \text{Eq. 5.2-4}$$

Where  $d\lambda$ , a positive scalar, is called the plastic multiplier. Based on the consistency condition, the plastic multiplier is determined. In fact, the stress state should stay in the yield surface ( $f = 0$ ), so with the time steps,  $df = 0$ .

### 5.2.3. Hypoplasticity

Hypoplasticity is based on a simple mathematical formulation in which the inelastic behaviour of a material is formulated using a single nonlinear tensorial equation of the rate-type. The hypoplastic constitutive equations are substantially different from the elastoplastic constitutive ones; in fact, it does not include concepts like the yield function, the plastic potential, the hardening and the additive decomposition of the deformation into elastic and plastic components.

These two types of models do not address only the nonlinearity in the soil, the influence of density, the dilatancy, and the pressure level, but they take into consideration the deformation history in the soil.

### 5.2.4. Literature revue

A considerable number of constitutive models exist in literature to simulate the behaviour of soils, with a variable level of complexity depending on the application and the precision needed. In literature the constitutive models were classified based on the soil type, the theory used in the model and the number of tensor space as well used in the model.

#### 5.2.4.a. Models used to simulate the aggregates behaviour

Most of the models are based on experimental observations of the granular soils behaviour in triaxial tests. The granular materials present complex behaviours that depend on the stress state, the density and the load history.

There are elastoplastic models based on one shear of the mechanism (Monnet and Gielly, 1979). Moreover, there are more complicated models like the Drucker and Gibson (1957) model, the DiMaggio F (1971) model, the CJS2 model (Maleki et al., 2000), and the Hardening soil model (Vermeer, 1978; Schanz et al., 1999). These models are elastoplastic models with two mechanisms, especially developed for the granular soils. An isotropic hardening is added to these models, which allows to simulate the behaviour of granular material under monotonic load.

The Mohr-Coulomb model is an elastic - perfectly plastic model widely used in geotechnical engineering to simulate the behaviour of granular and cohesive soils. This constitutive model is characterized by a linear isotropic elasticity of Hooke ( $E, \nu$ ), a constant yield surface in the space without any hardening law and a plastic potential. This model is described by two failure parameters: the cohesion  $c$ , and the friction angle  $\varphi$ . This model describes the shear failure of a soil. In our application, this model was used to simulate the behaviour of the base course layer as described in

Section 5.3.8, since it is the most widely used model to simulate the granular behaviour, and since we are focusing more on the subgrade soil behaviour. A strain-hardening/softening model also implemented in FLAC 3D allows the representation of nonlinear material softening and hardening behaviour based on prescribed variations of the Mohr-Coulomb model properties (Cohesion, dilation, tensile strength) as functions of the deviatoric plastic strain.

Special models in literature were developed to simulate the granular behaviour under cyclic load (Ghaboussi and Momen, 1979; Schwer and Murray, 1994; Manzari and Dafalias, 1997; Desai, 1980; Fang, 2003). These models are based on kinematic and mixed hardening mechanisms. However, in this present work, we will keep on the basic Mohr-Coulomb model regarding the gravel.

#### 5.2.4.b. Models used to simulate the clay behaviour

The most commonly used models for the clay behaviour are the Cam Clay model (Roscoe et al., 1958) and the modified Cam Clay model (Roscoe, 1968). The Cam Clay model was successfully used to simulate the behaviour of soft soil, especially the normally consolidated clay. This constitutive model was developed based on the compression test (oedometer test) and the shear tests (shear box and triaxial tests). This model is based on the concept of the critical stress state. The critical state is when a high distortion occurs in the soil without volumetric and stress variation. The Cam Clay model does not take into consideration the clay anisotropic behaviour. Moreover, this model can simulate the clay behaviour under monotonic load, but its limits are reached under cyclic loading. Melanie model was developed at LCPC by Kattan (1990) in order to study the clay anisotropy. The Lee and Oh (1995) model is based on the anisotropic hardening and allows the clay plasticity simulation. Authors in literature developed the Cam Clay model to simulate clay behaviour under cyclic load (Al-Tabbaa and M. Wood, 1989; Al - Tabbaa and O'Reilly, 1990). The yield surface in these models is called "bounding surface".

In the presented work, the Cap-Yield model implemented model in FLAC 3D will be used to simulate the behaviour of the soft soil under monotonic.

#### 5.2.4.c. Unified models

Some models were developed in literature to insure the simulation of both granular and cohesive soils behaviour (Aubry and Hujeux (1982); Crouch et al., 1994; CASM model (Yu, 1998); Khong et Yu, 2002; Matsuoka et al., 2005). These models were developed based on the Cam Clay model with the critical state concept. Moreover, these models allow the simulation of the soil dense and loose states.

### 5.3. The numerical computation code: FLAC 3D

FLAC software is a computational software that allows the resolution of stress-strain problems of continuous media. The calculation code is based on the differential element method: the variables are known in the discretized element of the space without the constitution of the overall-medium



rigidity matrix. The code uses an explicit resolution method; the stress and strain computation in one element is independent from the elements around.

The software FLAC is based on a numerical formulation called 'Lagrangian Element Method (Billiaux & Cundall, 1993).

### 5.3.1. The computation code background

The differential element method allows the differential equations system resolution based on the initial and /or boundary conditions. Each derivative in the differential equations system is replaced by an algebraic expression in the discretized medium in term of stress or strain variation. This numerical method does not require the computation and storage of the overall domain rigidity matrix. Unlike the 'Eulerian' formulation, the 'Lagrangian' formulation allows the variation of the node position and the mesh deformation for each time step, which provides a practical method to deal with large deformation boundary problems.

The resolution method implemented in FLAC consists on the application of the non-traditional explicit method. This method is based on the resolution of a static problem through the dynamic formulation. In fact, part of the deformation energy accumulated in the system is dissipated in the medium as kinematic energy. Figure 5.3-1 shows the computation scheme used at each time step, which takes into consideration the dynamic movement equations. Indeed, the equations of motion are used to determine the new velocity and displacement from the stresses and forces.

For a deformable body in a Lagrangian referential, the Newton equation of motion is expressed as:

$$\rho \frac{\partial u_i}{\partial t} = \frac{\partial \sigma_{ij}}{\partial x_j} + \rho g_i \quad \text{Eq. 5.3-1}$$

Where,  $\rho$  is the volumetric mass,  $t$  is the time,  $u_i$  is the velocity,  $x$  is the position vector and  $g$  the gravitational acceleration constant.

The strain rate is then derived from the velocity gradient. In addition, the stresses are determined of the material constitutive model. Details are given in the next Section.

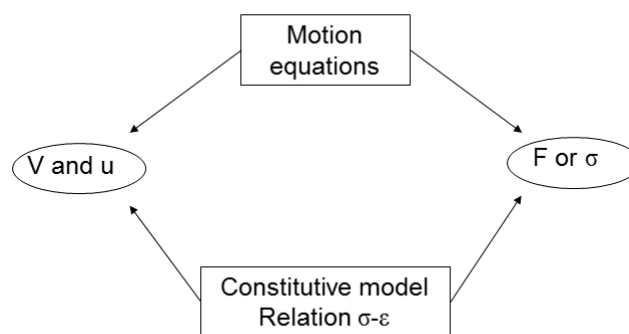


Figure 5.3-1: General computation sequence(Billiaux & Cundall (1993))

The resolution method implemented in FLAC presents advantages and disadvantages comparing to the implicit method used in the Finite Element Method.

For a linear problem expressed in small deformation hypothesis, the small time step imposed in the explicit scheme results in a number of iterations to reach the solution, which is not the case in an implicit scheme. However, the explicit scheme allows the non-linear computations without additional iterations. Indeed, this scheme does not require the computation and storage of the overall rigidity matrix. This shows that the advantage of an explicit method is in the resolution of non-linear problems assuming large strains or instabilities for example.

The explicit method is then an appropriate numerical tool for addressing the type of problems we are dealing with.

### 5.3.2. Numerical formulation

The solid body is divided, by the user, into a finite difference mesh composed of quadrilateral elements. Internally the software subdivides each element into two overlaid sets of constant-strain triangular elements. The four triangular sub-elements are termed *a*, *b*, *c* and *d*. The deviatoric stress components of each triangle are maintained independently, requiring sixteen stress components to be stored for each quadrilateral ( $4 \times (\sigma_{xx}, \sigma_{yy}, \sigma_{zz}, \sigma_{xy})$ ). The force vector applied on each node is the mean value of the two force vectors applied by the two overlaid quadrilaterals.

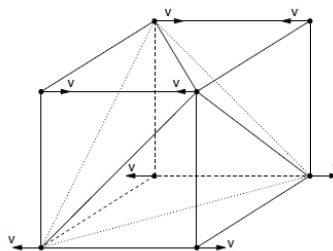


Figure 5.3-2: A discretized quadrilateral element used in FLAC.

The difference equations for a triangle are derived from the generalized form of Gauss divergence theorem:

$$\int_S n_i f ds = \int_A \frac{\partial f}{\partial x_i} dA \quad \text{Eq. 5.3-2}$$

Where,  $\int_S$  is the integral around the boundary of a closed surface,  $n_i$  is the unit normal to the surface *S*, *f* is a scalar, vector or tensor,  $x_i$  are the position vectors, *dS* is an incremental arc length and  $\int_A$  is the integral over the surface area *A*.

The strain rate  $\dot{\epsilon}_{ij}$  is written in terms of the node velocity using the gauss theorem:

$$\frac{\partial u_i}{\partial x_j} = \frac{1}{2A} \sum_s (\dot{u}_i^{(a)} + \dot{u}_i^{(b)}) n_j \Delta s \quad \text{Eq. 5.3-3}$$

$$\dot{\epsilon}_{ij} = \frac{1}{2} \left[ \frac{\partial u_i}{\partial x_j} + \frac{\partial u_j}{\partial x_i} \right] \quad \text{Eq. 5.3-4}$$

Where,  $\Delta s$  is the distance between the two consecutive nodes a and b, and A is the element area,  $\dot{u}$  the velocity vector.

The constitutive model and rotation adjustment are then used to derive a new stress tensor from the strain-rate tensor. Once the stresses have been calculated, the equivalent forces applied on each nodal point are determined. At each node, the forces from all surrounding quadrilaterals are summed, in order to give the net nodal force vector,  $\sum F_i$ . If the body is at equilibrium, or in steady-state flow,  $\sum F_i$  on the node will be zero. Otherwise, the node will be accelerated according to the finite difference of Newton's second law of motion:

$$\dot{u}_i^{(t+\frac{\Delta t}{2})} = \dot{u}_i^{(t-\frac{\Delta t}{2})} + \sum F_i^{(t)} \frac{\Delta t}{m} \quad \text{Eq. 5.3-5}$$

For large-strain problems, the new coordinate of the gridpoint is determined:

$$x_i^{(t+\Delta t)} = x_i^{(t)} + \dot{u}_i^{(t+\frac{\Delta t}{2})} \Delta t \quad \text{Eq. 5.3-6}$$

To solve static problems, the equation of motion must be damped to provide static or quasi-static solutions. The damping used in standard dynamic relaxation methods is the velocity-proportional. This is conceptually equivalent to a dashpot fixed to the ground at each nodal point.

The convergence criteria which controls the end of the iterations is based on the elements equilibrium. After each time step, an equilibrium test is performed and the unbalanced force is registered. The equilibrium is obtained when a very small unbalanced force defined by the user is reached. When the equilibrium occurs, the nodes' velocity is very small (a criterion of  $10^{-7}$ m/s is assumed acceptable).

### 5.3.3. Constitutive model in FLAC

A certain number of constitutive models are implemented in the software FLAC, which can be divided into three groups:

- The null model: a null material model is used to represent a material that is removed or excavated.
- Elastic model group: Elastic isotropic model and Elastic transversely isotropic model.
- Plastic model group: Drucker-Prager model, Mohr-Coulomb model, ubiquitous model, strain-hardening/softening model, bilinear strain hardening/softening ubiquitous-joint model, double-yield model, modified Cam-Clay model, Hoek-Brown model and Cysoil model.

All the models are implemented using the same algorithm formulation: from the previous stress state computed at the last time step and the total strain increment at the actual time step, the stress increment is calculated and the new stress state is determined. It is also possible to implement a new constitutive model in FLAC.

### 5.3.4. Interface elements

FLAC provides interfaces that are characterized by Coulomb sliding and/or tensile separation model. Interfaces have friction, cohesion, dilatancy and shear stiffness and tensile strength properties. An interface can be specified between structural elements and a grid (in our application case) or between structural elements. An interface is represented as a normal and shear stiffness between two planes, which may be in contact with each other. FLAC uses a contact logic, which is similar to the one employed in the distinct element method, on either side of the interface (Cundall and Hart, 1992).

Under some circumstances, it may be necessary to use an interface to join two sub-grids. This type of interface is declared as “glued” on the INTERFACE command, thus preventing any slip or separation; values of friction, cohesion and tensile strength are not needed in this case, and are ignored if given. However, shear and normal stiffness must be provided. FLAC does ‘mass scaling’ based on stiffness so the response and solution convergence will be very slow if very high stiffness are specified. It is recommended that the lowest stiffness consistent with small interface deformation be used. A good rule-of-thumb is that  $K_n$  and  $K_s$  be set to ten times the equivalent stiffness of the stiffest neighboring zone. Where  $K_n$  and  $K_s$  are respectively the normal and the shear stiffness of the interface, and the apparent stiffness of a zone in the normal direction is:

$$\max \left[ \frac{(K + \frac{4}{3}G)}{\Delta z_{min}} \right] \quad \text{Eq. 5.3-7}$$

Where  $K$  &  $G$  are respectively the bulk and shear moduli; and  $\Delta z_{min}$  is the smallest width of an adjoining zone in the normal direction.

This method is reasonable if the material on the two sides of the interface are similar, and the variations of stiffness occur only in the lateral directions. However, if the material on one side of the interface is much stiffer than that on the other side, the Eq. 5.3-7 should be applied to the softer side. In this case, the soft side dominates the deformation of the whole system; making the interface stiffness ten times the soft-side stiffness will ensure that the interface has minimal influence on system.

### 5.3.5. Structural elements

The structural elements can either be independent or coupled to the grid representing the solid continuum. The structural-element logic is implemented with the same explicit Lagrangian formulation procedure as the rest of the code. Large displacements, including geometric nonlinearity, can be used by specifying a large-strain solution formulation, and the full dynamic response of the system in the time domain can also be obtained with the dynamic-analysis option.

Six different structure elements can be defined in FLAC. Each of these members can be joined to one another and/or the grid: Beam Structural Elements, Cable Structural Elements, Pile Structural Elements, Shell Structural Elements, Geogrid Structural Elements and Liner Structural Elements.

### 5.3.6. Geogrid structural elements

The mechanical behaviour of each geogrid can be divided into the structural response of the geogrid material itself, and into the way in which the geogrid element interacts with the medium.

Geogrids elements are used to model flexible membranes whose shear interaction with the soil are important, such as geotextiles and geogrids.

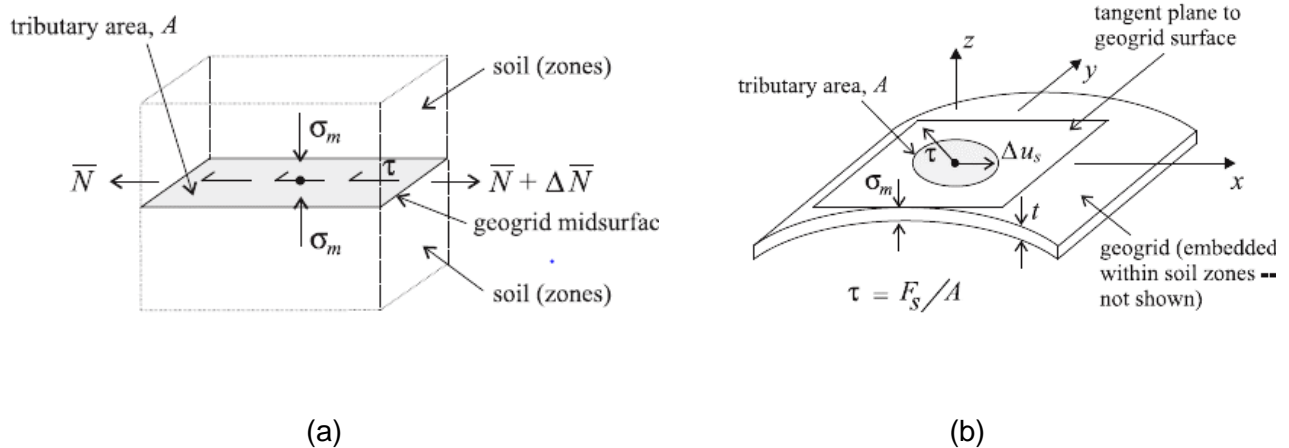


Figure 5.3-3: (a) Stresses acting on the geogrid elements surrounding a node, (b) Interface behaviour of a geogrid node (FLAC manual report).

The geogrid behaves as an isotropic or orthotropic linear elastic material with no failure limit. The behaviour at the geogrid-soil interface is summarized in Figure 5.3-3, it is a shear behaviour controlled by Mohr-Coulomb model. The stresses, consisting of an effective confining stress  $\sigma_m$  and of a total shear stress  $\tau$ , are balanced by the membrane stresses developed within the geogrid itself. The interface behaviour is represented numerically at each geogrid node by a rigid attachment in normal direction and spring-slider in the tangent plane to the geogrid surface.

### 5.3.7. Cap-yield model implemented in FLAC

The CYSoil model is a soil model presented in FLAC version 6. This model is a strain-hardening constitutive model that is characterized by a frictional Mohr-Coulomb shear envelope and an elliptic volumetric cap in the  $(p_0, q)$  plane. The model uses three-yield surfaces that includes deviatoric (shear), volumetric (cap) and tension cut off. The CYSoil model in FLAC3D 6 is an updated version of the FLAC3D 5 CYSoil model with the following built-in features:

- A cap hardening law to capture the volumetric power law behaviour observed in isotropic compaction tests.
- A friction-hardening law to reproduce the hyperbolic stress-strain law behaviour observed in drained triaxial tests;
- A compaction/dilation law to model irrecoverable volumetric strain taking place because of soil shearing.

The formulation of this model is detailed as follow:

- Incremental elastic law
- Shear yield and Potential functions

- Volumetric Cap Criterion
- Tensile Yield Criterion
- Friction Hardening
- Cap Hardening

### 5.3.7.a. Incremental elastic law

The elastic behaviour is expressed using Hooke's law. The incremental law expression in terms of principal stress and strain has the following form:

$$\begin{aligned}\Delta\sigma_1 &= \alpha_1\Delta\varepsilon_1^e + \alpha_2(\Delta\varepsilon_2^e + \Delta\varepsilon_3^e) \\ \Delta\sigma_2 &= \alpha_1\Delta\varepsilon_2^e + \alpha_2(\Delta\varepsilon_1^e + \Delta\varepsilon_3^e) \\ \Delta\sigma_3 &= \alpha_1\Delta\varepsilon_3^e + \alpha_2(\Delta\varepsilon_1^e + \Delta\varepsilon_2^e)\end{aligned}\tag{Eq. 5.3-8}$$

Where  $\alpha_1 = K^e + \frac{4G^e}{3}$ ,  $\alpha_2 = K^e + \frac{2G^e}{3}$ , and  $K^e$  and  $G^e$  are respectively current tangent elastic bulk and shear moduli.

The elastic bulk modulus  $K^e$  is derived internally, using the relation:

$$K^e = G^e \frac{2(1+\nu)}{3(1-2\nu)}\tag{Eq. 5.3-9}$$

It is obvious that the implemented elastic model is a hypo-elastic formulation which does not derive from a potential as proposed by Ziegler (1968), Ziegler & Wehrli, C. (1987), Collins & Houlsby (1997) and Collins & Hilder (2002).

### 5.3.7.b. Shear yield and Potential functions

The shear yielding is defined by a Mohr-Coulomb criterion:

$$f^s = M(p + c \cdot \cot\phi_f) - q\tag{Eq. 5.3-10}$$

Where  $M = 6 \sin\phi_m / (3 - \sin\phi_m)$ ,  $\phi_m$  is the mobilized friction, a quantity which can increase between an initial value and a final value  $\phi_f$  set by the user.

With a non associated potential function:

$$g^s = M^* - q^*\tag{Eq. 5.3-11}$$

Where  $q^* = -[\sigma_1 + (\delta^* - 1)\sigma_2 - \delta^*\sigma_3]$ ,  $\delta^* = (3 + \sin\Psi_m) / (3 - \sin\Psi_m)$ ,  $M^* = 6 \sin\Psi_m / (3 - \sin\Psi_m)$ , and  $\Psi_m$  is the mobilized dilatancy angle.

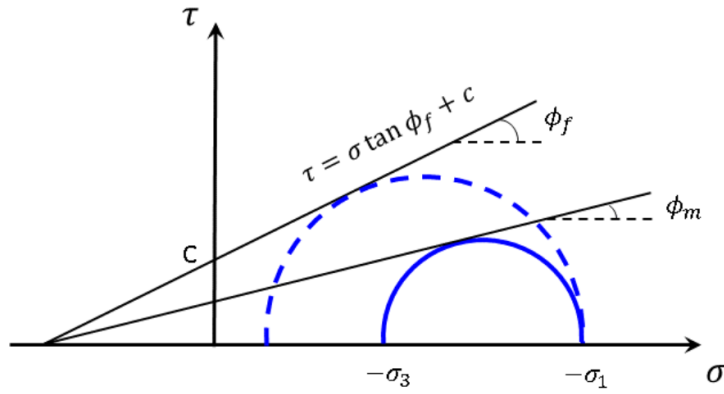


Figure 5.3-4: Mohr circles at in-situ stress and at failure.

### 5.3.7.c. Volumetric Cap Criterion

Yield on the cap is associated with the criterion:

$$f^s = g^s = \frac{q^2}{\alpha^2} + p^2 - p_c^2 \quad \text{Eq. 5.3-12}$$

Where  $\alpha$  is a dimensionless parameter defining the shape of the elliptical cap in the (p, q) plane, and  $p_c$  is the current cap pressure.

### 5.3.7.d. Tensile Yield Criterion

The tensile yield function is the same as that used for the Mohr-Coulomb model:

$$f^t = g^t = \sigma^t - \sigma_3 \quad \text{Eq. 5.3-13}$$

Where  $\sigma^t$  is the tensile strength.

### 5.3.7.e. Friction Hardening

For most soils, the curve of deviatoric stress versus axial strain obtained in a drained triaxial test can be approximated by a hyperbola. The CYSoil model incorporates a friction-strain hardening law to capture this trend.

The evolution law for mobilized friction,  $\phi_m$  is given by Eq. 5.3-14

$$\sin \phi_m = \sin \phi_0 + \frac{\beta \gamma^p (1 + R) G_{ref} (\sin \phi_f - \sin \phi_0)}{(\sin \phi_f - \sin \phi_0) + \beta \gamma^p (1 + R) G_{ref} R_f} \quad \text{Eq. 5.3-14}$$

Where  $\phi_f$  is the ultimate/failure friction angle,  $\phi_0$  is an internal constant (which, by default is set equal to the user-provided mobilized friction angle under in-situ conditions),  $R_f$  is the failure ratio and one of the material parameters (less than 1.0 with a default value of 0.9),  $\beta$  is the calibration factor of the hardening rule,  $\gamma^p$  is the plastic shear strain, the R parameter is the ratio between the elastic and plastic rates of the volumetric strain.  $G_{ref}$  is a dimensionless elastic shear modulus reference specified by the user.

The mobilized plastic shear modulus can be expressed in terms of plastic shear strain:

$$\frac{G_m^p}{G_{m,i}^p} = \left( \frac{1}{1 + A\gamma^p} \right)^2 \quad \text{Eq. 5.3-15}$$

Where  $G_{m,i}^p$  is the value of  $G_m^p$  under in-situ conditions, and A is defined as follow:

$$A = \beta \frac{(1 + R)G_{ref}R_f}{\sin \phi_f - \sin \phi_0} \quad \text{Eq. 5.3-16}$$

### 5.3.7.f. Cap Hardening

Soil stiffness usually increases in a nonlinear way as a function of isotropic pressure. In the CYSoil model, the following power law describes soil volumetric behaviour in an isotropic compaction test:

$$\frac{dp}{d\varepsilon} = K_{ref}p_{ref} \left( \frac{p}{p_{ref}} \right)^m \quad \text{Eq. 5.3-17}$$

Where  $\varepsilon$  is the volumetric strain taken positive in compression,  $K_{ref}$  is the tangent elastic bulk modulus number, the product  $K_{ref}p_{ref}$  is the slope of the laboratory curve for  $p$  versus  $\varepsilon$  at reference effective pressure,  $p_{ref}$ , and  $m$  is a constant ( $0 < m < 1$ ).

The hardening modulus, H is defined as follow:

$$H = \frac{dp_c}{d\varepsilon^p} = K_{ref}p_{ref} \frac{(1 + R)}{R} \left( \frac{p_c}{p_{ref}} \right)^m \quad \text{Eq. 5.3-18}$$

Where  $p_c$  is expressed in terms of  $\varepsilon^p$ , the plastic volumetric strain:

$$p_c = p_{ref} \left[ K_{ref}(1 - m) \frac{(1 + R)}{R} \varepsilon^p \right]^{\frac{1}{(1-m)}} \quad \text{Eq. 5.3-19}$$

The tangent elastic modulus,  $k^e$  is expressed in terms of the hardening modulus H:

$$k^e = RH = K_{ref}p_{ref}(1 + R) \left( \frac{p_c}{p_{ref}} \right)^m \quad \text{Eq. 5.3-20}$$

### 5.3.7.g. Dilation Hardening

There are two options regarding the flow rule model: The flow rule is defined in terms of the relationship between the plastic volumetric strain and plastic deviatoric strain in a way that



$$\frac{d\varepsilon_s^p}{d\gamma^p} = \sin \Psi_m \quad \text{Eq. 5.3-21}$$

The first option of the plastic potential uses a constant dilation angle, similar to that of the Mohr-Coulomb model where a dilation angle ( $\Psi$ ) is defined and controls the dilation tendency of the material.

In the second option, the mobilized dilation angle is calculated based on the mobilized friction angle.  $\Psi_m$  is the mobilized dilation angle. The evolution law for mobilized dilation angle  $\Psi_m$  is given by the following law, based on Rowe's stress-dilatancy theory (1962):

$$\sin \Psi_m = \frac{\sin \phi_m - \sin \phi_{cv}}{1 - \sin \phi_m \sin \phi_{cv}} \quad \text{Eq. 5.3-22}$$

Where  $\sin \phi_m$  is given in terms of  $\gamma^p$ , and  $\sin \phi_{cv}$  is a constant given by the following expression:

$$\sin \phi_{cv} = \frac{\sin \phi_f - \sin \Psi_f}{1 - \sin \phi_f \sin \Psi_f} \quad \text{Eq. 5.3-23}$$

Where  $\phi_f$  and  $\Psi_f$  are respectively ultimate values of friction and dilation.

This constitutive model was used to simulate the behaviour of the soft soil supporting the granular platform in the unpaved roads application. In fact, the CYSoil model is a shear and volumetric hardening/softening model that provides a comprehensive exhibition of the nonlinear behaviour of soils. This double-yield model can present a more realistic representation of the loading/unloading response of soils (Itasca Group, 2012).

### 5.3.8. Model geometry

The plate load test performed in Chapter 3 was simulated using FLAC3D software. Due to the symmetry, only the quarter of the domain is modelled. The quarter of a cylinder with a radius of 900 mm represents the quarter soil layers with 600 mm of subgrade and 220 mm of base course. Two different simulations with and without reinforcement were performed in order to compare the reinforcement effect. An interface is placed between the subgrade and the base course for both cases, and another interface is added between the geosynthetic and the base course in the reinforced simulation.

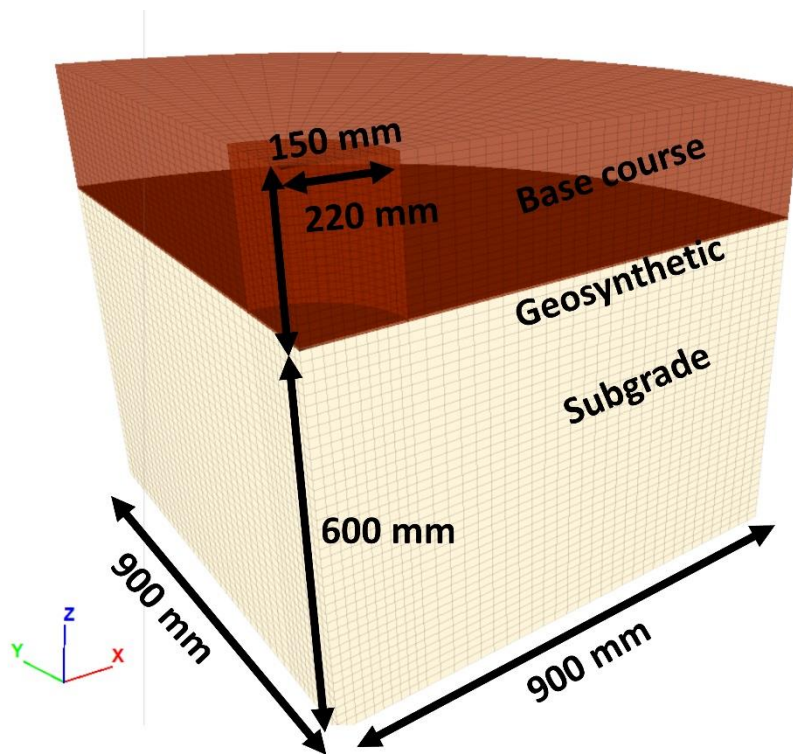


Figure 5.3-5: The model geometry.

The boundary conditions are imposed regarding the symmetry and the physical model. In fact, the displacement in the z direction at the bottom face and the displacement in the normal directions of the model lateral faces were blocked.

The influence of the boundary conditions and the domain limits was studied by changing the domain dimensions and looking at its influence on the results in terms of displacements and stresses states. This study showed no boundary effects with the current model dimensions. Moreover, a sensibility analysis was conducted using different element sizes to determine a suitable mesh that brings balance between accuracy and computing time. The model is composed of 48,000 zones and 5,101 grid points.

## 5.4. Parameters calibration

The characterisation of the soil materials used in the physical model was based on the laboratory geotechnical Chapter 2 (triaxial and shear box test). The results of these characterisation tests were used to calibrate the constitutive models parameters used in the numerical simulation.

### 5.4.1. Base course

Table 5.4-1: The base course Mohr-Coulomb Model calibrated properties.

Density (kN/m <sup>3</sup> )	18
K (Elastic bulk modulus) (MPa)	125
G (Elastic shear modulus) (MPa)	58
$\nu$ (Poisson's ratio)	0.3

$\varphi$ (friction angle)(°)	37
$\Psi$ (dilation angle)(°)	15
C (cohesion)(kPa)	10

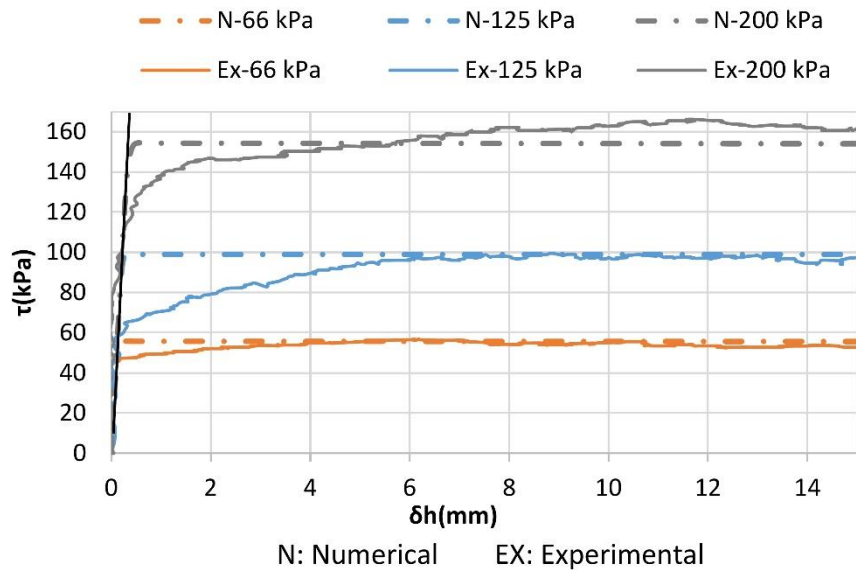


Figure 5.4-1: Shear stress versus displacement in the numerical and physical simulations of the shear box test, on the base course material.

The base course material used in the physical model was characterised using a large shear box test. In order to simulate the same base course performances in the numerical model, a numerical shear box test was performed. As mentioned before, the Mohr-Coulomb constitutive model was used for the base course material. The comparison between the numerical and experimental stress versus the displacement curves at the three different normal stresses (66 kPa, 125 kPa, 200 kPa) is illustrated in Figure 5.4-1. The illustrated elastic perfectly plastic curves correspond to the parameters shown in Table 5.4-1. The Mohr-Coulomb constitutive model requests a minimum number of parameters. The granular material presents a non-linear behaviour that cannot be taken into consideration in the used constitutive model. The focus in this study was on the subgrade behaviour, therefore, another more complex constitutive model was not chosen for the base course material.

## 5.4.2. Subgrade

The focus in this study is on the behaviour of the soft soil material. The Cap-yield constitutive model implemented in FLAC was used to illustrate the subgrade behaviour. A shear and volumetric hardening/softening model that can simulate the nonlinear behaviour of the soil and the loading unloading behaviour.

The model was calibrated based on a monotonic triaxial test and a cyclic triaxial test. Moreover, the parameters were validated based on a large-scale monotonic plate load test.

### 5.4.2.a. The triaxial test

Three triaxial experimental tests were performed on the extracted specimens, from the installed and compacted large-scale platform, with three different confinement stresses (50 kPa, 100 kPa and 200 kPa). An undrained experimental test was performed on an unsaturated soil (soil at 72% of saturation). The experiments give the apparent cohesion ( $C_{UU}$ ) of 19 kPa and the apparent friction angle ( $\varphi_{UU}$ ) of 28° of the unsaturated soil. However, in the numerical simulations the soft soil is assumed to be a dry soil. The apparent behaviour of the unsaturated soil was used to calibrate the behaviour of the dry soil in the numerical simulations. It is obvious that the experimental undrained test is not performed as an isochoric (no volume changes) tests, the water is simply not allowed to move outward or inward.

Table 5.4-2: Subgrade Cap-Yield Model calibrated properties.

Density (kN/m <sup>3</sup> )	19
K (Elastic bulk modulus) (MPa)	57.5
G (Elastic shear modulus) (MPa)	26.5
$\nu$ (Poisson's ratio)	0.3
$\varphi$ (friction angle)(°)	28
$\Psi$ (dilation angle)(°)	5
C(cohesion) (kPa)	19
Rf (Failure ratio)	0.9
$\varphi_f$ (Ultimate friction angle) (°)	28
$\beta$ (Calibration factor)	0.3
Shear reference	200
Critical friction angle(°)	19
Pressure-reference (kPa)	100
Exponent m	0.99

The parameters given in Table 5.4-2 are the final parameters that gave the matching curves presented in Figure 5.4-2. The parameters that affected most the calibration are:

- The shear – reference  $G_{ref}$  a dimensionless elastic shear modulus, the failure ratio  $R_f$  and the calibration factor of the hardening rule that affect the friction hardening rule. These calibrated parameters are the same for the three models with the three different confinement stresses.

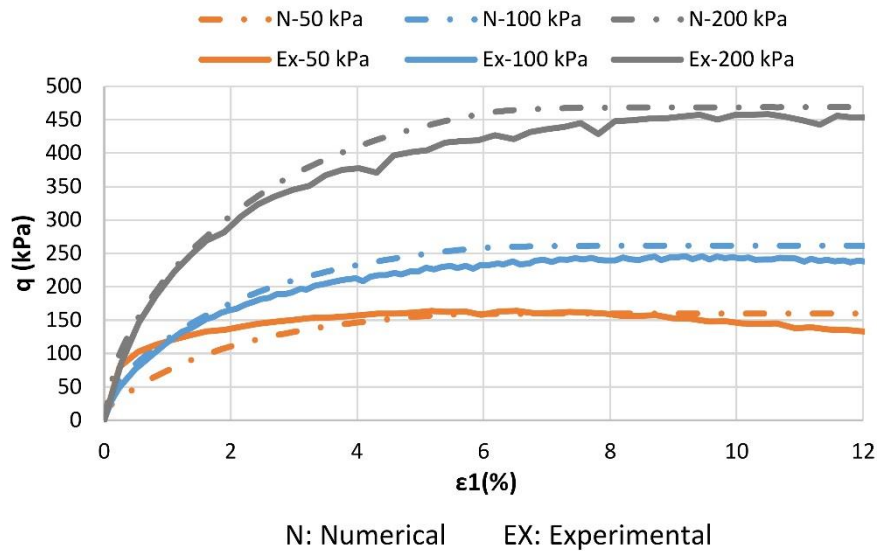


Figure 5.4-2: Deviatoric stress versus the axial strain in the numerical and physical simulations of the triaxial test, on the subgrade material.

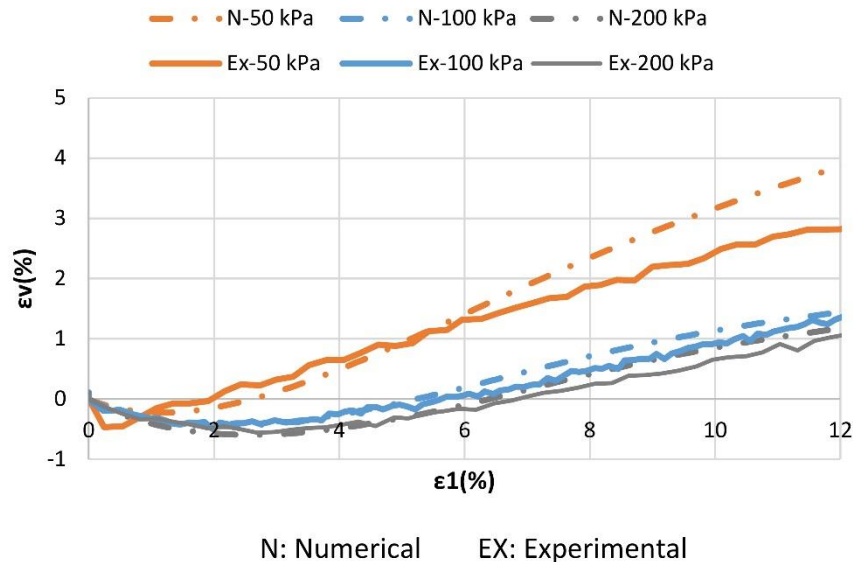


Figure 5.4-3: Volumetric strain versus the axial strain in the numerical and physical simulations of the triaxial test, on the subgrade material.

The second option proposed for the dilation-hardening (section 5.3.7) rule was chosen for this simulation since it can predict the volumetric strain changes with the axial strain variation. The mobilized dilation angle is calculated based on the mobilized friction angle.  $\Psi_m$  is the mobilized dilation angle. The evolution law for mobilized dilation angle  $\Psi_m$  depends on the mobilized friction angle and  $\phi_{cv}$ . where  $\phi_{cv}$  is a function of the ultimate friction angle and dilatancy angle. For the triaxial test with the confinement stress of 50 kPa the  $\phi_{cv}$  taken is equal to 15°. While for the confinement stress of 100 and 200 kPa the  $\phi_{cv}$  taken is equal to 19°.

Moreover, the cap-yield constitutive model simulates the loading-unloading state of the soil and the residual deformation and moduli. The simulation of the soil behaviour on the soil was performed based on cyclic triaxial tests performed on the extracted specimens under 100 kPa of confining

stress. The Figure 5.4-4 shows close numerical and experimental curves especially for the first loading-unloading cycle. However, the cap-yield model does not include the material hardening under cycles, it can only predict the first loading-unloading cycle.

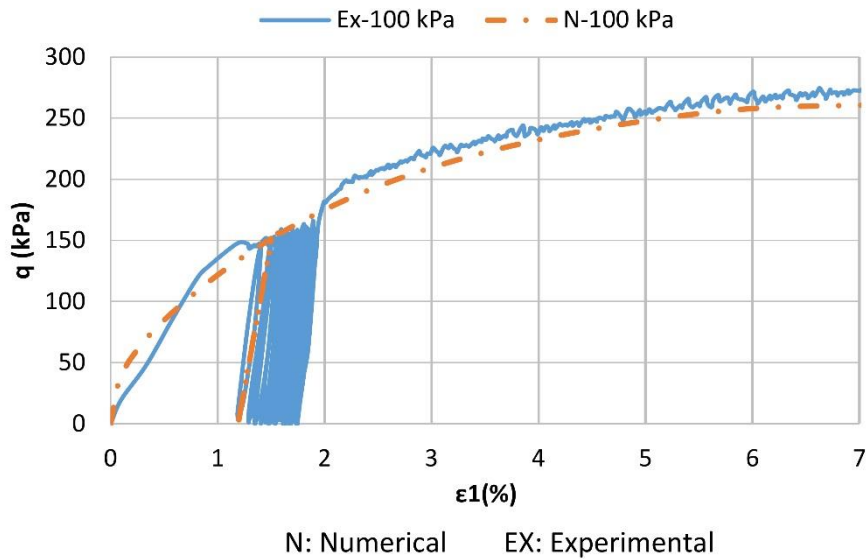


Figure 5.4-4: Deviatoric stress versus the axial strain under cyclic load in the numerical and physical simulations of the triaxial test, on the subgrade material.

### 5.4.3. Base course/Subgrade interface

As mentioned before the interfaces provided by FLAC are characterized by Coulomb sliding and/or tensile separation. FLAC manual recommends a method to determine the interface stiffness in the case of contact between a material much stiffer than the other. This method considers that the  $K_s$  and  $K_n$  should be equal to ten times the equivalent stiffness of the softer neighbouring zone given by the Eq. 5.3-7. The cohesion and friction angle are equal to the soft soil parameters.

Table 5.4-3: The Base course/Subgrade interface.

Normal stiffness (MPa)	9 280
Shear stiffness (MPa)	9 280
Friction angle(°)	28
Cohesion (kPa)	19

#### 5.4.3.a. The plate load test

In order to reproduce the behaviour of the soft soil exhibiting large strain a comparison between a physical and numerical plate load test applied on the soft subgrade directly was conducted.

The aim of this experimental test was to reduce the problem of the subgrade in order to verify the behaviour of the soft soil without the interfaces, reinforcement and base course influences.

The experimental test was performed in the same geotechnical box, the same installation procedure, subgrade properties and thickness as in the full test with the base course layer. The load was applied via a 600 mm diameter plate with an external applied load of 80 kN that results in a contact stress of 280 kPa (Figure 5.4-5), which is the average applied load on the subgrade surface during the full

plate load test with the base course layer. The subgrade was instrumented as in the full test. Earth pressure cells were placed at the subgrade surface under the plate to verify the applied stress. Settlement sensors were placed under the plate to measure the settlement. On the subgrade surface five earth pressure cells were placed at different positions from the plate centre: under the plate centre, 100 mm, 200 mm 400 mm and 600 mm from the plate centre. The settlement sensors were placed at the same positions under the pressure cells. Moreover, earth pressure cells were placed in the subgrade depth. The earth pressure cells in the subgrade depth were placed at the plate centre at 200 mm, 400 mm and 600 mm in depth.



*Figure 5.4-5: Plate load test performed directly on the subgrade soil.*

Due to the symmetry, the quarter of the domain is modelled. The quarter of a square with 900 mm in dimension, represents the quarter soil layer with 600 mm in depth of soft subgrade. The simulation was resolved as a large-strain problem, in which the coordinate of new positions was calculated and updated for each step. In the physical simulation, the load was imposed on the plate surface, since the plate is a stiff plate the displacement at the surface is the same on the subgrade surface as under the plate, and the vertical stress is maximum at the plate edges; this was measured by the pressure cells. In the numerical model, the displacement measured in the experiment was imposed at the subgrade surface. The numerical stresses were determined and compared to the experimental measured stresses. Figure 5.4-6 shows the numerical model geometry according to the physical model geometry.

Figure 5.4-7 shows the surface settlement obtained in the numerical and physical models. The experimental settlements as given by the settlement sensors shows the same values under the plate of about 50 mm. This plate displacement was imposed on the subgrade surface in the numerical simulation as seen in the same Figure 5.4-7.

Figure 5.4-7 shows the surface settlement obtained in the numerical and physical models. The experimental settlements as given by the settlement sensors shows the same values under the plate

of about 50 mm. This plate displacement was imposed on the subgrade surface in the numerical simulation as seen in the same Figure 5.4-7.

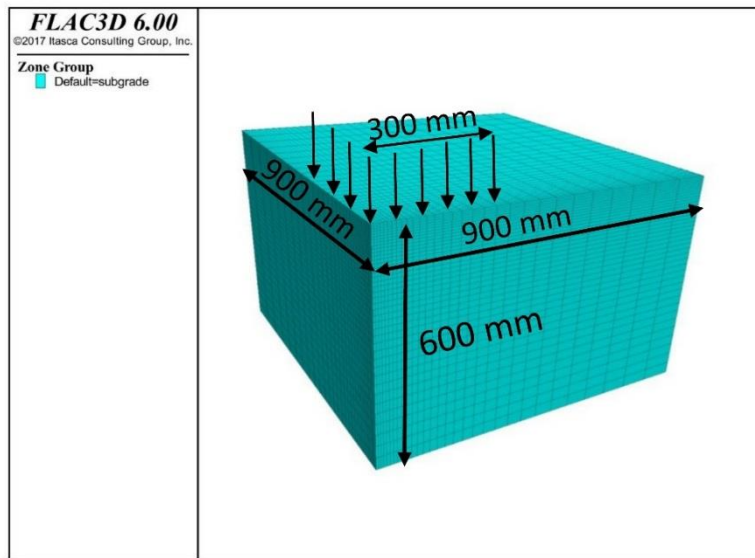


Figure 5.4-6: Subgrade loading simulation geometry.

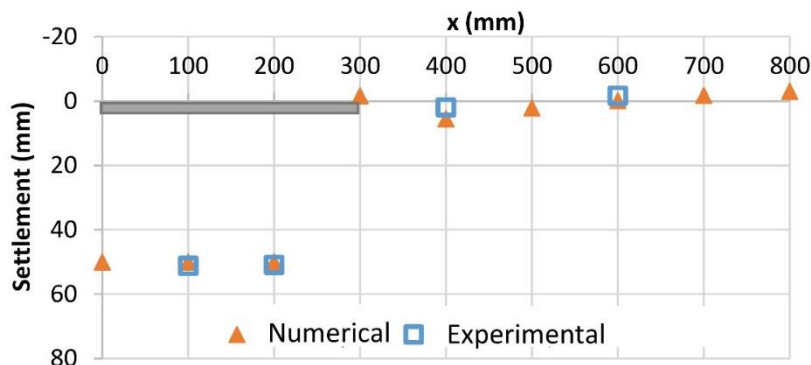


Figure 5.4-7: Surface settlement in the numerical and physical models.

The surface stress distribution shows in both numerical and physical models an edge localisation of about 300 kPa that decreases by getting closer to the centre to reach 200 kPa, which can capture the stress distribution under a stiff plate. The surface stress distribution in Figure 5.4-8, shows that the numerical constitutive model can predict the soft soil behaviour even under large-strain conditions.

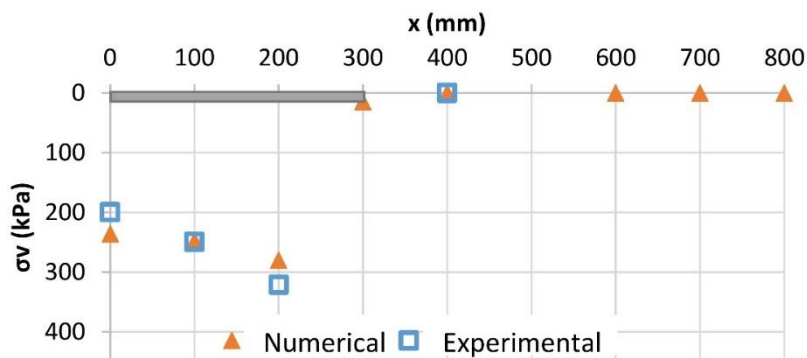


Figure 5.4-8: Surface stress developed in the numerical and physical models.



Figure 5.4-9 shows the numerical and experimental stresses under the plate centre in the subgrade depth. The curves show that the numerical model can capture the stress distribution in the subgrade depth. These comparison results verify the choice of the Cap-Yield constitutive model and its parameters calibration for the soft soil simulation. In fact, it shows that the numerical simulations capture the experimental behaviour of the subgrade behaviour.

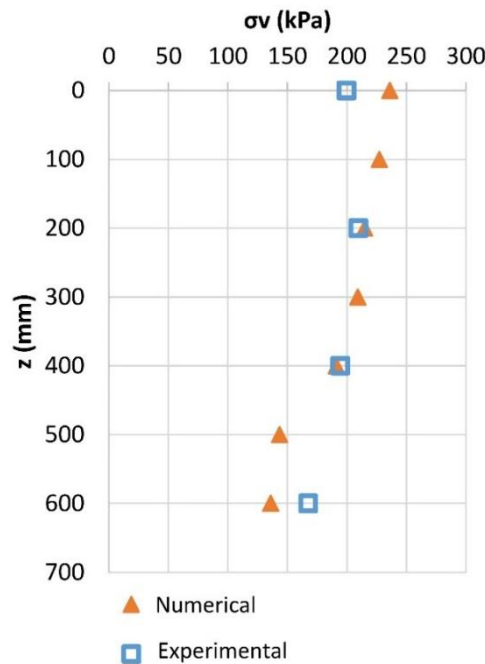


Figure 5.4-9: Stress developed at the plate centre in the subgrade depth in the numerical and physical models.

#### 5.4.4. Geosynthetic

The geogrid is simulated as a membrane characterized by an elastic behaviour in its plane. The experimental tests used to verify the numerical simulation are the ones conducted using GSY 1 as a reinforcement: a knitted coated geogrid with 1,000 kN/m as stiffness at 2% of strain. The membrane thickness taken is equal to 3 mm, so the Young modulus is equal to the geogrid stiffness expressed in kN/m and divided by the membrane thickness.

Table 5.4-4: Geosynthetic properties.

Isotropic material young modulus (MPa)	333
Poisson's ratio	0.33
Thickness (m)	3e-3

#### 5.4.5. Base course/Geosynthetic interface

The geogrid GSY 1(a knitted coated geogrid with 1,000 kN/m as secant stiffness at 2% of deformation) and base course interface was characterised using the same large shear box test used to characterise the base course material. A numerical shear box test was performed with geosynthetic placed at the interface. As mentioned before, the Mohr-Coulomb constitutive model was used on the geosynthetic interface. The comparison between the numerical and experimental shear stress versus the displacement curves at the three different normal stresses (66 kPa, 125 kPa,

200 kPa) is illustrated in Figure 5.4-10. The illustrated elastic perfectly plastic curves correspond to the parameters shown in Table 5.4-5. The Mohr-Coulomb constitutive model requests a minimum number of parameters. However, the interface presents a non-linear behaviour that cannot be taken into consideration in the used constitutive model.

Table 5.4-5: Interface Base course/Geosynthetics interface properties.

Coupling-cohesion-shear (kPa)	15
Coupling-friction-shear (°)	39
Coupling-stiffness-shear (MPa)	360

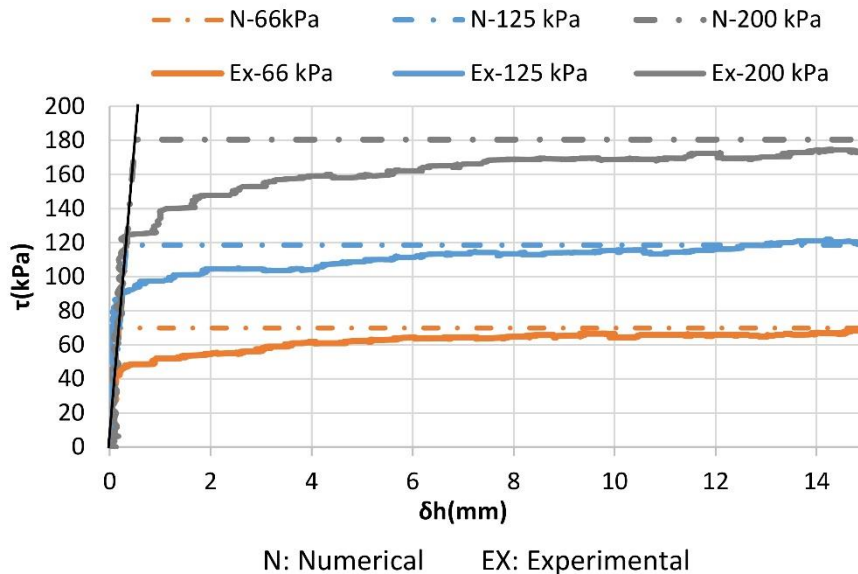


Figure 5.4-10: Shear stress versus displacement in the numerical and physical simulations of the shear box test, on the Geosynthetic and base course interface.

## 5.5. Monotonic loading simulation

The plate load tests performed and presented in Chapter 3 were simulated in this Chapter using Differential Element Methods. The geometry model is defined in Section 5.3.8 and the calibrated parameters are presented in Section 5.4. In this Section, the results of monotonic load plate simulations are presented. In details, a monotonic displacement was applied in this case on the top surface of the base course and the results were compared to the first load application results obtained from the experimental tests. In the numerical simulations, a displacement rate was applied until the average vertical stress at the surface reaches 560 kPa. This simulation was conducted for a reinforced and unreinforced case with two base course thicknesses: 220 mm and 350 mm. The simulation was resolved as a large-strain problem, in which the coordinate new positions are calculated and updated for each step.

## 5.5.1. Base course thickness 220 mm

### 5.5.1.a. Settlement

As mentioned above, a displacement rate was imposed at the base course surface, in order to have the same displacement over the plate surface as in the physical model. Figure 5.5-2 shows the settlement colour maps for both the reinforced and unreinforced models. It can be seen in both cases that the settlement is concentrated under the plate load. In order to analyse closely the results, the settlement profile on the subgrade surface is plotted and compared to the experimental settlement results in Figure 5.5-1. Under the plate centre line for the reinforced model, numerically the settlement is about 24 mm, experimentally 26 mm. For the unreinforced model, numerically the settlement is about 28 mm, experimentally 30 mm. By comparing the reinforced and unreinforced centre line settlement results, it can be noted that the reinforcement reduces the central settlement by 13% in both numerical and experimental models under monotonic load.

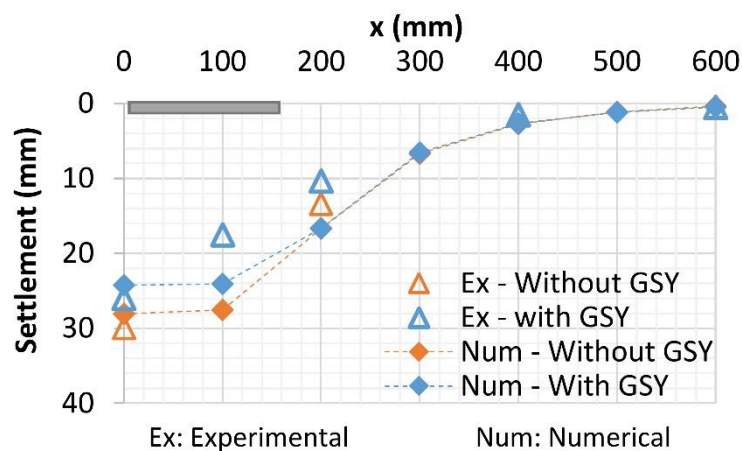
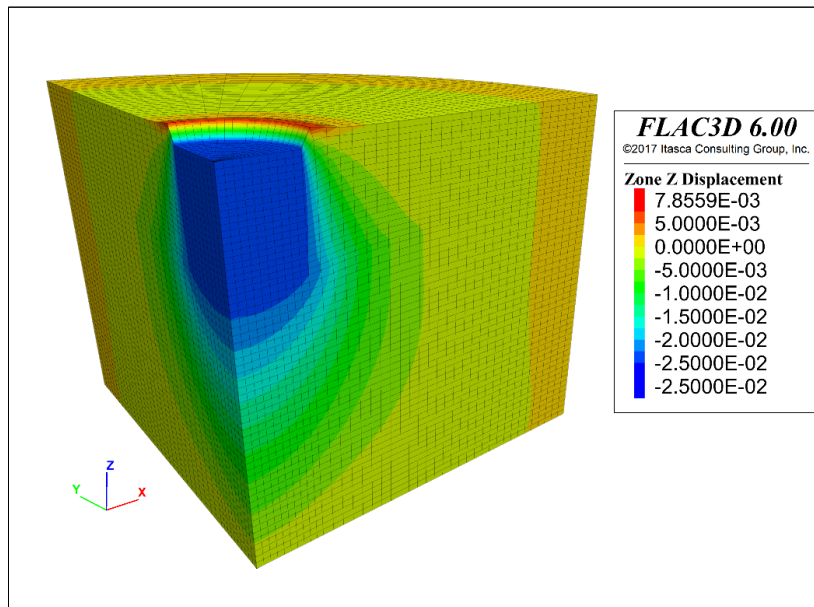
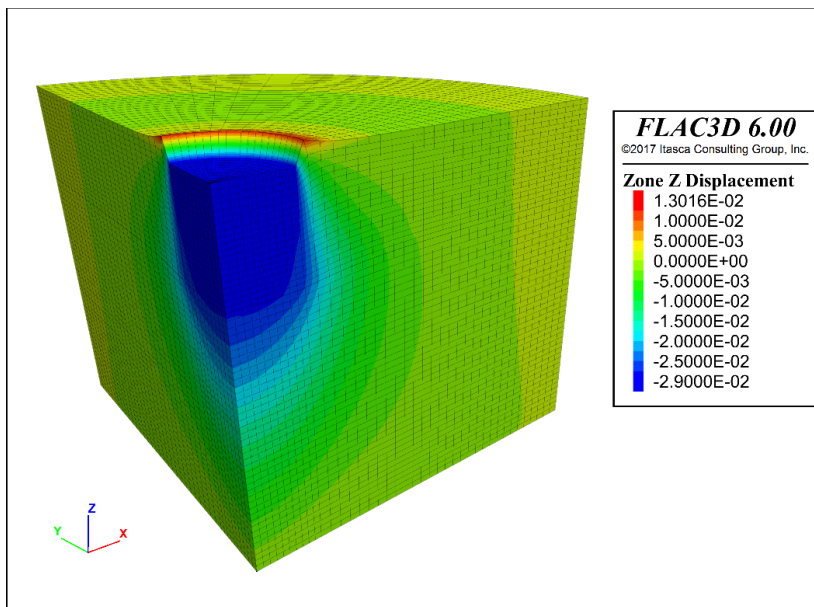


Figure 5.5-1: Subgrade surface settlement for the reinforced and unreinforced numerical and physical model.

However, it was proven experimentally, in the previous Chapters that with the settlement accumulation under cyclic load the reinforcement effect increases. More importantly, it is shown in Figure 5.5-1 that the settlement reaches zero at 400 mm from the plate centre line in the numerical and experimental models. Which proves that the stress distribution angle is not affected by the reinforcement. It is important to point out that the numerical and experimental settlement differ at 100 mm and 200 mm from the plate centre line. These differences can be due to the non-regular base course stiffness in the experimental tests and the uncontrolled phenomenon related to the compaction, or to the simplified constitutive law used for the Base course layer.



(a)

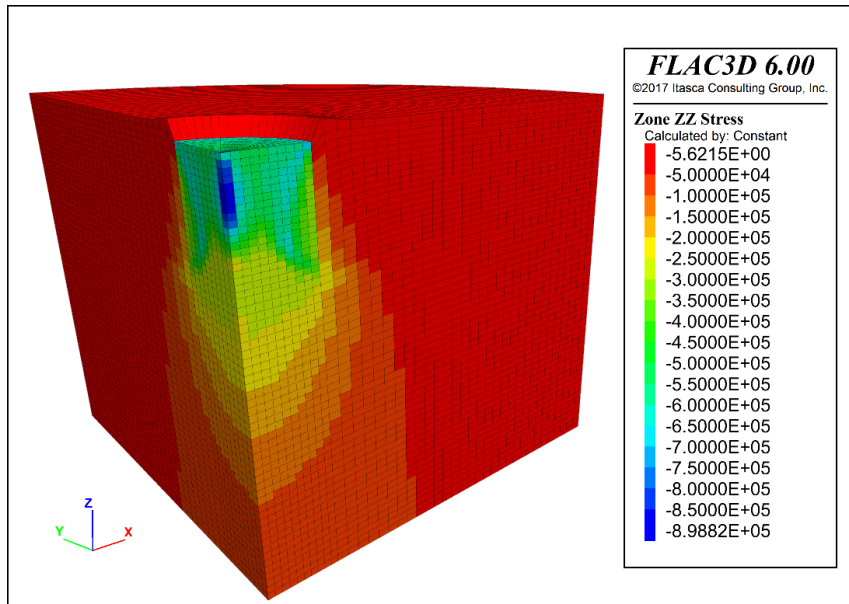


(b)

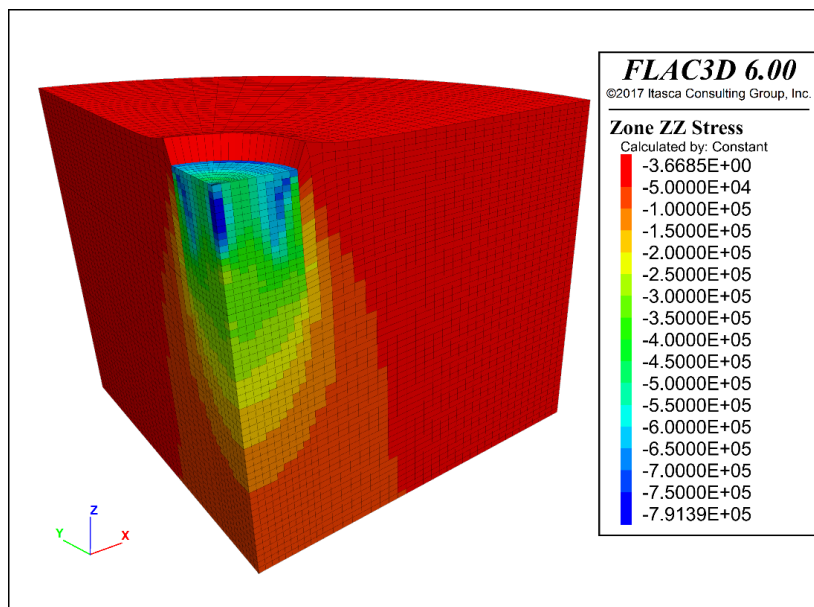
Figure 5.5-2: Settlement (a) reinforced model, (b) unreinforced mode in m.

### 5.5.1.b. Vertical stress

The vertical stress colour maps in the reinforced and unreinforced models are shown in Figure 5.5-3. It shows a non-constant vertical stress distribution under the plate, which is the case under a stiff plate. Moreover, it shows a variation in the stress distribution between the reinforced and unreinforced models. In order to analyse the results the vertical stress distributions on the subgrade surface were plotted in Figure 5.5-4.



(a)



(b)

Figure 5.5-3: Vertical stress distribution (a) reinforced model, (b) unreinforced model in Pa.

Figure 5.5-4 shows the comparison between the reinforced and unreinforced experimental and numerical vertical stress distributions on the subgrade surface.

For the unreinforced platform, close results are observed between the experimental and numerical stresses at the plate centre, and at a distance of 200 mm and 300 mm from the plate centre line. In fact, at the plate centre, the numerical and experimental vertical stresses are about 306 kPa.

For the reinforced platform a difference between the experimental and numerical results is observed particularly under the plate. Indeed, the numerical vertical stress at the plate centre line is 242 kPa, the experimental vertical stress is 200 kPa. However, for the reinforced and unreinforced platforms, the numerical and experimental vertical stresses reach zero between 300 and 400 mm from the plate centre. These slight differences can be due to local interface phenomenon between the aggregates and the geogrid apertures that are not perfectly simulated in this model and to the uncertainties of the stress measurements.

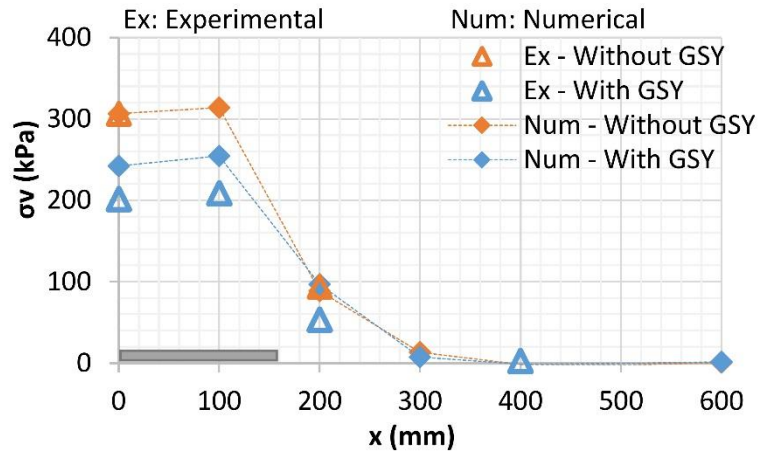


Figure 5.5-4: Subgrade surface vertical stress distribution for the reinforced and unreinforced numerical and physical model.

Figure 5.5-5 presents the vertical stresses under the plate centre in the layers depth at the end of loading. The experimental unreinforced platform curve is predicted in the numerical model. However, the predicted reinforced curve shows differences in the experimental curve especially at 400 mm of depth.

The numerical and experimental curves converge to the same value at 800 mm in depth, which shows again that the boundary conditions have no effect on the results.

It is worth noting that the vertical stress distribution measurements using the earth pressure cells in a soft soil is not accurate, due to the cell displacement and rotation during the measurement. Moreover, the measured stress is an average stress applied on the cell area of 100 x 200 mm. These measured stresses are compared to local stresses given by the numerical model.

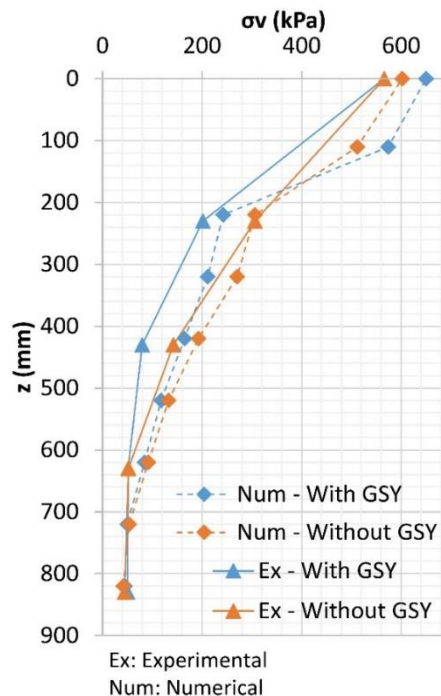


Figure 5.5-5: Vertical stress in depth under the plate centre for the reinforced and unreinforced numerical and physical model.

### 5.5.1.c. The Geosynthetic developed efforts

Figure 5.5-6 shows the geosynthetic nodes' displacement in the x-direction. The coloured map shows a maximum node displacement between 150 and 350 mm from the plate centre. Indeed, the geosynthetic follows the subgrade settlement curve, and the maximum curvature is observed between 150 and 350 mm. The nodes' displacement in the geosynthetic creates deformation in which it generates tension in the geosynthetic. An upward resultant within the GSY reduces the stress distribution on the subgrade soil and increases the platform bearing capacity due to the membrane effect.

Figure 5.5-7 shows the developed nodes resultant force in the x-direction in the membrane plane. Experimentally this resultant force in kN/m was deduced using the deformation measured by the optical fibre. Figure 5.5-8 shows a comparison between the numerical and the experimental developed force in kN/m in the geosynthetic. It shows a match between the experimental and the numerical developed force. It can be seen that the numerical simulation underestimates the developed force. Actually, in the average maximum developed force, the numerically geosynthetic is 10 kN/m and experimentally 12 kN/m. Moreover, the geosynthetic presents experimentally a larger area of tension than the numerical case. These differences can be due to the interface aggregates and geogrid apertures interaction that is reduced in this model to a simple shear law.

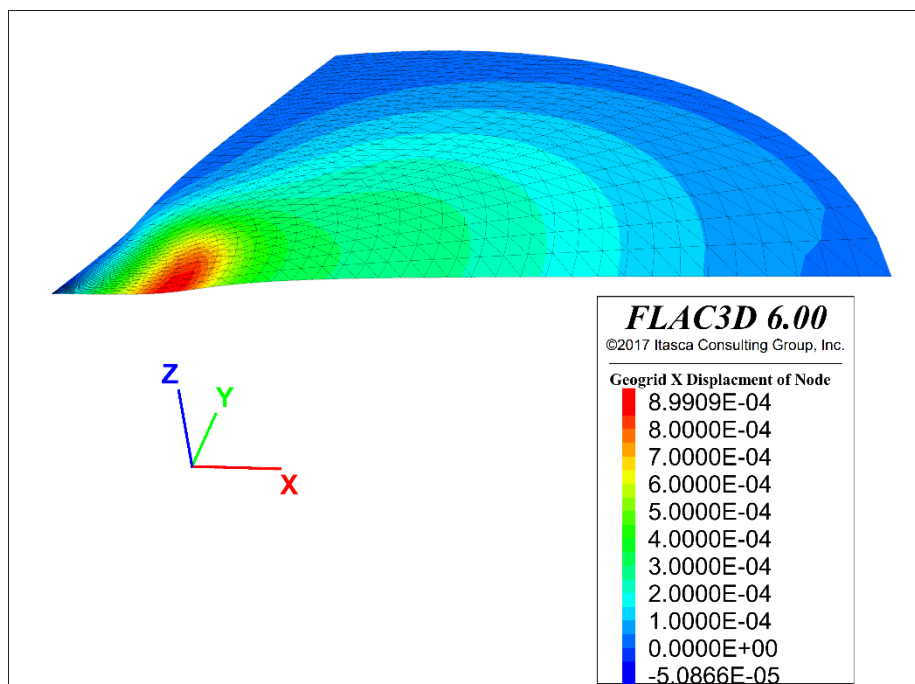


Figure 5.5-6: Geosynthetic nodes displacement in X-direction in m.

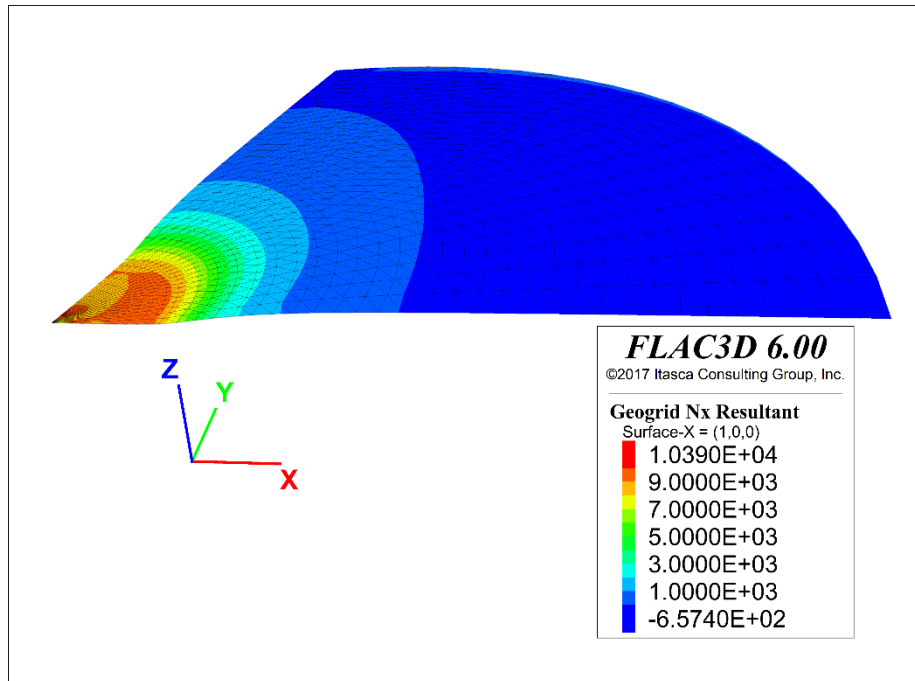


Figure 5.5-7: Geosynthetic nodes resultant force in X-direction in N/m.

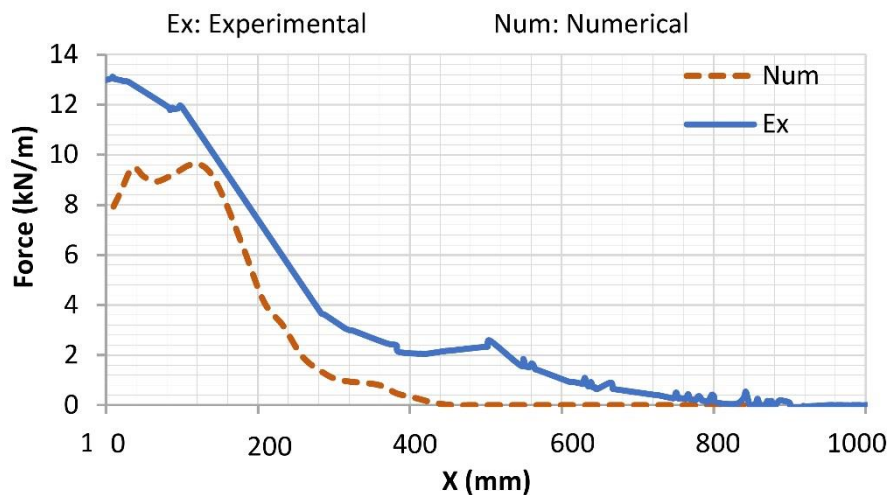


Figure 5.5-8: Force in kN/m developed in the geosynthetic in the numerical and physical model.

The interaction between the geogrid and aggregates is reduced in this model to a Mohr-Coulomb shear law. Figure 5.5-9 shows the developed shear stress on the base course / geosynthetic interface. The illustrated colour map shows a maximum developed shear between 150 and 400 mm from the plate centre line. The maximum developed shear varies between 130 and 100 kPa. These shear non-negligible values show an impact of the horizontal interface interaction on the reinforcement mechanisms. The impact of the interface stiffness will be studied later on in this Chapter.



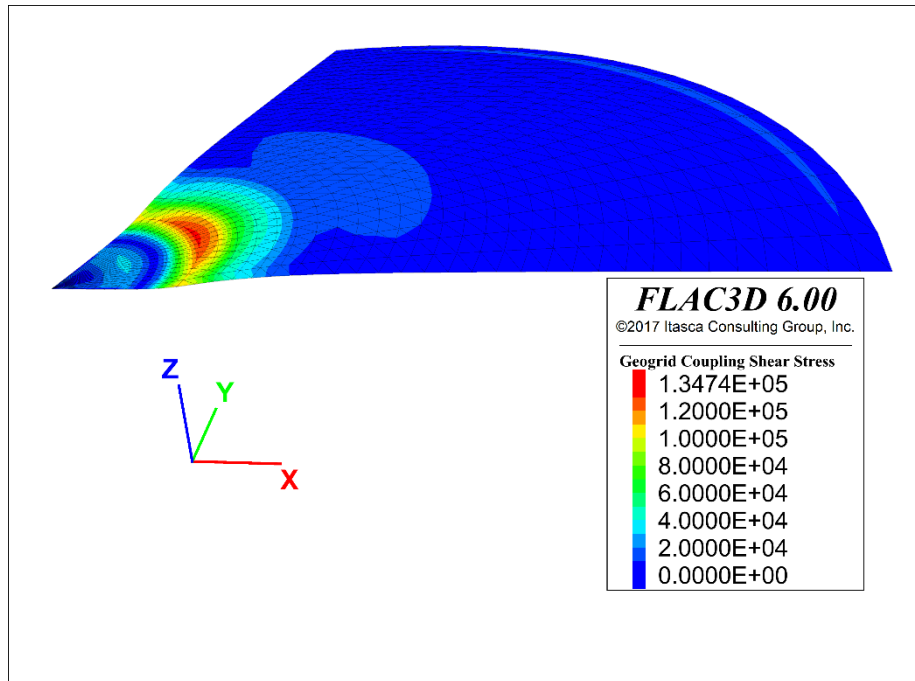


Figure 5.5-9: Geosynthetic/Base course interface shear stress in Pa.

### 5.5.2. Base course thickness 350 mm

Another numerical simulation was performed using the same calibrated parameters used previously for the model with 220 mm of base course thickness, but this time with 350 mm of base course thickness. The results of the numerical simulation were compared to the physical reinforced and unreinforced models results. However, as seen in Chapter 3, experimentally the reinforcement has no effect on the platform with 350 mm of base course thickness. The reinforced platform showed a larger displacement than the unreinforced one under the first cycle. This difference can be due to the uncontrollable compaction conditions. In this section, we will focus on the experimental displacement range to compare it with the numerical results.

Figure 5.5-10 illustrates the subgrade settlement of the reinforced and unreinforced platforms for the experimental tests, the model with the calibrated parameters and another model with  $45^\circ$  as a base course friction angle instead of  $37^\circ$ .

Differences in the settlement can be seen when comparing the results of the experimental tests and the numerical model to the calibrated parameters. The subgrade maximum settlement experimentally measured ranges between 5 and 10 mm, the calibrated model shows a maximum settlement around 15 mm. This difference is seen in the distributed vertical stress on the subgrade too. Figure 5.5-11 shows the vertical stress distribution on the subgrade surface for the physical and the two numerical models. A gap is observed between the experimental tests and the models with the calibrated parameters. Experimentally a maximum stress between 100 and 120 kPa is observed, numerically and with the above calibrated parameters it shows a maximum vertical stress between 160 and 180 kPa.

This gap can be due to the experimental base course compaction with three layers for the 350 mm instead of two for the 220 mm. So the lower two base course layers and the surface of the subgrade are subjected to more compaction than in the case of 220 mm.

Therefore, a change in the base course friction angle from  $37^\circ$  to  $45^\circ$  was imposed to have closer numerical results in the experimental ones. In fact, the model with  $45^\circ$  of base course friction angle presents between 12 and 13 mm of maximum settlement and between 130 kPa and 140 kPa of maximum stress. Moreover, the vertical stress distribution curve is closer to the experimental tests with this new calibrated parameter.

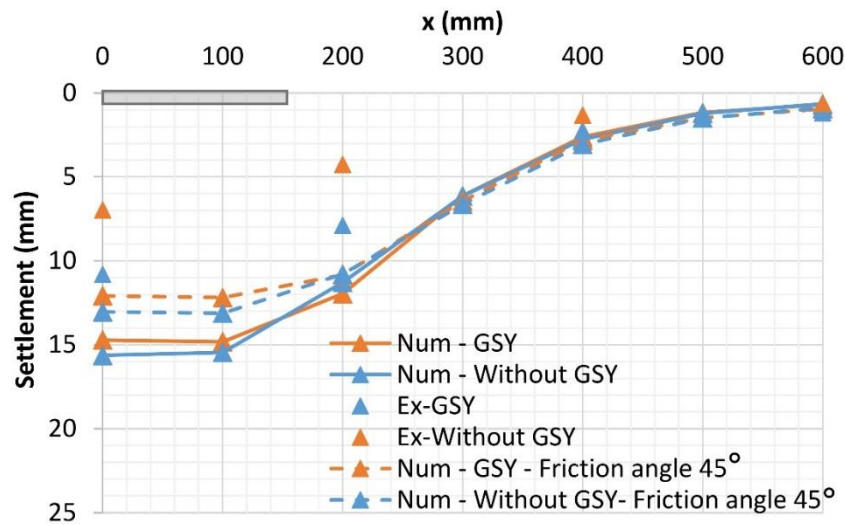


Figure 5.5-10: Subgrade surface settlement for the reinforced and unreinforced numerical and physical model.

However, it can be seen that the calibrated model based on the 220 mm experimental tests gives a higher estimation of the settlement and the stresses. More importantly, for the numerical results, the reinforcement effect is not as important in that case of 350 mm base course thickness as seen experimentally.

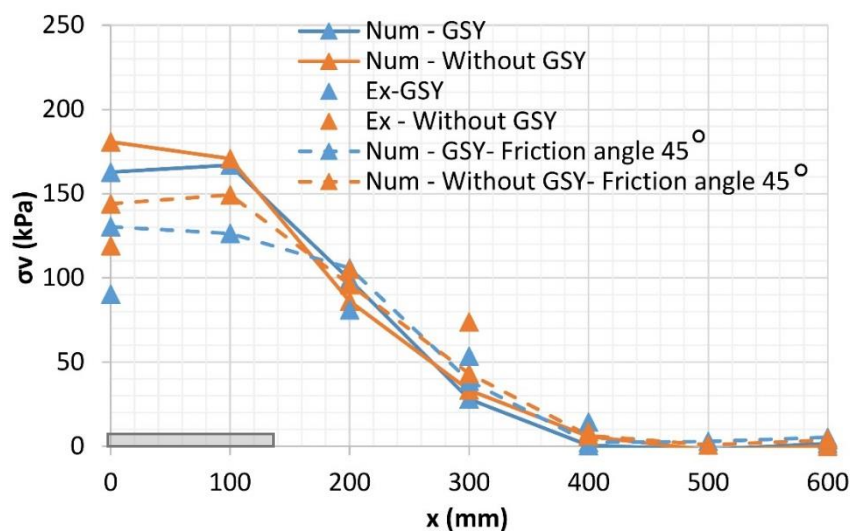


Figure 5.5-11: Subgrade surface vertical stress distribution for the reinforced and unreinforced numerical and physical model.

The settlement developed in this case is not enough to develop the required tension in the geosynthetic and to improve the bearing capacity of the platform. In addition, this was shown in Figure 5.5-12 that illustrates the developed force in the geosynthetic in the numerical models with 220 and 350 mm of base course thicknesses. The maximum tension developed in the geosynthetic

for 220 mm is about 9 kN/m and for the 350 mm is about 6 kN/m. In the latter case, the reinforcement is less loaded by 35% than the reinforcement of 220 mm of base course thickness.

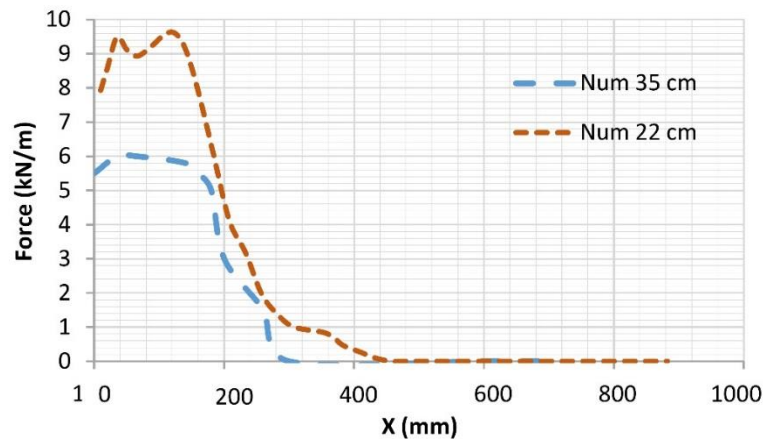


Figure 5.5-12: Force in kN/m developed in the geosynthetic in the numerical model with two base course thicknesses (220 mm and 350 mm).

## 5.6. Parametric sensitivity study

In order to better understand the mechanisms' developed and how the parameters affect the stress distribution on the subgrade surface, a numerical parametric sensitivity was performed on the reinforced 220 mm of base course model. It is worth pointing out that in this Section the reference parameters correspond to the parameters values previously calibrated in Section 5.4 and validated experimentally in Sections 5.5.

### 5.6.1. Base course parameters effect

The base course parameters' (Dilatancy  $\Psi$ , Friction angle  $\varphi$ , Young modulus  $E$ ) effects on the stress distribution under large-strain conditions were studied. Under the same loading condition previously presented, the same subgrade properties and the same reinforcement conditions, the variation of the base course parameters was performed.

Figure 5.6-1 illustrates the effect of the parameters on the maximum vertical stress developed at the subgrade surface plate centre. In the graph (Figure 5.6-1), the x-axis is a dimensionless ratio. It is a ratio between the modified and the reference parameters. The reference parameters correspond to the parameters previously calibrated and compared experimentally to the 220 mm of the reinforced and unreinforced models ( $\varphi_{ref} = 37^\circ$ ,  $\Psi_{ref} = 37^\circ$ ,  $E_{ref} = 150$  MPa). Only one parameter varied while the other were fixed to the reference parameters. It is observed that, when plasticity occurs in the base course layer, the elastic modulus is the parameter that affects the least the stress distribution as seen in Figure 5.6-1. It is the friction angle and the dilatancy that dominate the stress distribution.

In literature, Leng & Gabr (2006) developed an analytical design method based on Odemark's method. This method is based on the elastic layer analysis, and the vertical stresses distribution are related to the base course and subgrade elastic moduli ratio. However, for large displacement

problems like this problem, the plastic state is reached in the base course layer and the elastic approach is not valid.

In conclusion, the friction angle affects highly the vertical stress distribution in this large – strain application, which means that even for a monotonic load the analytical elastic approaches are not applicable.

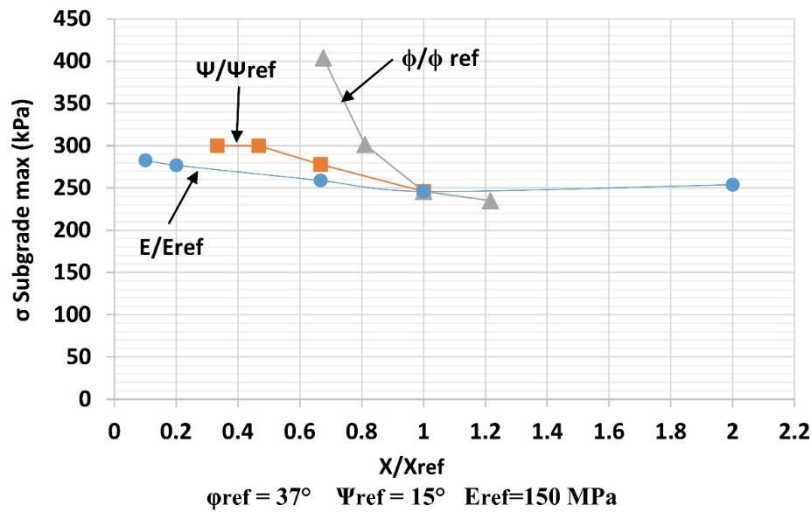


Figure 5.6-1: Base course dilatancy, friction angle and elasticity modulus effect on the maximum vertical stress on the subgrade surface.

## 5.6.2. Base course thickness effect

The base course thickness highly affects the stress distribution angle. The estimation of the thickness sensitivity under these conditions was performed and presented in Figure 5.6-2. The linear equation slope is equal to -150. The curves show a high influence of the base course thickness. In fact, if the base course thickness is doubled from 100 mm to 200 mm, then the maximal vertical stress decreases from 250 kPa to 100 kPa.

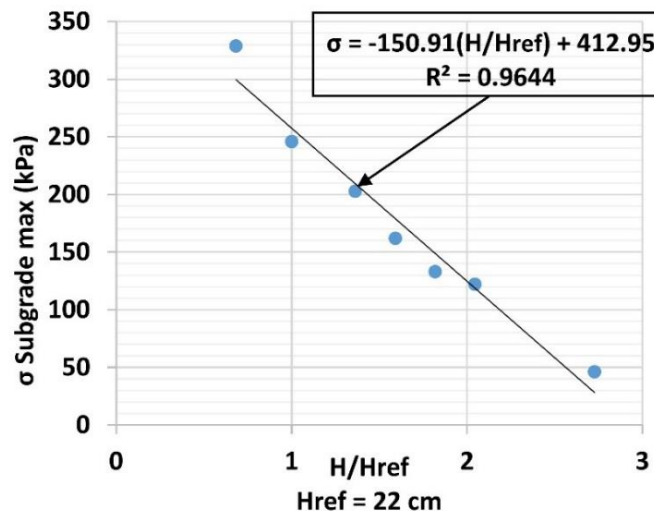


Figure 5.6-2: Base course thickness effect on the maximum vertical stress on the subgrade surface.

### 5.6.3. Geosynthetic/ base course interface effect

One of the reinforcement mechanisms is the confinement of the base course by the interlocking between the aggregates and the geogrid apertures or by the friction in the case of a geotextile. In the continuous-based differential element method model the interface between the geogrid and the aggregates is reduced to a shear friction constitutive law. In order to verify the effect of the interface interaction friction on the load distribution in the developed model of 220 mm of base course the interface friction and elastic modulus were varied. Figure 5.6-3 shows the effect of the ratio between the friction angle and the reference parameter ( $\Phi_{ref} = 39^\circ$ ) on the maximum vertical stress. Similarly, the effect of the Young modulus ratio on the vertical stress distribution is illustrated in Figure 5.6-3. The linear equations of both the friction angle and the elastic modulus show relatively small slopes, of -17 for the friction angle and -24 for the elastic modulus. These results show the limited effect of the interface properties on the global behaviour of the reinforcement in the case of large-strain problem.

We should emphasize the limitation of the continuum models to reduce the geogrid and aggregates interface to a shear friction constitutive law. In order to investigate deeply the interlocking mechanism and its effect on the vertical stress distribution, the numerical discrete element method can be used to simulate the interlocking mechanism in a more realistic way.

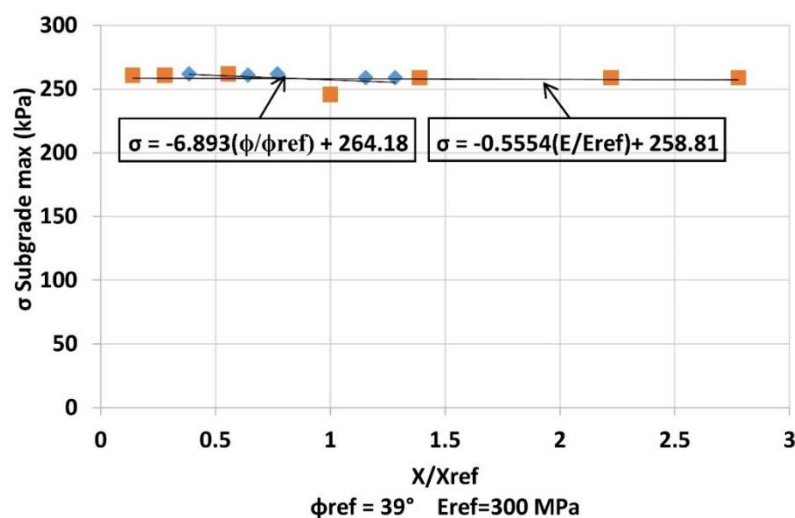


Figure 5.6-3: The interface elastic modulus and friction angle effect on the maximum vertical stress on the subgrade surface.

### 5.6.4. Subgrade / Base course interface effect

The subgrade and base course interface exists in both reinforced and unreinforced models. In fact, when the reinforcement is added the interface between the base course and GSY is added to the interface of the subgrade and the base course. These interface properties are determined in a way to have the subgrade dominance on the interface behaviour. The friction angle and the cohesion of this interface are equal to the subgrade friction angle and cohesion. In this section the variation of the interface friction angle was performed.

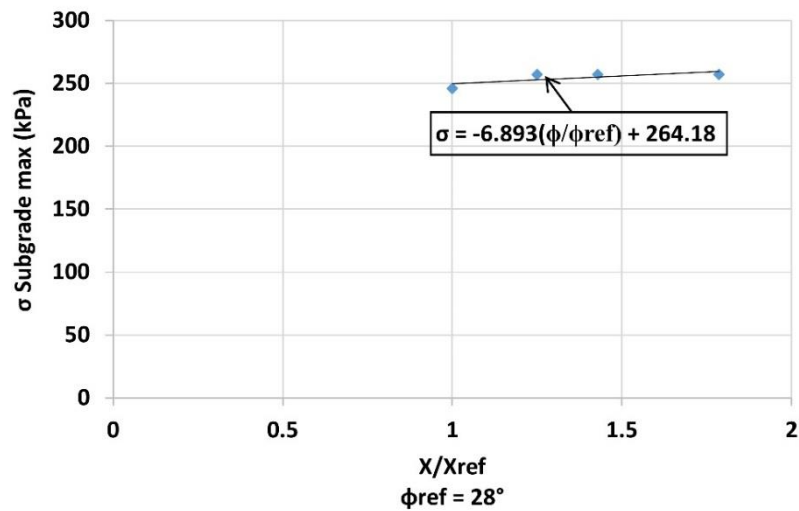


Figure 5.6-4: Interface subgrade/ base course friction angle effect on the maximum vertical stress on the subgrade surface.

Figure 5.6-4 shows the variation of the maximum vertical stress on the subgrade surface with the variation of the subgrade/base course interface friction angle. The result shows no influence of this interface property on the stress distribution.

### 5.6.5. Geosynthetic stiffness effect

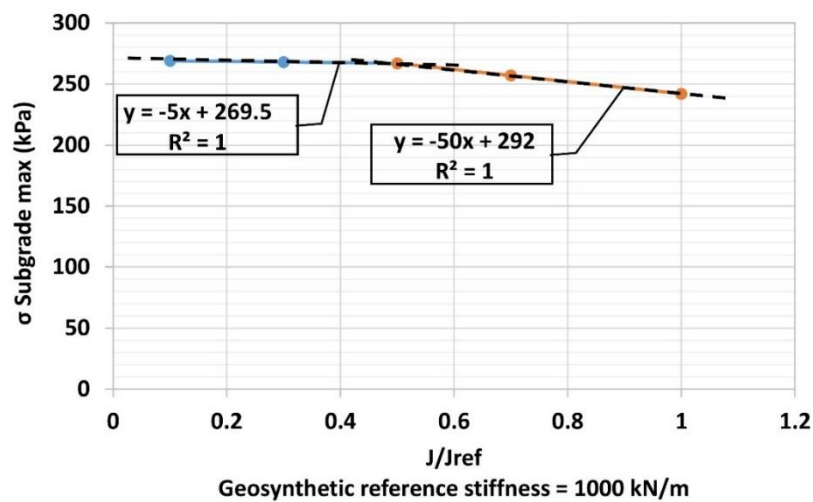


Figure 5.6-5: Geosynthetic stiffness effect on the maximum vertical stress on the subgrade surface.

The geosynthetic stiffness was varied to observe its effect on the maximum vertical subgrade surface stress. It is seen in Figure 5.6-5 that two linear equations are distinguished, one before a reinforcement stiffness equal to 500 kN/m and another following this point. The first linear equation presents a lower slope than the other equation. This shows the important effect of the geosynthetic stiffness on the stress distribution for a stiffness higher than 500 kN/m. In fact, the membrane tension effect is dominant in this large-strain problem model.

## 5.6.6. Geosynthetic position effect

### 5.6.6.a. For 220 mm of base course thickness

The geosynthetic position was changed to study its effect on the stress distribution. The geosynthetic is usually placed at the base course subgrade interface. Two other positions were considered (100 mm in depth and 150 mm in depth). Figure 5.6-6 shows a linear correlation between the position depth ratio and the maximum stress at the subgrade surface. The linear equation shows a relatively small slope, representing the small reinforcement position contribution. Moreover, the interface's position between the subgrade and the base course is considered as the most effective position in this model.

In the numerical model, the base course is modelled as a rigid platform and the deformation of the platform itself is not taken into account. The reinforcement placed into the aggregates platform may affect the platform deformation and the aggregates arrangement, but these behaviours can't be seen in this model.

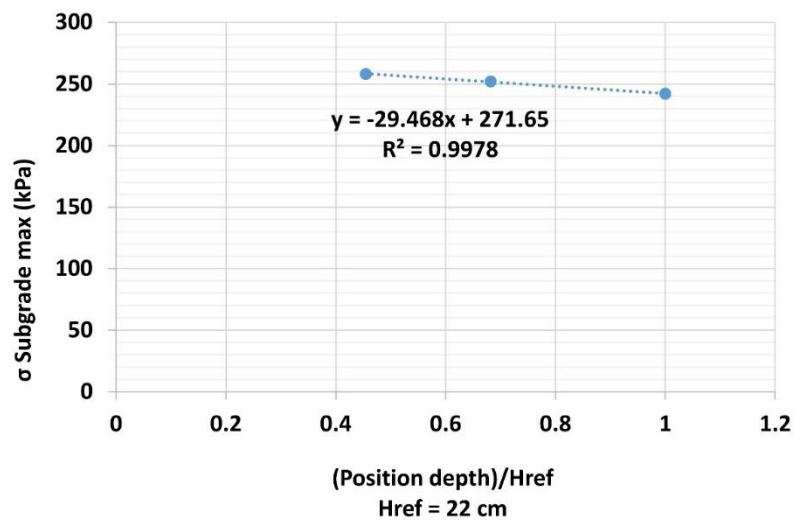


Figure 5.6-6: Geosynthetic position depth effect on the maximum vertical stress on the subgrade surface.

### 5.6.6.b. For 350 mm of base course thickness

The GSY location was as well studied, for the 350 mm base course with a 37° and 45° of base course friction angle.

Figure 5.6-7 shows the variation of the subgrade maximum vertical stress with the reinforcement position. The graphs demonstrate no reinforcement position influence in both cases. In this simulation, the base course is modelled as a rigid platform and the displacement at the top and bottom of the base course is the same.

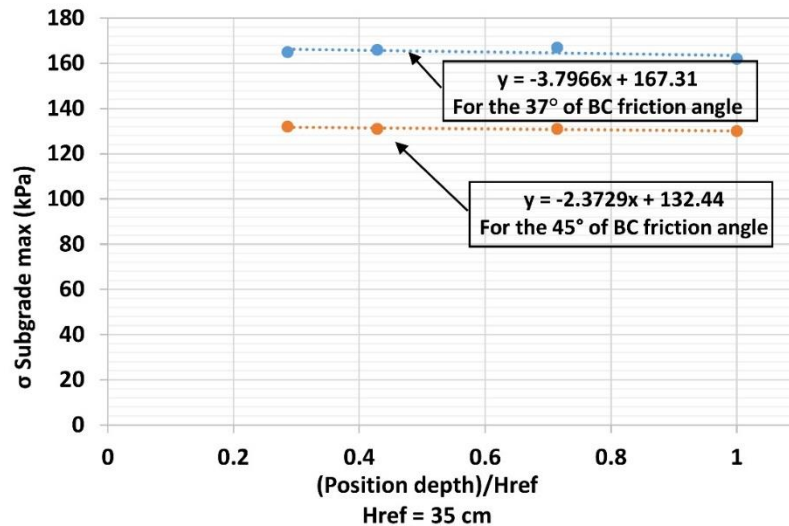


Figure 5.6-7: Geosynthetic position depth effect on the maximum vertical stress on the subgrade surface  
 $H = 350 \text{ mm}$ .

## 5.7. Geosynthetic effect regarding the developed settlement

The parametric study showed that the dominant mechanism in this numerical model is the tension membrane effect. Actually, the reinforcement stiffness affects the stress distribution of the subgrade surface more than the interface base course/reinforcement parameters and the base course elastic modulus. However, the tension membrane mechanism depends on the settlement rate and the tension developed in the reinforcement. So in order to investigate the efficiency of the reinforcement dependency on the surface settlement, the imposed load on the top surface was switched to a maximum imposed displacement instead of a maximum imposed stress. In details, five models with five surface imposed settlement (5, 10, 15, 20 and 25 mm) were performed.

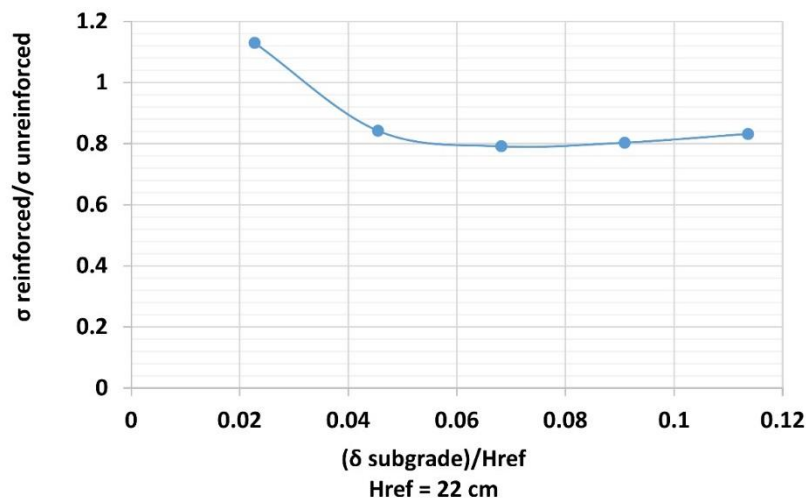


Figure 5.7-1: Ratio of maximum vertical stress on the subgrade in the reinforced and unreinforced model versus the ratio of subgrade maximum settlement over the base course thickness.

Figure 5.7-1 shows the variation of the maximum vertical reinforced and unreinforced stress with the ratio of the surface displacement normalized by the base course thickness. When the surface



displacement is equal to 2% of the base course thickness the figure shows no reinforcement effect on the maximum vertical stress. The effect of the reinforcement increases until the displacement reaches more than 5% of the base course thickness. In fact, when the displacement is equal to 5% of the base course thickness the maximal vertical stress decreases of about 20% and the stress ratio is equal to 0.8 and stays constant at 0.8 with the increasing of the surface settlement.

The tension membrane effect depends on the geosynthetic curvature. Figure 5.7-2 shows the subgrade settlement for the five imposed settlements (5, 10, 15, 20 and 25 mm). In order to compare the curvature of the reinforcement between these five cases, the osculating circle at the point P was drawn geometrically and the radius was determined. The curvature at the point P is the inverse of the radius ( $k=1/R$ ). The following curvatures were determined:

$K_{5\text{ mm}} = 0.00585$ ,  $k_{10\text{ mm}} = 0.0143$ ,  $k_{15\text{ mm}} = 0.0248$ ,  $k_{20\text{ mm}} = 0.0323$  and  $k_{25\text{ mm}} = 0.0444$ .

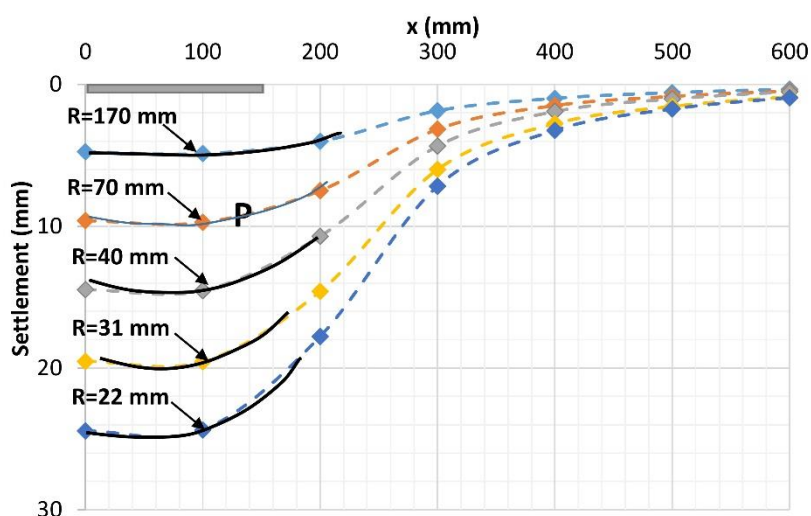


Figure 5.7-2: The subgrade surface settlement for the five imposed settlements models with reinforcement (5, 10, 15, 20 and 25 mm), with the radius of curvature at the point P.

Figure 5.7-3 shows the stress distribution on the subgrade surface of the reinforced and unreinforced models at the five settlement states. The first curves show the vertical stress of the reinforced and unreinforced platform at 5 mm of deformation that correspond to 2% of the base course thickness and 0.00585 of curvature at the point P. It can be seen that there is no effect of reinforcement at this settlement stage, the stress distribution remains the same with and without reinforcement. At 10 mm of settlement, the curvature at P is equal to 0.0143, the reinforcement shows a difference in the stress distribution. The effect of the reinforcement is more obvious with the higher settlement and curvature. In fact, the stress distribution without reinforcement shows a maximum stress at the plate centre line, the reinforcement reduces this maximum stress at the plate centre line by a tension force developed in the membrane. The Figure 5.7-3 shows that in all stages the stress distribution tends to zero at 300 mm from the plate centre line for the reinforced and unreinforced cases, which confirms more the limited role of the confinement mechanism in this model.

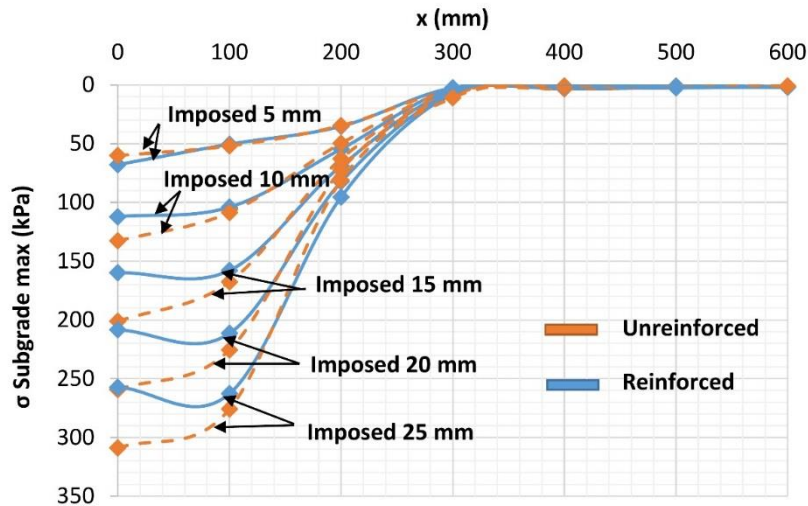


Figure 5.7-3: The subgrade surface vertical stress in the reinforced and unreinforced models for the five imposed settlements (5, 10, 15, 20 and 25 mm) for base course thickness of 220 mm.

## 5.8. Conclusion

In order to better understand the geosynthetic reinforcement behaviour in the case of unpaved roads under soft subgrade a numerical model was developed and calibrated.

The continuous-based differential element method with the software FLAC 3D was used to simulate the behaviour of this structure. The model geometry is based on the physical plate load test. The numerical model was subjected to a monotonic load and compared to the experimental results of the first plate load cycle. The model was solved as a large-strain problem since we are dealing with large displacements. The advantage of using the differential element methods in this case is that the explicit numerical method used by FLAC allows the non-linear computations without additional iterations.

The constitutive model used to simulate the soft subgrade is the Cap-yield model. It is a shear and volumetric hardening/softening model that can simulate the non-linear behaviour of the soil, and it can model the loading-unloading behaviour. Triaxial tests under monotonic and cyclic load were used to calibrate the subgrade properties. In addition, a comparison between a monotonic plate load experimental and numerical test under the soft soil only was performed to validate the soft soil constitutive model and the calibrated parameters under large deformations.

The base course layer was modelled using Mohr-Coulomb constitutive model. The experimental behaviour of the base course under a shear box test showed a non-linear behaviour that can not be taken into consideration in the elastic perfectly plastic model of Mohr-Coulomb.

The reinforcement was modelled as a membrane and characterized by an elastic behaviour in its plane.

The base course/subgrade interface was modelled based on the software recommendations in a way that the soft soil dominates the interface behaviour. The base course/geosynthetic interface was reduced to a shear elastic perfectly plastic behaviour.

Reinforced and unreinforced platforms were simulated with 220 mm of base course thickness and compared to the first cycle of the experimental reinforced and unreinforced results. The numerical

and experimental displacement curves showed that the numerical model can capture the experimental soft soil displacement. Moreover, the stress distribution on the soft subgrade surface was predicted by the numerical model. Differences were shown in the stress values especially in the reinforced model, but it can be assigned to the inaccurate stress measurements in a soft soil. The values can indeed be affected by the sensor displacement and rotation during the loading or the arch effect around the sensor. Moreover, the force developed in the geosynthetic was investigated. Using the fibre optics, the geosynthetic deformation was measured experimentally and from these measurements the force developed in the reinforcement was estimated. The comparison between the numerical and experimental geosynthetic developed force showed that the numerical model can predict the reinforcement behaviour.

The comparison between the reinforced and unreinforced numerical results showed the effect of the reinforcement in reducing the maximum vertical stress on the subgrade, which reduced the surface settlement. Moreover, the results showed no reinforcement effect on the stress distribution angle.

A parametric study was performed to investigate the parameters influences and their participation in the reinforcement mechanisms. The important effect of the base course friction angle and the minor effect of the elastic modulus were shown. In fact, the failure occurs in the base course under large displacement and the analytical elastic approaches are not applicable anymore.

The base course thickness influence was investigated, and it was seen that this parameter affects the most the vertical stress distribution.

The reinforcement parameters were investigated too. This study showed no base course/geosynthetic interface parameters influence on the vertical stress distribution in our simple approximation. It showed the reinforcement stiffness effect on the maximum subgrade stress reduction.

In order to investigate closely the reinforcement developed mechanism, several values of the settlement were imposed as well as their effects on the reinforcement. In fact, different models with different displacements were compared. And the results showed that the reinforcement effect on reducing the maximum stress is highly related to the settlement. These results showed the dominance of the tension membrane mechanism in this model.

It is worth pointing out that, in this model, the non-linear behaviour of the base course related to the grains rearrangements is not taken into consideration. Moreover, the base course/geosynthetic interface is reduced to an elastic perfectly plastic behaviour. More developed model regarding the aggregates behaviour and the interlocking mechanism is needed to better investigate the interface behaviour and the lateral movement of the aggregates under the load.

# Conclusions

---

Using a large-scale laboratory setup for reinforced and unreinforced unpaved roads, the reinforcement's efficiency was highlighted and quantified, the mechanisms developed at the interface were identified for certain geogrid types and the loading type was shown to be an influencing factor on the platform behaviour and the reinforcement's efficiency. More in details, the Conclusions were divided into five parts: which concerns the developed protocol, the base course thickness effect, the geogrids performances, the solicitation effect, and the numerical simulations.

The protocol developed in this research project aimed for the preparation of an artificial soft soil and a laboratory unpaved tested platform in order to control all the environmental conditions, limit the preparation work required for the large in situ tests, and insure the tests repeatability. The quality control tests were an efficient tool used to control the prepared platform properties:

- The quality control tests showed that the developed installation protocol allowed the preparation of homogeneous layers over the depth and the targeted properties can be precisely reached. Moreover, the measured properties showed similarities between the prepared platforms; each platform corresponds to a test.
- The repeatability plate load tests performed verified the protocol efficiency by showing similar results.

The circular plat load tests performed on the reinforced and unreinforced platforms with 350 mm of base course thickness showed that the reinforcement has a negligible effect on the overall platform's behaviour. Moreover, under these test conditions 350 mm of base course thickness is considered good without any reinforcement.

When subjected to the circular plate load test, the platforms with 220 mm of base course thickness showed that:

- The knitted geogrid with the highest stiffness (GSY 2) provided the most significant rut reduction after 10,000 cycles of about 35%, while the knitted geogrid with a smaller stiffness (GSY 1) reduced the rut of about 25%. The extruded geogrid (GSY 3) presented the least significant reduction percentage of 12%.
- A difference between the GSY 1 and GSY 3 behaviour was observed especially on the subgrade surface settlement evolution. Indeed, the results showed that the GSY 3 was more efficient than the GSY 1, under a relatively low settlement. In fact, due to its particular geometry and manufacturing type the GSY 3 performed better in lateral restrain mechanism. However, under large settlement (>2,000 cycles) the GSY 1 in tension performed better with the tension membrane effect.

- The GSY 1 placed at the base course half depth showed a limited effect on the platform improvement. For the same stress level the subgrade showed indeed more settlement. The subgrade performed differently under these two configurations. In fact the GSY 1 in tension, placed at the interface provided a confinement to the subgrade and resulted in the reduction of the subgrade settlement. This mechanism did not exist when the GSY 1 was placed at the base course half depth.
- The maximum stress measured in the subgrade layer was significantly reduced by the reinforcement during the first cycles. However, it increased with the cycles, after 10,000 cycles a reduction of 15% and 10% with the GSY 1 and GSY 2 is observed, whereas no stress reduction is observed with GSY 3 after 10,000 cycles.
- The strain developed in the geogrid showed that 900 mm from the applied load centre is enough to have a natural geogrid anchorage due to the interaction with the aggregates.
- It was shown that under the gravel installation the geogrid GSY 2 and GSY 1 were mobilized under 0.3% of strain. Moreover, after 1,000 cycles the developed strain in the GSY 1 reached 1.5%, and 60% of this developed total strain is a plastic strain.
- A comparison between the existing empirical and analytical design methods showed that these methods overestimate the base course thickness of an unreinforced platform under the proposed test conditions. Moreover, the analytical design method proposed by Giroud and Han (2004) underestimated the reinforced base course thickness using the GSY 3 under the proposed test conditions. These showed that further calibration works are needed to improve these existing methods.

Between the particular plate load and traffic load tests the reinforcement efficiency changed:

- Under both loading types, the GSY 3 and GSY 2 showed the same settlement reduction ratio. Actually, under the plate load test both reinforcements showed a surface settlement reduction of 30% after 10,000 cycles, while under the traffic load they showed 40% of subgrade surface reduction after 1,200 cycles.
- During gravel installation, the GSY strain measured using the fibre optics showed that GSY 3 was more mobilized than GSY 2, probably because of its particular geometry and its capacity to interlock with the aggregates.
- Moreover, the developed strain in the geogrid under the first load showed that the GSY 3 was more mobilized than the GSY 2, and this pursued over the cycles. This can explain its more significant efficiency under a more localized load

The comparison between the plate and traffic load test showed that the traffic load test is a more damaging load. Under the first 10 cycles, the base course surface settlement under the traffic load reached more than 50 mm of apparent rut. Under the traffic load the gravel lateral movement and surface repulsion was observed especially on the surface, which was not seen under the plate load test. In addition to the base course important thickness variation, the subgrade presented a higher settlement under the traffic load.

However, the results analysis of the circular and particular plate load tests showed that the extruded geogrid GSY 3 performed better under the particular plate load test. This can be due

to the fact that under a more localized load the aggregates lateral restraint movement is more important, so the GSY 3 is more mobilized.

A continuous-based differential element method was developed using FLAC 3D software to model the first monotonic applied load under the reinforced and unreinforced platforms:

- The results showed that the calibrated model predicted the experimental subgrade stress distribution, the subgrade settlement, and the strain developed in the geogrid.
- The analysis of the reinforced and unreinforced numerical models showed that the reinforcement reduced the surface settlement and the maximum stress, but showed no effect on the stress distribution angle.
- The parametric study showed that the base course factor that affected the most the subgrade stress distribution is the friction angle. This proved that failure occurs in the base course layer under the first cycle, and that the analytical methods based on the elastic approaches are not applicable anymore.
- The base course/geosynthetic interface parametric study showed no interface influence on the vertical stress distribution. This proves that the reduction of the interface to an elastic perfectly plastic behaviour do not simulate adequately the geogrids' apertures, it aggregates interlocking mechanisms, and reduces the geogrid reinforcement mechanism to a tension membrane.



# Further perspectives

---

This research project contributed to improve the knowledge obtained over thirty years in this field. More importantly, this work left a precious tool in the hands of future researchers, by main of the developed SAT machine and the valid testing protocol. In fact, now that the protocol and the traffic machine SAT were developed and validated, series of tests and investigations can be performed, in an optimized time and preparation works since this was one the objectives while developing this protocol. Here are some further tests suggestions:

- Tests using different products and manufacturing types such as geotextile, geocell, extruded biaxial geogrid, and knitted geogrid with different aperture size.
- Test using two GSY 1 layers, one placed at the interface and one placed at the base course half depth.
- Tests using the same geogrids, with an initial applied tension before the gravel installation. In fact, a geogrid subjected to a pretension may provide a better contribution to the platform improvement.
- For more precise results under the SAT machine, a dense base course platform is needed, even if it does not represent the most used base course material in France.
- In situ tests using real compactors can be performed under the SAT machine, in order to eliminate the first settlements that can be eliminated under the heavy compactors circulation on site.
- Further tests can be performed using the SAT machine with a dual wheel in order to increase the wheel contact area and increase the applied load to 40 kN.
- Tests using a saturated subgrade soil, in order to investigate the pore pressure effect on the platform behaviour. Moreover, a geocomposite combining the drainage, separation and reinforcement functions product can be tested under these conditions.
- The performed tests showed that each geogrid product provide improvements based on its specific mechanism. In fact, the extruded geogrid provided the lateral restrain mechanism, while the knitted geogrid, due to its high tensile stiffness, provided the tension membrane effect. A more efficient product can be a product that provides both mechanisms.

However, the developed numerical model showed limitations regarding the base course non-linear behaviour and the geogrid apertures and aggregates interaction. A more realistic model is needed to better investigate the interface behaviour and the aggregates lateral movement. In fact, this model can be a combination between a continuous domain representing the soft subgrade soil and a discontinuous domain representing the aggregates and geogrids. Moreover, more complex models are needed to simulate the material behaviour under cyclic load.





# Bibliography

---

- AASHTO. (1993). AASHTO Guide For Design Of Pavement Structures, pp. II–69.
- AASHTO Committee 4E, Geosynthetic reinforcement of the aggregate base/subbase courses of pavement structures: Report prepared by AASHTO Committee 4E
- Abu-Farsakh, Murad Y. & Chen Q. (2012). Evaluation of the base/subgrade soil under repeated loading: phase II, in-box and ALF cyclic plate load tests.
- Abu-Farsakh, Murad Y., Akond, I. & Chen Q. (2016). Evaluating the performance of geosynthetic-reinforced unpaved roads using plate load tests. *International Journal of Pavement Engineering*, 17(10), pp.901-912.
- Aubry D. & Hujeux JC. (1982). A double memory model with multiple mechanisms for cyclic soil behaviour.
- Akond I. (2012). Laboratory Evaluation of Geosynthetics to Stabilize/Reinforce the Subgrade/Base in Unpaved Roadways.
- Al-Tabbaa A. & Wood D. M. (1989). An experimentally based bubble model for clay. In *International Symposium on Numerical Models in Geomechanics*, Elsevier Applied Science Publishers (3rd: 1989), pp. 91-99.
- Al Tabbaa, A. & O'Reilly M. P. (1990). Some observations on the modified Cam-clay bubble model. In *Proceedings of the 3rd International Conference on Numerical Methods in Engineering*, Elsevier, Vol. 2, pp. 779-787.
- Allen T. M. & Bathurst R. J. (1994). Characterization of geosynthetic load-strain behavior after installation damage. *Geosynthetics International*, 1(2), pp.181-199.
- Bathurst R. J., Huang B. & Allen T. M., (2011). Analysis of installation damage tests for LRFD calibration of reinforced soil structures. *Geotextiles and Geomembranes*, 29(3), pp.323-334.
- Berg R. R. (2000). Geosynthetic Reinforcement of the Aggregate Base/Subbase Courses of Pavement Structures.
- Bhandari A. & Han J. (2010). Investigation of geotextile–soil interaction under a cyclic vertical load using the discrete element method. *Geotextiles and geomembranes*, 28(1), pp.33-43.
- Bloise N. & Ucciardo S. (2000). On site test of reinforced freeway with high-strength geosynthetics. In *Eurogeo 2000: Proceedings of the second European geosynthetics conference. Volume 1: mercer lecture, keynote lectures, geotechnical applications*.
- Brady K. C., McMahon W. & Lamming G. (1994). Thirty-year ageing of plastics. Project Report 11. Transport Research Laboratory, E472A/BG, ISSN, pp.0968-4083.
- Brown S. F., Kwan J. & Thom N. H. (2007). Identifying the key parameters that influence geogrid reinforcement of railway ballast. *Geotextiles and Geomembranes*, 25(6), pp.326-335.
- Burd H. J. & Houlsby G. T. (1986). A large strain finite element formulation for one dimensional membrane elements. *Computers and Geotechnics*, 2(1), pp.3-22.

- Billiaux D. & Cundall P. (1993). Simulation des géomatériaux par la méthode des éléments Lagrangiens. *Revue française de Géotechnique*, (63), pp. 9-21.
- Cancelli A. & Montanelli F. (1999). In-ground test for geosynthetic reinforced flexible paved roads (No. Volume 2).
- Calvarano L. S., Palamara R., Leonardi L. & Moraci N. (2016). Unpaved road reinforced with geosynthetics. *Procedia Engineering*, 158, pp.296-301.
- Chen, Q., Abu-Farsakh M. & Sharma, R. (2009). Experimental and analytical studies of reinforced crushed limestone. *Geotextiles and Geomembranes*, 27(5), pp.357-367.
- Christopher, B. R., Cuelho, E. V. & Perknis S. W. (2008). Development of geogrid junction strength requirements for reinforced roadway base design. In *Proceedings of GeoAmericas 2008 Conference*, Cancun, Mexico, pp. 1003-1012.
- Collin, J. G., Kinney T. C. & Fu, X. (1996). Full scale highway load test of flexible pavement systems with geogrid reinforced base courses. *Geosynthetics International*, 3(4), pp.537-549.
- Collins, I. F. & Houlsby G. T. (1997). Application of thermomechanical principles to the modelling of geotechnical materials. *Proceedings of the Royal Society of London. Series A: Mathematical, Physical and Engineering Sciences*, 453(1964), pp.1975-2001.
- Collins I. F. & Hilder T. (2002). A theoretical framework for constructing elastic/plastic constitutive models of triaxial tests. *International Journal for Numerical and Analytical Methods in Geomechanics*, 26(13), pp.1313-1347.
- Cook J., Dobie M. & Blackman D. (2016). The development of APT methodology in the application and derivation of geosynthetic benefits in roadway design. In *The Roles of Accelerated Pavement Testing in Pavement Sustainability* (pp. 257-275). Springer, Cham.
- Cuelho E. & Perkins S. (2009). Field investigation of geosynthetics used for subgrade stabilization (No. FHWA/MT-09-003/8193). Montana. Dept. of Transportation. Research Programs.
- Cuelho E. V. & Perkins S. W. (2017). Geosynthetic subgrade stabilization–Field testing and design method calibration. *Transportation Geotechnics*, 10, pp.22-34.
- Cundall P. A. & Hart R. D. (1993). Numerical modeling of discontinua. In *Analysis and design methods*, Pergamon, pp. 231-243.
- Crouch R. S., Wolf J. P. & Dafalias Y. F. (1994). Unified critical-state bounding-surface plasticity model for soil. *Journal of engineering mechanics*, 120(11), pp.2251-2270.
- Demir A., Laman M., Yildiz A., & Ornek M. (2013). Large scale field tests on geogrid-reinforced granular fill underlain by clay soil. *Geotextiles and Geomembranes*, 38, pp.1-15.
- Desai C. S. (1980). A general basis for yield, failure and potential functions in plasticity. *International Journal for Numerical and Analytical Methods in Geomechanics*, 4(4), pp.361-375.
- DiMaggio F. L., & Sandler I. S. (1971). Material model for granular soils. *Journal of Engineering Mechanics*.
- Drucker D. C. (1957). Soil mechanics and work-hardening theories of plasticity. *Trans. ASCE*, 122, pp.338-346.
- Dong Y. L., Han J. & Bai X. H. (2010). Bearing capacities of geogrid-reinforced sand bases under static loading. In *Ground Improvement and Geosynthetics*, pp. 275-281.

- Dong Y. L., Han J. & Bai X. H. (2011). Numerical analysis of tensile behavior of geogrids with rectangular and triangular apertures. *Geotextiles and Geomembranes*, 29(2), pp.83-91.
- FHWA , Federal Highway Administration (2008). “Geosynthetic design and construction guidelines reference manual.” FHWA NHI-07-092, U.S. Dept. of Transportation, Federal Highway Administration, Washington, DC.
- Floss R. & Gold G. (1994). Causes for the improved bearing behaviour of the reinforced two-layer system. In Proc. 5th Int. Conf. Geotextiles, Geomembranes, and Related Products, Vol.1, pp. 147-150.
- GEIPOT (2008). Annual statistical report on paved and unpaved roads in Brazil. GEIPOT/Brazilian Ministry of Transportation, at. [www.geipot.gov.br/anuario2001/rodoviario/rodo.htm](http://www.geipot.gov.br/anuario2001/rodoviario/rodo.htm) (in Portuguese).
- Gabr M. (2001). Cyclic plate loading tests on geogrid reinforced roads. Research rep. To Tensar earth technologies, inc.
- Ghosh C. & Madhav M. R. (1994). Reinforced granular fill-soft soil system: Membrane effect. *Geotextiles and Geomembranes*, 13(11), pp.743-759.
- Giroud J. P. & Noiray L. (1981). Geotextile-reinforced unpaved road design. *Journal of Geotechnical and Geoenvironmental Engineering*, 107(ASCE 16489).
- Giroud J. P., Ah-Line C., & Bonaparte R. (1984). Design of unpaved roads and trafficked areas with geogrids. In *Polymer grid reinforcement*, Thomas Telford Publishing, pp. 116-127.
- Giroud J. P. & Han J. (2004). Design method for geogrid-reinforced unpaved roads. II. Calibration and applications. *Journal of Geotechnical and Geoenvironmental Engineering*, 130(8), pp.787 - 797.
- Giroud J. P. (2009). An assessment of the use of geogrids in unpaved roads and unpaved areas. In jubilee symposium on polymer geogrid reinforcement. Identifying the direction of future research, ice, London, 8th September.
- Giroud J. P. & Han J. (2016). Mechanisms governing the performance of unpaved roads incorporating geosynthetics. In *Geosynthetics*, Vol. 34, No. 1.
- Greenwood J. H. (1998). The nature of mechanical damage. In *Seminar Volume on installation damage in geosynthetics*, Leatherhead, Surrey, UK.
- Ghaboussi J. & Momen H. (1979, April). Plasticity model for cyclic behavior of sands. In 3rd international conference on numerical methods in geomechanics, Aachen. Balkema, pp. 423-434.
- Hammit G. M. & Aspinall Iii W. (1970). Thickness Requirements for Unsurfaced Roads and Airfields; Bare Base Support (No. AEWES-TR-S-70-5). Army Engineer Waterways Experiment Station Vicksburg Miss.
- Han J., Zhang Y. & Parsons R. L. (2008). Development of a performance-based laboratory test method for evaluating geosynthetic-soil confinement, No. 08- pp.2380.
- Hufenus R., Rügger R., Flum D. & Sterba I. J. (2005). Strength reduction factors due to installation damage of reinforcing geosynthetics. *Geotextiles and Geomembranes*, 23(5), pp.401-424.
- Hufenus R., Rueegger R., Banjac R., Mayor P., Springman S. M. & Brönnimann R. (2006). Full-scale field tests on geosynthetic reinforced unpaved roads on soft subgrade. *Geotextiles and Geomembranes*, 24(1), pp.21-37.
- Huntington G. & Ksaibati K. (2000). Evaluation of geogrid-reinforced granular base. *Geotechnical fabrics report*, 18(1).

- Hussein M. G. & Meguid M. A. (2016). A three-dimensional finite element approach for modeling biaxial geogrid with application to geogrid-reinforced soils. *Geotextiles and Geomembranes*, 44(3), pp.295-307.
- Jenner C. G. & Paul J. (2000). Lessons learned from 20 years experience of geosynthetic reinforcement on pavement foundations. In *EUROGEO 2000: Proceedings of the 2nd European geosynthetics conference. Volume 1: Mercer lecture, keynote lectures, geotechnical applications*.
- Jersey S. R., Tingle J. S., Norwood G. J., Kwon J., & Wayne M. (2012). Full-scale evaluation of geogrid-reinforced thin flexible pavements. *Transportation research record*, 2310(1), pp.61-71.
- Kareem A. I., Sofia G. G. & Ibrahim S. F. (2012). Experimental Study on Geogrid-Reinforced Subbase over Soft Subgrade Soil under Repeated Loading. *Journal of Engineering and Sustainable Development*, 16(3), pp.218-240.
- Kattan A. (1990). Fluage et consolidation des sols satures et quasi-satures-analyse numerique. These de doctorat de l'ecole nationale des ponts et chaussees.
- Kim W. H., Edil T. B., Benson C. H. & Tanyu B. F. (2006). Deflection of prototype geosynthetic-reinforced working platforms over soft subgrade. *Transportation research record*, 1975(1), pp.137- 145.
- Knapton J. & Austin R. A. (1996). Laboratory testing of reinforced unpaved roads. *Earth reinforcement*, pp.615-618.
- Koemer G. R. & Koemer R. M. (1990). The installation survivability of geotextiles and geogrids. *Geotextiles, Geomembranes, and Related Products: Canals, reservoirs and dams. Waste disposal. Geomembrane properties and testing. Mechanical damage. Creep and durability*.
- Khong C. D. & Yu H. S. (2002). Computational aspects of a unified critical state model for clay and sand. *Proc. of 8th NUMOG*, pp.71-277.
- Leng J. & Gabr M. A. (2006). Deformation–Resistance Model for Geogrid-Reinforced Unpaved Road. *Transportation research record*, 1975(1) , pp.146-154.
- Lee S. R. & Oh S. (1995). An anisotropic hardening constitutive model based on generalized isotropic hardening rule for modelling clay behaviour. *International journal for numerical and analytical methods in geomechanics*, 19(10), pp.683-703.
- Liu H. & Ling H. I. (2007). Unified elastoplastic–viscoplastic bounding surface model of geosynthetics and its applications to geosynthetic reinforced soil-retaining wall analysis. *Journal of engineering mechanics*, 133(7), pp.801-815.
- Martin D. (1988). Die trennfunktion der geotextilien in ungebundenen verkehrswegebefestigungen. 1. Tagung kunststoffe in der geotechnik, hamburg, pp.77-86.
- Maxwell S. (2005). Effectiveness of geosynthetics in stabilizing soft subgrades. *Wisconsin Highway Research Program*.
- Maleki M., Dubujet P. & Cambou B. (2000). Modélisation hiérarchisée du comportement des sols. *Revue Française de génie civil*, 4(7-8), pp.895-928.
- Manzari M. T. & Dafalias Y. F. (1997). A critical state two-surface plasticity model for sands. *Geotechnique*, 47(2), pp.255-272.
- Matsuoka H., Yao Y. P. & Sun D. A. (2005). SMP criterion-based unified constitutive model for geomaterials. In *Soil Constitutive Models: Evaluation, Selection, and Calibration*. pp.333-357.
- Monnet J. & Gielly J. (1979). Détermination d'une loi de comportement pour le cisaillement des sols pulvérulents-Application au calcul d'essais triaxiaux. *Revue Française de Géotechnique*, (7), pp.45 - 56.

- McDowell G. R., Harireche O., Konietzky H., Brown S. F. & Thom N. H. (2006). Discrete element modelling of geogrid-reinforced aggregates. *Proceedings of the Institution of Civil Engineers-Geotechnical Engineering*, 159(1), pp.35-48.
- Mekkawy M. M., White D. J., Suleiman M. T. & Jahan C. T. (2011). Mechanically reinforced granular shoulders on soft subgrade: Laboratory and full scale studies. *Geotextiles and Geomembranes*, 29(2), pp.149-160.
- Meyer N., & Elias J. M. (1999). Dimensionierung von Oberbauten von Verkehrsflächen unter Einsatz von multifunktionalen Geogrids zur Stabilisierung des Untergrundes. 6. Tagung Kunststoffe in der Geotechnik, Munich, pp.261-268.
- Milligan G. W. E., Jewell R. A., Housley G. T. & Burd H. J. (1989). A new approach to the design of unpaved roads-Part 1. *Ground Engineering*, 22(3).
- Miura N., Sakai A., Taesiri Y., Yamanouchi T., & Yasuhara K. (1990). Polymer grid reinforced pavement on soft clay grounds. *Geotextiles and Geomembranes*, 9(1), pp.99-123.
- Müller-Rochholz J. & Koslowski C. (1996). Creep prediction. In *Proceedings of the 1st European Conference on Geosynthetics, EuroGeo1, Maastricht, the Netherlands* .pp.1027-1030.
- Norwood G. J. & Tingle J. S. (2014). Performance of Geogrid-Stabilized Flexible Pavements. US Army Engineer Research and Development Center, Geotechnical and Structures Laboratory.
- Orsat P., Khay M., & McCreath M. (1998). Study on creep rupture of polyester tendons: Full-scale tests. In *Proceedings of the Sixth International Conference on Geosynthetics*. Vol. 2, pp.675 - 678.
- Palmeira E. M. & Antunes L. G. (2010). Large-scale tests on geosynthetic reinforced unpaved roads subjected to surface maintenance. *Geotextiles and Geomembranes*, 28(6), pp.547-558.
- Perkins S. W. & Ismeik M. (1997). A synthesis and evaluation of geosynthetic-reinforced base layers in flexible pavements-part i. *Geosynthetics International*, 4(6), pp.549-604.
- Perkins S. W. (2000). Constitutive modeling of geosynthetics. *Geotextiles and Geomembranes*, 18(5), pp. 273-292.
- Perkins S. W., Christopher B. R., Cuelho E. L., Eiksund G. R., Schwartz C. S. & Svanø G. (2009). A mechanistic-empirical model for base-reinforced flexible pavements. *International Journal of Pavement Engineering*, 10(2), pp.101-114.
- Perkins S. W., Christopher B. R., Lacina B. A. & Klompaker J. (2012). Mechanistic-empirical modeling of geosynthetic-reinforced unpaved roads. *International Journal of Geomechanics*, 12(4), pp.370-380.
- Qian Y., Han J., Pokharel S. K. & Parsons R. L. (2011). Stress analysis on triangular-aperture geogrid-reinforced bases over weak subgrade under cyclic loading: An experimental study. *Transportation research record*, 2204(1), pp.83-91.
- Qian Y., Han J., Pokharel S. K. & Parsons R. L. (2013). Performance of triangular aperture geogrid-reinforced base courses over weak subgrade under cyclic loading. *Journal of Materials in Civil Engineering*, 25(8), pp.1013-1021.
- Robinson W. J., Tingle J. S. & Norwood G. J. (2017). Full-Scale Accelerated Testing of Multi-axial Geogrid Stabilized Flexible Pavements (No. ERDC/GSL TR-17-9). ERDC-GSL Vicksburg United States.
- Roscoe K. H., Schofield A. & Wroth A. P. (1958). On the yielding of soils. *Geotechnique*, 8(1), pp. 22 - 53.
- Roscoe K. H. (1968). Soils and model tests. *Journal of strain analysis*, 3(1), pp. 57-64.

- Sarici T., Demir A., Tutumluer E., Demir B., Gungor A. G., Epsileli S. E. & Ok B. (2016). Evaluation of geogrid reinforced unpaved roads using large scale tests. In Proceedings of the 6th European Congress on Geosynthetics, Ljubljana, Slovenia.
- Szatmári T. (2016). Investigation of the geogrid-granular soil combination layer with laboratory multi-level shear box test.
- Sun X., Han J., Kwon J., Parsons R. L. & Wayne M. H. (2015). Radial stresses and resilient deformations of geogrid-stabilized unpaved roads under cyclic plate loading tests. *Geotextiles and Geomembranes*, 43(5), pp.440-449.
- Schanz T., Vermeer P. A. & Bonnier P. G. (1999). The hardening soil model: formulation and verification. *Beyond 2000 in computational geotechnics*, pp.281-296.
- Schwer L. E. & Murray Y. D. (1994). A three-invariant smooth cap model with mixed hardening. *International journal for numerical and analytical methods in geomechanics*, 18(10), pp.657-688
- Tang X., Chehab G. R. & Palomino A. (2008). Evaluation of geogrids for stabilising weak pavement subgrade. *International Journal of Pavement Engineering*, 9(6), pp.413-429.
- Tang X., Abu-Farsakh M., Hanandeh S., & Chen Q. (2015). Performance of reinforced–stabilized unpaved test sections built over native soft soil under full-scale moving wheel loads. *Transportation Research Record*, 2511(1), pp.81-89.
- Tang, X., Stoffels S. M., & Palomino A. M. (2016). Mechanistic-empirical approach to characterizing permanent deformation of reinforced soft soil subgrade. *Geotextiles and Geomembranes*, 44(3), pp.429-441.
- Vermeer P. A. (1978). A double hardening model for sand. *Geotechnique*, 28(4), pp.413-433.
- Walters D. L., Allen T. M. & Bathurst R. J. (2002). Conversion of geosynthetic strain to load using reinforcement stiffness. *Geosynthetics International*, 9(5-6), pp.483-523.
- Watts G. R. A., & Brady K. C. (1990). Site damage trials on geotextiles. In *Fourth International Conference on Geotextiles, Geomembranes and Related Products*, Den Haag. pp. 603-607.
- Watts G. R. A., Blackman D. I. & Jenner C. G. (2004). The performance of reinforced unpaved sub-bases subjected to trafficking.
- Watn A., & Chew S. H. (2002). Geosynthetic damage-from laboratory to field. In *geosynthetics: state of the art-recent developments. Proceedings of the seventh international conference on geosynthetics, 7-icg, held 22-27 september 2002, nice, france. Volume 4.*
- Yang X., Han J., Pokharel S. K., Manandhar C., Parsons R. L., Leshchinsky D., & Halahmi I. (2012). Accelerated pavement testing of unpaved roads with geocell-reinforced sand bases. *Geotextiles and Geomembranes*, 32, pp.95-103.
- Yu H. S. (1994). State parameter from self-boring pressuremeter tests in sand. *Journal of geotechnical engineering*, 120(12), pp.2118-2135.
- Ziegler H. (1968). *Principles of Structural Stability*, Waltham, Mass. Blaisdell Pub. Co.
- Ziegler H., & Wehrli C. (1987). Free Energy and the Dissipation Function. *Advances in applied mechanics*, pp.183.



FOLIO ADMINISTRATIF

THESE DE L'UNIVERSITE DE LYON OPEREE AU SEIN DE L'INSA LYON

NOM : KHOUEIRY

DATE de SOUTENANCE : 16/04/2020

Prénoms : Nicole

TITRE : Étude du comportement des plateformes granulaires renforcées par géosynthétiques sur sol de faible portance: approches expérimentale et numérique

NATURE : Doctorat

Numéro d'ordre : 2020LYSEI027

Ecole doctorale : MEGA (Mécanique-Energétique-Génie Civil-Acoustique)

Spécialité : Génie Civil

RESUME :

Les géosynthétiques sont utilisés depuis les années 70 dans le renforcement des plateformes granulaires reposant sur des sols de faible portance pour des applications de routes non revêtues. La complexité des mécanismes développés et la diversité des produits de renforcement nécessitent encore d'étudier ces plateformes renforcées. Un essai au laboratoire permettant de tester des plateformes à échelle réelle a été développé. Une plateforme granulaire non revêtue reposant sur un sol de faible portance a été reproduite. Un protocole de mise en place de ce sol a été élaboré pour assurer son homogénéité et la répétabilité des essais. Une instrumentation spécifique a été développée pour collecter le maximum de mesures utiles pour l'interprétation du transfert de charge et du comportement des géogrilles utilisées. Trois types de géogrille ont été testées : une géogrille extrudée et deux géogrilles tricotées de rigidité différente. Après de nombreux essais de faisabilité, dix essais ont été effectués sous un chargement cyclique sur plaque circulaire, la plateforme testée a été placée dans un banc d'essai de 1,8 m de large, 1,9 m de long et 1,1 m de haut. Sur la base du même protocole de mise en œuvre, des essais de circulation avec un Simulateur Accélérateur de Trafic (SAT) ont été effectués. Ce simulateur a été spécifiquement conçu et construit pour cette application. Pour ces essais, la plateforme testée a été placée dans le banc d'essai allongé à 5 m. La plateforme a été soumise à deux types de sollicitations : un chargement cyclique sur plaque et un chargement de circulation. Des essais de répétabilité ont permis de vérifier le protocole mis en place. A partir des essais, plusieurs observations ont pu être faites sur le comportement des plateformes granulaires, le sol peu porteur, et sur l'efficacité du renforcement. De plus, ces essais ont permis de montrer que le chargement de circulation est beaucoup plus endommageant que le chargement sur plaque. Parallèlement à ces essais, un modèle numérique a été développé en se basant sur la méthode des différences finies avec le logiciel FLAC 3D. Cette modélisation a permis de prédire le comportement de la plateforme sous le premier chargement de plaque.

MOTS-CLÉS : Routes non revêtue, essai à grand échelle, géosynthétique, géogrille, sol de faible portance, sol support, couche de forme, charge cyclique sur plaque, charge de circulation, modèle numérique, méthode des différences finies.

Laboratoire (s) de recherche : Laboratoire GEOMAS

Directeur de thèse: Ali DAOUADJI  
Laurent Briançon

Président de jury :

Composition du jury : Pascal VILLARD  
Philippe DELMAS  
Mathilde RIOT  
Laurent BRIANÇON  
Philippe REIFFSTECK  
Nathalie TOUZE  
Ali DAOUADJI